Monitoring Glycation through the Intrinsic Fluorescence of Biological Fluorophores.

Rhona Muir

A thesis submitted to the University of Strathclyde for the degree of Doctor of Philosophy with Integrated Study:

Optical Medical Imaging with Healthcare Innovation & Entrepreneurship

Photophysics Research Group

Department of Physics

University of Strathclyde

Glasgow

2022

.

Abstract

The high blood glucose levels associated with diabetes affect various cells and proteins in the body. In response to high blood glucose the proteins collagen, keratin, and human serum albumin (HSA) experience glycation, and the cofactor reduced nicotinamide adenine dinucleotide (NADH) is also known to be affected in some way. This work aims to establish if the intrinsic fluorescence of these compounds could be used to monitor the impact of glucose, and thus offer an alternative method to monitoring long term glycaemic control.

We have studied the evolution of the intrinsic fluorescence of four compounds in response to glucose *in vitro* using steady state and time-resolved fluorescence spectroscopy techniques. For NADH, although significant changes were seen in the sample when in a phosphate buffered saline (PBS) buffer, no similar changes in fluorescence were observed when a Trizma buffer was used. As such, we conclude that glycation does not have an impact on the intrinsic fluorescence of NADH.

Changes in the intrinsic fluorescence of collagen, keratin, and HSA however were observed. For collagen, TRES revealed changes in the intrinsic fluorescence kinetics, caused by both collagen aggregation and glycation. In keratin, the addition of glucose caused an increase in the fluorescence intensity at the characteristic wavelength of 460 nm, due to faster formation of new cross-links, and glucose may also cause the formation of two new fluorescent complexes that emit at longer wavelengths. For HSA, fluorescence intensity decay analysis indicates that glycation can be detected through a decrease in the short lifetime component when decays are fitted to a 2-exponential model, however fitting to a non-Debye model more clearly highlights the impact of glucose.

We also studied the intrinsic fluoresce of mouse skin and human fingernails. In an initial pilot study on mouse skin, our results suggested that collagen, keratin, and NADH can be detected from a skin autofluorescence (AF) measurement, and that there may be a relationship between skin AF and blood glucose. Using fingernails, it appeared that although both the peak emission wavelengths, and the fitted exponential parameters indicated that we can detect keratin fluorescence, there was no evidence that glycated keratin can be sensed through a nail clipping. Furthermore, neither our steady state or time resolved analysis

exposed a correlation between any of the extracted fluorescence parameters and glycated haemoglobin (HbA1c).

In conclusion, monitoring the intrinsic fluorescence of particular biological proteins *in vitro* suggests that this method could be used as a method to monitor long term glycaemic control in patients with diabetes. Further studies would be required to translate these findings into an in vivo environment.

Acknowledgements

I am grateful for all the support I have received over the past 4 years while working on my PhD. Firstly, I would first like to thank my supervisor Dr. Olaf Rolinski for his support and guidance throughout the entirety of this project. In particular, I would like to thank him for his help in exploring new avenues of research, which allowed me to keep working during the restrictions of the Covid 19 pandemic. I would also like to thank my supervisor Prof. Shareen Forbes, who guided me in my *in vivo* research, and Dr Alastair Wark, whose input on our NADH work was invaluable.

I would also like to thank all those at the Optima CDT for the opportunity to pursue this PhD. This program also showed me the many different career paths that a PhD can lead to through the courses undertaken at the University of Edinburgh.

Finally, I would like to thank my family and friends, for their continued support and belief in me. I couldn't have done it without them.

Publications and Conference Proceedings

Muir, R.; Forbes, S.; Birch D.J.S.; Rolinski, O.J. Collagen glycation detected by changes in its intrinsic fluorescence. Oral Presentation, Strathclyde Doctoral School Multidisciplinary Symposium 2020, Glasgow.

Muir, R.; Forbes, S.; Birch, D.J.S.; Vyshemirsky, V.; Rolinski, O.J. Collagen Glycation Detected by Its Intrinsic Fluorescence. *The Journal of Physical Chemistry B* **2021**, *125* (39), 11058-11066.

O.Rolinski, R.Muir, Intrinsic fluorescence kinetics in proteins, Chapter 39 in Springer Series on Fluorescence, 4243, in press.

Hargreaves, T.; Muir, R.; As AI powers more and more medical technology don't overlook patenting. The Scotsman 2021.

Muir, R.; Forbes, S.; Birch D.J.S.; Rolinski, O.J. Monitoring glycation using the intrinsic fluorescence of biological fluorophores. Oral Presentation, SPIE Optics and Photonics 2022, San Diego.

Muir, R.; Forbes, S.; Birch D.J.S.; Rolinski, O.J. Keratin intrinsic fluorescence as a mechanism for non-invasive monitoring of its glycation. *Methods and Applications in Florescence* (in press).

Abbreviations

AF	Autofluorescence
AFR	Autofluorescence reader
AGE	Advanced glycation end products
AI	Artificial Intelligence
ALI	Arginine–lysine imidazole
ATP	Adenosine triphosphate
ATR	Attenuated total reflectance
CGM	Continuous glucose monitoring
CML	N-carboxymethyllysine
DNA	Deoxyribonucleic acid
ECM	Extra cellular matrix
FAD	flavin adenine dinucleotide
FLIM	Fluorescence Lifetime Imaging Microscopy
FRET	Förster Resonance Energy Transfer
FTIR	Fourier transform infrared spectroscopy
GA	Glycated albumin
HSA	Human serum albumin
IC	Internal conversion
IDO	Indoleamine 2,3-dioxygenase
IF	Intermediate filament
IRF	Instrumental response function
ISC	Inter system crossing
LASER	Light amplification by the stimulated emission of radiation
LED	Light emitting diode
LOX	Lysyl oxidase
MCA	Multi-channel analyser
MGO	Methylglyoxa
NAD	Nicotinamide adenine dinucleotide
NADH	Reduced nicotinamide adenine dinucleotide
NADP	Nicotinamide adenine dinucleotide phosphate
NADPH	Reduced nicotinamide adenine dinucleotide phosphate
NHS	National health service
NICE	National Institute for Health and Care Excellence
NIR	Near infra red
NLLS	Nonlinear least squares method
PBS	Phosphate buffered saline
PMT	Photomultiplier detector
RAGE	Receptor for AGEs
SIF	Skin intrinsic fluorescence
SMBG	Self-monitoring of blood glucose
STZ	Streptozotocin
T1DM	Type 1 diabetes mellitus
T2DM	Type 2 diabetes mellitus

TAC	Time-to-amplitude converter
TCSPC	Time-Correlated Single Photon Counting
TDO	Tryptophan 2,3-dioxygenase
TRES	Time-resolved emission spectra
UV	Ultraviolet
VR	Virtual Reality

Table of Contents

Contents

1. Introduction

This thesis discusses the results of various *in vitro* and *in vivo* autofluorescence based studies, with the aim to develop an alternative method for monitoring protein glycation, and ultimately long-term glycaemic control in patients with diabetes.

1.1 Diabetes

1.1.1 Disease Background

Diabetes Mellitus is a chronic, progressive disease characterised by elevated blood glucose levels. It is sub-categorised into 2 main types: type 1 diabetes (T1DM) where a person's pancreas cannot produce insulin, and type 2 diabetes (T2DM) where often a person's cells have become resistant to the action of insulin and insulin is not produced in enough quantities to compensate for this[7]. In both cases blood glucose levels cannot be properly regulated.

Both T1DM and T2DM are characterised by prolonged hyperglycaemia, resulting from insulin deficiency or resistance[8]. 2-hr plasma glucose levels above 11.1 mmol/l are defined as hyperglycaemic, and if a person's blood glucose levels are above this threshold, or their fasting plasma glucose levels are greater than 7 mmol/l, they receive a diagnosis of diabetes[7]. Sustained blood glucose levels above this threshold can eventually lead to complications from diabetes. Various studies[9] have shown the association between this prolonged hyperglycaemia, and late-stage diabetes complications. Complications of diabetes are particularly dangerous since many organs can be affected: diabetes can cause cardiovascular[10] and vascular[11] diseases, stroke[12], kidney failure[13], retinopathy[14], neuropathy[15], and lower limb amputation[7]. The complications of the disease can cause mortality via the above mentioned micro and macro-vascular diseases it can trigger.

As one of the major causes of morbidity and mortality worldwide[16], the impact of diabetes on global health is huge. It is among the top 10 leading causes of death worldwide[17], with it being responsible for an estimated 4 million deaths in 2017 alone[18]. Diabetes has a huge international presence, and the number of patients is increasing every year: in 2009 the global prevalence of this disease was estimated at 285 million people[19], and by 2019 this had increased to an estimated 463 million[20], which is 9.3% of the population. This is predicted to increase again to 578 million by 2030. The rise is largely due to the increase in the number of people diagnosed with T2DM, which accounts for more than 90% of all diabetes cases[21]. The

greatest risk factor for T2DM is obesity[7], and the increase in the number of people with this risk factor is thought to be responsible for a large proportion of the global diabetes burden.

1.1.2 Current Monitoring Methods

1.1.2.1 Blood Glucose Monitoring

There is currently no cure for diabetes, but good glycaemic control is extremely important to prevent any long-term complications[22]. In patients with type 1 diabetes who are on insulin, blood glucose levels must be carefully monitored daily, and most commonly this is done by self-monitoring of blood glucose (SMBG). In patients with T2DM daily blood checks are not required, but long-term blood glucose levels are monitored using HbA1c, which is discussed in the next section.

SMBG is done at home by the patient multiple times a day (NICE Guidelines recommend at least 4 times each day[23]) using a home finger-prick test. An example of such a test device is shown in Figure 1.1. Most devices are based on an electrochemical principle, where blood from a finger prick puncture is dropped onto a disposable biosensor test strip which contains the enzyme glucose oxidase as the recognition material, and a ferrocene- or quinine-based electron transfer mediator[24]. The mediator shuttles electrons from the reduced form of the enzyme to the electrode to generate a signal, and so provide a blood glucose reading.

Figure 1.1. The GlucoRx Nexus Blood Glucose Meter, an NHS recommended brand.

Although recent advances in technology have improved blood glucose meters in several ways, such as decreasing the blood volume required, decreasing measurement time, and being able to store hundreds of results, there are still many disadvantages of this method of SMBG. It is painful and inconvenient, and various studies have shown that SMBG has poor

adherence[25]. Also, clinically significant dips and spikes in blood glucose could be missed if the patient is not testing regularly enough.

More recently flash glucose monitoring systems and continuous glucose monitoring (CGM) systems have been developed to try and solve these problems. The products available on the NHS for these purposes are the Freestyle Libre 2 and the Freestyle Libre 3 respectively, which are free to patients with T1DM.

Instead of measuring blood glucose levels, both of these devices measure the glucose level in the interstitial fluid[26] (the fluid found in the space between cells). The devices use a sensor that must be placed on the back of the user's arm, and when applied a small flexible fibre inserts under the skin. The current measured by the implanted sensor is then transmitted wirelessly to a separate monitor (or to an app on the user's smartphone), which converts the result to an easily readable blood glucose reading.

The main difference between flash systems and CGM systems (the Freestyle Libre 2 versus the Freestyle Libre 3) is the frequency of data transmission. To obtain a glucose reading, the flash system requires the user to scan the sensor using a smartphone app or a separate reader, and the previous 8 hours of data are then transmitted and can be read by the user. CGM systems however transmit glucose readings automatically, transmitting one reading every minute. The primary advantage of both of these systems is that they provide more data over a prolonged time period, and so it is easier to see trends and patterns in the patient's blood glucose. Any clinically significant spikes and dips, which may have been missed when carrying out random fingerpick tests, are also recorded, and the data can be shared directly with the user's care team. The care team can then obtain a deeper understanding of the patient's glycaemic control, and adjust any treatment accordingly. Flash and CGM systems can also incorporate alarms for when blood glucose is too high or low, and the devices can be set so that a carer is alerted to this. These devices also allow for fewer finger-prick tests to be carried out every day, which may improve quality of life for patients.

Although the advantages of such systems are apparent, there are a few disadvantages associated with this technology. Initially, one of the principal drawbacks that was argued was that the readings provided by flash glucose monitoring or CGM systems are not as precise or reliable as SMBG, since they measure glucose in the interstitial fluid rather than blood. Interstitial fluid glucose levels typically lag behind blood glucose, however data shows that in the Freestyle Libre 2 flash glucose sensors this delay is only 2.4 minutes in adults[27], and thus

the lag seems minor. The sensors of these devices also need replaced approximately every 7-14 days[28], and wearing a visible sensor may not appeal to some patients: for example, they may not want to wear it when playing contact sports, or may prefer to keep their diagnosis private.

The benefits of these systems however are clear: various studies have found that a flash system can reduce the time and frequency of hypoglycaemia[29] and reduce HbA1c level[30,31],which are both important for managing diabetes. Recently NHS England announced that everyone living with T1DM would be eligible for a flash system on the NHS[32], which will improve not only blood glucose control among the patient population, but also their quality of life.

1.1.2.2 Long Term Monitoring

Longer term monitoring of blood glucose levels is just as important as instantaneous blood glucose checks for monitoring glycaemic control in patients with diabetes. Glycated haemoglobin, HbA1c, is the primary marker of long-term glycaemic control. The higher the HbA1c value, the greater the risk of developing diabetes complications[33]. HbA1c is measured approximately every 3-6 months[23] in those with diabetes, and it gives a 2–3 month average of blood glucose concentrations. It is the current gold standard of care for monitoring diabetes control.

There are some instances however where HbA1c can misrepresent diabetes control. For example, when there is a change in the normal lifespan of red blood cells, this falsely affects HbA1c level. In patients with anaemias associated with reduced red blood cell turnover, for example iron, vitamin B12, or folate deficiency[34,35], or chronic kidney disease[36], glycated haemoglobin levels can be misleadingly high. The opposite is true in patients who undergo dialysis, where red blood cells have a much faster turnover. In addition, factors such as blood loss, chronic alcohol consumption, pregnancy, and the presence of haemoglobin variants can all affect HbA1c values[34].

Other methods of long-term monitoring of diabetes have therefore been studied as an alternative to HbA1c, with a particular focus on methods that do not rely on red blood cells as many factors can affect their life span and thus HbA1c level. The amount of glycated human serum albumin (GA), which is a plasma protein found in the blood, increases in those with diabetes[37], and thus it can also reflect glycaemic control. This measure considers a

shorter time period than HbA1c, giving information on the glycaemic status over the previous 2 to 3 weeks[38].

Measuring GA has been found to be a more sensitive and accurate method of determining glycaemic control in patients with chronic kidney disease (a potential complication of diabetes)[39,40], and to be a better indicator of glycaemic control in haemodialysis patients[41], compared to HbA1c. This is because GA is not influenced by any red blood cell related conditions or treatments. This method however does still require a blood sample to carry out the analysis.

Research into alternative methods for monitoring diabetes control still has much interest, with a primary goal being to develop non-invasive techniques. This would allow painless testing, and thus allow it to be carried out more frequently. One major avenue of research investigates auto- fluorescence, which will be discussed in a later section.

1.2 Glycation and AGEs

1.2.1 AGE Formation

The elevated blood glucose levels associated with diabetes lead to adverse effects in numerous cells and proteins in the body, affecting them all in different ways[42]. Proteins undergo glycation in response to hyperglycaemia, and this glycation can lead to the formation and accumulation of compounds known as advanced glycation end products (AGEs)[8]. Alongside the acute changes in cellular glucose metabolism, the build-up of AGEs is the primary cause of the development of diabetic complications[43].

Glycation is the process in which a protein molecule bonds to a sugar molecule, for example glucose or fructose, without enzyme control[8]. This process is often referred to as the Maillard reaction, so named after the biochemist Louis Camille Maillard who first observed this reaction by heating glycine with glucose in 1912[44]. It has since been established that this reaction is the driving force of AGE formation[45].AGE formation is often described in three discrete stages: early, intermediate, and late[42]. This process is outlined in Figure 1.2.

In the early stage of this reaction glycation is initiated by the condensation reaction of a carbonyl group of a reducing sugar, for example glucose, with a free amino group of a protein by nucleophilic addition. This results in the formation of a Schiff base[46], which then undergoes reorganisation at the intermediate stage to form a more stable Amadori product. The formation of both the Schiff base and the Amadori products are reversible[45]. The

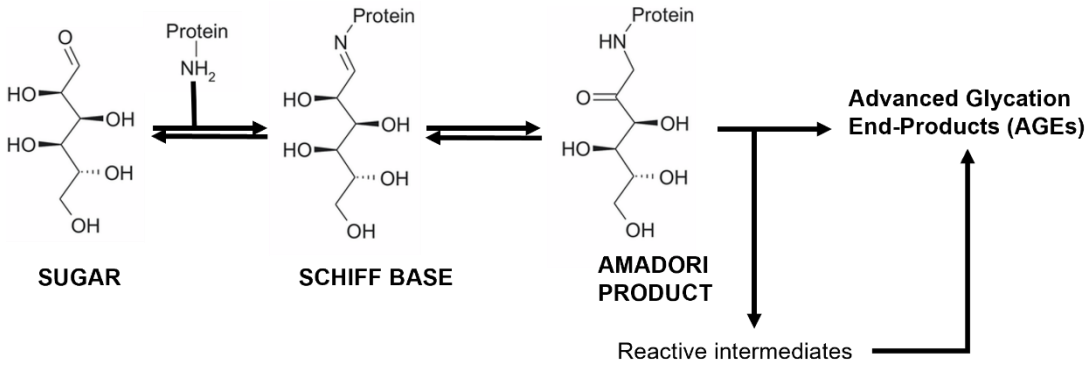

Figure 1.2. The glycation pathway, leading to AGE formation

Amadori products can then degrade releasing a variety of reactive dicarbonyl compounds, for example 3-deoxyglucosone (3-DG) and methylglyoxal (MGO)[42], which themselves can form AGEs, or can rearrange to form AGEs directly. This final stage in the AGE formation is irreversible[47] , and is achieved through dehydration, cyclization, oxidation, cross-linking, and polymerisation reactions[46].

These end products are relatively stable at physiological temperature and pH[45], and their rate of accumulation is dependent upon various factors including the availability of metal ions, redox balances, and the longevity of the modified proteins[48]. There are 3 primary ways in which AGEs can affect cells: as adducts on modified serum proteins, as endogenous adducts formed from glucose metabolism, or as ECM-immobilised modifications on long-lived proteins[48].

Only long lived proteins go through this last stage of irreversible AGE formation due to the fact that Amadori rearrangement takes place over several days and even weeks[46]. Over 12 types of AGEs have been detected in tissue, and these can broadly be split into 3 categories: fluorescent cross-linking AGEs (e.g. pentosidine), non-fluorescent cross-linking AGEs (e.g. arginine–lysine imidazole (ALI)), and non-crosslinking AGEs (e.g. N-carboxymethyllysine (CML))[49].

1.2.2 Consequences of Glycation

AGE accumulation on long-lived proteins can impair physiological function. The amino acid side chains become glycated, which modifies their structure and inhibits function[45]. This occurs through various means such as altering enzymatic activity, disrupting molecular conformation, interfering with receptor recognition, and reducing degradation capacity[50]. Glycation also encourages crosslinking in elastic proteins such as collagen and elastin, which results in stiffening of the tissues[51]. Furthermore, soluble AGEs can bind to AGE receptors,

the most common of which is known as RAGE. These receptors are activated by AGEs, and can then trigger various intracellular signalling pathways[52]. Several studies have shown that AGE accumulation leads not only to diabetes complications, but also contributes to the pathogenesis of renal insuffciency[53] and Alzheimer's disease[54].

1.2.3 AGEs and Diabetes

In diabetes, the production and accumulation of AGEs increases due to the increased levels of glucose in the blood[45]. AGEs can be found circulating in the bloodstream, and in tissue where they affect more long-lived proteins. Various studies, which are discussed below, have established the relationship between AGE levels, the presence of diabetes, and diabetic complications.

Increased circulating serum AGES have been found both in T1DM[55] and T2DM[56] . A 1999 study[56] showed that levels of AGEs in serum are higher in those with type 2 diabetes, and that serum levels of AGEs were further increased in patients with T2DM and coronary heart disease. High serum levels of the AGE pentosidine have been found to correlate with increased arterial stiffening in T2DM[57], and immunological studies have shown that serum-AGE levels correlate with pre-clinical stages of nephropathy and early retinopathy[58]. However, AGE-modified circulating proteins are regularly cleared from the bloodstream (apart from in renal failure), and so quantification in serum is not always a robust biomarker[48]. For this reason, AGE accumulation in long-lived proteins has been of interest as a potential biomarker for diabetes complications, and various studies have investigated this.

The largest of such studies was the Diabetes Control and Complications Trial (DCCT) that began in 1983 and took place over 10 years, with follow ups at intervals after trial completion[59]. This study has provided extensive data on the relationship between diabetes complications and AGEs, with the first major finding demonstrating that good glycaemic control slowed the rate of development of microvascular and neuropathic diabetes complications. It was also concluded that inhibition of AGE formation reduces the chances of developing any long-term complications. Further studies showed that skin AGE levels correlate with disease duration and the severity of diabetic complications[60, 61]. The DCCT-EDIC sub-study found a significant association of cross-linked AGEs on skin proteins with progression of diabetic retinopathy and nephropathy[62], and there is evidence showing that AGE concentration in skin biopsies is higher in patients with neuropathy[63]. Furthermore,

studies in mice have shown that AGEs and RAGE could play an active role in the development of diabetes induced cardiac dysfunction[64].

This prior research establishes the relationship between AGE levels and diabetes complications, and conclusively proves that AGEs in long-lived proteins have potential use as a biomarker for diabetes complications.

1.3 Autofluorescence

Fluorescence is the emission of light by a molecule due a transition from a higher excited state to the ground state[65], and auto-fluorescence (AF) is fluorescence that is emitted naturally by biological molecules[66]. Many biological molecules are auto-fluorescent. This allows them to be detected using fluorescence techniques without the addition of any extrinsic fluorophore that may disturb its native environment. AF is therefore a useful method that has been used extensively to investigate biological structures and processes in vivo[67].

1.3.1 Intrinsic fluorophores

Intrinsic fluorophores are fluorophores that occur naturally. These include chlorophyll found in plants, but more relevant to this work, they include the three aromatic amino acids that exist in the body. These three aromatic amino acids, phenylalanine (Phe), tyrosine (Tyr), and tryptophan (Trp), are responsible for the fluorescence of many biological proteins[1], and their excitation and emission spectra are shown in Figure 1.3.

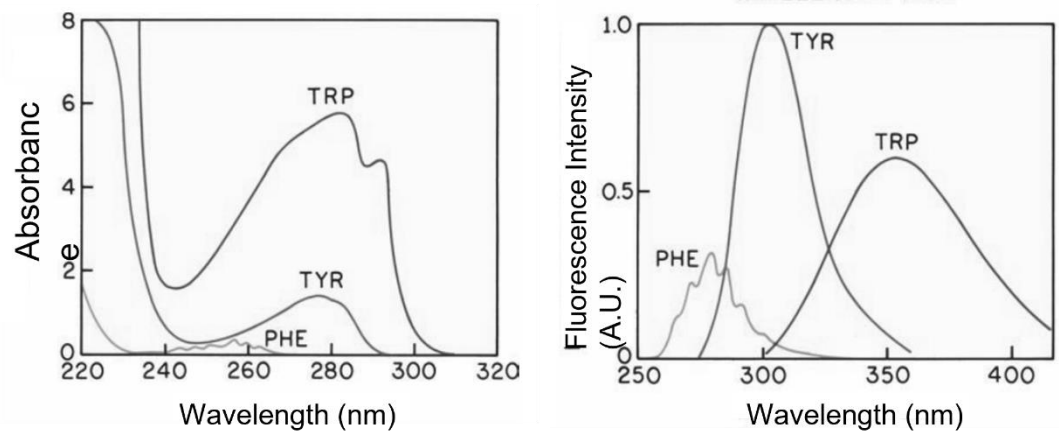

Figure 1.3. Absorption and emission spectra of the three aromatic amino acids. Adapted from [1].

Alongside these three residues, there are numerous other biological structures in the body that auto-fluoresce. These are listed in Table 1.1, with their respective excitation and emission wavelength[68-70].

Table 1.1. Auto-fluorescent fluorophores found in the human body, alongside their maximum excitation and emission wavelengths.

Fluorophore	λ_{ex} (nm)	λ_{em} (nm)
Flavins	450	535
Porphyrin	405	600
Collagen	335, 370	390, 460
Elastin	420, 460	500, 540
Keratin	370	460
NAD(P)H	~340	~460

Using intrinsic fluorophores for biological and biomedical studies offers the primary advantage that no extrinsic fluorophore, which may influence the behaviour of the system, is needed. Using intrinsic fluorophores also means that there are less regulatory requirements that must be met for use in clinical applications than are needed when an extrinsic fluorophore is ingested or injected. The difficulty in using intrinsic fluorophores however is that, as shown in Table 1.1, many of the emission and excitation spectra overlap, which may complicate fluorescence measurements when investigating biological samples. In addition, ultraviolet (UV) light has relatively shallow penetration depth in tissue, and so only fluorophores near the tissue surface may be excited.

1.3.2 AGE Auto-Fluorescence

As outlined, AGE accumulation is thought to contribute to the severe complications associated with diabetes. It has been established that several AGEs exhibit AF[6], including pentosidine, crosslink, fluorolink and vesperlysine A, B, and C. Detection of the fluorescence of these AGEs have been used to estimate the levels of AGE in serum, urine, saliva, and tissue samples[71].

However, like discussed previously, it is the AGE accumulation in long-lived proteins, for example skin proteins, that are of more relevance. Various studies have looked to skin fluorescence, and correlated skin fluorescence with AGE levels. The first instance was in 2004 in a report by Meerwaldt et al.[6], which showed that skin fluorescence was related to AGE levels in dermal biopsies in diabetic patients and in healthy controls. This has been confirmed

in subsequent studies[72] and thus it can be concluded that dermal fluorescence reflects AGE levels.

Skin fluorescence has also been related to diabetes complications: a study carried out in 1997 showed increased skin fluorescence in patients with diabetes using non-invasive skin capillary microscopy[73]. Further studies were able to correlate pentosidine levels in skin with the severity of complications in diabetes patients[61], and show that pentosidine and collagen-linked fluorescence are good predictors of the progression of diabetic retinal and renal microvascular complications[74].

This research therefore shows that skin fluorescence could be used as a biomarker in AGE-related diseases such as diabetes mellitus, offering improvements over current methods due to the non-invasive nature of such measurements. Skin AF is a more useful clinical tool for measuring AGEs than the classical blood or urine sample, since these do not accurately reflect tissue AGE level, and thus do not reflect the potential for AGE-related diseases[75].

1.3.3 Skin AF Devices

Due to the potential for clinical use, simple devices that can assess skin fluorescence have been developed, and so far two devices have been used in clinical studies. The first of these is the SCOUT DS device (VeraLight, USA), which was granted a CE Mark for non-invasive diabetes screening in 2011. It is shown in Figure 1.4. This instrument measures various biomarkers of diabetes in the skin, including AGEs like pentosidine and crosslines, but also indicators for oxidative stress and cell metabolism, for example reduced nicotinamide adenine dinucleotide (NADH) and flavin adenine dinucleotide (FAD)[4].

Figure 1.4. SCOUT DS Device used to measure auto-fluorescence of skin on the volar side of the forearm[4].

The device uses light emitting diodes (LEDs) centred at multiple wavelengths to excite the fluorophores in the skin, with the light focused onto the left volar side of the forearm. The fluorescence and reflectance of the skin is measured and transmitted via a fibre optic probe to a spectrograph and camera. The optical signals are then converted into a score between 0 and 100 with higher scores indicating a higher probability of disease. Patients with a score greater than or equal to 50 are then referred for blood tests to confirm a diabetes diagnosis. The SCOUT DS device also has the ability to account for the amount of melanin and haemoglobin in a patient's skin, which could otherwise affect the results. To do this, the reflectance of each excitation LED is measured, and then the brightness of each LED and the camera exposure time is automatically altered to account for the variations in these pigments between subjects. This allows the device to be used in a wide range of skin tones[4].

The second device developed for assessment of skin fluorescence is the AGE Reader (prototype AFR Reader) (DiagnOptics Technologies, BV, The Netherlands)[6]. This device illuminates 1 cm^2 of the skin, again on the volar side of the arm, with a light source with peak excitation of approximately 350 nm. Light emitted and reflected from the skin is then measured using an in-built spectrometer in the 300-600 nm range, which was then replaced with photodiodes in later versions. This specific range was chosen as it corresponds to the fluorescence of major AGEs such as pentosidine. The skin auto-fluorescence is calculated as a ratio of excitation light to emitted light, and expressed in arbitrary units. The AGE Reader has been validated as a tool for non-invasive assessment of AGE accumulation in skin and has since been used to measure skin AGE accumulation as a predictor for diabetic complications[76, 77]. The graph shown in Figure 1.5 shows a typical AGE reader measurement.

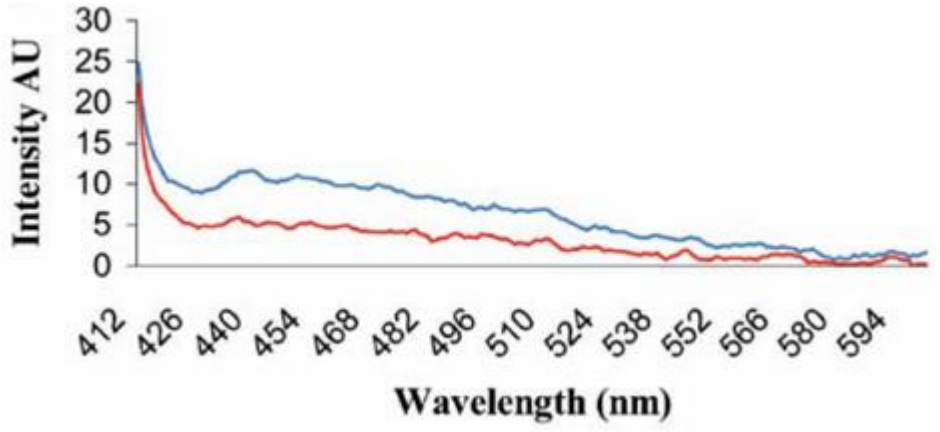

Figure 1.5. Fluorescence emission spectrum from a participant with diabetes (blue line) and a control participant (red line) measured using the AFR. Peak excitation is ~350 nm wavelength[6].

The red line shows the skin fluorescence of a healthy person, or control, and the blue line shows the skin fluorescence of a patient with diabetes. This device therefore shows that there is a difference in skin fluorescence between these two patient groups, and so could be a useful tool for diabetic screening.

There are numerous advantages of these types of devices for diagnostic screening. They eliminate the need for overnight fasting, they are non-invasive, and they are quick. There have also been various studies showing skin AF measurements are comparable to the classical HbA1C test in detecting abnormal glucose levels[4, 78]. Overall, these devices prove that skin AF can be used as a cost-effective, simple and reproducible test for diabetes screening.

1.4 Thesis Content

The overarching aim for this thesis is to investigate how the intrinsic fluorescence of different physiological fluorophores' changes in response to glucose. If fluorescence techniques can be used to monitor these glucose-induced changes, this could offer the potential to develop a new, non-invasive method for monitoring diabetes control.

In addition to the traditional steady-state fluorescence measurements that have been used previously for this application, this work will also incorporate time-resolved fluorescence measurements, in the hope that this provides more information on any time-dependent processes, and thus on the excited state kinetics. This would lead to a deeper understanding of the underlying processes occurring during glycation.

The next chapter in this thesis, chapter 2, outlines the physical principles and instrumentation that is the foundation of this work. The core fluorescence principles are discussed, alongside the techniques and instrumentation used to carry out the research. It includes details on traditional steady state measurements such as absorbance and fluorescence emission, and details on fluorescence decay, alongside the various fitting methods that can be used to model decays. Finally, a procedure known as time-resolved emission spectra (TRES) is discussed, alongside a modelling technique that can be used to extract useful information from this type of spectra.

These techniques were used in the subsequent six experimental chapters. Chapters 3, 4, 5, and 6 report on in vitro studies, investigating how the intrinsic fluorescence of a specific fluorophore evolves in response to glucose. A chapter each is dedicated to collagen, NADH,

keratin, and human serum albumin (HSA). These specific proteins were chosen as each of them exhibits changes in response to glucose, and they are auto-fluorescent. Their detection could thus offer a means of monitoring diabetes control. In addition, collagen and NADH are found in the skin, and keratin is found in nails, and thus they have the potential to be detected noninvasively.

The final 2 experimental chapters then include details on *in vivo* measurements. Chapter 7 investigates skin fluorescence and includes some preliminary studies carried out on mice, and Chapter 8 then contains the results of research carried out on human fingernails. The final chapter in this thesis then outlines the main conclusions from this work and attempts to relate the *in vivo* measurements to the kinetics revealed for the individual proteins in the *in vitro* studies.

2.Physical Principles and Instrumentation for Fluorescence

2.1 Fluorescence Principles

The phenomenon of fluorescence was first observed by Sir John Frederick William Herschel in 1845 when he noted that sunlight caused emission of blue light from a quinine solution[1]. This was not known as 'fluorescence' until 1852, when Stokes coined the name after studying the same phenomenon in multiple different substances[79]. Since then, the development of numerous techniques has allowed the use of fluorescence in a wide range of applications including lighting, medicine, chemical analysis, and sensing. The growing use of fluorescence in the fields of biosciences and healthcare is of particular interest and has influenced its use in the work in this thesis. Fluorescence is a particularly efficient sensing technique in these settings because fluorescence occurs in nanosecond timescales and at nanometre distances, which is ideally matched to many physiological processes[80].

2.1.1 Photoluminescence

The emission of light from a substance can be split into 2 categories: incandescence and luminescence. Incandescence is the emission of light following excitation from a heat source, while luminescence does not require heat[81]. Photoluminescence is one type of luminescence, and is the emission of light from an atom or molecule following photoexcitation i.e. the absorbance of a photon which excites an electron to the excited state. Photoluminescence is sub-categorised into phosphorescence and fluorescence, with fluorescence being the focus of this work.

Fundamentally, the fluorescence of a molecule is the spontaneous emission of light by that molecule, due to a transition from a higher excited state to the ground state[65]. This phenomenon is typically explained using a Jablonski Diagram[82], which is a schematic representation of the various spontaneous molecular relaxation processes that can occur following excitation of a molecule. An example of such is shown in Figure 2.1.

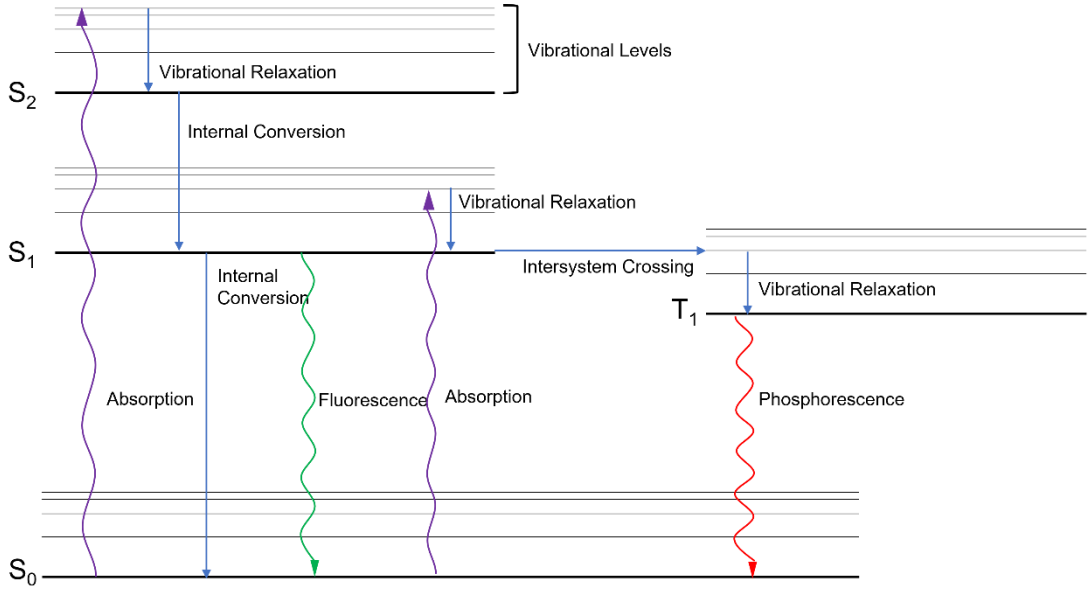

Figure 2.1 Jablonski Diagram

Each electronic state S is made up of vibrational and rotational (not shown) levels. The energy of a state is the sum of it's electronic (el), vibrational (vib), and rotational (rot) energies

$$E_{Snmo} = E_{S_n}^{el} + E_{S_{nm}}^{vib} + E_{S_{nmo}}^{rot} \quad [2.1]$$

where n, m and o correspond to the electronic, vibrational, and rotational states respectively. For the purpose of the following analysis, rotational elements are not included.

Absorption of a photon of appropriate energy excites an electron from the ground state $S_{0m,}$ to a singlet excited state ($S_{1m,}$ $S_{2m',\ldots}$). The energy and vibrational level the electron is excited to is dependent upon the energy transferred from the absorbed photon. This photon energy is proportional to the wavenumber v and inversely proportional to the wavelength λ as shown by equation 2.2

$$E = \frac{hc}{\lambda} = hv \quad [2.2]$$

where E is the photon energy, h is Planck's constant, and c is the speed of light. The energy of a photon emitted between two electronic states ($S_{n'm'} - S_{nm}$) is therefore equal to the energy gap $E_{S_{n'm'}} - E_{S_{nm}}$:

$$hv_{nmn'm'} = \left(E_{S_{n'}}^{el} - E_{S_n}^{el}\right) + \left(E_{S_{n'm'}}^{vib} - E_{S_{nm}}^{vib}\right) \quad [2.3]$$

When in an excited state the electron is unstable, and so energy is quickly lost. This can be done through vibrational relaxation (VR), where the electron returns to the lowest vibrational

level of its excited electronic state, or internal conversion (IC), where the electron drops to a lower excited electronic state. Once in the lowest vibrational level of the excited electronic state, the excited electron can undergo various processes: it can return to the ground state $S_{0,}$ emitting fluorescence; it can lose its energy non-radiatively through processes such as quenching; or it can undergo intersystem crossing (ISC). ISC is a process where the electron returns to the ground state through a metastable triplet state T. The triplet excited state differs from the singlet excited state in that the excited electron has a parallel spin state to the ground state in the excited triplet state, while electrons in the singlet excited states have opposite spin to ground state. Returning to the ground state from an excited triplet state $T_{1,}$ again involves ISC, and results in light being emitted in the form of phosphorescence, rather than fluorescence[1]. Phosphorescence happens on a much longer timescale than fluorescence (ms-s compared with ns) since the triplet to singlet state is a forbidden transition, and thus the $T_{1,}$ to $S_{0,}$ transition has low probability.

As outlined in Figure 2.1, fluorescence is the emission of photons accompanying the $S_{10,}$ to $S_{0m,}$ relaxation. The emission spectrum is therefore independent of the excitation wavelength, as described by Kasha's Rule[83].

The emission spectrum $G(v)$ is given by

$$G(v) = \sum_{m} \frac{64\pi^4 v^3}{3h} \left|\mu_{S_{om}S_{10}}\right|^2 \delta(v - v_{S_{om}S_{10}}) \qquad [2.4]$$

where $\left|\mu_{S_{om}S_{10}}\right|^2$ is the electric dipole moment matrix element for the $1{,}0 - 0, m$ transition, and $\delta(v - v_{S_{om}S_{10}})$ is the delta function of a photon's position after absorption and radiative decay[84,85].

The Franck Condon factor must also be defined, which derives from the Franck-Condon Principle. This principle explains the intensity of vibronic transitions, and states that during an electronic transition, a change from one vibrational energy level to another is more likely to happen if the two vibrational wave functions overlap more significantly[86,87]. The Franck-Condon Factor is essentially a measure of the overlap between the ground and excited state vibrational wavefunctions, and is defined as:

$$FCF_{S_{nm}S_{n'm'}} = \int \varphi_v{}' \varphi_v \, d\tau_n \qquad [2.5]$$

where φ_v and $\varphi_v{}'$ are the vibrational wavefunctions of the initial and final states respectively.

Using the approach suggested by Condon[88], and developed by Herzberg[84], $|\mu_{S_{nm}S_{n'm'}}|^2$ can then be expressed in terms of the fixed nuclei electronic transition dipole moment $|\mu_{S_{nn'}}|$ and the Franck- Condon factor $FCF_{S_{nm}S_{n'm'}}$.

$$|\mu_{S_{nm}S_{n'm'}}|^2 = |\mu_{Snn'}|^2 FCF_{S_{nm}S_{n'm'}} \quad [2.6]$$

Defining a constant a:

$$a = \frac{64\pi^4}{3h} \quad [2.7]$$

a function $S_{vib}(v)$:

$$S_{vib}(v) = \sum_m FCF_{S_{om}S_{10}}\, \delta(v - \frac{E^{vib}_{S_{10}} - E^{vib}_{S_{0m}}}{hc}) \quad [2.8]$$

and a parameter $v_{S_{01}}$:

$$v_{S_{01}} = \frac{1}{hc}(E^{el}_{S_1} - E^{el}_{S_0}) \quad [2.9]$$

Equation 2.4 can be simplified, giving the equation for the single molecule emission spectrum

$$G(v) = av^3 S_{vib}(v - v_{01})|\mu_{01}|^2 \quad [2.10]$$

Fluorescence emission, in general, is at a longer wavelength than the absorption, and this is due to the energy lost in the excited state due to vibrational relaxation[89]. This was first demonstrated by Stokes in 1852, and so this statement then became known as Stokes Shift[79]. This is illustrated by the absorption and emission spectra shown in Figure 2.2, where the emission occurs at a longer wavelength, and thus lower energy, than the absorption.

The exception to this rule is when two photon excitation (TPE) is used to excite the fluorophore. Two photon excitation (TPE) (or two photon absorption (TPA)) is the absorption of two photons by a fluorophore in in quick succession, where their combined energy is used to excite the fluorophore to the excited state[1]. In this instance, the emitted fluorescence will have a shorter wavelength than the absorption. TPE is useful for *in-vivo* and *ex-vivo* applications, such as those discussed later in this thesis, as it allows light with longer wavelengths, and thus deeper penetration depth in tissue, to be used for excitation.

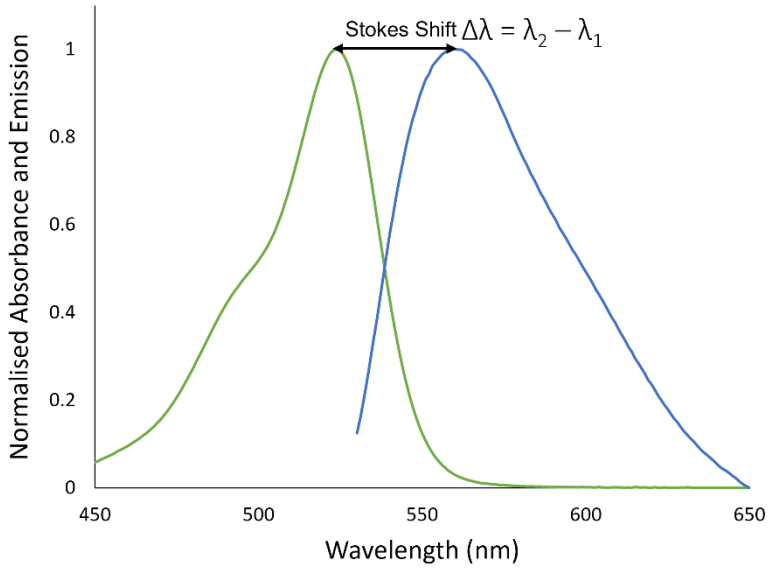

Figure 2.2 The absorbance (green) and emission (blue) spectra of rhodamine 6G, highlighting Stokes Shift

2.1.2 Quantum yield

The quantum yield (Ø) of a fluorophore is an important characteristic of a fluorescing species: it determines how 'bright' the fluorescence is. It is the ratio of the number of photons emitted by the fluorophore compared to the number of photons absorbed, and it is given by equation 2.11

$$\emptyset = \frac{k_r}{k_r + k_{nr}} \qquad [2.11]$$

where k_r is the emissive rate of the fluorophore, and k_{nr} is the rate of non-radiative decay[1]. The non-radiative decay accounts for the fact that not all of the excited molecules actually emit fluorescence, since there are numerous other de-excitation pathways competing, such as IC and ISC[65]. Measuring absolute quantum yield is difficult and rarely used in the context of biomolecules, since their natural environment contains a lot of oxygen, which quenches the fluorescence signal[80].

2.1.3 Fluorescence Intensity Decay

Fluorescence intensity decay is often measured for a fluorescing sample. This is particularly useful for biological samples, where tissues have unclear or overlapping fluorescence spectra, but very different, well-defined lifetimes[90]. Fluorescence intensity decay can be reduced to 'fluorescence lifetime' if the decay is single exponential, however fluorescence decays are often more complex, and require multi exponential kinetics.

The fluorescence lifetime of a molecule is the average time it spends in the excited state before emitting a photon[80]. It must be thought of as a statistical average and not an absolute time since each molecule will emit fluorescence randomly throughout the decay[1]. Fluorescence lifetime is an intrinsic property of the molecule, and independent of both the fluorescence intensity and the concentration[80]. An instance however when fluorescence lifetime is affected by concentration is when self-quenching is present in the fluorophore. This is a type of quenching (discussed in detail in the following section) where interactions between separate fluorophore molecules results in a decrease in the fluorescence intensity. This is particularly evident in high concentrate solutions, where self-quenching results in a decrease in the fluorescence lifetime[91].

The fluorescence lifetime τ is generally in the region of nanoseconds, and can be defined in terms of the intramolecular processes as given by equation 2.12

$$\tau = \frac{1}{k_r + k_{nr}} \qquad [2.12]$$

where k_r is the emissive rate of the fluorophore and k_{nr} is the rate of non-radiative decay. When no extrinsic factors are present, the rate of non-radiative decay can be discounted, and the natural lifetime τ_n of the fluorophore is given by

$$\tau_n = \frac{1}{k_r} \qquad [2.13]$$

In time-resolved fluorescence experiments, lifetime is measured as a parameter of the fluorescence intensity decay. Consider firstly a decay with one-exponential kinetics. A population of molecules M are excited with an infinitely sharp pulse of light known as a δ-function. This results in an initial population of molecules in the excited state. These molecules will then decay to the ground state through radiative and non-radiative processes, where the rate of decay is given by

$$\frac{d[M^*]}{d(t)} = -(k_r + k_{nr})[M^*] \qquad [2.14]$$

where $[M^*]$ is the concentration of molecules in the excited state at time t. Integrating equation 2.14 gives the fluorescence decay as

$$[M^*] = [M^*]_0 \exp\left(\frac{-t}{\tau}\right) \qquad [2.15]$$

where $[M^*]_0$ is the initial concentration of excited molecules at $t = 0$. Fluorescence intensity is proportional to the decaying concentration of excited molecules therefore equation 2.15 becomes

$$I(t) = I_0 exp\left(\frac{-t}{\tau}\right) \quad [2.16]$$

where $I(t)$ is the fluorescence intensity at time t, and I_0 is the intensity immediately after excitation. Mean lifetime $\bar{\tau}$ can also be calculated, and is the average amount of time a fluorophore remains in the excited state following excitation. It is obtained by averaging t over the intensity decay:

$$\bar{\tau} = \frac{\int_0^\infty t\, I(t)\, dt}{\int_0^\infty I(t)\, dt} \quad [2.17]$$

Integrating equation 2.17 gives the denominator equal to τ and the numerator equal to τ^2 . Thus for a single exponential decay $\bar{\tau} = \tau$. This is not true when the fluorescence intensity decay is more complex, such as multi-exponential, or non exponential decays. An average lifetime can still be calculated using equation 2.17, however this will be a complex function of the parameters describing the actual fluorescence decay, and so caution is needed when interpreting the result.

2.1.4 Fluorescence Quenching

The fluorescence intensity that is emitted from a sample can be reduced by various molecular and non-molecular processes, which together are known as quenching. Non-molecular mechanisms are not as significant, and includes for example the attenuation of incident light by an absorbing species.

Molecular mechanisms of quenching include static and collisional quenching, with the latter being more frequently observed. Static quenching occurs in the ground state, and refers to the process of a fluorophore forming a non-fluorescent complex with another molecule[1]. Conversely, collisional quenching occurs in the excited state, and is when the excited fluorophore loses its energy on contact with another molecule[1]. Unlike in static quenching, collisional quenching does not chemically alter the fluorophore.

For collisional quenching, the decrease in fluorescence can be described by the Stern-Volmer Equation:

[2.18]

$$\frac{F_0}{F} = 1 + K[Q] = 1 + k_q \tau_0 [Q]$$

where F_0 and F are the fluorescence intensities without and with a quencher present respectively, K is the Stern-Volmer quenching constant which indicates how sensitive a fluorophore is to a quencher, k_q is the biomolecular quenching constant, τ_0 is the unquenched lifetime, and $[Q]$ is the quencher concentration. Many molecules can act as collisional quenchers, including oxygen[92] and halogens[93].

2.1.5 Förster Resonance Energy Transfer (FRET)

Förster Resonance Energy Transfer (FRET) is a molecular mechanism that can be taken advantage of to monitor molecular interactions in vivo, since the molecular distances that play a key role in FRET are comparable with protein size and membrane thickness[1]. FRET is the radiation-less transmission of energy from a donor molecule in the excited state to an acceptor molecule in the ground state using dipole-dipole interactions[1]. The donor molecule is a fluorophore, and so with appropriate excitation energy, its electrons will transition from the ground state to the excited state. The fluorophore will then decay to ground state, either non-radiatively or through emission of a photon, or in the case of FRET, transfer its energy to an acceptor molecule. When FRET occurs donor fluorescence is quenched and acceptor fluorescence is enhanced (if the acceptor molecule is fluorescent).

For FRET to be possible, specific conditions must be met. The emission spectrum of the donor molecule must overlap with the absorbance spectrum of the acceptor molecule[94], like shown in Figure 2.3.

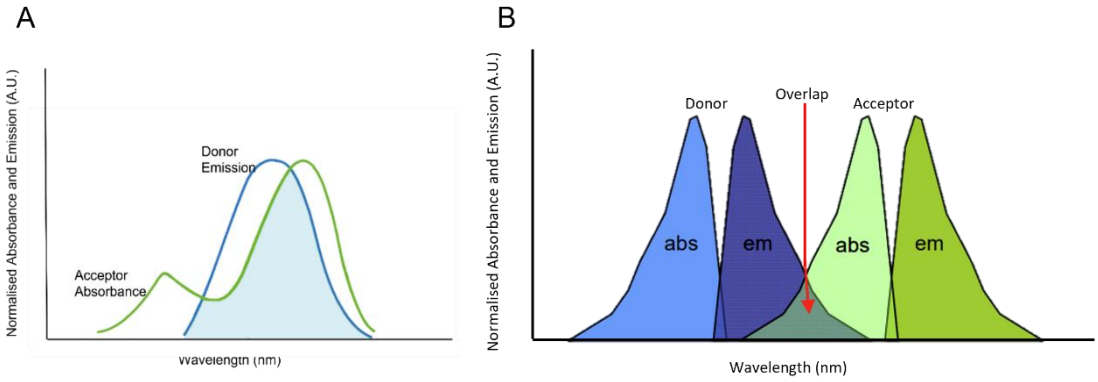

Figure 2.3. Examples of overlapping spectra in which FRET could occur. (A)Adapted from Lakowicz 2006[1] and (B) adapted from Horiba FRET Technical Note[5] .

The distance between molecules is also important: unlike collisional quenching, the donor and acceptor molecules do not need to be in contact for this transfer in energy, but they must be in close proximity, typically 10-100A[95]. The distance between the donor-acceptor pair, the extent of spectral overlap, and the orientation of the dipoles all determine the rate of FRET k_{DA}

$$k_{DA} = \frac{1}{\tau_D}\left(\frac{R_0}{r}\right)^6 \quad [2.19]$$

where τ_D is the lifetime of the un-quenched donor, R_0 is the Forster distance at which 50% of the energy has been transferred and r is the distance between the donor and the acceptor. FRET efficiency is therefore inversely proportional to separation between molecules, making it an extremely sensitive technique for studying intermolecular distances and protein interactions in in vivo applications[96].

2.1.6 Time-Dependent Spectral Shifts

Time-dependent spectral shifts are significant when studying fluorescence. There is no singular theory that can explain all time-dependent shifts, as in proteins this can be the result of conformational changes in the molecule, solvent/dielectric relaxation, or a combination of these processes.

Solvent relaxation is the term given to the process where solvent molecules re-orient around an excited fluorophore. When in the ground state, the dipole moments of the fluorophore and solvent interact to give an ordered distribution of solvent molecules around the fluorophore. Upon fluorophore excitation, this difference in energy induces a change in dipole moment of the fluorophore, and thus is followed by a mutual re-orientation of the solvent molecules and fluorophore, usually within a picosecond timescale. The rate of solvent relaxation can depend on many factors, such as the temperature and viscosity of the solvent,

The fluorophore reaches the excited state much faster than the time required for solvent and fluorophore molecules to re-orient themselves, and so there is a time delay between excitation, and re-orientation. This re-orientation process lowers the energy level of the excited state, and so reduces the energy separation between the ground and excited states. As a result, the fluorescence emission of the fluorophore is shifted to longer wavelengths, that is red shifted[85].

In solvents, the relaxation response is predictable by considering the dielectric relaxation time τ_D. The dielectric relaxation time is the time it takes molecules in the excited state to reorient in response to an electric field[1].

Even in simple solvents spectral relaxation can be complex, since solvents can display multiple dielectric relaxation times. When considering proteins, an extra layer of complexity is added, and spectral relaxation becomes even more difficult to interpret.

2.2 Fluorescence Techniques and Instrumentation

Fluorescence intensity is a multi-variable function, which depends on wavelength, time, temperature, polarisation, and fluorophore position within the sample. Changes in any of these factors will affect the fluorescence of the sample.

Fluorescence spectroscopy encompasses many different techniques that are used to monitor changes in sample fluorescence. These include steady state fluorescence spectra, time-resolved fluorescence measurements, fluorescence anisotropy, and fluorescence microscopy. In this work, we focus on steady state and time-resolved fluorescence measurements.

Steady state measurements include absorbance and emission spectra, which are time-averaged measurements recorded under continuous illumination. These are important since they provide the fundamental fluorescence characteristics of a fluorophore. Due to the time averaging however, no information on time-dependent processes can be extracted.

For this reason, time-resolved measurements are often used. This technique uses pulsed light sources for sample excitation, and information on time-dependent processes, as well as more in-depth information on the fluorophore's environment, can be obtained. Time-resolved measurements allow recovery of the parameters of the fluorescence kinetics, which helps to determine the mechanisms of molecular processes like conformational changes in the molecule, information on the excited state processes, etc[1]. In this chapter the main techniques and instrumentation used for recording both the steady state and time-resolved fluorescence measurements are discussed.

2.2.1 Absorbance

UV-Vis spectroscopy measures the light absorbed by a sample across a range of wavelengths in the UV-visible range. In this work, all such measurements were carried out on a PerkinElmer Lambda 2 UV-Vis spectrometer. The typical set up of such a spectrometer is shown in Figure 2.4.

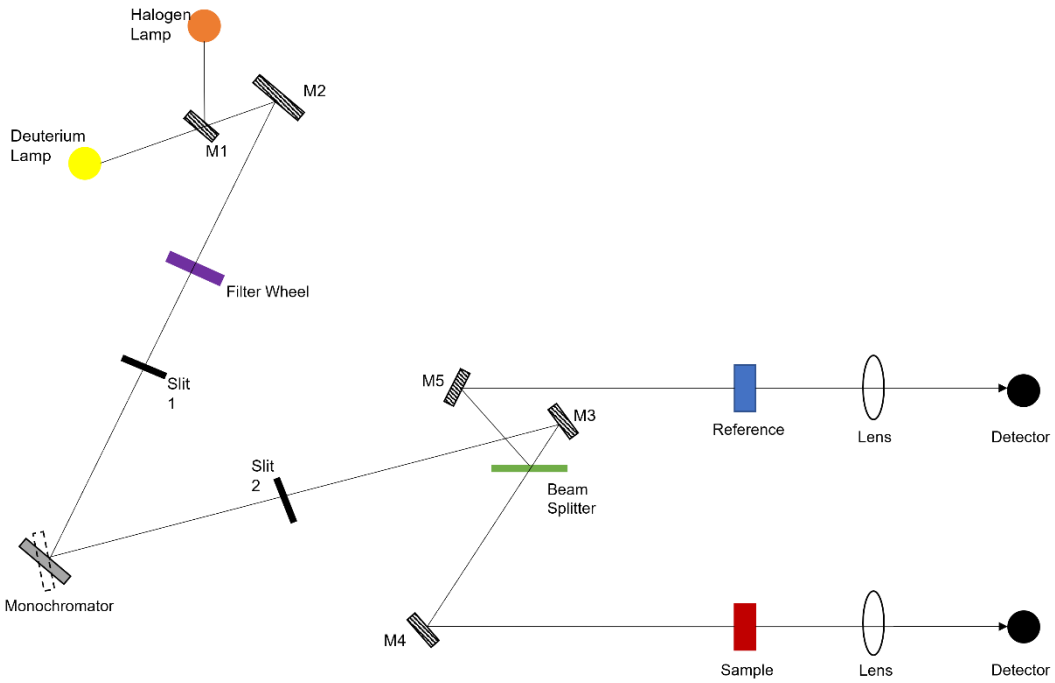

Figure 2.4. Schematic set up of a PerkinELmer Lambda 2 UV-Vis spectrometer. M1, M4, and M5 are plane mirrors, M4 is a toroidal mirror, and M3 is a spherical mirror.

The spectrometer has 2 excitation sources, a deuterium lamp and a halogen lamp, to cover the full wavelength range of the spectrometer. When working in the UV range (190-350 nm) mirror M1 is raised to allow radiation from the deuterium lamp onto mirror M2, and block radiation from the halogen lamp. When working in the visible range (300-1100 nm), mirror M1 blocks radiation from the deuterium lamp, while allowing radiation from the halogen lamp onto mirror M2. The switch in sources occurs automatically during measurements. From mirror M2 the light is reflected through an optical filter on the filter wheel, where the appropriate filter is selected according to the wavelength being produced. This pre-filters the light beam before it enters the monochromator. The pre-filtered light passes through the entrance slit (slit 1) of the monochromator and is then dispersed to produce a spectrum. The

monochromator can rotate, which enables it to send only a small segment of the spectrum through the exit slit (slit 2) to mirror M3. Mirror M3 reflects the light, and a beam splitter then splits the beam, allowing 50% of the radiation to pass to mirror M4, while 50% is reflected to mirror M5. M4 focusses the radiation to the sample compartment which contains the sample in a cuvette, while M5 focusses the radiation onto the reference compartment which contains an identical cuvette with just the solvent. In both cases the light then passes through a convex lens, and onto a detector. The intensity detected from the reference compartment is $I_0(\lambda)$ while the intensity detected from the sample compartment is $I(\lambda)$.

The absorbance $A(\lambda)$ can then be written as

$$A(\lambda) = log_{10}\left(\frac{I_0(\lambda)}{I(\lambda)}\right) = log_{10}\left(\frac{1}{T(\lambda)}\right) \quad [2.20]$$

where $T(\lambda)$ is the transmission. Since this is a comparative measurement, where the intensity of light transmitted is measured relative to a reference, any non-ideal behaviour of the spectrometer is cancelled out, and the signal does not need to be corrected.

The Beer Lambert law is useful when considering absorbance. It states that the absorbance of a sample is directly proportional to the molar extinction coefficient $\varepsilon(\lambda)$, the concentration c, and path length l

$$A(\lambda) = \varepsilon(\lambda)cl \quad [2.21]$$

Firstly, this equation can be used to determine the extinction coefficient when sample concentration is known. In addition, the linear relationship between concentration and absorbance means that absorbance measurements are often used to calculate the concentration of samples.

There are a few instances where deviations from the Beer-Lambert Rule occur. Examples include when the sample is only partially soluble[1] , when the particles are highly scattering[97], and when large aggregates form[98], which is particularly common in biological samples. Formation of bigger complexes results in Rayleigh scattering. The spectrometer cannot separate scattered light, and so the scatter could be mis-interpreted as absorbed light. However, as Rayleigh scattering is proportional to $1/\lambda^4$, it can be easily recognised in an absorbance spectrum.

2.2.2 Fluorescence Emission

Fluorescence emission spectra are the second type of steady state fluorescence measurement considered. These are relatively simple to measure and give information on the energy levels of a fluorophore. This means fluorescence emission spectra can be used to obtain data on the fundamental characteristics of a molecule, but also explore any local interactions it may have with its environment. Conversely to absorbance, where the transmitted light is detected in-line with the incident light, fluorescence emission must be measured off-axis, normally perpendicular to the incident light. This is to ensure no excitation light is recorded at the detector which would overwhelm the much smaller fluorescence signal.

In this work, both in vitro and in vivo fluorescence emission measurements have been carried out, which required two different types of fluorometer.

2.2.2.1 In Vitro Fluorescence Emission

For all *in vitro* fluorescence emission measurements, a Horiba Scientific Fluorolog was used, and the typical set up of such a device is shown in Figure 2.5.

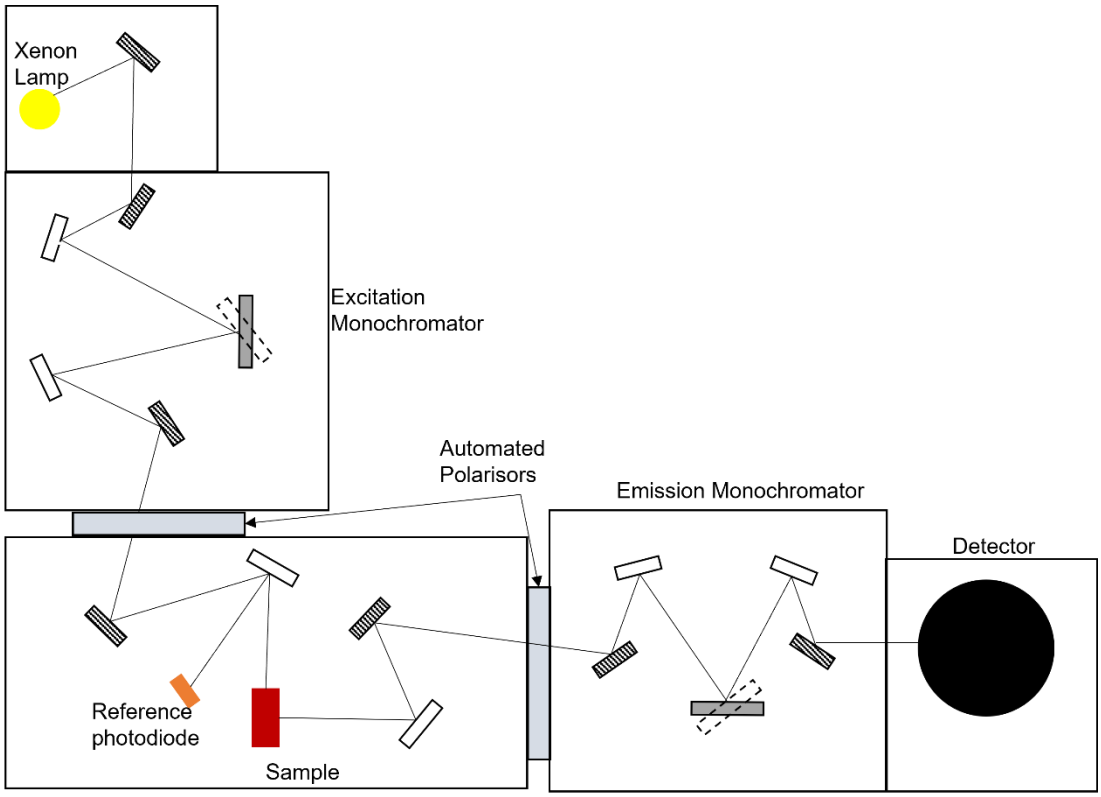

Figure 2.5. Schematic diagram for the HORIBA Scientific Fluorolog fluorescence spectrometer

A xenon lamp acts as the radiation source and produces photons which are then passed to the excitation monochromator. This filters the light, ensuring only a single wavelength of light can pass to the sample compartment and excite the sample. The excitation wavelength remains constant for the duration of the measurement. Before reaching the sample, approximately 8% of the excitation light is directed to the reference photodiode in order to correct for any fluctuations in the excitation source intensity. The sample then responds to the excitation light, and any emitted fluorescence is collected at 90 degrees to this excitation light. The fluorescence then passes to the emission monochromator, which scans across the desired wavelength range, before reaching the photomultiplier (PMT) detector.

Wavelength correction factors are applied to both the reference signal ($R(\lambda)$) collected at the reference photodiode and the fluorescence signal ($S(\lambda)$) collected at the PMT detector. This accounts for fluctuations in the excitation source intensity, dark counts, and any wavelength dependencies of the system optics. Thus the signal used in these measurements is $S(\lambda)_c/R(\lambda)_c$.

2.2.2.2 In Vivo Fluorescence Emission

To record *in vivo* fluorescence emission spectra, such as the fluorescence emission of skin, a difference spectrometer was required. For this purpose, a Horiba Scientific SkinSkan was used. This is a spectrofluorometer specifically designed for in vivo surface measurements on skin, and so can record precise spectra from highly scattering samples such as skin. A diagram of this fluorometer is shown in Figure 2.6. In principle, this works in the same way as the previously described Fluorolog, where excitation light from a 125-W continuous-output xenon lamp, with output from 240 nm to > 1000 nm, is focussed through an excitation monochromator and onto a sample. Fluorescence emission is collected, and is then passed through an emission monochromator and focussed onto a PMT detector. Both monochromators of the SkinSkan are subtractive double monochromators, which provide better resolution and block more stray light, and all slits are set at 0.5 nm. Like before, a reference photodiode detector is included to correct for variations in the lamp, the lamp's power supply, and the excitation monochromator.

The main feature of the SkinSkan that makes it highly useful for in vivo measurements is the bifurcated fibre optic cable and probe that is used to direct the light, excite the sample, and collect the emission. The probe is held flat to the skin, and the long cable allows measurements to be recorded at a distance from the SkinSkan, allowing skin fluorescence to be measured easily.

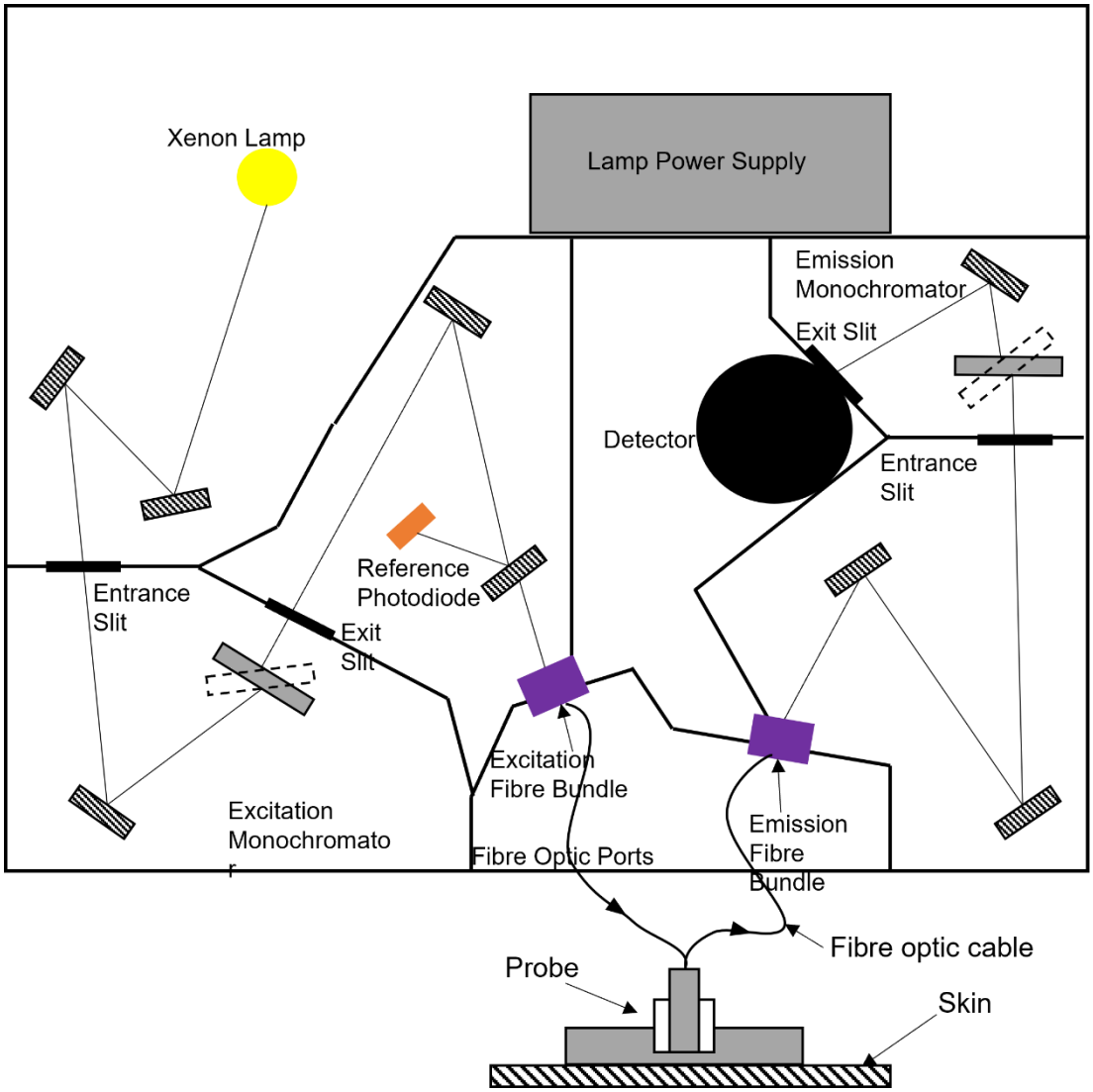

Figure 2.6. Schematic diagram for the HORIBA Scientific SkinSkan fluorescence spectrometer.

2.2.3 Fluorescence Intensity Decay

Fluorescence lifetime spectroscopy, also known as time-resolved spectroscopy, involves measuring the time a molecule remains in the excited state. Lifetime measurements are able to give further information on the fluorophore, specifically on any time-dependent processes and the underlying fluorescence kinetics.

There are 2 primary methods for measuring fluorescence lifetime: pulse fluorometry in the time domain and phase modulation fluorometry in the frequency domain. Phase modulation fluorometry uses an intensity modulated light source to excite the sample. The excitation light is modulated at high frequency, and therefore the emitted light is also modulated at the

same frequency. The excitation-fluorescence process in the sample causes the emission to be delayed in time (phase shifted), and to have a reduced peak to peak height (demodulation) relative to the excitation light. For one exponential decay, both the phase shift and the demodulation effect can be used to calculate the decay time[1]. For more complex decays, the phase shifts for a series of modulation frequencies are measured, and a complex set of equations is solved to reveal the parameters of the assumed model of fluorescence intensity decay. Phase modulation fluorometry does offer many advantages, but in this work pulse fluorometry was used for all fluorescence lifetime measurements. Thus, this method is discussed in more detail.

2.2.3.1 Time Correlated Single Photon Counting

The technique most often used in pulse fluorometry for measuring the fluorescence lifetime is Time-Correlated Single Photon Counting (TCSPC). TCSPC offers numerous advantages, the key advantage being that it offers sensitivity down to the single molecule limit. It also has sensitivity on the nanosecond timescale, which is useful for biological applications. The scheme of the equipment used for TCSPC is shown in Figure 2.7.

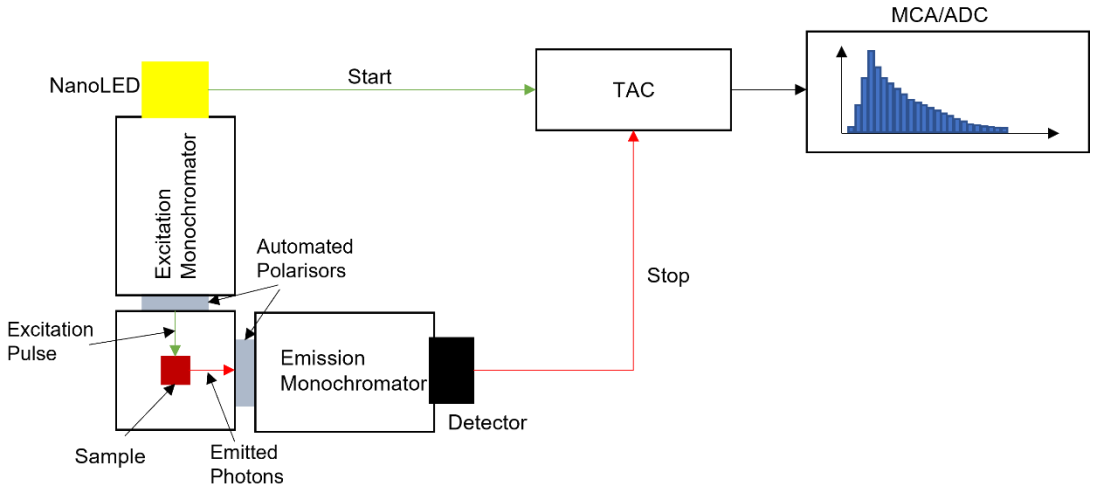

Figure 2.7. The block diagram of the TCSPC-based instrumentation used for fluorescence intensity decay measurements.

TCSPC is based on time-of-flight measurements of individual photons. The NanoLED produces a pulse of light which passes through the monochromator to excite the sample, while simultaneously sending a 'start' signal to the time-to-amplitude converter (TAC). The sample absorbs the excitation light, and then emits a photon. This emitted photon passes through the emission monochromator to the photomultiplier (PMT) detector. Once the emitted

photon is detected, the detector sends a 'stop' signal to the TAC, signalling the end of the time-of-flight measurement. The TAC produces an analogue voltage through the charging of a capacitor which is proportional to the time between the start and stop signals. The analogue voltages are converted to a digital value and stored in a histogram via the multi-channel analyser (MCA). This process is repeated millions of times, typically until one histogram 'bin' reaches 10,000 counts. The histogram is then representative of the fluorescence decay, where each bin represents a certain time interval.

The system used in this work was the HORIBA Deltaflex system, which uses monochromators in the excitation and emission channels. The excitation monochromator is optional, since the light source used in all experiments is monochromatic, and the emission monochromator is used to select the desired detection wavelength for the sample. This system also incorporates polarisers in the excitation and the detection channels in order to remove any rotational effects from the fluorescence decay[99]. The excitation polariser is vertically orientated (only fluorophore molecules whose absorption dipoles align with vertically polarised light are excited), while the emission polariser is set to 54.7 degrees. These conditions are known as the magic angle conditions, and correct for the fact that the emission for the same fluorophore can be different depending on if the emitted light is polarised or unpolarised. Using these conditions results in a signal that is proportional to the total fluorescence intensity.

When carrying out fluorescence decay measurements, the instrument response function (IRF) must be measured. This is the instrument's response to a sample with no lifetime, thus is the shortest measurable profile that the system can record[1]. It characterises the distribution of propagation traces in the components of the instrumentation, and the actual profile of excitation pulse. Ideally, the IRF should be a δ-pulse, however due to imperfect system components, this profile is often widened. For measuring the IRF both polarisers are vertically oriented. For the IRF measurement, the Rayleigh scatter from a cuvette containing a dilute LUDOX SM-AS silica solution is detected.

When measuring the emitted fluorescent photons from a sample, it is important that only one photon is detected per excitation pulse. This is because the detector and electronics have a dead time after a photon is detected in which they cannot process another photon event. If photons arrive at the detector during this dead time, they will not be registered, giving a bias towards shorter lifetimes. This is known as the pile up effect[100], and is avoided by

ensuring only 1-2 photons are detected per 100 excitation events. Experimentally, this is achieved by ensuring the stop-to-start ratio (α value) is less than 2%[101].

The process explained here, and illustrated in Figure 2.7, is based on the forward mode of the lifetime system. However, if the dead time of the electronics is long, reverse mode can be utilised to speed up the acquisition time of the fluorescence decay. In reverse-mode, the start signal is initiated when the photon is detected, and the stop signal is given when the nanoLED initiates a pulse of light. The timing electronics are therefore only triggered upon detection of a photon, and the system only undergoes dead time for a detected photon, and not for every excitation pulse.

2.2.3.2 Fluorescence Lifetime Data Analysis

To fully analyse fluorescence decays, and extract useful parameters such as the fluorescence lifetime, several model fluorescence decay functions are fitted to the experimental fluorescence decay. Traditionally, a multiexponential model has been used for this, since the excited state population is usually expected to decay exponentially[1], however, recent research has shown that a non-exponential model can also be used to model fluorescence decays[102,103]. Both models will be discussed in detail.

Multiexponential Model

Like previously stated, neither the excitation profile nor the IRF is a perfect δ-function: both are widened due to imperfect system components. To overcome this problem, the IRF is treated as a series of δ-functions, and the expected fluorescence decay $F(t)$ as a series of exponential decays that result from these δ-functions. The decay profile collected from TCSPC is therefore a convolution (*) of the IRF $P(t)$ and the fluorescence impulse response $I(t)$. The expected fluorescence decay $F(t)$ is thus

$$F(t) = \int_0^t P(t')I(t-t')dt' = P(t) * I(t) \qquad [2.22]$$

where t' is the moving time delay corresponding to the instant in which each δ-function of the IRF generates a fluorescence response.

The parameters of $I(t-t')$, and thus the fluorescence lifetimes, are obtained by convolution of $P(t)$ with a theoretical model $I(t)$ and then fitting it to experimental $F(t)$ by manipulating model parameters. The term $I(t-t')$ is sequentially iterated to find the

values of the theoretical model that best describe the data, to produce a function $F(t)$. Traditionally a multi-exponential model is used

$$I_{\alpha,\tau}(t) = \sum_{i=0}^{n} \alpha_i exp\left(\frac{-t}{\tau_i}\right) \quad [2.23]$$

where α_i and τ_i represent the pre-exponential factor and fluorescence lifetime respectively, and t represents the time after excitation. The analysis software incorporates an additional parameter B to represent the background signal, and thus the following model is used:

$$I_{exp} = B + I(t) \quad [2.24]$$

Non-Debye Model

Problems with the multi exponential model in complex biological environments have been outlined by Rolinski et al in 2016[104]. The multi-exponential model may not be supported by a real physical model, and so information within the raw fluorescence decay could be lost. Furthermore, the fluorescence decays of proteins are highly complex due to solvent or dielectric relaxation in the fluorophore's environment, and due to the microheterogeneity of the environment. Thus, protein fluorescence decay is nonexponential, and the multi-exponential model is required to parameterise the decay, however individual parameters have no physical meaning.

Therefore an alternative model has emerged to describe the fluorescence decay, which provides a more general description of fluorescence kinetics, rather than exponential. It can therefore describe fluorescence decays when the fluorophore decays non-exponentially, and when it is characterised by a distribution of lifetimes. It has been used previously to study protein intrinsic fluorescence such as tryptophan in HSA[103]. This type of model may be more useful at interpreting fluorescence behaviour in more complex environments such as cells. First derived in the theory of dipole kinetics in solid materials[105] , in this instance, the fluorescence decay $I_{\alpha,\kappa}(t)$ is given by

$$I_{\alpha,\kappa}(t) = exp\left[-\frac{1}{\kappa}\int_0^{\kappa\left(\frac{t}{\tau_0}\right)^{\alpha}} \left(1 - exp\left(\frac{1}{x}\right)\right) dx\right] \quad [2.25]$$

Where τ_0 is the fluorescence lifetime and κ and α represent the stable distributions of the fluorescence transition rates. Special cases of equation 2.25 occur when $\alpha = 0$ and $\kappa = 0$ (the

exponential, model), when $\alpha<1$ and κ =0 (stretched exponentials), and $\alpha=1$ and when κ >0 (Becquerel function)[106].

This alternative approach to fluorescence decay can be combined with the process of dielectric relaxation in heterogeneous media, thus is more applicable in complex biological environments.

Goodness of Fit

The nonlinear least squares method (NLLS), and the χ^2 goodness of fit- criterion are used to find the parameters of assumed $I(t)$ model that best describe the acquired data. The analysis software starts with assumed model and parameter values and attempts to minimise the goodness of fit value by iteratively refining these values. The χ^2 value is calculated from the following equation:

$$\chi^2 = \sum_{i=1}^{N} \left[\frac{Y(i) - F_d(i)}{\sigma(i)} \right]^2 \qquad [2.26]$$

where $Y(i)$ and $F_d(i)$ are the measured data and the fitted function respectively, and $Y(i) - F_d(i)$ expresses the deviation of the model from the experimental data at each channel. The expected standard deviation is $\sigma(i)$, and due to Poisson statistics, this can also be expressed as $\sqrt{Y(i)}$. N is the number of data channels, however due to the dependence of χ^2 on this parameter, for a large number of data points χ^2 will be large and not an accurate depiction of the goodness of fit. In these cases, the reduced χ^2 value χ_R^2 is used, which is calculated using χ^2, the number of data points N, and the number of parameters p:

$$\chi_R^2 = \frac{\chi^2}{N - p} \qquad [2.27]$$

A χ_R^2 = 1 is considered a perfect fit, and 0.9 < χ_R^2< 1.2 is generally accepted as a good fit. A χ_R^2 >1.2 is not thought to be a good fit, and suggests a different model must be used to describe the data[107].

Weighted residuals W_t are also used to assess how well the fitted model represents the measured data.

$$W_t = \frac{Y(i) - F_d(i)}{\sigma(i)} \qquad [2.28]$$

A random distribution of residuals around 0 indicates a good fit, however if the distribution is not random, this could indicate either an additional component is required in the model, or there are systematic effects interfering with the measurement. An example of the measured data, fitted model, and weighted residuals is shown in Figure 2.8.

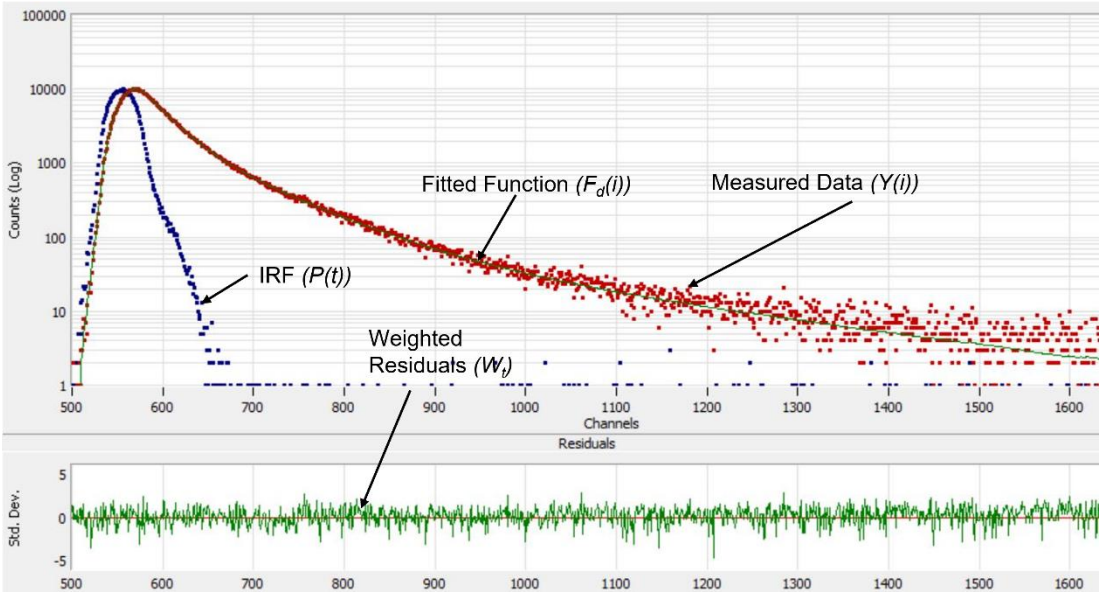

Figure 2.8. An example of measured lifetime data, the fitted model, and the weighted residuals

Scattered Light

In certain cases, scattered light may have to be considered when analysing fluorescence lifetime data. This is particularly relevant to biological samples such as those used in this work, as they are highly scattering[108]. If there is a substantial contribution of scattered light to the decay signal, this may distort the decay, particularly at shorter wavelengths. An additional component $C_\lambda(t)$ representing the scattered light is therefore used to correct this in the model for fluorescence decay[102].

$$I_{exp}(t) = B + C_\lambda(t) + I(t) \qquad [2.29]$$

Including the actual scattered excitation light $C_\lambda(t)$ (the fraction of the prompt function shifted in time due to the detecting photomultiplier's temporal dependence on wavelength) into the model of experimental curve enables accurate fluorescence decay fitting also in the case when the experimental decay has large contribution of the scattered light[102]. In this work, $I(t)$ can be equation 2.23 or equation 2.25.

For fitting data to the exponential model, Appendix A1 presents some comparative examples, where the same decay data is fit to equation 2.29 (when $I(t)$ is exponential), and to the traditional model decay (equation 2.23, with an extra exponential component that is fixed to ½ of the MCA time calibration value to represent the scattered light). Collagen and collagen glucose-samples are used as examples, and the result is presented in Figures A1.1-A1.6. The differences in the results obtained in both approaches are mostly negligible, and so in this thesis we use the results recovered from fitting equation 2.29 to any lifetime decay data, as the model of the measured signal assumed in this approach is more realistic. The examples in Appendix A1 consider the comparison only for the case of fitting to an exponential model, however when using the general relaxation function (equation 2.25), scattered light is always taken into account following equation 2.29.

2.2.4 Time-Resolved Emission Spectra (TRES)

2.2.4.1 Constructing TRES

Time-resolved emission spectra $I(\lambda, t)$, or TRES, are a series of fluorescence emission spectra obtained at discrete times throughout the fluorescence decay[109]. These time-resolved spectra offer an advantage over steady-state emission spectra since steady state measurements are time-averaged. Any time-dependent processes are therefore lost. TRES are able to resolve any time-dependant processes, such as excited state kinetics, and thus more information on the system can be obtained.

TRES can be measured directly or indirectly using TCSPC. When TRES are measured directly, the photons arriving at the detector within a short time interval are recorded. The time interval is selected by setting the output pulses from the TAC to be within a range of voltage values, and then the emission spectrum is recorded using a monochromator. In this method, the TRES contain distortions due to convolution with the excitation pulse.

For this reason, TRES tend to be recorded indirectly, which allows the spectra to be corrected for these distortions. The fluorescence decay is measured at a range of wavelengths that span the emission spectrum of the sample, as shown in Figure 2.9, with the spectral resolution increasing as the number of detection wavelengths increases[110].

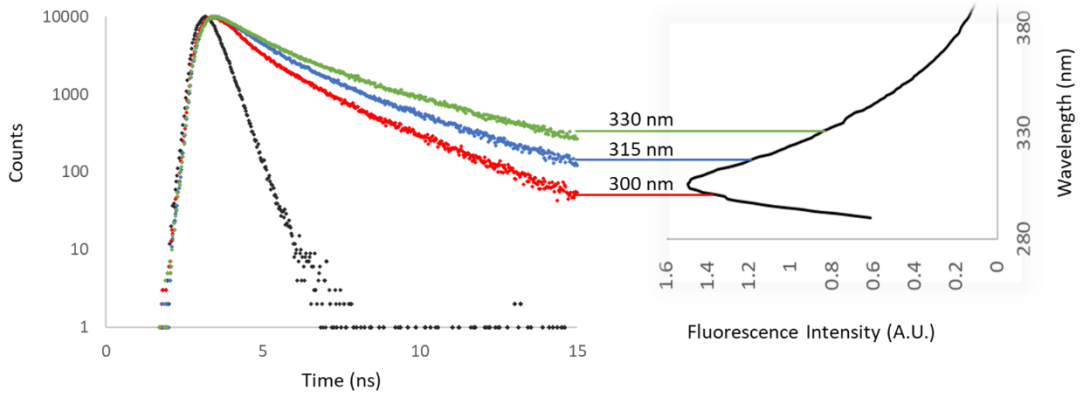

Figure 2.9. Schematic of how to measure time resolved emission spectra (TRES). The emission spectrum is first measured to determine the appropriate detection wavelength range for fluorescence lifetime decay measurements

Each decay is then fit to the multi-exponential model as shown in equation 2.23, with the resultant parameters a function of wavelength. The parameters found from fitting to this model do not bear any physical significance: they are used to create an accurate mathematical representation of the fluorescence decays that will be used to construct the TRES.

Once values for $\alpha_i(\lambda)$ and $\tau_i(\lambda)$ have been determined, they can be used to calculate TRES

$$I_t(\lambda) = \frac{I_\lambda(t)S(\lambda)}{\sum_i \alpha_i(\lambda)\tau_i(\lambda)} \qquad [2.30]$$

where $S(\lambda)$is the steady-state fluorescence intensity at the wavelength at which fluorescence decay was recorded. TRES are usually presented as a function of wavenumber ν (since the function used to model TRES is a function of ν), and so the $I_t(\lambda)$ calculated according to equation 2.30 is converted to

$$I_t(\nu) = \lambda^2 I_t(\lambda). \qquad [2.31]$$

This procedure generates a series of fluorescence intensity spectra as a function of wavenumber ν, with each spectra representing fluorescence at a different time t after excitation.

2.2.4.2 Toptygin Modelling

To extract further information from the TRES, they can be modelled using multiple modified Gaussian distributions. These distributions can represent the spectral shape of different fluorescent components within the system. A Gaussian function is often used in statistics,

and is able to describe how random variables are distributed. The graphical representation is given in Figure 2.10 where v_i and σ_i are the centre (mean) and the half-width of the distribution respectively.

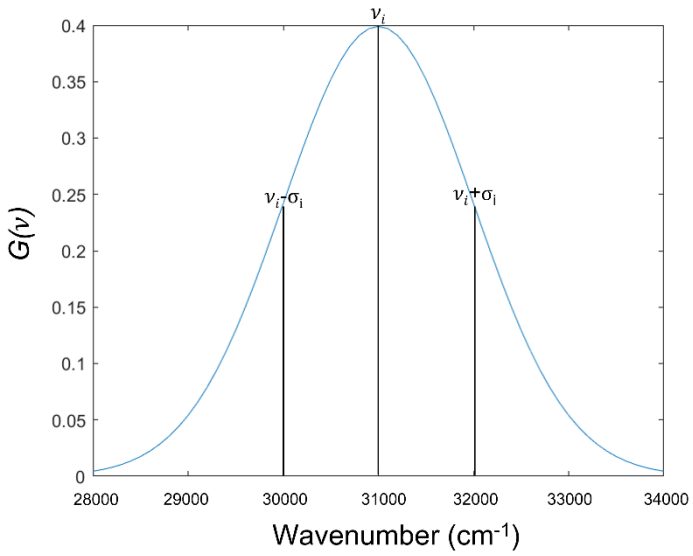

Figure 2.10. Diagram of a Gaussian distribution, where the peak position, $v_{i,}$ and the standard deviation $\sigma_{i,}$ are shown.

Mathematically, the Gaussian Function is given by

$$G(v) = \frac{1}{\sqrt{2\pi\sigma_i}} exp\left(-\frac{(v - v_i)^2}{2{\sigma_i}^2}\right) \quad [2.32]$$

where again v_i and σ_i are the mean and standard deviation of the distribution.

Using the equation for the single molecule emission spectrum in equation 2.10, the spectrally- and time-resolved emission intensity $F_v(v,t)$ can be calculated. It is equal to the single molecule emission spectrum multiplied by the number of fluorescent molecules in the excited state $N(t)$ at time t

$$F_v(v,t) = av^3 S_{vib}(v - v_{01}(t))|\mu_{01}(t)|^2 N(t) \quad [2.33]$$

Based on the Toptygin approach[85], the v^3 parameter is thus included in the model used to represent TRES spectra. Combining with the Gaussian Function, the model used to represent TRES $F(v,t)$ becomes

$$F(v,t) = \sum_{i=1}^{N} \frac{C_i(t)}{\sqrt{2\pi}\sigma_i(t)v_i(t)(v_i(t)^2 + 3\sigma_i(t)^2)} v^3 exp\left(\frac{-(v - v_i(t))^2}{2\sigma_i(t)^2}\right) \quad [2.34]$$

In this model *N* is the number of spectral components, C_i is the contribution of each component to fluorescence, v_i is peak position, and σ_i is the half-width of the distribution. It should be noted that the $1/(\sqrt{2\pi}\sigma_i(t)v_i(t)(v_i(t)^2 + 3\sigma_i(t)^2))$ term is the normalisation factor for this equation. The Franck−Condon factor envelope[85] is approximated here by a Gaussian function instead of a more realistic skewed function, allowing a reduction in the number of model (equation 2.34) parameters, which was necessary because of the limited number of experimental TRES points which tend to be calculated in TCSPC analysis. The benefit of fitting TRES to this model is that these parameters can be extracted and then monitored over time for each spectral component, which is not possible in steady state spectra. A disadvantage of this model however is that it can become slightly distorted at the high energy end of the spectrum, which may be due to insufficient spectral resolution, or errors in spectral correction[85].

2.2.4.3 Akaike's Information Criterion

When modelling TRES Akaike's Information Criterion (AIC) was used to measure the appropriateness of the model. It is based on the residual sum of squares RSS from the nonlinear least squares fitting, the number of parameters k, and the number of data points n. In this work, when modelling TRES the sample size is small, and so an additional correction factor is used, giving the corrected Akaike's Information Criterion (AIC_c)

$$AIC_c = nlog\left(\frac{RSS}{n}\right) + nlog(2\pi) + n + 2k + \frac{2k(k+1)}{n-k-1} \qquad [2.35]$$

Since n is the same in all our cases, the constant terms can be dropped giving

$$AIC_c = nlog\left(\frac{RSS}{n}\right) + n + 2k + \frac{2k(k+1)}{n-k-1} \qquad [2.36]$$

A smaller AIC_c indicates a more parsimonious model i.e. the simpler model with the least assumptions and variables, but the greatest explanatory power[111].

2.2.6 Fluorescence of Bacteria and Contaminants

This work includes various in vitro protein studies, in which a protein is dissolved in phosphate buffered saline (PBS). These samples are kept in a sealed cuvette either at room temperature or at 37°C for a long period of time (up to 56 days), with fluorescence measurements being carried out at regular intervals. This presents a potential problem: PBS is a good culture medium for bacteria, which is itself fluorescent[112]. Bacteria could therefore grow as the experiments progress and interfere with the measured fluorescent signal.

Therefore, to ensure that signals recorded were indeed caused by the intrinsic fluorescence of the studied fluorophore, and not by bacteria growth or any impurities in the glucose that was used, reference samples were prepared using PBS, glucose in water, and glucose in PBS. The fluorescence emission of these samples was then recorded under the exact same conditions as used for the studied fluorophores. The result for this at the three excitation wavelengths 280, 340, and 370 nm (the full range of excitation wavelengths used for the protein studies) are presented in Figure 2.11.

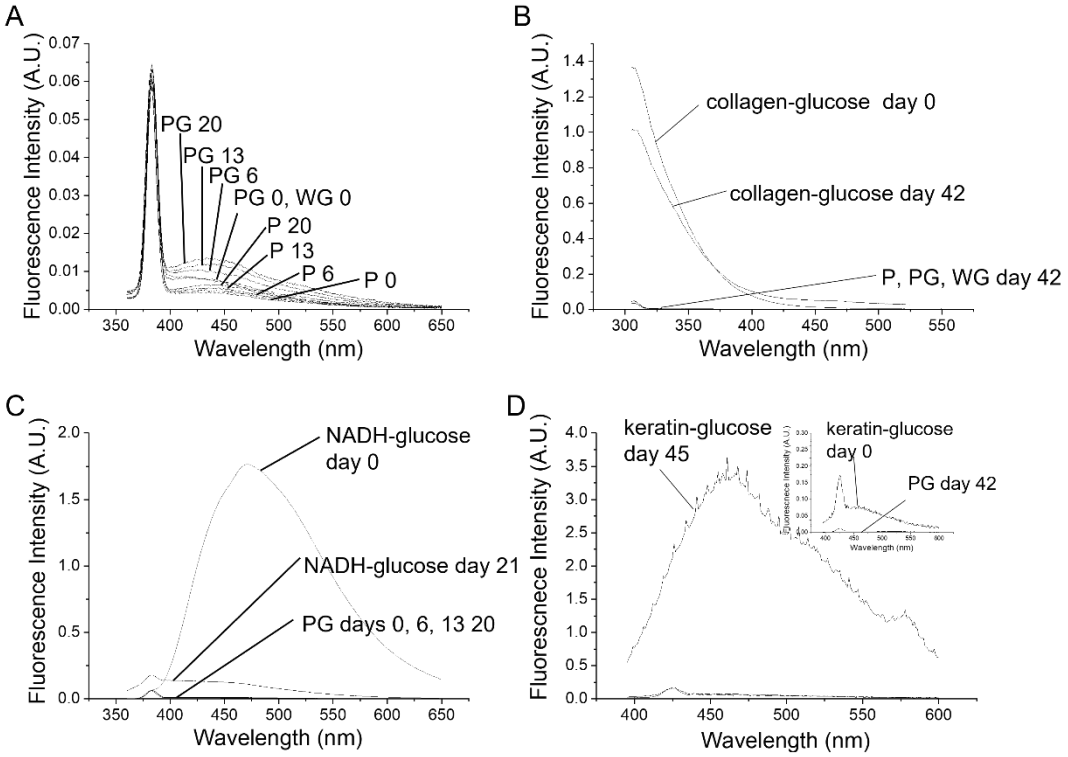

Figure 2.11. Part A shows the evolution of fluorescence emission spectra for PBS (P), PBS-glucose (PG), and water-glucose (WG) samples when excited at 340 nm. Part B, C, and D, show examples of protein-glucose spectra alongside the PBS-glucose spectra for comparison, when excited at 280 nm, 340 nm, and 370 nm respectively. Scales are in arbitrary units, but spectra on the same plots have the same scale.

Figure 2.11A shows the fluorescence emission spectrum of PBS (P), PBS-glucose (PG) and water-glucose (WG) samples on various days after preparation when excited at 340 nm (this excitation wavelength was used for collagen and NADH studies). Although the fluorescence signal from each sample increases over time, the overall fluorescence intensity is still very low. Figures 2.11 B, C, and D show the emission spectrum of the reference samples alongside emission spectrum for protein-glucose samples. These plots demonstrate that the impact of

potential bacteria growth and impurities on the protein fluorescence is negligible for all excitation wavelengths, and thus any changes in the fluorescence signal seen in *in vitro* studies are not due to bacteria growth.

2.2.7 Errors

With any type of measurement, there is the possibility of error in the result. A measurement error is the difference between the true value and the value indicated by the instrument. There are two primary categories of measurement error, systematic error and random error, both of which are discussed briefly below.

2.2.7.1 Systematic Error

A systematic error affects the accuracy of the data collected. It is a consistent or proportional difference between the observed and actual value of the quantity being measured. This can arise, for example, when an instrument is incorrectly calibrated. All physical quantity measurements are affected equally, and consistent differences in readings will be produced.

While systematic errors cannot be completely eliminated, as no laboratory protocol is perfect, they can be minimised by ensuring all instruments used are properly calibrated (in this work, instruments were calibrated on a regular basis), and by comparing measured values against accepted and published values for similar measurements.

2.2.7.2 Random Error

A random error affects the reproducibility of the data collected. A random error displaces the measured value by different magnitudes and directions, and has an unknown cause. It will cause repeated measurements to yield different results under the same conditions.

In this work, random errors were minimised by performing repeated measurements, and then calculating the average values. This technique was used when fitting fluorescence intensity decays to the model given by equation 2.29, and also when measuring spectra from the *ex-vivo* and *in-vivo* samples discussed in Chapters 7 and 8. In this way, any random errors in the results were minimised. Additionally the *in vitro* experiments investigating collagen, NADH, keratin, and HSA were repeated to ensure that the results obtained were repeatable, and not due to any error.

3.Collagen

3.1 Introduction

Collagen is one of the most abundant fibrous proteins in mammals[113], where it is found in the skin, tendons, blood vessels, bones and teeth[42]. The defining characteristic of collagen is its tensile strength, but alongside this it can display different properties depending on tissue type[114]. In skin for instance collagen provides both the structure and the flexibility required[115]. There are 28 different types of collagen, made from 46 distinct polypeptide chains[116]. These are categorised first into fibrillar or non-fibrillar collagen, and then subdivided further into specific types. In skin, fibrillar collagen is the most dominant, with type I and type III collagen being the principal types[117].

3.1.1 Collagen Structure

Collagen molecules are approximately 300 nm in length, with a diameter in the region of 1.6 nm[118]. All molecules are comprised of three polypeptide chains known as α chains[119]. Within these chains there is always at least one region with the repeating amino acid sequence Gly-Xaa-Yaa[120], where Gly is glycine and Xaa and Yaa can be any amino acid, but these are typically proline and hydroxyproline respectively[119]. These α chains fold into left-handed polyproline-II like helices, which then coil around each other to form the right-handed collagen triple helix[116].

This triple helix is very tightly packed, which is why it is essential to have a glycine residue at every third position: this is the only residue small enough to fit into the space in the centre of the triple helix[121]. The amino acids at the Xaa and Yaa positions are often proline and hydroxyproline because these are both very rigid, which helps to stabilise the triple helix[119]. Once fully formed, the N- and C-terminal ends of the triple helix are cleaved by enzyme action to leave the fully mature collagen molecule[122].

There are slight variations in the structure of collagen molecules between different collagen types. Type I collagen is one of the most common types of collagen found in skin, and follows the above structure, where two of the polypeptide chains are α1 helices and one is an α2 helix[122]. The second most abundant type of collagen found in skin is also a fibrillar collagen, type III collagen. Again this has a structure similar to that outlined above, except this type is made from three α1 polypeptide chains[119], and contains a structure known as the disulphide or cysteine knot. The cysteine knot is a defining characteristic of type III collagen, and is located between the triple helix region and the C-terminal telopeptide[123] (the end part of the

amino acid sequence which is removed upon maturation of the collagen[124]). It is comprised of three inter-chain disulphide bonds, and it acts to stabilize the triple helix[119].

In humans, collagen is an integral part of many hierarchically structured biological tissues[115]. In order to form these macroscopic tissues and organs, individual collagen triple helices self-assemble in a complex ordered manner[116]. The specific way in which such a tissue (or organ) is assembled differs greatly between tissues, and this accounts for the variability in mechanical properties observed in different collagen rich tissues[115]. For example collagen is responsible for stiff bone, elastic skin and soft cartilage[113]. Tissues such as the skin are comprised of collagen fibres. Each fibre is made from smaller collagen fibrils, which are assembled from microfibrils. Microfibrils in turn consist of individual collagen molecules[122]. An outline of this is shown in Figure 3.1.

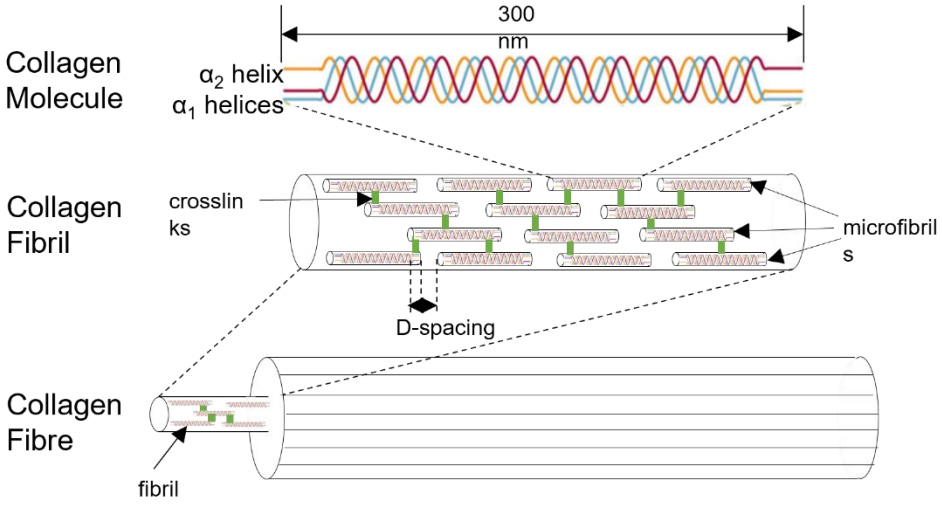

Figure 3.1. An illustration of how collagen molecules assemble into fibres

Collagen triple helices self-assemble in line with each other to form microfibrils. These right handed microfibrils can then interdigitate with neighbouring microfibrils to create a spiral like structure: the mature collagen fibril[124]. Assembly of the microfibrils into fibrils involves the formation of staggered arrays with some overlap and gap regions. This creates an oscillating surface topography of axially repeating bands along the fibril length. This is known as the periodicity of the fibril, or it's D-spacing[125]. The theoretical value for the D-spacing is 67 nm, but in reality the D-spacing of collagen fibrils is a distribution around this value[126]. The fibrils are stabilised within these arrays via intramolecular and intermolecular crosslinks[127]. Collagen crosslinks can be enzymatic, or non-enzymatic, but enzymatic crosslinking

specifically is a vital phase in the development and repair of collagen connective tissues[128]. Furthermore, the absence of these intermolecular bonds reduces the strength of the fibril, and compromises its function[129].

The formation of these enzyme -mediated crosslinks occurs during maturation of the fibril, and one of the best characterised crosslinks is that mediated by lysyl oxidase (LOX)[129]. LOX-mediated crosslinks are essential for proper development of the fibril structure and its mechanical integrity[128]. LOX acts on lysine or hydroxylysine in the collagen molecule, which results in an immature crosslink. These later transform into more stable crosslinks that increase collagen interconnectivity, fibril stability, and mechanical integrity[129]. This formation of these crosslinks then stops when the collagen fibril is fully mature[128].

Collagen fibrils then aggregate together in a three-dimensional cylindrical structure to form a collagen fibre. These are the building blocks of collagen-based tissues, including skin[130].

3.1.2 Collagen Glycation

As discussed in a previous chapter, increased glucose levels, such as in diabetes, leads to glycation, and the formation and accumulation of AGEs. Proteins with a long biological half-life are more likely than other proteins to experience this process. Collagen half-life varies between tissues and in skin is approximately 10 years[131], which makes it highly susceptible to glycation and AGE formation[132]. On collagen glucose binds to a free lysine residue[133] to form a Schiff Base and follows the classical glycation pathway outlined previously. The AGEs can be in the form of adducts or crosslinks within or between the proteins[134]. Accumulation of crosslinking AGEs in collagen has several detrimental effects: the collagen triple helix becomes less soluble and flexible[131], and it can lead to reduced arterial and myocardial compliance, increased vascular stiffness, and increased diastolic function and systolic hypertension[135]. Collagen glycation also augments formation and migration of myofibroblasts, which contributes to fibrosis in diabetes[136]. Glycation of collagen is also related to the duration and severity of hyperglycaemia[59, 137].

Collagen AGEs can accumulate in skin, and it has been established that the risk of diabetes complications can be predicted by identifying the presence of AGEs in dermal tissue. The studies have found[62] that long term treatment of hyperglycaemia reduced the levels of AGEs in skin collagen. This suggests that skin AGEs, including collagen AGEs, can be used as a biomarker for diabetes complications[138].

3.1.3 Collagen Fluorescence

In this chapter we study the potential for using the time-resolved intrinsic fluorescence of collagen as a biomarker of its glycation. Fluorescence spectroscopy has been used extensively to study the formation and accumulation of AGEs both in vitro[139, 140] and in vivo [138, 141]. Specifically, the use of three naturally fluorescent amino acids: phenylalanine, tryptophan, and tyrosine[1], allows non-invasive study of biological structures and processes without the addition of any extrinsic fluorophore.

Collagen's fluorescence in human skin[141] originates from 2 sources: tyrosine (Tyr)[142, 143] and collagen crosslinks. As there are no tryptophan[144] or phenylalanine[145] residues in collagen, they do not interfere with Tyr. It can be excited at approximately 275 nm, and has peak fluorescence emission at 305 nm[143].

There are 2 types of collagen crosslinks[141]: pepsin-digestible and collagenase-digestible. The former are excited at approximately 340 nm and emit at 400 nm, and the latter are excited at 360 nm with fluorescence emission peak at 440 nm[146]. Although it is not clear what structural differences there are between these two sets of cross-links, it has been confirmed experimentally[141] that fluorescence from collagen cross-links does have two distinct bands. Kollias et al.[146] showed that the fluorescence intensity at 400 nm greatly reduced following pepsin digestion, but this had no effect on the fluorescence emission peak at 440 nm. The opposite was true for collagenase digestion, where there was no effect on the 400nm peak, but the emission at 440 nm almost disappeared

AGE accumulation drives more crosslinking within collagen fibres, and so impacts its intrinsic fluorescence[147], making fluorescence emission spectra a valuable tool for monitoring AGE accumulation[6, 148]. Indeed, previous studies have used skin auto-fluorescence as a means of studying glycation induced changes both in diabetic patients, and healthy controls[6, 148]. The steady state technique however, is not able to fully explain the mechanisms of glycation and so help in the search for anti-glycation factors that could prevent AGE formation.

In this chapter we propose a more comprehensive detection of intrinsic fluorescence by performing systematic time- and wavelength-resolved measurements, instead of performing a single measurement of the fluorescence intensity decay at the arbitrary selected excitation and detection wavelengths. Our method explores the time-resolved emission spectra (TRES) obtained at discrete times throughout the fluorescence decays[109]. We aim to verify whether the alterations in fluorescence triggered by collagen glycation are sufficient to help in

understanding the actual mechanisms of glycation, and thus potential pathways of its prevention.

3.2 Methodology

3.2.1 Collagen Sample Preparation

We have studied the time-resolved responses of tyrosine (excitation at 280 nm) and of pepsin-digestible cross-links (excitation at 340 nm) in collagen. Two samples were analysed: free collagen and collagen-glucose solutions.

Tyrosine: Sample preparation followed the same protocol in both cases. Collagen type 1 solution from rat-tail and phosphate buffered saline pH 7.4 (PBS) were purchased from Sigma-Aldrich and used to prepare a free collagen sample of concentration 10 µM. The collagen-glucose sample was then prepared by adding glucose powder (Sigma-Aldrich) to make a sample containing 10 µM collagen and 20 mM glucose. Both samples were stored in an oven at 37ºC for the duration of the experiments. All measurements were carried out using 4x1x1cm quartz cuvettes.

Pepsin digestible cross-links: The collagen sample had concentration 20 µM, and the collagen-glucose sample contained 20 µM collagen and 40 mM glucose. Higher concentrations of both collagen and glucose were used to optimise the experiment, as the experiments at the original lower concentration showed that the fluorescence intensity at 340 nm excitation wavelength was too low, compromising the proper signal-to-noise ratio.

In the glucose-containing samples, the glycated collagen was not purified from the non-glycated one. The first fluorescence measurements were taken within ~20 min of glucose being added to the sample.

3.2.2 Fluorescence Measurements

Corrected fluorescence emission spectra were obtained on a Fluorolog (Horiba Scientific) using a resolution of 1 nm, with both the excitation and emission monochromators set to a slit width of 5 nm. The fluorescence intensity decay measurements, and therefore the TRES, were obtained using a DeltaFlex fluorescence lifetime system (Horiba Jobin Yvon IBH Ltd, Glasgow), which uses time-correlated single photon counting (TCSPC) to record fluorescence decay. Two NanoLEDs with repetition rate 1MHz and the peak excitation wavelengths at 280 nm (pulse duration <1ns) and 340 nm (pulse duration <1ns) were used to study tyrosine and pepsin-digestible cross-links, respectively. To determine TRES, the fluorescence decays were recorded at a range of detection wavelengths (300-400 nm for Tyr, 380-500 nm for cross-

links), in increments of 10 nm. The fluorescence decay analysis, and details of how TRES were constructed was discussed in Chapter 2, and so will not be repeated here.

The data was fitted to equation 2.29, and for the data obtained for both collagen and collagen-glucose samples, a 3-exponential model (N=3) (eq. 2.23) was found to be sufficient to describe all fluorescence decays on the basis of the goodness-of-fit criterion (χ^2) and the distributions of residuals (see examples in Appendix B1). Contrary to the common approach, however, we do not claim that this indicates a 3-exponential kinetics, rather the 3-exponential function is a good mathematical representation of the observed decays.

TRES were calculated using equations 2.30 and 2.31, and the Toptygin model function 2.34 was fitted to the experimental TRES points, and the potential mechanisms of the observed changes in TRES were discussed on the basis of the goodness of fit obtained for different M, and the changes in $v_i(t)$, $C_i(t)$, and $\sigma_i(t)$ values. The experimental TRES points and the corresponding model TRES curves were found for day 0, and for various subsequent days after preparation. The examples of the obtained plots are shown in Appendix B2 (Figures B2.1 and B2.2)

3.3 Results and Discussion

3.3.1 Tyrosine Response (Excitation 280 nm)

Figure 3.2 shows the fluorescence emission spectra for free collagen and collagen-glucose over 56 days, where the samples were excited at 280 nm to observe the response of tyrosine. The absolute fluorescence intensities of both collagen and collagen−glucose decrease over the 56 days, as shown in Figure 3.2A. We note that in repeat experiments (which considered the same conditions, and also the case where concentration of glucose was increased), the same result was observed, where in both samples the fluorescence intensity decreased over time. Changes observed in both collagen and collagen-glucose samples could be due to aggregation and/or glycation, as both processes may affect the conformation of the protein, including the local micro-environment of tyrosine.

Figure 3.2B presents the pairs of spectra at individual days normalised to 1. The narrower spectra observed in the collagen−glucose sample may be a result of glycation, where the presence of the collagen−glucose aggregates reduces the formation of bigger collagen aggregates and consequently reduces the broadening of the spectrum reflecting the narrower range of the π electron spatial distribution. This hypothesis is further supported by TRES results discussed in the later section. It should be noted that we do not consider the

potential degrading effects of UV illumination on the sample, as the intensities of light used in our measurements are minimal.

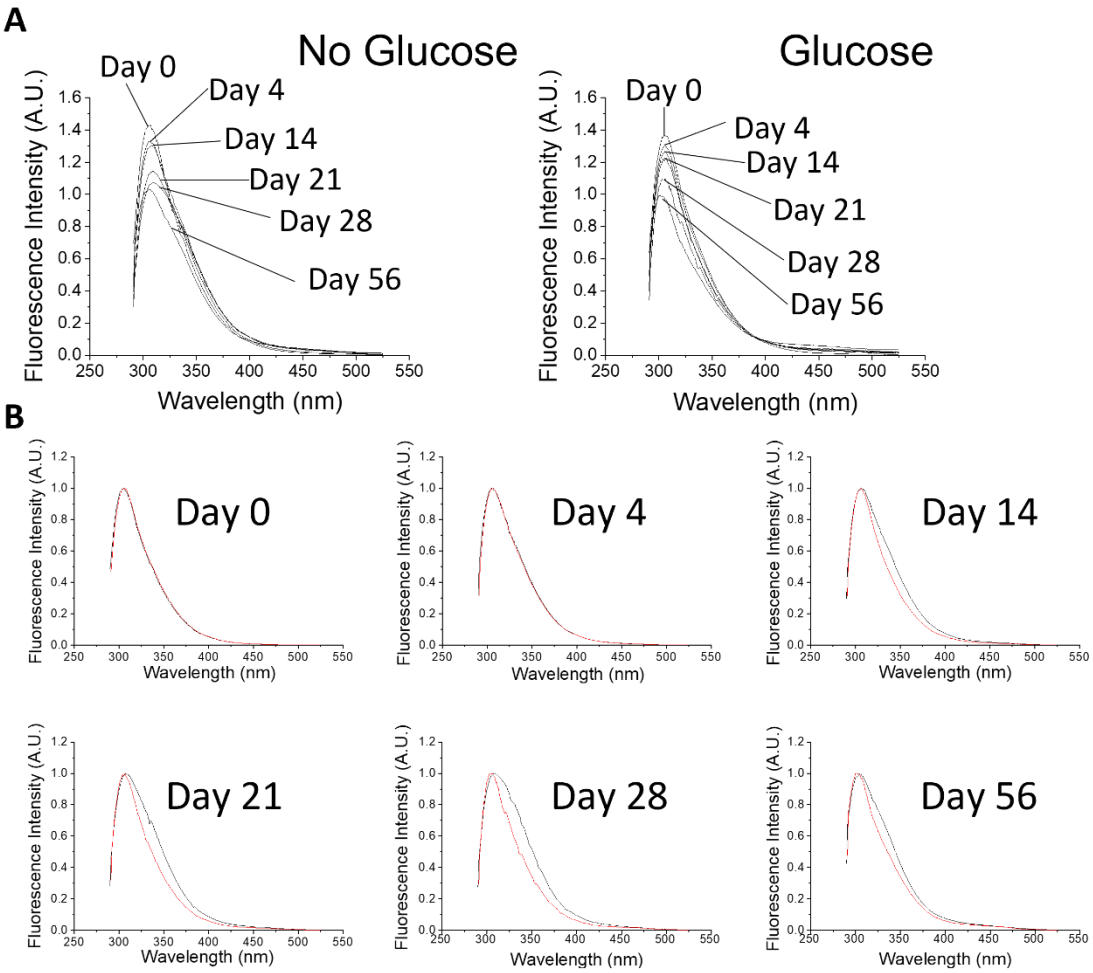

Figure 3.2. Fluorescence emission spectra for free collagen and collagen glucose when excited at 279nm. (A) shows fluorescence changes over time for collagen and collagen-glucose at days 0, 4, 14, 21, 28 and 56. (B)shows collagen (black) and collagen-glucose (red) on days 0, 4, 14, 21, 28, and 56, with both samples spectra normalised to their peak fluorescence.

Additional information has been extracted from the analysis of TRES of both samples. This was implemented through a series of fluorescence intensity decays recorded when exciting the collagen's Tyr at 280 nm. The decays were detected at the range 300-400 nm in increments of 10 nm (as in the example for day 0 shown in Figure 3.3). Figure 3.3 demonstrates a strong lifetime-wavelength dependence, where fluorescence at shorter detection wavelengths decays more rapidly than at longer wavelengths. This is consistent with the lifetime-wavelength correlation observed in proteins[104] and is usually caused by dielectric relaxation of intrinsic fluorophores.

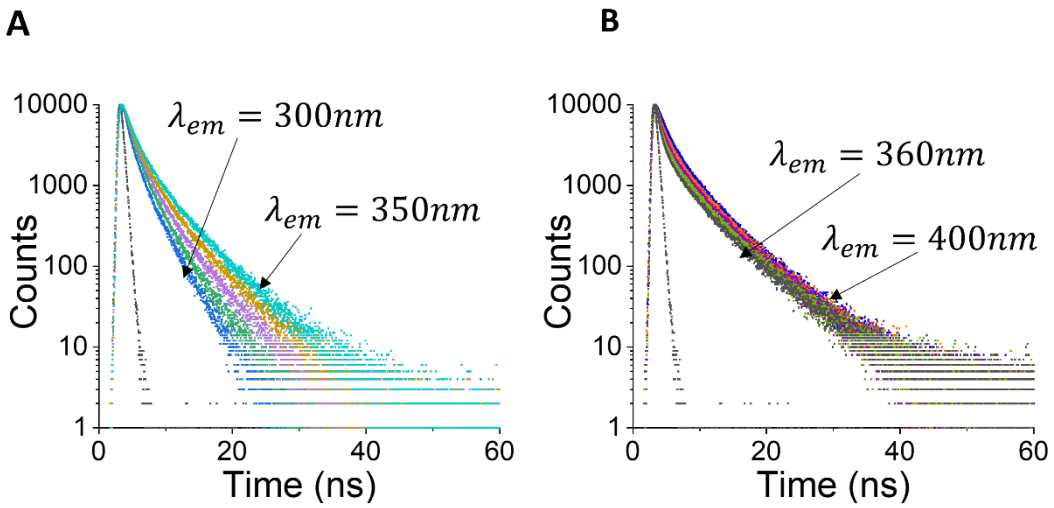

Figure 3.3. Fluorescence Intensity decays for collagen on day 0, excited at 279nm. Part A shows the emission wavelengths from 300-350nm in increments of 10nm, and part B shows the emission wavelengths from 360-400nm. Both plots are shown with the prompt signal (black).

The decays recorded at various times after sample preparation were used to calculate the TRES for both collagen and collagen−glucose samples. These plots, along with their related normalisation plots, are shown in Figure 3.4.

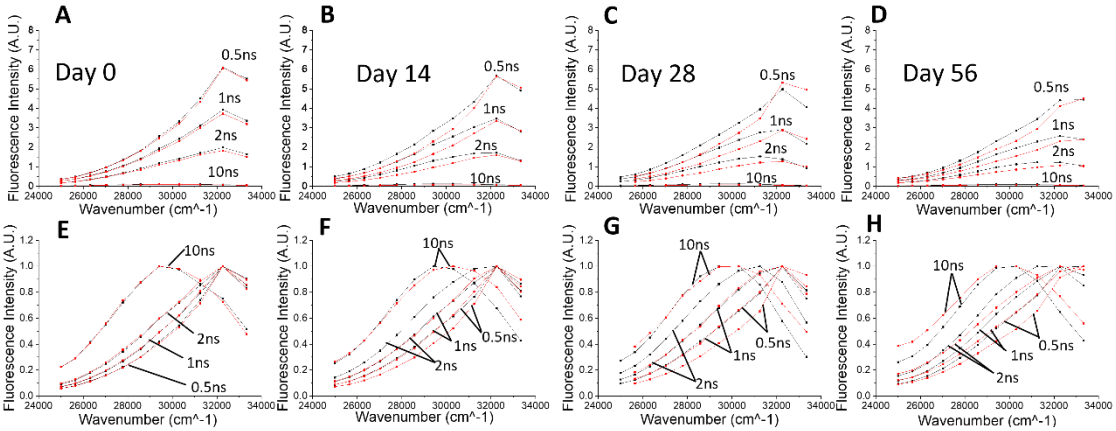

Figure 3.4. TRES spectra of free collagen (black) and collagen-glucose (red) on day 0 (A), day 14 (B), day 28 (C), and day 56 (D). Plots (E), (F), (G) and (H) show the same spectra after normalisation.

Part A (absolute spectra) and E (normalised spectra) show the result obtained for both samples on day 0, where no effect of glycation is expected. In this case, the spectra for both the free collagen and collagen−glucose samples are very similar, with the intensity gradually decreasing within nanoseconds. This similarity demonstrates the robustness of the

experimental and data processing procedures that were used for TRES calculation. Indeed, the similarity of the TRES obtained for Day 0 demonstrates the reproducibility of the experimental and data processing techniques, including the fitting procedures used to fit the experimental decays to the three-exponential model.

At the later times after sample preparation, differences in the TRES of both samples are observed, indicating changes in the evolution of collagen spectra caused by the presence of glucose. To obtain more quantitative information on the detected effects, the technical model of TRES (eq. 5) was fitted to experimental TRES data. We used the Akaike information criterion[111] (for definition see Appendix B3) to optimise the number M of the components of eq. 5. It has been found (see Table B3.1 Appendix B3) that to avoid over parametrisation of the model, only one component (M= 1) should be used. Note that such a result does not imply homogeneous dielectric relaxation, because the same shapes of normalised TRES are not observed here. The evolution of the recovered $v_i(t)$, $C_i(t)$, and $\sigma_i(t)$ values are plotted in Figure 3.5.

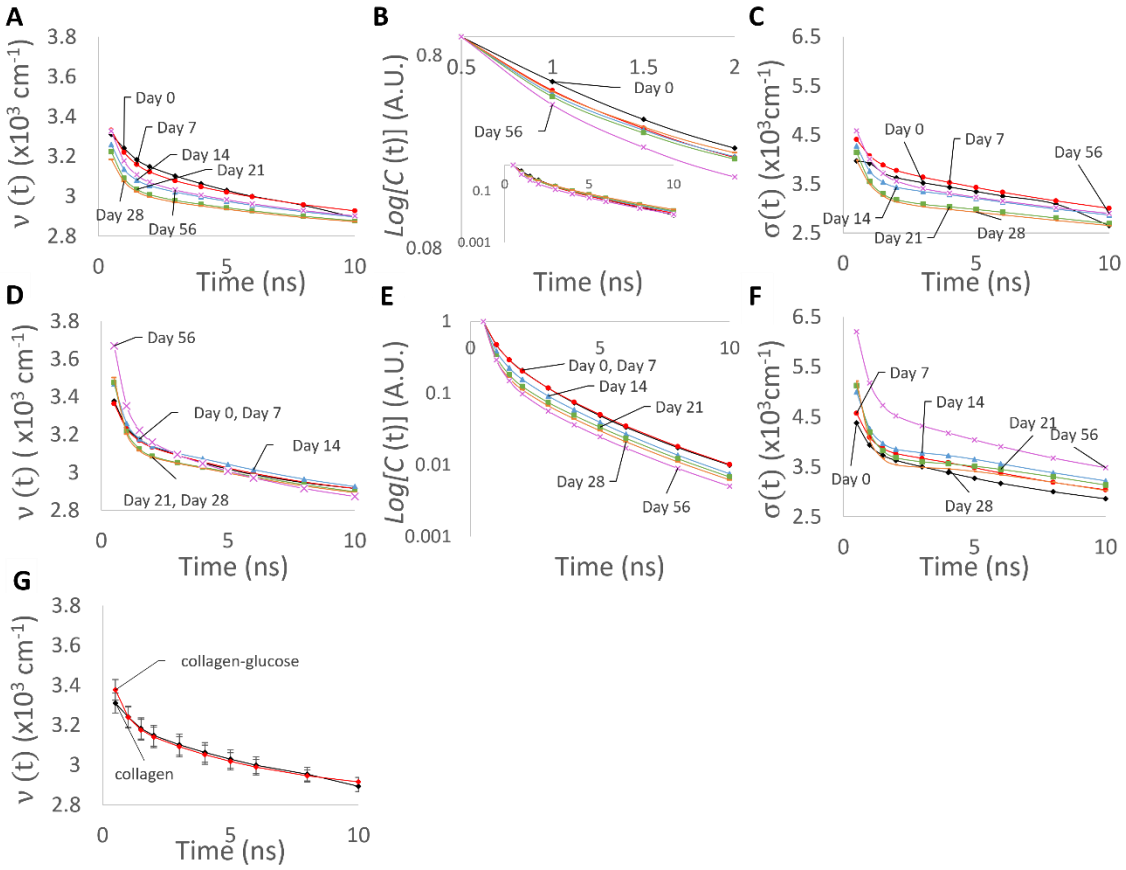

Figure 3.5. Plots A, and D show the time evolution of the peak position $\nu(t)$ of the emitting fluorophores for collagen and collagen-glucose respectively. The time evolution of fluorescence intensity C(t) is shown for collagen and collagen-glucose in plots B and E, with each spectra normalised. The insert shows the same data over a longer time range. Plots C and F show the time evolution of the distribution of the emitting fluorophores for collagen and collagen-glucose respectively. The six lines show day 0, day 7, day 14, day 21, day 28, and day 56. Part G shows $\nu(t)$ for collagen and collagen-glucose on day 0 for comparison, with the error bars showing the 90% confidence intervals for the fitted values.

Initially, at day 0, the peak position of the emitting fluorophore $\nu(t)$ is ~31,500 cm^{-1} for both samples. Over the 10 ns following excitation, the peaks show a shift to longer wavelengths, ending at ~29,200 cm^{-1}. We note that at day 0 there was no difference between the spectral shifts in the free collagen and glucose-collagen samples (see Figure 3.5G). Over the 56 days, however, the initial peak position $\nu_{peak}(t)$, of the un-glycated sample (Figure 3.5A) steadily decreased, still following the same pattern of a spectral shift toward longer wavelengths, thus suggesting collagen aggregation. On the other hand, the $\nu(t)$ in the glycated sample (Figure 3.5D) remained similar over the 56 days. This indicates that the aggregation of collagen is hindered by the glycation process. This observation is consistent with the narrower steady-state fluorescence spectra shown in Figure 3.2B.

Moreover, Figure 3.5B,E shows that the normalised fluorescence decays $C(t)$ of tyrosine in collagen and collagen−glucose samples, do not change substantially. Figure 3.5C,F presents falls in $\sigma(t)$ factors occurring on the ns time scale, indicating that the spectrum becomes narrower at the later times after excitation. We explain this observation by the existence of the collagen aggregates characterised by a continuous and narrow distribution of spectral peaks and dielectric relaxation times, rather than two or more distinct aggregates, which would lead to the optimal M= 2 or more in data analysis.

To conclude this section, the broader Tyr steady-state fluorescence spectra and the systematic red shift of the TRES in the sample of free collagen suggest collagen aggregation, which leads to increasing volumes of the individual aggregates. Moreover, the narrower steady-state spectra and reduced changes in the spectral shifts observed in the presence of glycation indicates that the collagen aggregation is limited by glucose. However, glucose does not affect the fluorescence decay of the tyrosine in collagen.

3.3.2 Pepsin-Digestible Cross-Links Response (Excitation 340 nm)

The fluorescence responses of pepsin-digestible cross-links in collagen were studied by exciting the collagen and collagen−glucose samples at 340 nm. Figure 3.6A shows how the steady-state fluorescence spectrum of each sample evolves over time. Free collagen initially has the fluorescence peak at∼405 nm. The intensity of the spectrum then increases, mostly during the first 7 days, and undergoes a red spectral shift up to ∼425 nm on day 35. The fluorescence spectrum of the collagen−glucose sample increases steadily over the 35 days. It reaches a higher value and is broader than the spectrum of the free collagen sample.

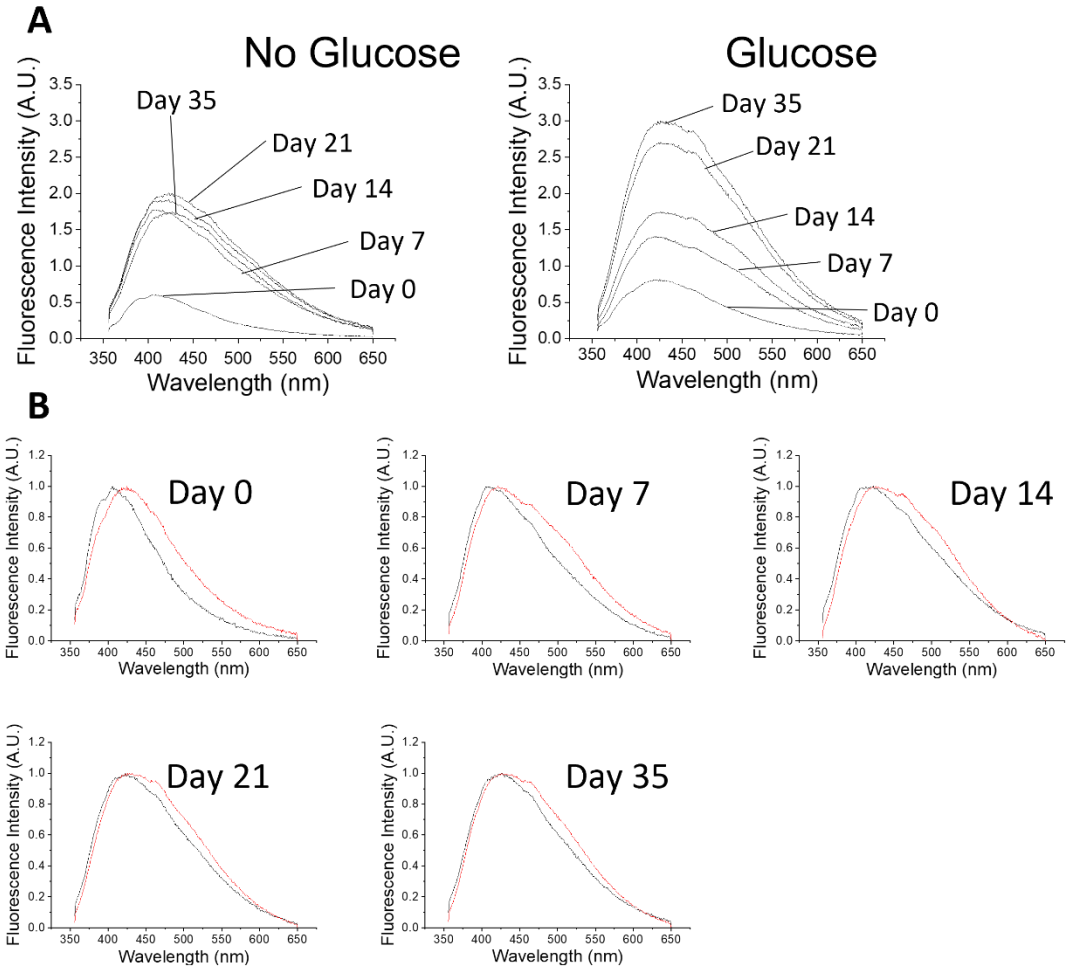

Figure 3.6. Fluorescence emission spectra for free collagen and collagen glucose when excited at 340 nm. (A) shows fluorescence changes over time for collagen and collagen-glucose at days 0, 7, 14, 21, and 35. (B)shows collagen (black) and collagen-glucose (red) on days 0, 7, 14, 21, and 35, with both samples spectra normalised to peak fluorescence.

Figure 3.6B allows for the comparison of the fluorescence emission of free collagen and collagen−glucose samples over 35 days, with both spectra normalised. From day 0, the sample with glucose shows a broader spectrum, and there is also a difference in the wavelength of peak fluorescence: ~405 nm for free collagen, which moves gradually to 425, and ~425 nm for collagen−glucose, which remains stable. We attribute the emission in the 400−430 nm range to the formation of dityrosine from the neighbouring tyrosine residues[149] and this process occurs in both the free collagen and collagen-glucose samples. However, the further increase in the fluorescence intensity and the shift of the spectra observed in the collagen−glucose sample only is likely to be an indication of multiple cross-links formed between glycated collagen molecules[138, 140].

To gain further information, TRES measurements were performed at various time points after sample preparation, at detection wavelengths from 390−500 nm. The absolute and normalised TRES for collagen and collagen−glucose are presented in Figure 3.7. We firstly note that at Day 0, the TRES obtained are different for the two samples. Due to our confidence in the experimental and data processing techniques used to obtain the TRES (discussed in the previous section), we are confident that this difference is significant, and not due to errors in the experimental technique. Additionally, repeat experiments (results not shown) also showed this difference at Day 0.

The TRES of free collagen (black curves) on day 0 show no change in their shape during the decay (see the plot of normalised spectra, black curves in Figure 3.7E), indicating no ns time scale processes. The broad peak of the spectrum at the range ~24,700-23,300 cm^{-1}, that is 405−429 nm, is consistent with the steady-state spectra. The measurements performed at later days show a peak at ~21,100 cm^{-1}, that is 475 nm, and the gradual transition of the fluorescence peak toward the red on a nanosecond time scale. In the sample containing glucose (red spectra), TRES data show a similar transition, but the emission peak at 475 nm is already apparent at day 0. This may suggest that glucose accelerates the formation of this fluorescent residue.

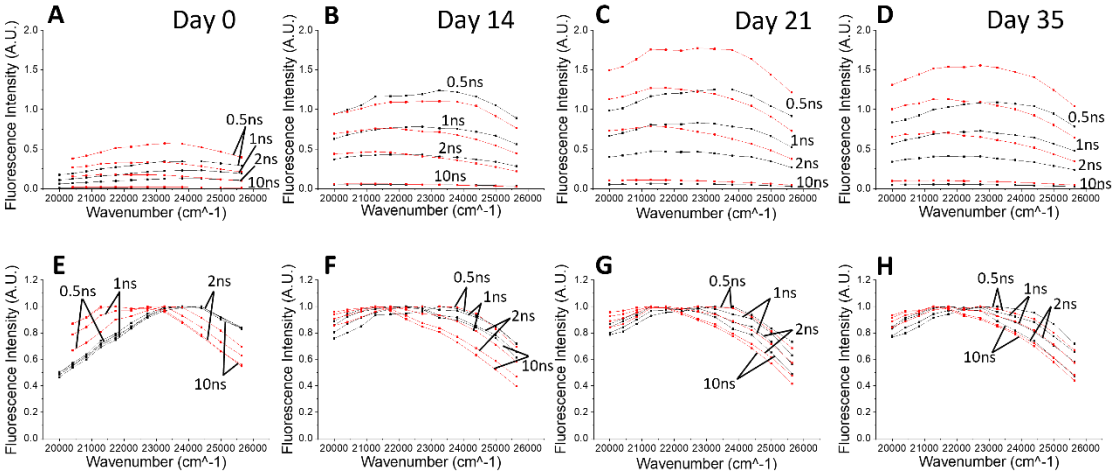

Figure 3.7. TRES spectra of free collagen (black) and collagen-glucose (red) on day 0 (A), day 14 (B), day 21 (C), and day 35 (D). Plots (E), (F), (G) and (H) show the same spectra after normalisation

Although direct inspection of TRES suggests the presence of at least two fluorescent residues, analysis of the Akaike information criterion (see Appendix B3 Table B3.1) again requires the consideration of a one-component Toptygin model (M= 1) to fit to the experimental TRES.

The analysis of the evolution of the $\upsilon(t)$ parameter however is characteristic for multi-component kinetics (Figure 3.8). This is explained below.

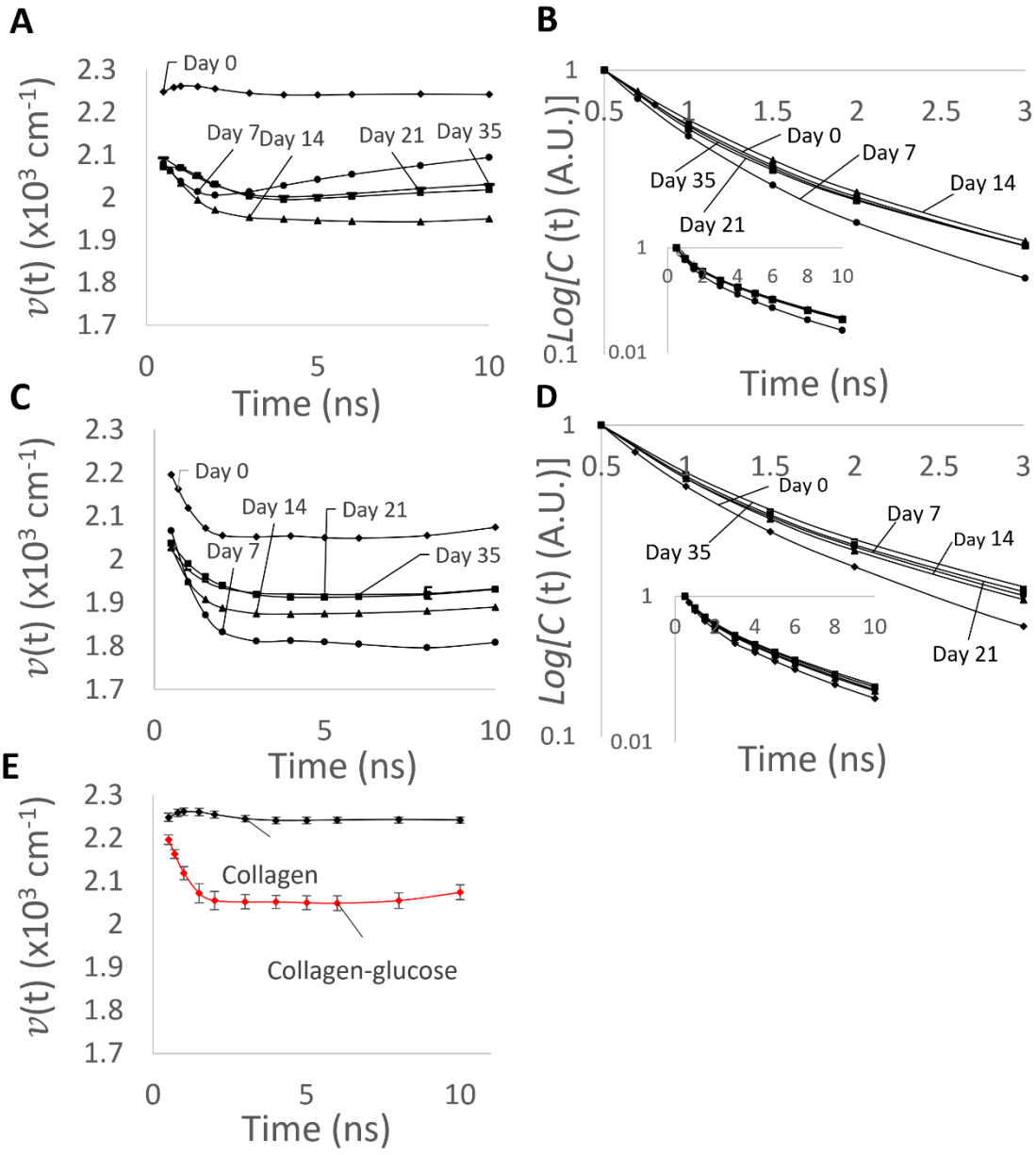

Figure 3.8. Plots A and C show the time evolution of the peak position $\upsilon(t)$ of the emitting fluorophores for collagen and collagen-glucose respectively. The normalised time evolution of fluorescence intensity C(t) is shown for collagen and collagen-glucose in plots B and D. The insert shows the same data over a longer timer range. The five lines show day 0, day 7, day 14, day 21, and day 35. Part E shows $\upsilon(t)$ for collagen and collagen-glucose on day 0 for comparison, with the error bars showing the 90% confidence intervals for the fitted values.

The initial (Day 0) peak position $v(t)$ is ~22,500 cm−1 for the free collagen sample (Figure 3.8A) and ~22,000cm−1 for collagen−glucose (Figure 3.8C). The error bars on Figure 3.8E show the 90% confidence intervals for the fitted values, which confirms that there is a statistically significant difference in $v(t)$ between collagen and collagen-glucose samples on Day 0.

Both samples behave differently over time, see Figure 3.8E for comparison. There is no shift in $v(t)$ following excitation for free collagen at day 0; the measurements taken on the later days however show a substantial drop of the initial $v(t)$ to ~20,900 cm^{-1}. All $v(t)$ dependencies show a further red shift during the first 2 ns, and then the $v(t)$ plots start to increase (which is most visible for the data obtained on day 7). Again, this observation contradicts the homogeneous dielectric relaxation process, where the monotonic red shift is expected. It can only be explained by the fluorescence of a number of species of individual fluorescence lifetimes, dielectric relaxation rates, etc. Obtaining M= 1 in the Akaike analysis, rather than the expected M=2, can again be explained by the presence of aggregates characterised by a distribution of fluorescence characteristics, rather than a small number of aggregates of distinctively different parameters.

The $v(t)$ for the collagen−glucose sample on day 0 drops from 22,000 to ~20,500 cm^{-1} during the first 2 ns. In the case of older samples, the starting value of $v(t)$ is ~20,600 cm^{-1} which is also followed by a similar red shift within the first 2 ns. This behaviour of $v(t)$ demonstrates that in the presence of glucose, the formation of cross-links occurs differently, leading to only one type of fluorescent cross-link.

The $\log(C(t))$ curves (Figures 3.8B, D) seem to confirm this observation. The changes in the rates of the decays on different days in the pure collagen sample (Figure 3.8B) are not monotonic. Indeed, the decay in Day 7 is faster than in Day 0, and then it slows down again at the later days. This suggests the presence of multiple fluorescent cross-links whose contributions change over time. The decays observed in the glycated sample (Figure 3.8D) however, show a stable trend of decreasing decay rates, which is likely to be observed when there is a single or a set of uniform fluorescent residues.

To conclude, in a pure collagen sample, more than one type of fluorescent cross-link is formed in the 35-day period, while in the collagen−glucose sample, a single fluorescent form is created, demonstrating a substantial impact of glycation on collagen aggregation

3.4 Conclusion

In this chapter, the effect of glucose on collagen's intrinsic fluorescence has been studied using a TRES-based technique. Our aim was to identify the characteristic features of the excited-state kinetics occurring in the glucose-triggered aggregation of collagen. Intrinsic fluorescence responses were collected for the excitation wavelengths 280 and 340 nm to observe changes in the fluorescence of intrinsic tyrosine and fluorescent cross-links.

It has been found that glucose does not have a substantial impact on the fluorescence of intrinsic Tyr (excitation at 280nm). Indeed, as glucose binds to collagen at lysine residues, and lysine makes up only 3.9% of collagen[139, 150],formation of lysine−glucose complexes is not likely to impact Tyr's local microenvironment. Nevertheless, the TRES of both free collagen and collagen−glucose samples excited at 280 nm do change over time, which is due to protein aggregation.

Glucose, however, does have a substantial influence on the formation of pepsin-digestible collagen cross-links emitting at λ > 400 nm (excitation at 340 nm). The observed changes in TRES show the impact of glucose on the formation pathways of new cross-links and protein aggregates. However, as the TRES approach that we have used does not assume any specific model of the underlying excited state kinetics, further studies will be required to identify the best fit model of the kinetics and to determine the molecular mechanisms involved.

4. NADH

4.1 Introduction

Nicotinamide adenine dinucleotide (NAD) and nicotinamide adenine dinucleotide phosphate (NADP) are essential co-factors in cellular metabolism[151] and are found in every living cell[152]. Although they have similar structure and functions, there are some significant differences between the two co-factors.

NAD is used by the enzymes responsible for catalysing substrate oxidation, while NADP is used by the enzymes that catalyse substrate reduction[151]. More specifically, NAD has a central role in DNA repair, signal transduction and post translational protein modifications and apoptosis[153]. It also drives adenosine triphosphate (ATP) production, and the redox state of this cofactor regulates the production of free radicals[154]. NADP however is used in macromolecular biosynthesis, and quenches reactive oxidative species. Its redox state is therefore key to antioxidant defence[155]. It is these pyridine nucleotides, along with their reduced equivalents (NADH and NADPH) that are therefore central in determining the redox state of a cell. A cells redox state decides its regulation of metabolism and energy production, and so plays a vital role in health and disease[156]. Thus, the redox balance of these cofactors is hugely important.

This work and thus this chapter will focus on NADH alongside its oxidised equivalent NAD+.

4.1.1 NADH Structure and Function

The structures of NAD+ and NADH are shown in Figure 4.1.

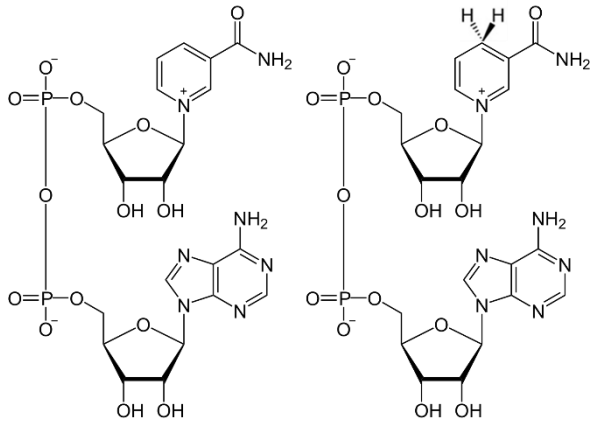

Figure 4.1. Structure of NAD+ and NADH

NAD+ is composed of 2 nucleotides which are joined through their phosphate groups. One nucleotide has an adenine base, while the other has a nicotinamide ring. NAD+ is an electron accepter, and it can accept 2 electrons and one H+ to become NADH. The cofactor cycles readily between these 2 states through the reduction reaction shown below

$$NAD^+ + 2e^- + H^+ \leftrightarrow NADH \quad [4.1]$$

As discussed above, NAD+ and NADH are responsible for catalysing oxidation reactions within a cell, such as ATP production. ATP is a cell's source of energy, and this is produced via cellular respiration, a process where NAD+ is crucial. Cellular respiration consists of 4 steps: glycolysis, pyruvate oxidation, the Krebs cycle, and oxidative phosphorylation. Together these pathways take glucose and break it down to carbon dioxide and water in a process that releases ATP. NADH is generated in the first three of these steps, where electrons released in the reactions are picked up by NAD+. NADH carries these electrons to the final step, oxidative phosphorylation, where they deposit the electrons at the electron transport train. Energy is released as electrons move down the chain, and this energy is used to pump protons out of the cellular matrix, forming a proton gradient. Protons flow back through the matrix, and ATP is synthesised.

4.1.2 NADH and Glucose

NAD+ and NADH are involved in glucose metabolism as outlined above, but excess glucose can have a significant effect on the redox balance of this co-factor. The NAD/NADH redox balance can be severely disturbed by glucose[157]. The major pathways involved in glucose metabolism and electron storage in NADH are listed above (the glycolytic pathway, pyruvate oxidation and the Krebs cycle[157]). When glucose levels are elevated, such as in diabetes, these pathways experience increased amounts of glucose[158], resulting in overproduction of NADH[159], and activation of the polyol pathway[160] (where glucose is converted to fructose) . Excess glucose can also lead to a depletion in NAD+ levels through various enzyme catalysed reactions where NAD+ is the substrate: excess glucose causes overactivation of enzymes (namely poly ADP ribose polymerases and sirtuins[161]) which diminishes the levels of NAD+ in the cell. All of these processes can shift the NAD+/NADH redox balance towards NADH, which can cause a number of problems. The excess NADH leads to reductive stress, which then leads to oxidative stress[162], and ultimately oxidative damage to macromolecules such as DNA and proteins[163]. This oxidative damage is a factor that contributes to the progression of

diabetes and its complications[157], with many studies highlighting the relationship between high NADH levels, and diabetic complications such as vascular disease[164].

4.1.3 NADH Auto-fluorescence

The NAD/NADH redox balance and its response to increased glucose levels has been extensively studied in cells[157, 165], and often fluorescence spectroscopy is used due to its non-invasive approach[166]. The reduced form NADH exhibits auto-fluorescence (AF), however the oxidised form NAD+ does not[152, 167]. Changes in the intensity of NADH fluorescence from live tissues is therefore correlated with changes in the balance of reduced forms relative to oxidised forms[168], and redox state can be determined via NADH AF intensity. Furthermore, as NADH is found in all living cells, it can be detected in skin cells such as fibroblasts and adipocytes[169]. Fluorescence therefore could offer an ideal non-invasive method to assess the redox imbalance.

In NADH (and NADPH) both the adenine moiety and the nicotinamide ring absorb light, however the fluorescence arises from the nicotinamide ring only. At the nicotinamide ring, NADH is excited at 350(±30) nm and has emission peak at 460(±40) nm[70]. Although NADH and NADPH have identical emission characteristics, it is found that their decay properties are different[170], and this can be used to separate the two cofactors.

The fluorescence decay of NADH has traditionally been modelled using a multi-exponential function. NADH decay is bi-exponential[171, 172], with one shorter component and one longer component. The explanation offered for this is that NADH can be found in the folded or extended state[171, 173], however there is great uncertainty if the 2 exponentials relate to the two molecular configurations, or if there are competing excited state processes. In live cells, the decay is more complex. NADH has been shown to have both 2[174]- or 3- exponential decays[169]. This suggests that multiple fluorescing species exist, for example enzyme bound NADH, and free NADH[168]. In various studies, enzyme- and protein-bound NADH has been seen to have an increased fluorescence lifetime compared with free NADH[175, 176] . In addition, the metabolic status of this co-enzyme is known to affect the fluorescence lifetime. As described above, increased glucose shifts the NADH/NAD+ redox balance towards NADH. Thus, in the oxidative phosphorylation step of glycolysis, there is increased binding of NADH to proteins of the respiratory chain. This increases the proportion of the protein-bound enzyme, which possesses a longer fluorescence lifetime[177]. Thus, glucose appears to increase the mean fluorescence lifetime of NADH.

However, a study[169]conducted in 2005 measured glucose-induced changes of adipocytes (cells containing NADH) using autofluorescence. Contrary to the more recent result described above[177], this study found that the addition of glucose caused an increase in fluorescence intensity, and a shortening of the mean lifetime. This study was concerned with NADH in cells, and thus there may have been other elements that influenced this result, and it is difficult to understand the underlying kinetics. A study that investigates the direct interaction of NADH and glucose *in vitro* would be helpful for this purpose.

In this work, we investigated how the intrinsic fluorescence of NADH changes in response to interaction with glucose. Glucose affects the relative amounts of NAD+ and NADH inside a cell, which can be detected via changes in fluorescence intensity of NADH, and as described above, changes in the mean lifetime. However, there is very little research into how glucose directly affects the intrinsic fluorescence of NADH.

We hypothesize that there is a direct interaction between NADH and glucose, where the interaction is a non-enzymatic glycation-type reaction. Filling this gap in understanding could be important, as if there is a significant change in NADH intrinsic fluorescence in response to increased glucose, this could improve the methodology for glucose control in patients with diabetes. In this work we study NADH *in vitro*, and use both steady state and time-resolved techniques to investigate the impact of glucose on the intrinsic fluorescence of NADH. *In-vitro* arrangements allowed us to focus on the impact made by glucose on the NADH fluorescence and not on the NAD+/NADH redox balance.

We have studied the changes in fluorescence of NADH in response to glucose by researching four samples: free NADH and NADH-glucose in phosphate buffered saline pH 7.4 (PBS), and free NADH and NADH-glucose in Trizma buffer pH 9.0.

Firstly, PBS was selected as it has a pH close to physiological conditions, and so this buffer would most accurately imitate NADH's environment in the human body. This has also been used previously to study NADH fluorescence[178], however in this study the samples were freshly prepared each day. Our study required long term stability of NADH in the buffer solution, as our experiment lasted ~3 weeks. Literature has described the poor long-term stability of NADH in PBS, and in fact PBS has been shown to accelerate the degradation of this co-factor[179]. For this reason, a second set of samples was prepared using Trizma buffer. Previous studies have used this solvent to study NADH fluorescence intensity[180,181] and fluorescence lifetime[180], and although its pH is significantly higher than physiological pH,

above pH 8.0, NADH degradation is known to be too slow to be measured[179]. Thus, in these samples, we can be sure that any potential fluorescence changes would be due to glucose and/or aggregation, and not due to degradation.

4.2 Methodology

Preparation of NADH and NADH-Glucose Samples

β-Nicotinamide adenine dinucleotide reduced disodium salt hydrate (NADH) and phosphate buffered saline pH 7.4 (PBS) were purchased from Sigma-Aldrich and used to prepare a free NADH/PBS sample of concentration 60 µM. The NADH-glucose/PBS sample was then prepared by addition of glucose powder (also Sigma Aldrich) to create a sample containing 60 µM NADH and 30 mM glucose. For the NADH/Trizma sample, 10mM Trizma buffer substance (Sigma Aldrich) was used to create a 60 µM NADH sample. The NADH-glucose/Trizma sample was then prepared by the addition of glucose powder to create a sample containing 60 µM NADH and 30 mM glucose. 3.5 ml of each sample was transferred to a 4x1x1 cm quartz cuvette, and sealed with a stopper and parafilm, ready for measurements. All samples were stored at room temperature, under identical conditions, for the duration of the experiment.

The chosen conditions were not physiologically or clinically relevant. Indeed, the glucose concentration is higher than the typical plasma sugar levels, and the NADH concentration is lower than expected in a cell. In addition, in the Trizma samples the pH is substantially higher than physiological pH. The selected conditions, including the absence of enzymes and cofactors, were intentionally applied to enhance the impact of glucose on NADH fluorescence, and to allow monitoring of this process over a long period of time, undisturbed by the NAD+/NADH balance. The samples were prepared with maintaining the spectroscopic purity but were not sterile.

To ensure that the NADH fluorescence was not disturbed by the intrinsic fluorescence of bacteria (which could potentially grow in the PBS samples over the duration of the experiment as PBS is a good culture medium for bacteria), and to check for potential impurities, we prepared the reference solutions of PBS, glucose in water, and glucose in PBS, and monitored their fluorescence. These samples were stored under identical conditions to the NADH and NADH-glucose samples.

Fluorescence Measurements

Absorption spectra were recorded using a PerkinElmer Lambda 2 UV-Vis spectrometer (using a PBS solution as a reference) with a resolution of 1nm. Corrected fluorescence emission spectra were obtained at the excitation wavelength 340 nm using a Fluorolog (HORIBA Scientific). Fluorescence spectra had a resolution of 1 nm, and the slit width on the excitation and emission monochromators was 5 nm.

The fluorescence intensity decay measurements were carried out on a DeltaFlex fluorescence lifetime system (HORIBA Jobin Yvon IBH Ltd, Glasgow), which uses time-correlated single photon counting (TCSPC) to record fluorescence decay. A NanoLED with repetition rate 1MHz and peak excitation wavelength 340 nm (pulse duration <1 ns) was used for excitation[182].

The decays measured at each wavelength λ were then fitted to the experimental fluorescence curve $Iexp(t)$ (equation2.29). In this instance, the fluorescence intensity decay $I_\lambda(t)$ was represented by a multi-exponential function (equation 2.23).

The steady state spectra and fluorescence intensity decays were measured on day 0 (within ~20 minutes of sample preparation) and on subsequent days after preparation for both samples.

4.3 Results and Discussion

Figure 4.2 shows the absorbance spectra for free NADH and NADH-glucose in PBS and Trizma over 25 days. In all plots, at day 0 there are 2 clear absorption peaks: adenine is responsible for the absorption at ~265 nm, while the peak at ~340 nm results from absorption at the nicotinamide ring[183].

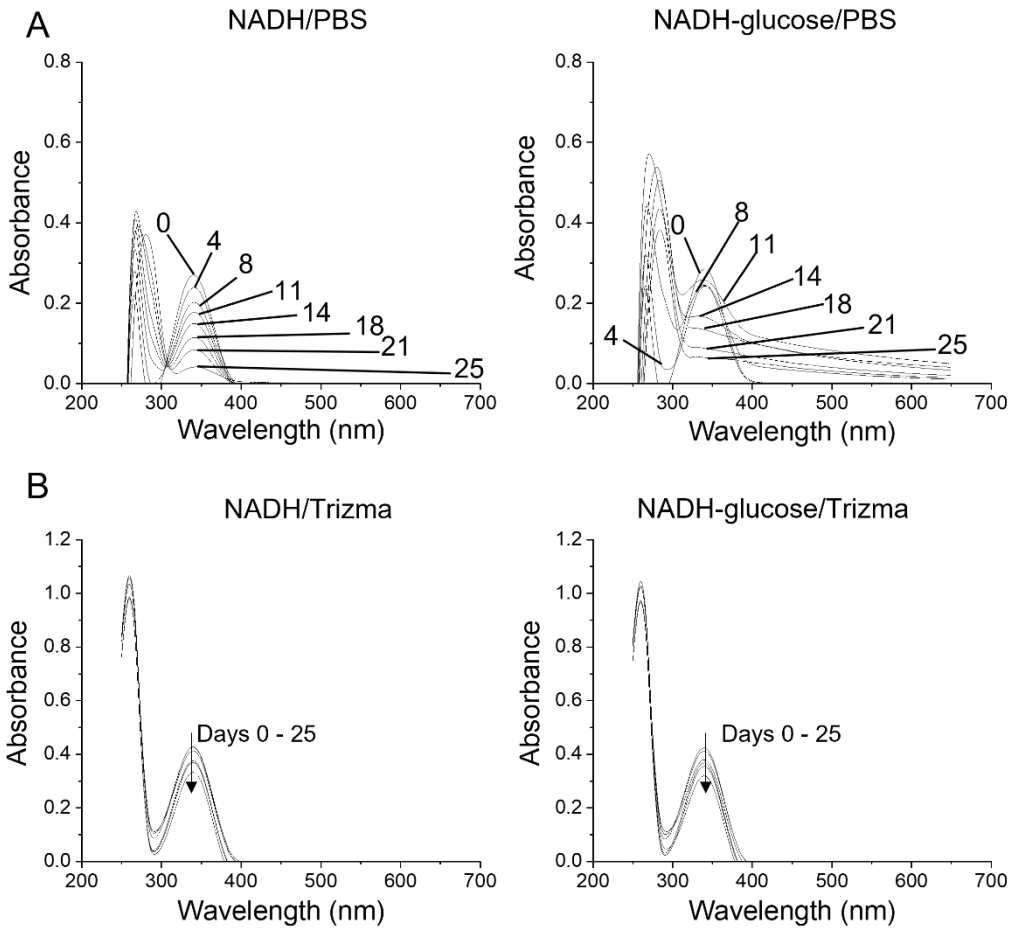

Figure 4.2. Absorption spectra of NADH and NADH-glucose in PBS (part A) and Trizma (part B). The numbers represent the spectra at the said number of days after sample preparation.

In the free NADH/PBS sample (Figure 4.2A) the absolute absorption at 340 nm decreases gradually over the 25 days, while the absorption at 265 nm seems to increase, and undergo a slight red shift, with the wavelength of peak absorption increasing to ~280 nm by day 25. In the sample with glucose, the red shift of adenine absorption peak is also present, and the absorption peak at 340 nm begins to flatten after approximately 2 weeks. It is combined with an appearance of the new broad band at longer wavelengths, which could be attributed to both scatter (the figure shows the signal increasing as the wavelength shortens, in a manner which is likely to be consistent with $1/\lambda 4$, the ratio provided for Rayleigh Scattering) and the formation of a new absorbing residue.

This result, the flattening of the peak at 340 nm and the appearance of a broad band at longer wavelengths, was also seen in a repeat experiment, and thus we are confident that this result is not due to any random errors present when carrying out the measurement.

Additionally, since this broad band is not present in the free NADH/PBS sample, instrumental errors in the absorption spectrometer cannot be responsible for this, and it does indeed seem to be an effect of glucose.

The increase in scatter in the glycated sample could be due to glucose binding to the NADH and forming larger complexes. Based on this result, we hypothesised that the glucose is binding to the NADH near the nicotinamide ring, and thus reducing its absorbing capability, resulting in gradual disappearance of the absorption peak at 340 nm. Indeed, if the interaction between NADH and glucose is a direct non-enzymatic glycation-type reaction, this would involve covalent coupling of the primary amine on NADH with a glucose hydroxyl group. There are two primary amine groups on NADH, but based on the absorbance (and fluorescence result presented later), we can associate the binding at a particular ring. If glucose binding is occurring, it appears that it may take place at the nicotinamide ring.

The results for the samples where Trizma is the buffer (Figure 4.2B) however seem to demonstrate stability of NADH, both in the presence and absence of glucose. In these samples, there is very little change over the duration of the experiment. Both the intensity and position of the two absorption peaks remain constant. Our result in Trizma shows that experimental errors are not responsible for the difference seen in the NADH/PBS-glucose sample.

Previous studies[179,184] have attributed the disappearance of NADH in PBS absorbance at 340 nm to NADH degradation. A 1988 study[184] investigated chemical stability of NADH in different buffers, and found a faster degradation in the phosphate buffer, which was assigned to the adduct formation between phosphate and NADH at the pyridine ring. A schematic from this study is shown in Figure 4.3 and shows the decomposition percentages of NADH in relation to various factors studied. The diagram shows that the most important factor for degradation is the buffer type, but temperature and pH also affect the stability.

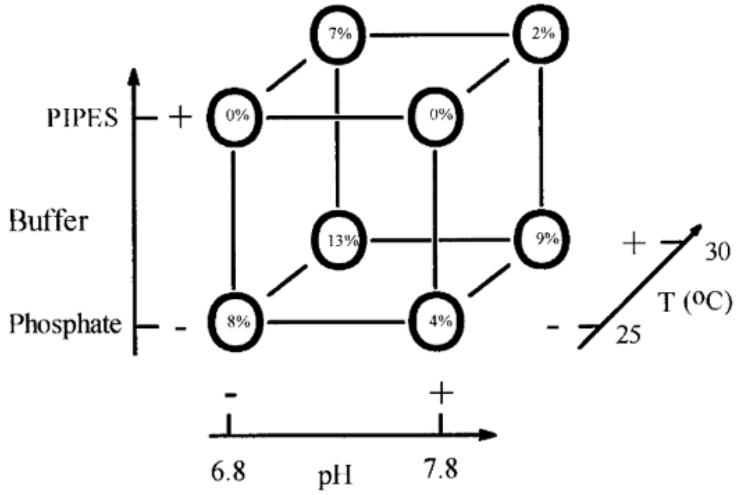

Figure 4.3. Representative diagram showing the decomposition percentages of a solution of 1.0 x10^{-4} M NADH (after 40 min) with respective factors studied.

In our work, as a reduction in absorbance at 340 nm is not seen in the samples in Trizma, we accept that NADH degradation may be responsible for this behaviour in PBS. As outlined above, the faster degradation in PBS is thought to be associated with the phosphate forming an adduct with the pyridine ring of NADH, and this occurs through a charge transference. The decomposition itself is a redox process, where the ribose sugar that is attached to the adenine base is reduced: hydrogen is replaced with a phosphate group. This decomposition is not a major breakdown in the structure of NADH itself, but this redox reaction takes place at a different location on the molecule to the the regular NAD/NADH redox cycle (as shown in Figure 4.1). This difference could be the reason for the faster degradation of NADH in phosphate buffer.

However, it is still unclear why the two PBS samples exhibit different behaviour. One possibility is that there is increased bacterial growth in the NADH-glucose/PBS sample, as glucose activates bacterial growth in PBS (a good culture medium for bacteria). Alternatively, the presence of glucose may slow down the rate of degradation, although further work in this area would be needed to investigate this.

The fluorescence emission spectra of all samples are shown in Figure 4.4, with parts A and C showing the absolute intensities, and parts B and D showing the same spectra normalised to the peak fluorescence intensity for the samples in PBS and Trizma respectively.

At day 0, all samples show identical fluorescence spectra with a peak at ~470 nm, as expected for NADH[70], although the NADH/Trizma and NADH-glucose/Trizma show a slightly higher

fluorescence intensity. For the PBS samples (Figure 4.4A,B), after day 0 both samples show a gradual reduction in fluorescence intensity as the experiment progresses, however the drop in intensity is accelerated in the sample with glucose. We note that while the results are not shown, the same trend was observed in our repeat experiment, where glucose accelerates a drop in fluorescence intensity.

Figure 4.4B shows that the shape of the spectra for free NADH does not change as the sample ages, the spectrum just becomes slightly narrower. A weak peak at ~384 nm we attribute to Raman scattering. In the NADH-glucose/PBS sample, however, after approximately 2 weeks the peak position starts to shift towards shorter wavelengths, and the spectrum broadens (again, this was also observed in repeat experiments, so we are confident that the result is not due to an error in any of the experimental techniques). Again, NADH behaviour in PBS suggests that glucose modifies the NADH molecule by binding near the nicotinamide moiety, which reduces not only the nicotinamide absorption but also its fluorescence, simultaneously leading to formation of a new fluorescent product which emits at shorter wavelengths and is evidenced by the presence of an isosbestic point at approximately 420 nm. Although we speculated that the new fluorescent form could be a layer of nicotinamide-glucose stacking, since ground-state aggregates usually have shorter wavelength fluorescence peaks than monomers, there is no direct evidence of this. The small glucose molecules are present in a much larger amount compared to the NADH molecules in the solution, and in addition, glucose contains no aromatic rings and is not particularly polar. Thus, molecular stacking may be unlikely.

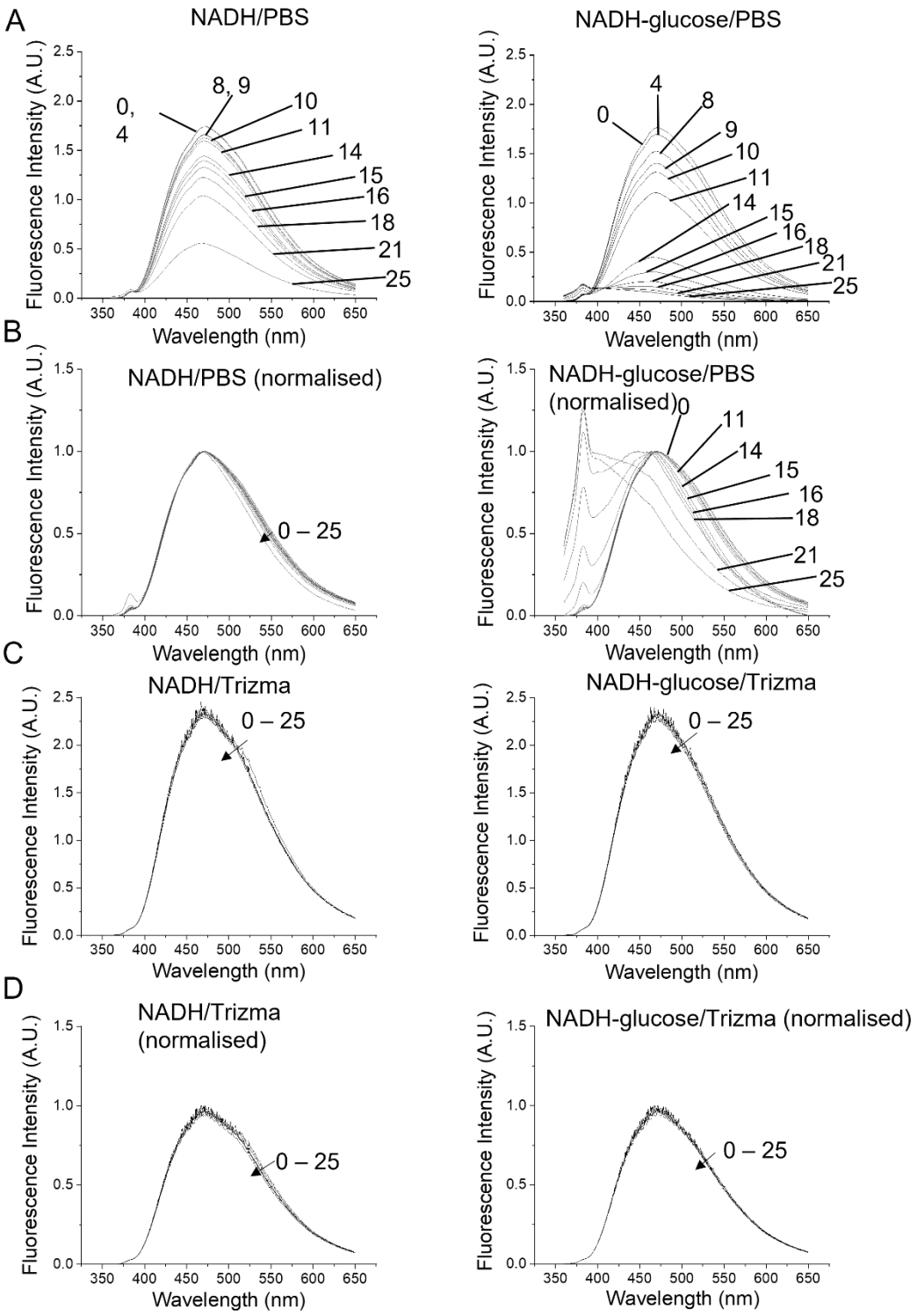

Figure 4.4. Fluorescence emission spectra of NADH and NADH-glucose in PBS (A,B) and Trizma (C,D) at various days after sample preparation. Parts A and C show the absolute fluorescence intensity while parts B and D show the same spectra normalised to peak fluorescence intensity. The numbers represent the spectra at the said number of days after sample preparation.

To investigate if the observed differences in the experimental fluorescence spectra in PBS could be quantified in more detail, a generic model of fluorescence spectrum[102] was fitted to these data, using the Toptygin model (equation 2.34) discussed in detail in section 2.2.4.

For all measurements of free NADH/PBS and for the first 10 days of measurements of NADH-glucose/PBS samples, a 1-component Toptygin model (M=1) was used. However, for NADH-glucose/PBS sample older than 10 days, a 2-component model had to be used. This was decided on the basis of the visible shape of the spectra and the χ^2 goodness of fit criterion. Moreover, an additional component was added to the model of the spectra to account for the Raman scatter that is visible in all curves as an extra peak at ~384 nm (26041 cm^{-1}, the Raman wavenumber for this excitation). Examples of the experimental fluorescence spectra plotted alongside the model function for NADH and NADH-glucose show relatively good agreement, as can be seen in Appendix C, Figure C1.1. The χ^2 goodness of fit criterion was between 1.0 and 1.2 for all spectra modelled, and thus the model could effectively represent the spectra.

The evolution of the recovered parameters of the spectra are plotted in Figure 4.5. Initially, the peak values $v_i(t)$ for both NADH/PBS and NADH-glucose/PBS samples are at the same level, approximately 20060 cm^{-1} (Figure 4.5A).

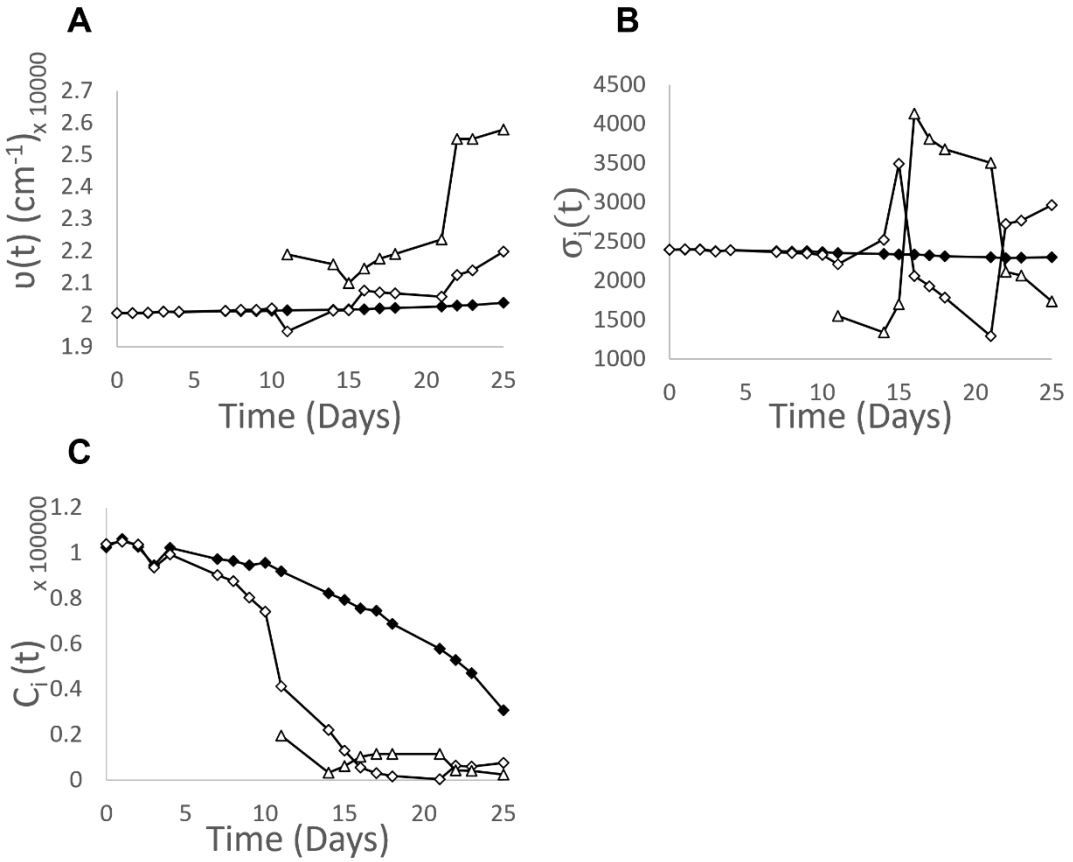

Figure 4.5. Plot A shows the time evolution of the peak position $v(t)$ of the emitting fluorophores for NADH (closed symbols) and NADH-glucose (open symbols) when in PBS buffer. The time evolution of the contribution to the fluorescence intensity C(t) is shown for NADH and NADH-glucose in plot C.

In the free NADH/PBS sample, the $v(t)$ shows a slight increase over 25 days, although this change is not significant (error bars showing the 90% confidence intervals for the fitted values have been removed from the plots for clarity, but confirm that there is no significant difference in the NADH/PBS $v(t)$ values over time). The contribution of the component *C* decreases gradually, maintaining the shape of the fluorescence spectrum, as seen in Figure 4.5B. We attribute these gradual changes to slow aggregation of NADH, which leads to decreasing quantum yield of the nicotinamide ring.

The fluorescence spectra of the NADH-glucose/PBS sample during the first 10 days are very similar to the fluorescence of the free NADH/PBS, except that the decrease of its intensity is faster. After day 10, the two-component model of the spectrum needs to be used to satisfy the goodness of fit criteria. The first component v_1 shows slight increase for the remaining 14 days. The second component $v_2(t)$, produced by the new residue formed by glucose with NADH, starts about 22,000 cm^{-1} and shows a much greater increase during this time, up to

~25800 cm^{-1}. This corresponds to the blue shift seen in the emission spectra observed in Figure 4.4A,B. The presence of two peaks in the later stages in the spectra of the NADH-glucose sample, both shifted towards blue, confirms that glucose substantially modifies the aggregation of NADH molecules and leads to accelerated reduction of nicotinamide ring fluorescence and formation of the new fluorescent nicotinamide-glucose aggregates.

Although this analysis seems to suggest a substantial impact of glucose on the intrinsic fluorescence of NADH, when we consider the fluorescence emission of NADH in Trizma (Figure 4.4C,D), this conclusion becomes more uncertain. Figure 4.4C,D shows that throughout the 25 days of the experiment, the fluorescence spectra for NADH/Trizma and NADH-glucose/Trizma remain almost identical, with no change in the intensity or the shape of the spectra. Similar to the result for absorption, where we noted that direct interaction via molecular stacking seemed unlikely, this result seems to suggest that it is NADH degradation in PBS that is the cause of the changes in fluorescence observed, rather than glucose having an effect on the intrinsic fluorescence of NADH. This is in keeping with the absorption spectra results.

To investigate this more fully, fluorescence spectra of 3 reference samples were monitored over the same time period as the NADH samples. This result is presented in Figure 4.6, which shows the fluorescence spectra of PBS, glucose in water and glucose in PBS, measured at exactly the same experimental settings as the NADH samples. The three reference samples have very low fluorescence, that is almost negligible when compared to NADH fluorescence at day 0. The main conclusion from this result however, is that NADH does not have long term stability in PBS. There is evidence that the molecule is degrading, and we accept that this could be causing the changes in fluorescence.

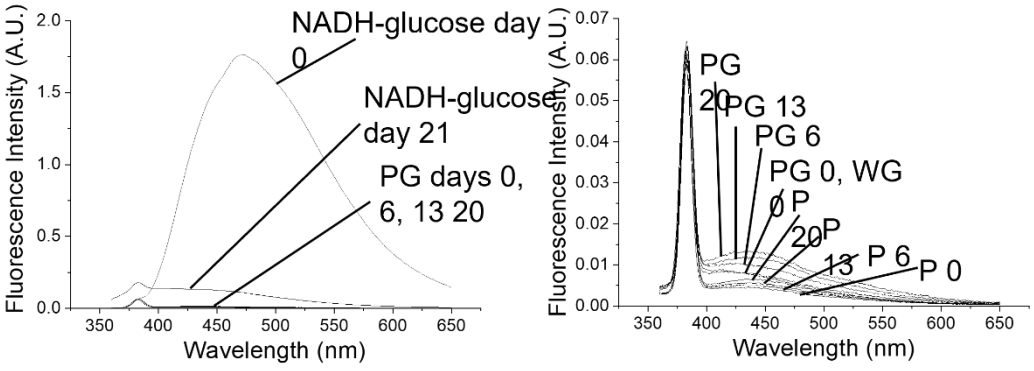

Figure 4.6 Fluorescence emission spectra for reference samples PBS (P), PBS-glucose (PG), and water-glucose (WG), alongside the NADH-glucose spectra for comparison.

The steady state data show that although glucose affects NADH fluorescence when the samples are in PBS buffer, the result in Trizma shows no evidence of NADH fluorescence changes. The fluorescence emission spectra obtained from Trizma however does show the robustness and accuracy of the experimental procedure, as on every day the peak wavelength was measured at a value between 468 nm and 472 nm for both samples. This is in line with the expected values for NADH fluorescence.

To gather more detailed information on the process occurring, time-resolved measurements were conducted. Fluorescence intensity decays, all at the excitation wavelength of 340 nm (corresponding to the peak absorption of the nicotinamide ring), were collected at three key wavelengths: 525, 470 and 390 nm.

Firstly, the fluorescence decays were detected at 525 nm. The raw decays for the NADH/PBS and NADH-glucose/PBS samples, as well as the plots for the resultant parameters from fitting these decays to a 3-exponential model, are shown in Figure 4.7. It should be noted for all fluorescence decays presented, each decay was fit to the 3-exponential model 3 times and the resultant parameters averaged.

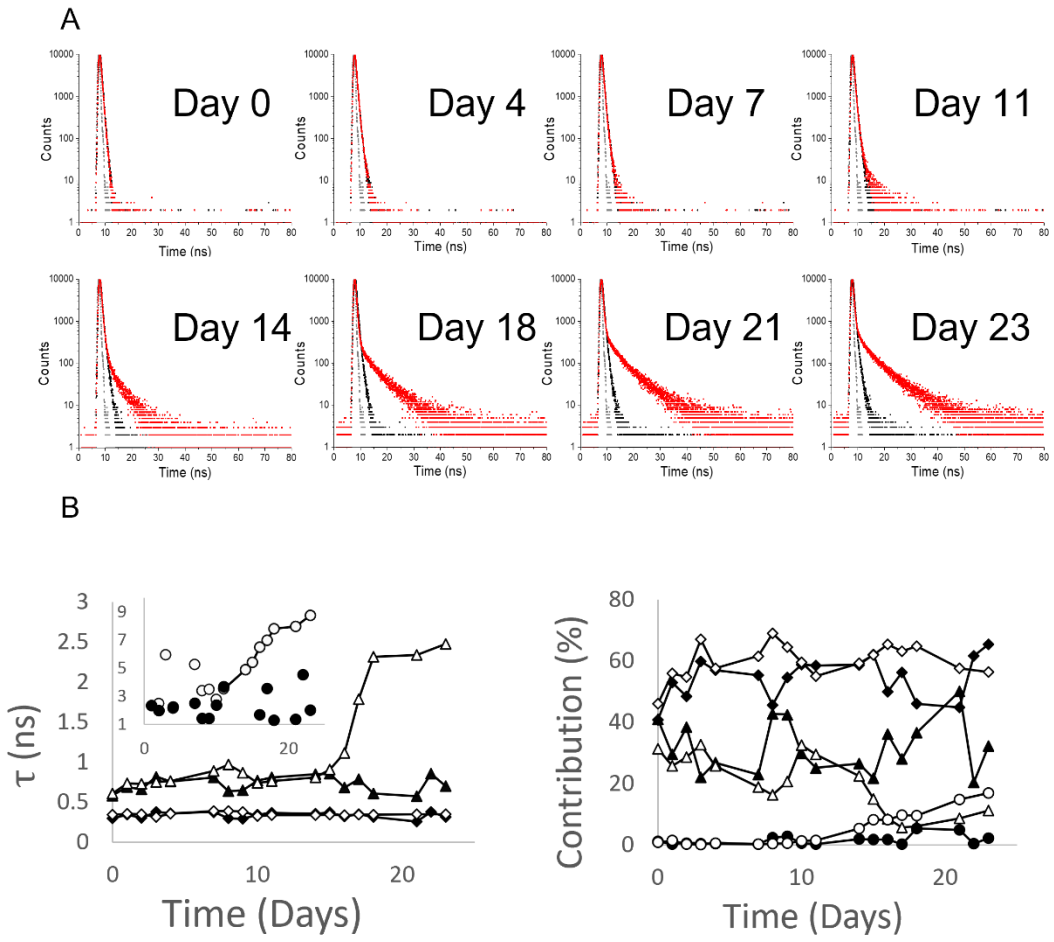

Figure 4.7. Part A shows fluorescence decay at 525 nm of NADH (black) and NADH-glucose (red) in PBS buffer alongside the instrument response function (grey) at various days after sample preparation. Part B shows the 3 lifetimes obtained when the decays are fitted to the 3-exponential model for NADH (closed symbols), NADH-glucose (open symbols). τ_1 is shown by diamonds, τ_2 is shown by triangles, and τ_3 is shown by circles. The percentage contribution of each component to the decay for each sample is also shown. The contribution of the scattered light to each decay has been left out for clarity.

The fluorescence decay curves for NADH and NADH-glucose are almost identical up to day 11 (Figure 4. 7A) , which was determined from direct inspection of the fluorescence decays, and also quantitatively though comparison of the fitted parameters. On Day 0, the two shorter lifetime components had values of 0.30 (+/- 0.017) ns and 0.58 (+/- 0.016) ns for NADH/PBS and 0.34 (+/- 0.019) ns and 0.61 (+/- 0.02)ns for NADH-glucose/PBS. Thus, it was determined that there is no statistically significant difference in the decays from the 2 samples at Day 0, and similarly, no differences were found up to Day 11. The same finding was obtained in a repeat experiment, where the fluorescence decays were not statistically different until Day 10. We further note that in the repeat experiment, comparable results were obtained for fitted values and mean lifetimes to the results presented in this work

(mean lifetimes of 0.88 ns (NADH/PBS) and 0.72 ns (NADH-glucose/PBS) vs. 0.81ns (NADH/PBS) and 0.76 ns (NADH-glucose/PBS) in the repeat). This demonstrates the robustness of the experimental and data processing techniques used, and thus indicates the results presented in the following section are not due to any random errors. When determining the accuracy of our results, it is more difficult to find values in literature for the fluorescence lifetime of NADH at 525 nm emission wavelength. However, as our lifetime values obtained at the 470 nm emission wavelength are in line values found in literature (discussed later), we are discussing the following results under the assumption our experimental technique is sound, and that the lifetime values obtained are accurate.

As illustrated in Figure 4.7A, From day 14 the mean fluorescence lifetimes in the sample containing glucose increase substantially: on Day 23 the mean lifetime of NADH/PBS was calculated to be 0.43 (+/- 0.033) ns, while in NADH-glucose/PBS this was 0.54 (+/-0.016)ns. Thus, there is a significantly significant difference between the two decays, with the fluorescence decay of the NADH-glucose/PBS sample increasing. Figure 4.7B shows the fitted lifetimes and percentage contributions of each component from Days 0 to 23. .

We noted in separate data analysis (not shown here) that all free NADH decays and the NADH-glucose decays during the first 9 days of the experiment could be represented sufficiently using a 2-exponential model (judged by the X^2 goodness of fit criterion alongside a plot of the residuals). Indeed, a 2-exponential model is usually used to represent the fluorescence decay of NADH when in solution[171, 172], where there is one short component and one longer component. These correspond to the folded and extended states of the molecule[171, 173]. This result normally refers to the instance where fluorescence is collected near the peak fluorescence intensity (430-490 nm).

However, in the case of the NADH-glucose sample measured on day 10 and later, a 3-exponential model was needed. Therefore, for comparison, we present here the results of fitting a 3-exponential model to both samples over all days. Examples of the fitted decays, the resultant values of the parameters, and the residual plots are shown in Appendix C2, Figure C2.1 and Figure C2.2.

The plots in Figure 4.7B show that all three lifetimes, and their corresponding pre-exponential factors, for the free NADH/PBS sample are quite stable throughout the experiment. For this sample the contribution of the third component is negligible, and these kinetics are consistent with the literature[171, 172].

In the NADH-glucose/PBS sample, the two shorter lifetimes have similar values to the free NADH/PBS sample until day 11, after which the longer of these lifetimes increases from 0.8 ns to 2.5 ns. This is combined with a reduction in the contribution of this component to the decay, from ~30% to between 5 and 10%. Alongside this, a third long lifetime component appears, which contribution is no longer negligible and by day 23, its contribution achieves almost 20%. The long lifetime increases during this time from ~2 ns to 8.5 ns. When considering solely the results in PBS, these data, when considered alongside the steady-state data, suggest that glucose affects the aggregation of NADH when in PBS by binding it close to the nicotinamide ring, which decreases its original fluorescence intensity, and a new, blue shifted fluorescent residue of long fluorescence lifetime is formed. As the NADH-glucose binding occurs in the ground state, glucose acts as a static quencher to the fluorescence of the free NADH, thus its mean fluorescence lifetime remains unchanged over the whole process. Note, that the contribution of this short wavelength form detected at 525 nm is very small. From literature, we note that enzyme-bound or protein-bound NADH has an increased fluorescence lifetime compared to free NADH[176]. This occurs when there is increased glucose in cells, as excess glucose causes an increased proportion of bound-NADH. Our result is therefore in line with literature, where the sample with glucose shows an increased fluorescence lifetime.

Fluorescence decay at detection wavelength 525 nm was also carried out for NADH and NADH-glucose samples in Trizma. The raw decays are presented in Figure 4.8A. Interestingly, the biggest difference between samples is observed at day 0, where the fluorescence intensity decay of NADH/Trizma is longer than that of NADH-glucose/Trizma. This difference reduces as the experiment progresses, and by day 24, the decay of the two samples is extremely similar (analysis showed the mean lifetimes to be 0.48 (+/- 0.023)ns and 0.43 (+/- 0.024) ns for NADH/Trizma and NADH-glucose/Trizma respectively on day 24). We hypothesize that the longer decay in the NADH/Trizma sample at day 0 could be due to the presence of a fluorescence residue that is competing with NADH fluorescence, who's presence disappears as the experiment progresses. The presence of glucose negates the effect of this residue.

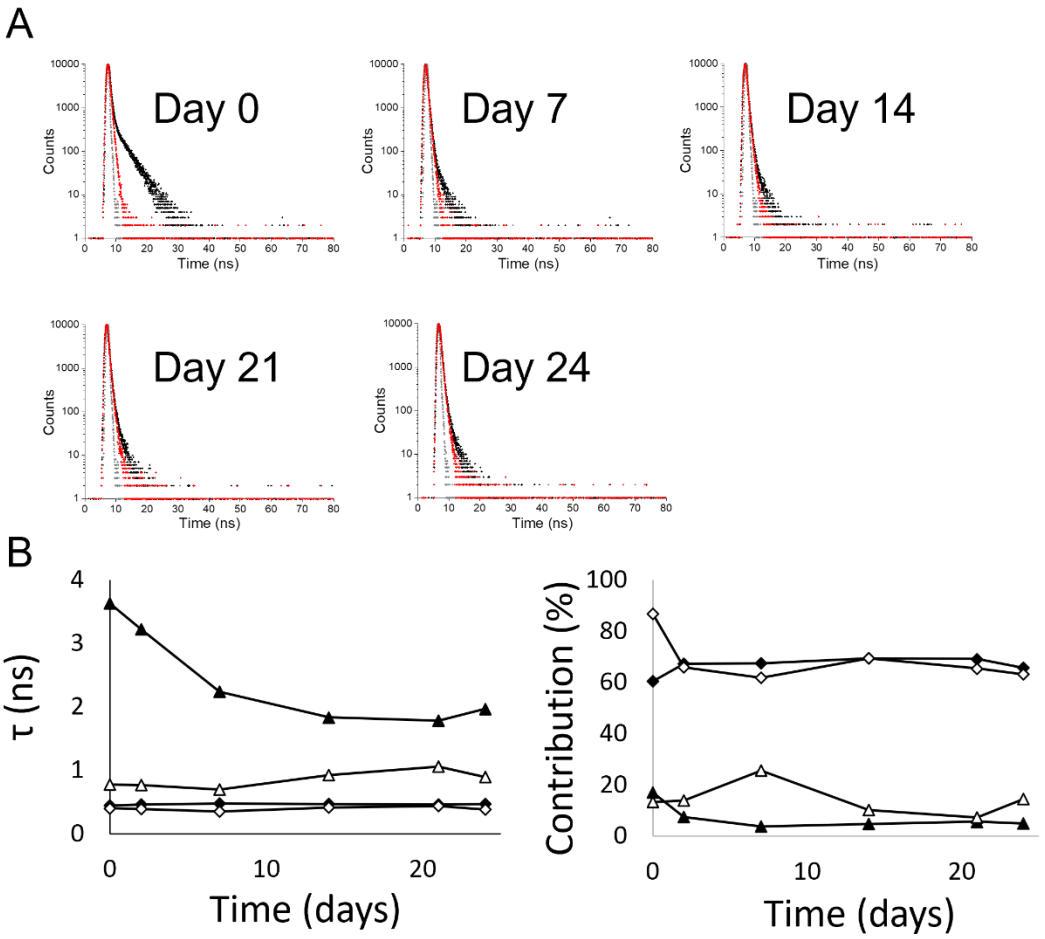

Figure 4.8. Part A shows fluorescence decay at 525 nm of NADH (black) and NADH-glucose (red) in Trizma buffer alongside the instrument response function (grey) at various days after sample preparation. Part B shows the 3 lifetimes obtained when the decays are fitted to the 3-exponential model for NADH (closed symbols), NADH-glucose (open symbols). τ_1 is shown by diamonds, τ_2 is shown by triangles, and τ_3 is shown by circles. The percentage contribution of each component to the decay for each sample is also shown. The contribution of the scattered light to each decay has been left out for clarity.

Figure 4.8B shows the fitted parameters for these decays, and contrary to what was observed in PBS, a 2-exponential model can describe the decays for both samples for the entire experiment duration (examples of fitted decays, the resultant values of the parameters, and the residual plots are shown in Appendix C Figures C2.3 and C2.4). There is no 3rd component required to fit the decay from either sample, and thus no evidence of a newly formed blue shifted fluorescent residue with long lifetime.

At day 0, the short lifetime component is ~0.4 ns for both samples, however there is a difference in the long lifetime component: 0.8 ns for NADH-glucose/Trizma (which makes this

result consistent with literature[185]) and 3.9 ns for NADH/Trizma. This difference is consistent with the raw decays in Figure 4.8A, and suggest that there is a long lifetime fluorescent residue, that emits at 525 nm, present in NADH/Trizma solution, however there is little evidence of this in the steady state spectra (Figure 4.4). This residue is likely competing with NADH fluorescence, and the presence of glucose negates the effect. As the experiment progresses, the value of the long lifetime component for NADH/Trizma decreases, but it does remain slightly higher than 0.8 ns, which is the consistent value for NADH-glucose/Trizma. The contribution of each component to the decay remains stable throughout the experiment, and similar between the two samples.

The result of measuring fluorescence decay at 525 nm again emphasises that NADH fluorescence behaves differently depending on buffer solution, consistent with our steady state results, and the results in literature already discussed.

The second detection wavelength considered was 470 nm. The decays for NADH/PBS, NADH-glucose/PBS and the instrument response function are shown in Figure 4.9A. From inspection of the plots, there are no substantial differences between the decays of both samples during the first 11 days (this is confirmed by the mean lifetimes, which on Day 0 were found to be 0.37 (+/-0.036) ns and 0.44 (+/- 0.034) ns for NADH/PBS and NADH-glucose/PBS respectively, and on Day 11 these values were 0.47 (+/- 0.013) ns and 0.48 (+/- 0.016) ns)). We also note that the mean lifetime for NADH during this time period is in line with that found in literature[178]. Differences begin to appear in the decay plots from day 14.

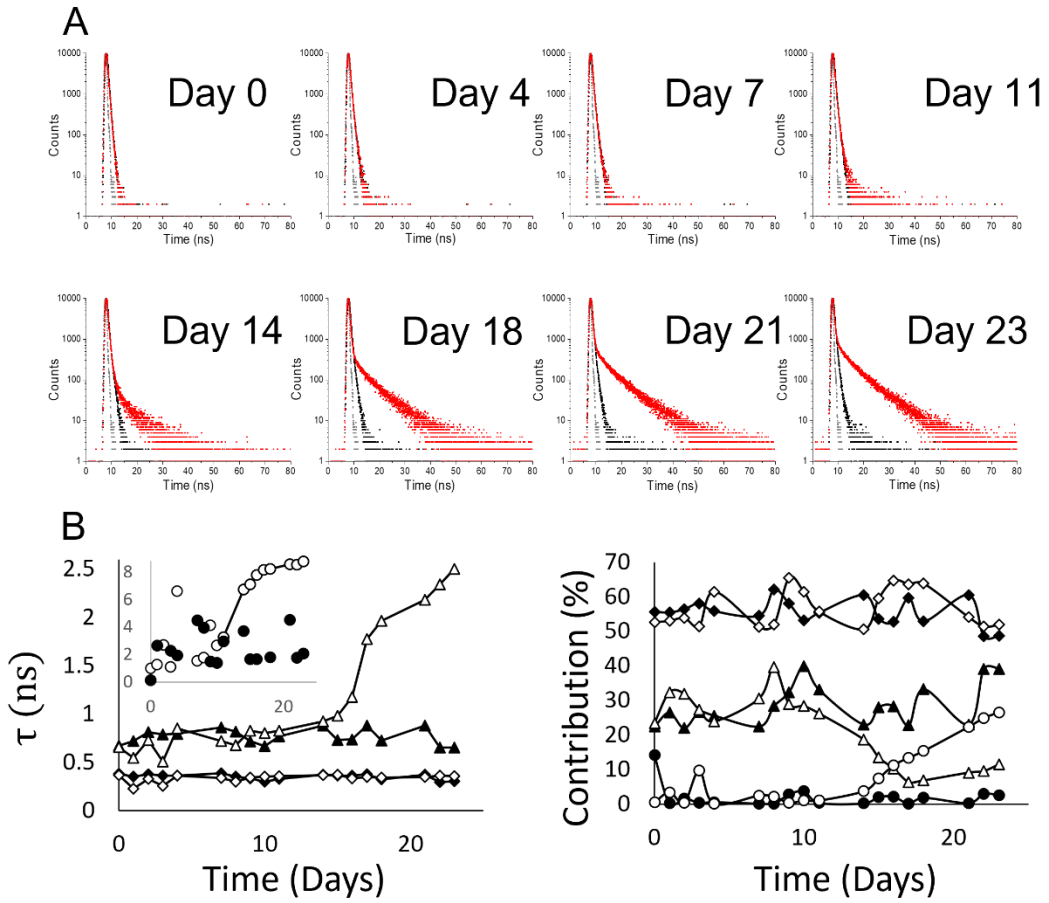

Figure 4.9. Part A shows fluorescence decay at 470 nm of NADH (black) and NADH-glucose (red) in PBS buffer alongside the instrument response function (grey) at various days after sample preparation. Part B shows the 3 lifetimes obtained when the decays are fitted to the 3-exponential model for NADH (closed symbols), NADH-glucose (open symbols). τ_1 is shown by diamonds, τ_2 is shown by triangles, and τ_3 is shown by circles. The percentage contribution of each component to the decay for each sample is also shown. The contribution of the scattered light to each decay has been left out for clarity.

Figure 4.9B shows the parameters of a 3-exponential model fitted to the decays. Like observed for detection at 525 nm, a third component was required after 11 days for NADH-glucose/PBS samples, and so for comparison, a 3-exponential model was used for both samples over all days. Examples of the fitted decays, the resultant values of the parameters, and the residual plots are shown in Appendix C, Figures C2. 5 and C2. 6.

Figure 4.9B shows that between days 10 and 23 the lifetime of the second component starts to increase significantly from 0.8 ns to 2.5 ns, and the lifetime of the third component increases from ~2 ns to 8.5 ns. At the same time, the contribution of the second component drops from 30% to 10%, while the contribution of the third component increases from negligible values to about 25%. This observation, the increased presence of a long lifetime

component, again suggests the presence of a new fluorescent residue that is competing with NADH fluorescence. This could be gradual conversion of the nicotinamide ring into another blue shifted fluorescent residue of longer fluorescence lifetime. its contribution at 470 nm is larger than at 525 nm. In a repeat experiment (results not shown), the same outcome was observed, where the fluorescence intensity decay of the NADH-glucose/PBS sample was longer compared to the sample without glucose, with the fitted parameters showing an increased contribution of the third component between days 10 and 25. Additionally, the fitted parameters were also comparable between experiments, thus suggesting there is reliability in the experimental and data processing techniques.

Fluorescence decays of free NADH/Trizma and NADH-glucose/Trizma for detection wavelength 470 nm are shown in Figure 4.10A, alongside the instrument response function. These results disaffirm what was observed in PBS: in Trizma, no differences can be seen between the sample with glucose and the sample without. This can be seen qualitatively by direct inspection of the plots, but calculation of the mean lifetime also confirmed this. At Day 0 the mean lifetime for both NADH/Trizma and NADH-glucose/Trizma was 0.44 ns, and at Day 24 this was 0.46 ns (standard deviations were small and have been omitted for readability). Figure 4.10B shows the fitted parameters for these decays, and following the same pattern as detection at 525 nm, a 2-exponential model can describe the decays for both samples for the entire experiment duration when in Trizma. Examples of fitted decays, the resultant values of the parameters, and the residual plots are shown in Appendix C Figures C2.7 and C2.8. This is again contrary to PBS samples which required a 3 component model. For Trizma samples, a 3rd component is not needed to fit the decay, and so there is no evidence of a newly formed fluorescent residue.

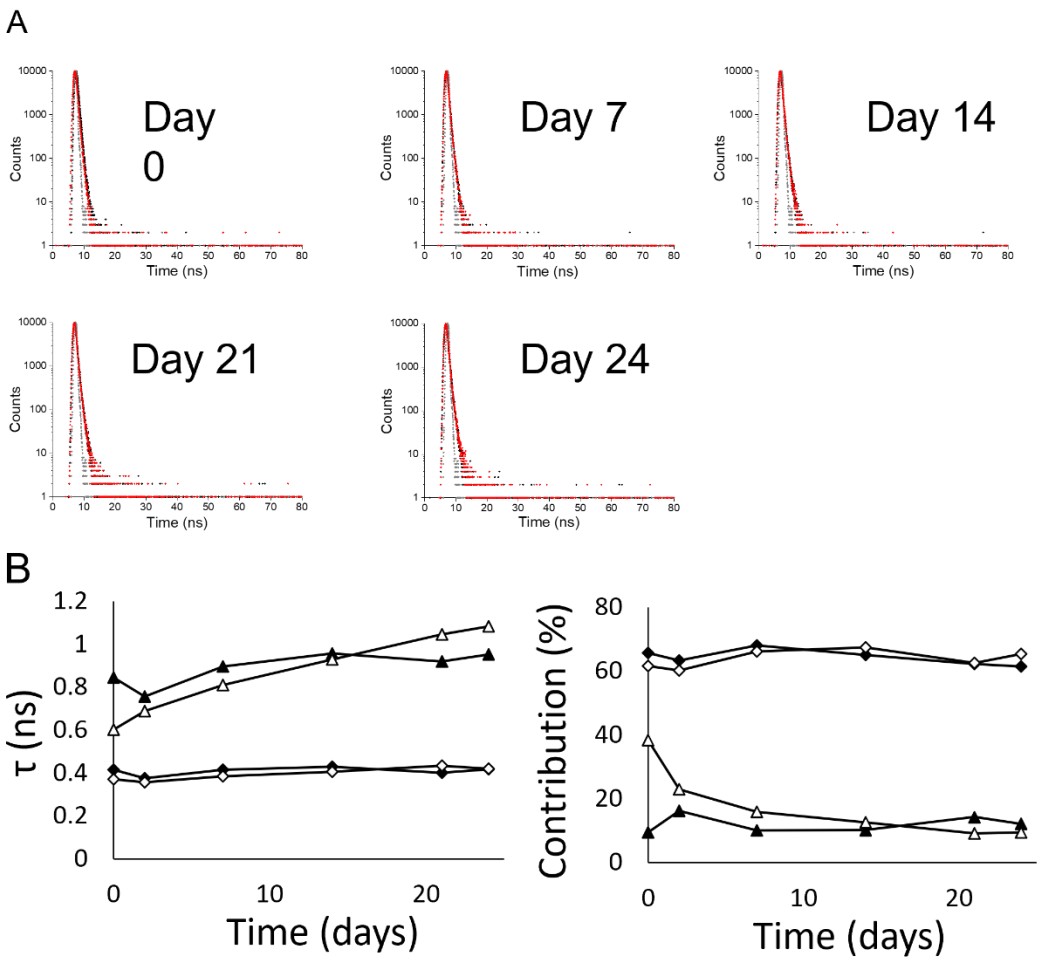

Figure 4.10. Part A shows fluorescence decay at 470 nm of NADH (black) and NADH-glucose (red) in Trizma buffer alongside the instrument response function (grey) at various days after sample preparation. Part B shows the 3 lifetimes obtained when the decays are fitted to the 3-exponential model for NADH (closed symbols), NADH-glucose (open symbols). τ_1 is shown by diamonds, and τ_2 is shown by triangles. The percentage contribution of each component to the decay for each sample is also shown. The contribution of the scattered light to each decay has been left out for clarity.

At day 0, both samples show the short lifetime component to have a value of ~0.4 ns, while the longer lifetime component is 0.85 ns and 0.6 ns for NADH/Trizma and NADH-glucose/Trizma respectively. For both samples, these are within the expected values for NADH fluorescence decay in solution[185], again showing that glucose does not have an effect on the fluorescence properties of NADH while in this buffer. The lifetime values and their contributions remain reasonably stable and equal between samples throughout the experiment.

The final detection wavelength for the fluorescence intensity decays was 390 nm. Figure 4.11A shows the raw fluorescence decays of NADH/PBS and NADH-glucose/PBS samples,

alongside the instrument response function. The raw decays of both samples show differences, although small from day 0 (the mean lifetime for NADH/PBS was 0.43 (+/- 0.005) ns while for NADH-glucose/PBS this was 0.45 (+/- 0.007) ns, and the changes observed in the decays of the NADH-glucose/PBS sample over time are significant. All raw decays indicate substantial contributions of the scattered light, i.e. high percentage of the shifted prompt function $C_\lambda(t)$ in the experimental decays. Figures C2.9 and C2.10(Appendix C2), showing examples of the fitted decays alongside the resultant fitted parameters, indicate high *C* parameters.

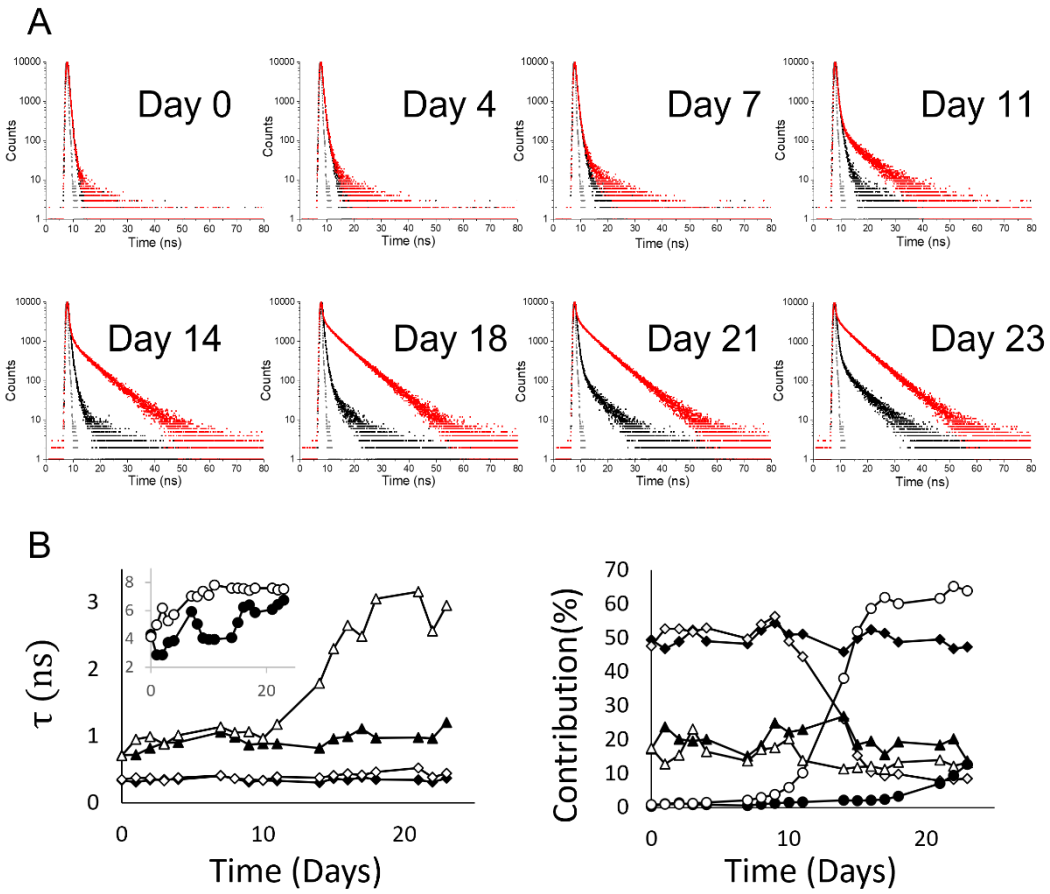

Figure 4.11. Part A shows fluorescence decay at 390 nm of NADH (black) and NADH-glucose (red) in PBS buffer alongside the instrument response function (grey) at various days after sample preparation. Part B shows the 3 lifetimes obtained when the decays are fitted to the 3-exponential model for NADH (closed symbols), NADH-glucose (open symbols). τ_1 is shown by diamonds, τ_2 is shown by triangles, and τ_3 is shown by circles. The percentage contribution of each component to the decay for each sample is also shown. The contribution of the scattered light to each decay has been left out for clarity.

A 3-exponential model was needed to fit the decays detected at 390 nm from the earliest stages of the experiment (Figure 4.11B), indicating that even from day 0, a long lifetime

component is present in the decay. During the first 10 days the recovered parameters of both samples do not change hugely: the differences between the two shorter lifetimes and their related pre-exponential factors are quite insignificant. There are differences in the long lifetime over the first 10 days, however since the contributions of the third component to the decays is very small during this time (less than 5% in both samples) it makes no meaningful part of the decays.

Significant differences start to appear in the fluorescence decays from day 11, and this is reflected in the fitted parameters. The contribution of the long lifetime becomes a much more dominating part of the decay in the sample with glucose as the sample evolves. Initially making up less than 5% of the decay, its contribution increases rapidly between days 11 and 16 up to ~65% where it stabilises. This occurs alongside a reduction in the contribution of the short lifetime component. The initial ~50% drops to ~10% after 2 weeks. On the other hand, in free NADH/PBS the contributions of all three components of the decay remain relatively stable, with the long lifetime component only increasing during the last 5 days.

Moreover, the intermediate lifetime remains stable at the level of ~1 ns for the NADH/PBS sample during the whole duration of the experiment. In the NADH-glucose/PBS sample it starts to rise after 10 days, reaching about 3 ns by the end of the experiment. The above observations are consistent with the changes in fluorescence intensity decays observed for detection in PBS at 525 and 470 nm. If we consider exclusively PBS samples, this result seems to confirm that the presence of glucose reduces the characteristic intrinsic fluorescence of NADH's nicotinamide ring, and supports formation of the new fluorescent residue, which is characterised by shorter peak emission wavelength and a longer fluorescence lifetime.

In a repeat experiment under the same conditions, the same result was observed, where the fluorescence decays of the sample containing glucose were longer compared to the free NADH/PBS sample. A comparison of the mean lifetime values for two experiments under the same conditions is presented in Table 4.1, and are extremely similar. This repeatability demonstrates minimal errors in the experimental and data processing techniques used.

Table 4.1. Mean lifetime $\bar{\bar{\tau}}$ alongside respective standard deviations for NADH/PBS and NADH-glucose/PBS samples at various days after sample preparation in two separate experiments. Each decay was fit to the 3-exponential model and the mean lifetime calculated using equation 2.17. The fitting procedure and calculation of mean lifetime was repeated three times, and the results averaged. The excitation wavelength was 340 nm, and emission wavelength was 390 nm.

	Exp 1 $\bar{\tau}$ (ns)	Exp 2 $\bar{\tau}$ (ns)
NADH/PBS Day 0	0.43 +/- 0.005	0.43 +/- 0.008
NADH-glucose/ PBS Day 0	0.45 +/- 0.007	0.44 +/- 0.006
NADH/PBS Day 11	0.46 +/- 0.006	0.47 +/- 0.005
NADH-glucose/ PBS Day 11	0.60+/- 0.005	0.56 +/- 0.017
NADH/PBS Day 23	0.57 +/- 0.016	0.60 +/- 0.012
NADH-glucose/ PBS Day 23	4.21 +/- 0.52	5.52 +/- 0.47

Finally, the fluorescence decays at detection wavelength 390 nm, alongside plots of the evolution of the fitted parameters are presented for both samples in Trizma in Figure 4.12. Similarly to what was observed at detection at 470 nm, the raw decays (Figure 4.12A) show no differences between samples at any point throughout the experiment (this was confirmed by there being no significant statistical differences in the mean lifetimes over time and also between samples).

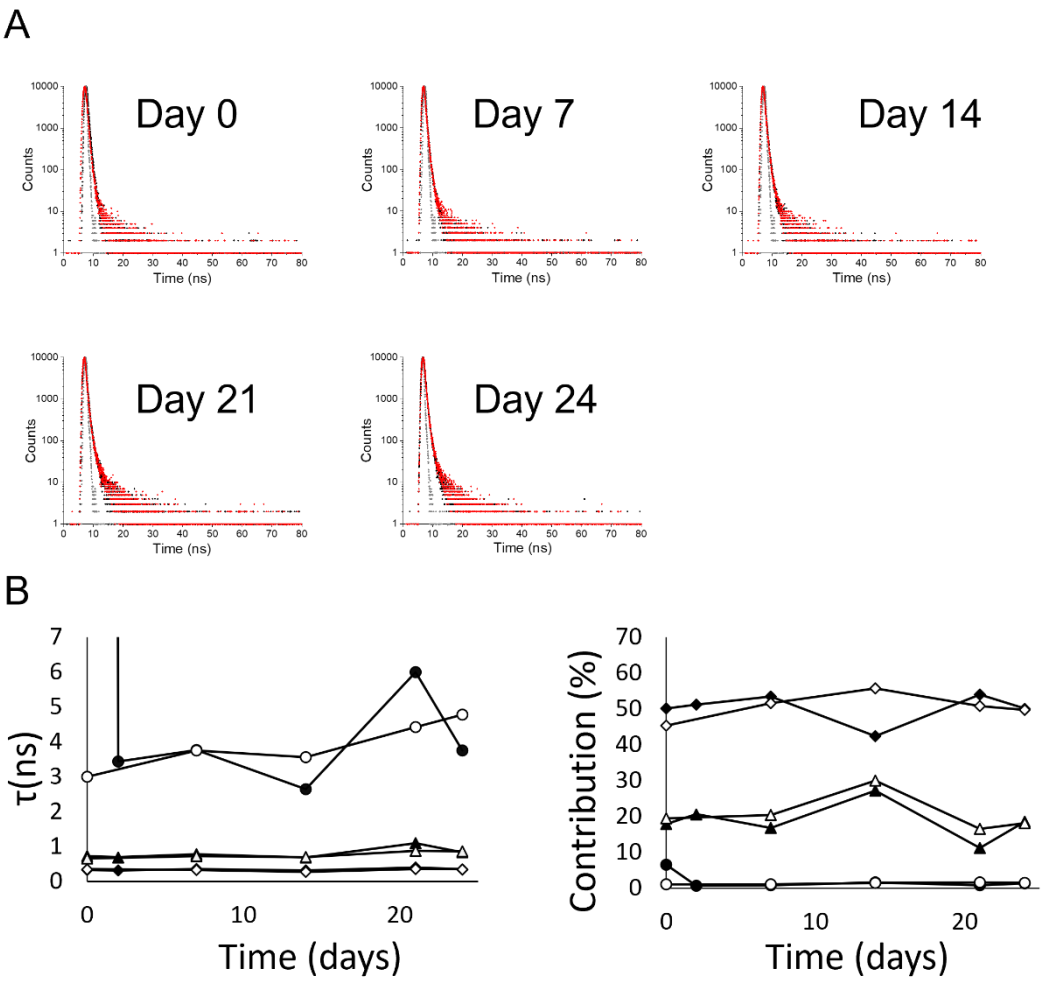

Figure 4.12. Part A shows fluorescence decay at 390 nm of NADH (black) and NADH-glucose (red) in Trizma buffer alongside the instrument response function (grey) at various days after sample preparation. Part B shows the 3 lifetimes obtained when the decays are fitted to the 3-exponential model for NADH (closed symbols), NADH-glucose (open symbols). τ_1 is shown by diamonds, τ_2 is shown by triangles, and τ_3 is shown by circles. The percentage contribution of each component to the decay for each sample is also shown. The contribution of the scattered light to each decay has been left out for clarity.

Figure 4.12B shows the resultant parameters from fitting to a 3-exoponential model: this was deemed the best model based on the χ^2 goodness of fit and the plots of residuals, examples of which are shown in Figure C2.11 and Figure C2.12 (Appendix C2), and is consistent to our result in PBS, where a 3-exponential model was required to fit the decay at 390 nm.

The fitted values follow a similar trend as previously observed, where there are 2 short lifetime components that make up the majority of the decay, and one longer lifetime component, whose contribution is very small. The three lifetime components for both samples at day 0 have values of ~0.4 ns, ~0.8 ns, ~4 ns, which match those calculated for the

PBS samples at day 0. Although the contribution of this long lifetime component is very small for the duration of the experiment (unlike in PBS where its presence grows in the presence of glucose), it does indicate that there is a fluorescent residue that emits at shorter wavelengths present in these samples. We hypothesize that this may be bacterial intrinsic fluorescence, that emits close to 390 nm, and is present in all samples at day 0. Glucose then causes the bacteria to grow in the PBS samples, causing the contribution of this component to increase significantly.

4.4 Conclusion

The data presented show that there is no evidence of NADH glycation. Although the fluorescence of NADH seems to change dramatically in the presence of glucose when in PBS buffer, we conclude that the changes observed are not due to glycation.

Our results also show that NADH is highly unstable in PBS buffer over a long time period: this is shown by the decrease in fluorescence intensity and absorbance in both NADH/PBS and NADH-glucose/PBS samples. We appreciate that there may be an effect due to glucose in this buffer, however it cannot be revealed in these experiments due to it being masked by the interaction with phosphate. This could be investigated in future work, where buffers and pH could be changed systematically, and the same experiments carried out. Additionally, different concentrations of glucose could be used, as in this work the concentration of glucose was high compared to that of NADH.

The fluorescence intensity decay measurements showed evidence of a new fluorescent residue at 390 nm, characterised by a longer lifetime, that was present in all samples. Its contribution however increases over time in the PBS samples, and grows significantly in the sample with PBS and glucose. We believe this may be fluorescence from bacteria, which is present in all samples, but grows in PBS due to it being a good culture medium for bacteria. Further work in this area could include carrying out similar measurements on PBS and PBS-glucose samples in order to confirm this.

Overall, the purpose of the work in this chapter was to determine if NADH glycation could be detected and monitored using its intrinsic fluorescence, which could in turn offer a potential method for monitoring long term glycaemic control. The findings from this research show no evidence of NADH glycation, and so focussing on the fluorescence of this skin fluorophore as a means for monitoring glycaemic control may not be a suitable approach. Future work is required to fully understand the fluorescence behaviour of this system, for example similar

studies in Trizma at pH 7 may provide greater insight and reveal any underlying processes that could not be seen in PBS.

5.Keratin

5.1 Introduction

Keratin is one of the most important biopolymers found in humans[186] (the other being collagen), and it is the most abundant structural protein found in epithelial cells[187]. It is one of the toughest biological materials[188], as well as being extremely durable and unreactive to diverse external environments. These characteristics serve the primary functions of keratin: protection, armour, aggression, and providing mechanical support[189]. In mammals, keratin makes up the epidermis of skin, wool, hair, horns, and nails, and in reptiles and birds, feathers, beaks, and claws are all composed of keratin.

There are 2 keratin types: α-keratin and β-keratin, and these two types exhibit different structures. α-keratin exhibits a helical structure, while in β-keratin the protein is arranged as parallel sheets of polypeptide chains. Furthermore, in α-keratin there are 2 protein types, a high-sulphur protein matrix and a low-sulphur protein filament[190, 191]. In β-keratin however, the filament and matrix are incorporated into one single protein[192].

Keratin can also be categorised into hard and soft keratins, and this classification is based on their method of biosynthesis[193] and the amount of sulphur cross-links[194]. Soft keratins are found almost exclusively in the outer layer of the skin, the stratum corneum, and have a lower sulphur content than the hard keratins, which are found in hair and nails[189]. The higher sulphur content in the hard keratins gives them a much more coherent structure, due the higher number of cross-links that will form.

This chapter focuses on α-keratin, as this is the type found in mammals, and is therefore the most relevant for this research. For example humans have approximately 30 α-keratin variants[186], and it can be found in nails, hair, and the skin. β-keratin on the other hand is found in birds and reptiles.

5.1.1 Keratin Structure

Keratin belongs to the family of intermediate filament (IF) proteins, so named because their diameter falls between that of the 2 other filamentous structures of the cytoskeleton: actin filaments and microtubules[195]. Over 50 different types of IFs have been identified, which are then classified into 6 groups based on similarities in their amino acid sequence[196]. Type I and type II keratin are two of these groups, and differ in that type I keratin is acidic, and thus includes more acidic amino acids such as aspartic acid and glutamic acid, while type II keratin is comprised of more basic amino acids such as arginine, lysine and histidine[197].

The structure of the α-keratin IF is illustrated in Figure 3.1. It is composed of 2 right-handed α-helix polypeptide chains with a central alpha-helical rod (approximately 46 nm in length) and non-helical N- and C-terminal regions[198]. The 2 chains coil together via disulphide cross-links to form a left-handed coiled coil. This coiled coil is known as a heterodimer, and it is the monomeric unit of the α-keratin IF. It, and therefore the IF, can only be formed if within each heterodimer one of the polypeptide chains is type I (acidic) keratin, and the other is type II (basic to neutral) keratin[199].

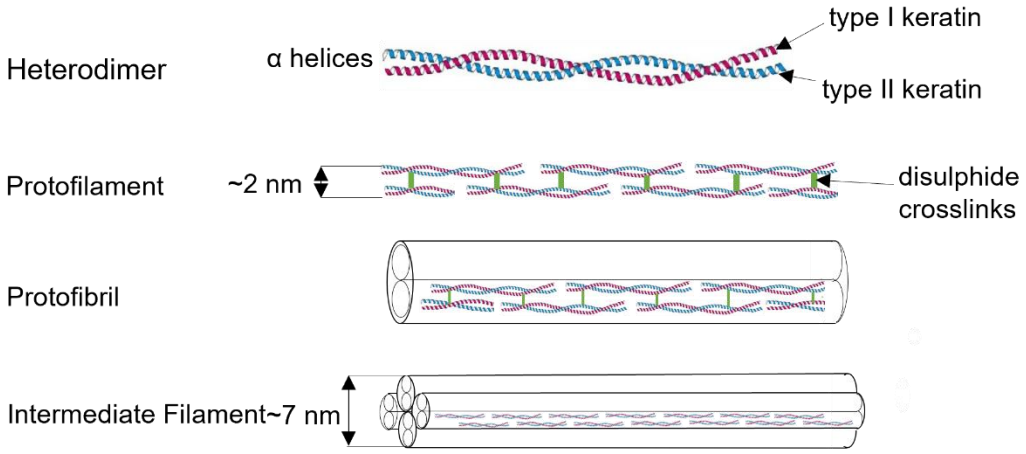

Figure 5.1. An illustration of how keratin intermediate filaments are assembled from keratin polypeptide chains.

These heterodimers then aggregate end to end and stagger side by side via disulphide bonds to form a protofilament (~2 nm in diameter)[200]. Two protofilaments then associate laterally into a protofibril, and 4 protofibrils combine into a helical IF, with a diameter of 7-10 nm[189].

The other aspect of keratin's structure is the protein matrix. Keratin molecules follow a filament-matrix structure[189] where the keratin IFs pack into a supercoiled conformation and link with a protein matrix[191] via bonding of the N- and C-terminals. The matrix proteins and end-terminals also wind around the filaments themselves[192, 201] to form the keratin structure. While keratin IFs have a low sulphur content[190], the keratin matrix consists of proteins that have a high sulphur content, as well as a high number of cysteine, glycine, tyrosine, or phenylalanine residues[202].

5.1.2 Keratin Glycation

Like collagen, keratin proteins can also experience non-enzymatic glycation[203-205], following the same process outlined earlier. The preferential target for glycation is the ε-amino group of a lysine residue or the α-amino group of an N-terminal residue[206], both of which are found

in keratin, making it susceptible to this process. In addition to these sites, glycation can also take place at side chains of arginine, tryptophan, histidine, and cysteine residues[207].

Like with collagen, an increase in glycated keratins has been observed in those with diabetes: diabetes patients have shown an increase in glycated keratin from the stratum corneum in the sole of the foot[205] , increased glycated keratin in hair[203], and increased glycated nail keratins[208-210]. Furthermore, a higher concentration of glycated keratins was found in those exhibiting complications such as diabetic retinopathy, nephropathy[209], and diabetic ulcers[205]. These findings suggest that monitoring the glycation of this protein could offer a further method for monitoring long-term diabetes control, and even the potential for developing complications of the disease.

5.1.3 Keratin Fluorescence

Previous studies have used several methods to determine the amount of glycated keratin in human tissues. For example, colorimetric analysis has been used to determine glycated keratin in the stratum corneum of the skin in vitro[208], near-infrared reflectance spectroscopy[210], ATR-FTIR spectroscopy[211], and chemical analysis using techniques such as borate affinity chromatography followed by gel electrophoresis[209] has been used to determine the levels of glycated keratin in nail clippings.

In this work, we aim to exploit the auto-fluorescence of keratin as a potential method for monitoring its glycation. Being auto-fluorescent, keratin's presence can be detected without the need for any extrinsic fluorophore. Its fluorescence originates from two sources: amino acids[212] and cross-links within the protein[213, 214].

Keratin contains the naturally fluorescent amino acids phenylalanine (Phe), tyrosine (Tyr), and tryptophan (Trp)[215]. It is however unlikely that Phe will contribute significantly to the intrinsic fluorescence of keratin due to its low absorption and quantum yield[216], and similarly, Tyr emission is often reduced in proteins by its interaction with the peptide chain or via energy transfer to Trp[1, 217]. Indeed, the amino acid derived fluorescence of keratin peaks at about 340 – 350 nm[213, 218], which corresponds to Trp fluorescence[1].

The exact number of Trp and Tyr residues in keratin is not known, and it differs between specific keratin types. Reports vary, however in α-keratin, which is the type found in mammals, it is thought that Trp and Tyr account for approximately 1% and 3% of the amino acids respectively[215, 219].

Keratin cross-links are the second source of its intrinsic fluorescence. These can be excited at 350 -370 nm, and emit fluorescence peaking at ~460 nm[68, 213]. These two distinct peaks (Trp and cross-links) have been seen in various keratin-containing tissues such as fingernails, hair, and the stratum corneum[218]. In collagen, which is a similar protein to keratin, glycation causes the formation of new cross-links[147], and so we believe that changes to the fluorescence of the keratin cross-links may offer the most insight into keratin glycation.

If keratin's intrinsic fluorescence changes as a result of glycation, this could provide an alternative method to monitor long-term diabetic control. Keratin is found in human hair, nails, and in the skin, and so this technique could be used to monitor diabetes through, for example, monitoring glycated keratin in nail clippings, rather than using blood samples. This offers advantage due to the non-invasive nature of the technique.

In this work we have studied keratin in vitro and have used steady-state and time-resolved fluorescence techniques to investigate the impact of glucose on this protein's intrinsic fluorescence.

5.2 Methodology

5.2.1 Preparation of Keratin and Keratin-Glucose Samples

The evolution of two samples, free keratin and keratin-glucose, have been studied. Keratin from human epidermis and phosphate buffered saline pH 7.4 (PBS) were purchased from Sigma-Aldrich and used to prepare a free keratin sample of concentration 20 µM and the keratin-glucose sample by the addition of glucose powder (also Sigma Aldrich) to create a sample containing 20 µM keratin and 20 mM glucose. 3.5 ml of each sample was then transferred to a 4x1x1 cm quartz cuvette, and sealed with a stopper and parafilm, ready for measurements. The samples were prepared with maintaining the spectroscopic purity, but were not-sterile, and both samples were stored at room temperature for the duration of the experiment. In the glucose-containing sample, the glycated keratin was not purified from the non-glycated one. To make sure that the spectra measured are not affected by the fluorescence caused by the bacteria growth in the samples, the measurements of a reference sample of glucose in PBS were carried out using the same experimental settings as for the keratin samples. All spectra show that the impact of potential bacteria growth on the keratin and keratin-glucose samples' fluorescence in negligible (discussed later).

5.2.2 Fluorescence Measurements

Corrected fluorescence excitation and emission spectra were obtained using a Fluorolog (Horiba Scientific). The excitation, emission, and the excitation/emission reference samples (discussed later) spectra were collected with a step of 1 nm, and the slit widths on the excitation and emission monochromators were 5 nm. The fluorescence intensity decay measurements were carried out on a DeltaFlex fluorescence lifetime system (Horiba Jobin Yvon IBH Ltd, Glasgow), which uses time-correlated single photon counting (TCSPC) to record fluorescence decay. A NanoLED with repetition rate 1MHz and peak excitation wavelength 370 nm (pulse duration <1 ns) was used for excitation.

The steady state spectra and fluorescence intensity decays were measured for both samples on day 0 (within ~10 minutes of sample preparation) and on subsequent days after preparation.

5.3 Results and Discussion

Figure 5.2. shows the excitation-emission matrix for keratin and keratin glucose at Day 0 and Day 44. The results at Day 0 are very similar for both samples. The greatest fluorescence intensity occurs for λ_{ex} = 280 nm, resulting in emission between 300 and 340 nm, corresponding to Tyr and Trp fluorescence in keratin. From the literature[213, 218] there should also be a fluorescence peak between 440 and 460 nm. Indeed, by day 44 there is an increase in fluorescence intensity at this wavelength in both samples, with the intensity substantially greater in the sample with glucose. Hence we have studied in more detail fluorescence of the samples for two excitation wavelengths, 280 nm and 370 nm.

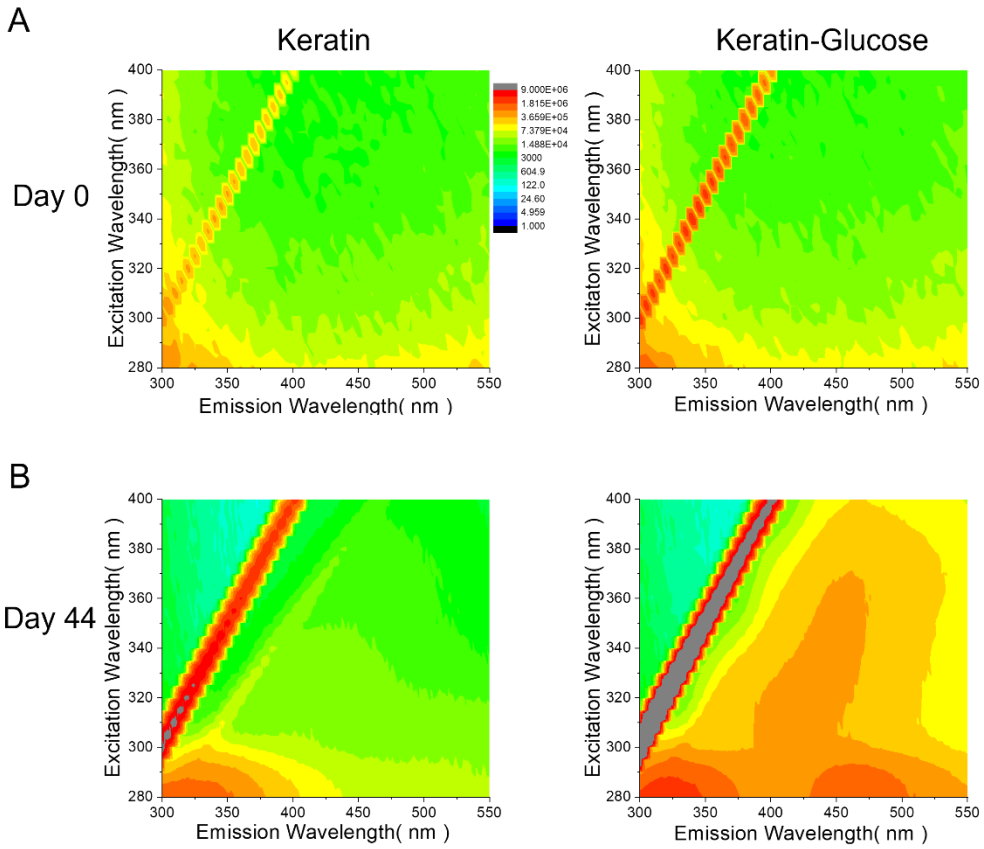

Figure 5.2. Excitation-emission matrix of keratin and keratin-glucose. Parts A and B show the spectra obtained for keratin and keratin-glucose on day 0 and day 44 respectively.

Figure 5.3 shows the excitation spectra of free keratin and keratin-glucose for the fluorescence associated with cross-links detected at 460 nm. At day 0, the spectra for the two samples are very similar, and the intensity is at a low level. Over time, the substantial changes can be seen in the keratin-glucose sample (Figure 5.3. and B). After approximately 10 days, a new broad band appears in the excitation spectra, with a peak wavelength of ~370 nm. The fluorescence intensity at this excitation wavelength grows considerably as the keratin-glucose sample evolves, before it stabilises after around 37 days. Absorption at 370 nm is known from literature as a characteristic of keratin cross-links[68]. Thus, we assume that glucose is causing the formation of new cross-links that can be excited directly at 370 nm and emit fluorescence at 460 nm.

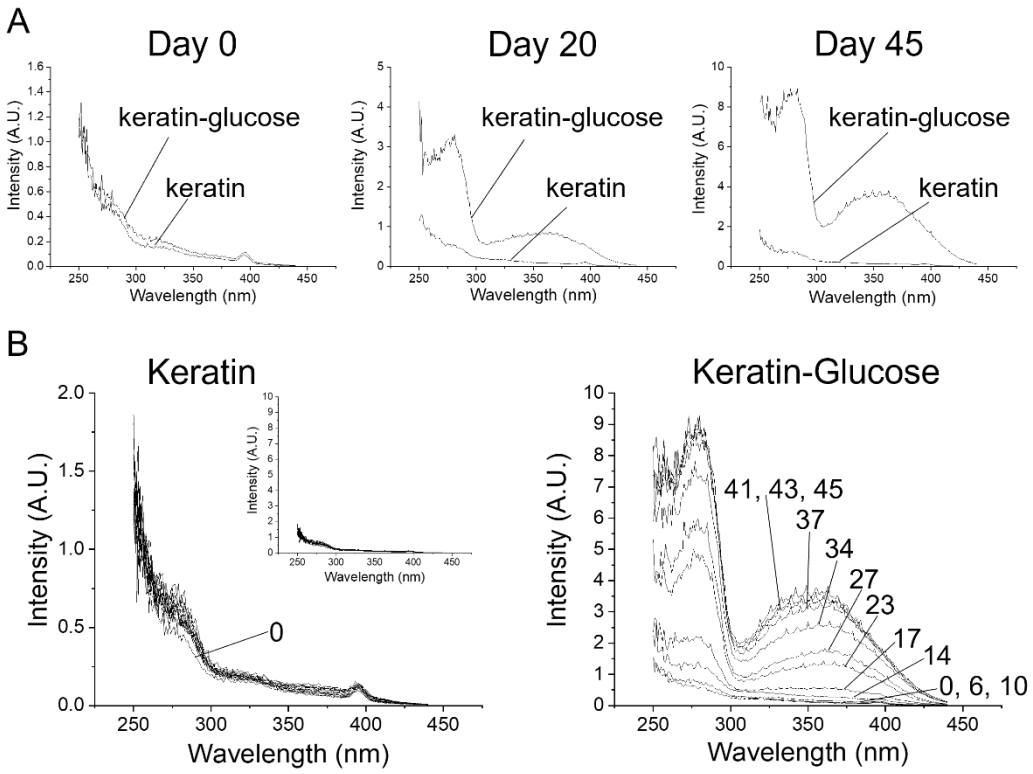

Figure 5.3. Fluorescence excitation spectra of keratin and keratin-glucose when emission was collected at 460 nm. Part A shows the spectra obtained for keratin and keratin-glucose on various days after sample preparation. Part B shows how the excitation spectra of each sample evolves over time. The units of all plots are the same.

Figure 5.3B also shows an increase over time in the 460 nm fluorescence intensity when the keratin-glucose sample is excited at 280 nm. A possibility is that this is fluorescence from kynurenine, which emits weakly at ~480 nm when excited at 365 nm[220], which is within the wavelength range considered. Kynurenine is a metabolite of Trp, however its formation requires the presence of certain enzymes[221] (Tryptophan 2,3-dioxygenase (TDO) or Indoleamine 2,3-dioxygenase (IDO)), which are not present in our *in vitro* set up. We therefore hypothesise that the Trp in keratin absorbs the energy at 280 nm, and then transfers this energy to the keratin cross-links, resulting in increased emission at 460 nm. This transfer of energy could be radiative (re-absorption) or non-radiative (FRET) and intensifies over time as the cross-links are being formed.

The fluorescence spectra in Figure 5.4 show that exciting keratin-glucose sample at 280 nm causes increase in Trp fluorescence at ~340 nm when the sample ages. Interestingly excitation at 280 nm also results in fluorescence emission at 460 nm, which correlates to the emission wavelength for keratin cross-links. Again, this seems to suggest that the Trp in keratin transfers its excitation energy to the cross-links, causing emission at 460 nm.

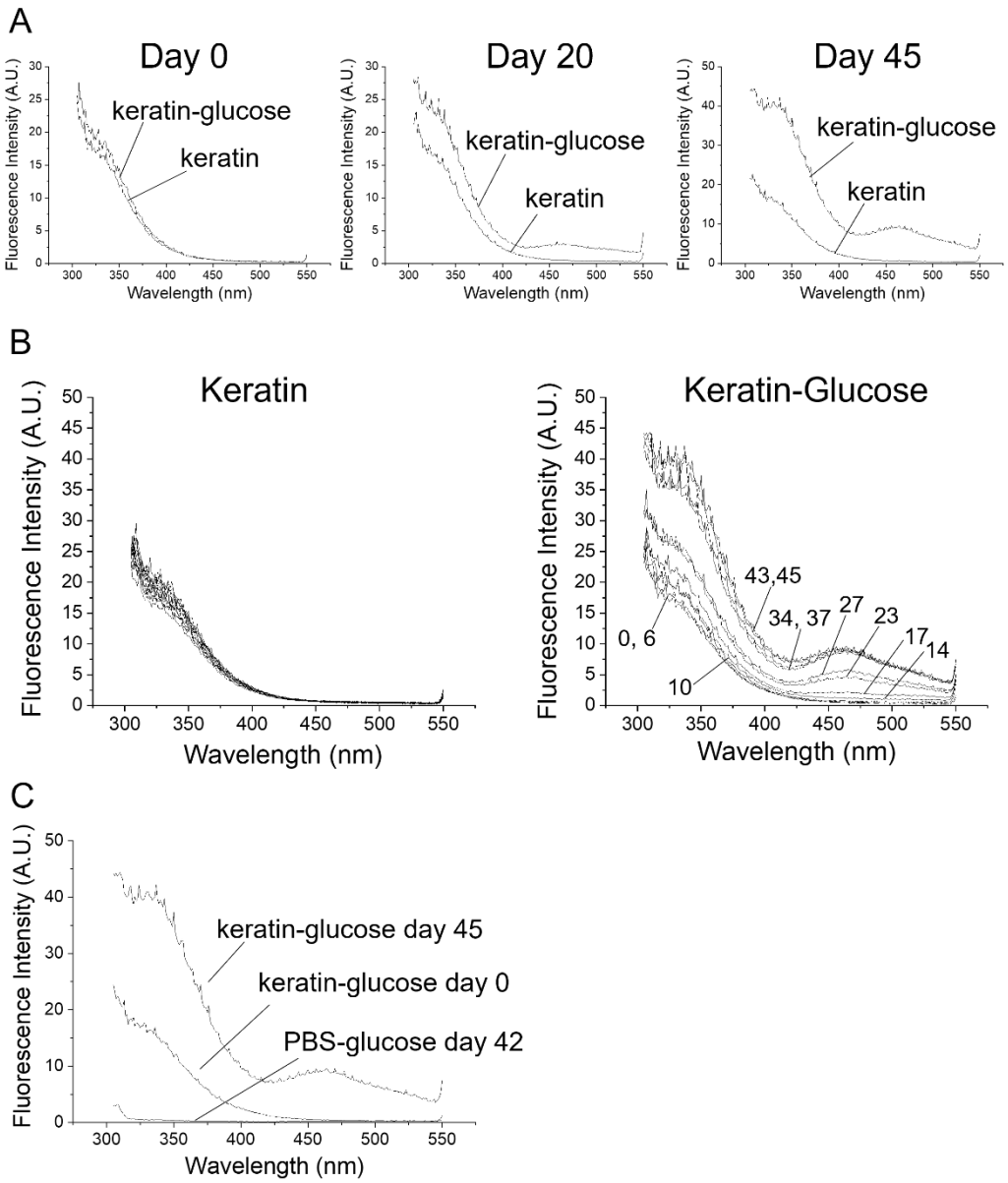

Figure 5.4. Fluorescence emission spectra of keratin and keratin-glucose when excited at 280 nm. Part A shows the spectra obtained for keratin and keratin-glucose on various days after sample preparation. Part B shows how the emission spectra of each sample evolves over time. The units of all plots are the same. Part C shows the fluorescence emission spectra obtained for a PBS-glucose sample, alongside the keratin-glucose spectra for comparison.

The fact that both Trp and keratin cross-links fluorescence increase suggests an increase in the Trp quantum yield, possibly due to reduced quenching by water as crosslinks shield the Trp sites. Figure 5.4C shows the fluorescence of a reference PBS-glucose sample excited at 280 nm, 42 days after its preparation and storing it in the same conditions as the free keratin

and keratin-glucose samples. Negligible emission from this sample demonstrates that there is no detectable bacteria growth in the glucose/buffer environment used in keratin samples.

Using the wavelength 370 nm allowed direct excitation of the cross-links (Figure 5.5). Again, both spectra on day 0 are very similar and contain the peak at 424 nm, which is the Raman shift for excitation at 370 nm. This was calculated using the Raman shift for water (3400-3600 cm^{-1}) and the equation

$$\lambda = \frac{1}{1/\lambda_{ex} - Raman\ shift/1 \times 10^{7}} \quad [5.1]$$

where λ_{ex} is the excitation wavelength used. Both day 0 spectra also show the broad fluorescence band with the peak at ~460 nm, associated with the cross-links.

Figure 5.5B shows that in the pure keratin sample the intensity of this fluorescence increases only slightly with time. In the keratin-glucose sample, however, the fluorescence intensity grows substantially as the sample ages, and the dominating peak remains stationary at 460 nm. We also observe the formation of two new peaks at longer wavelengths. After 10 days a second peak starts to appear at ~ 525 nm, and after 21 days, the third peak can be seen at ~575 nm. These keratin-glucose complexes form much slower than that responsible for the 460 nm emission and are not observed at all in the free keratin sample.

Similarly like Figure 5.4C, Figure 5.5C also shows that the potential impact of bacteria growth on the keratin and keratin-glucose samples' fluorescence at 370 nm is negligible, and thus any changes observed in the spectra are solely the result of the interaction with glucose and/or protein aggregation.

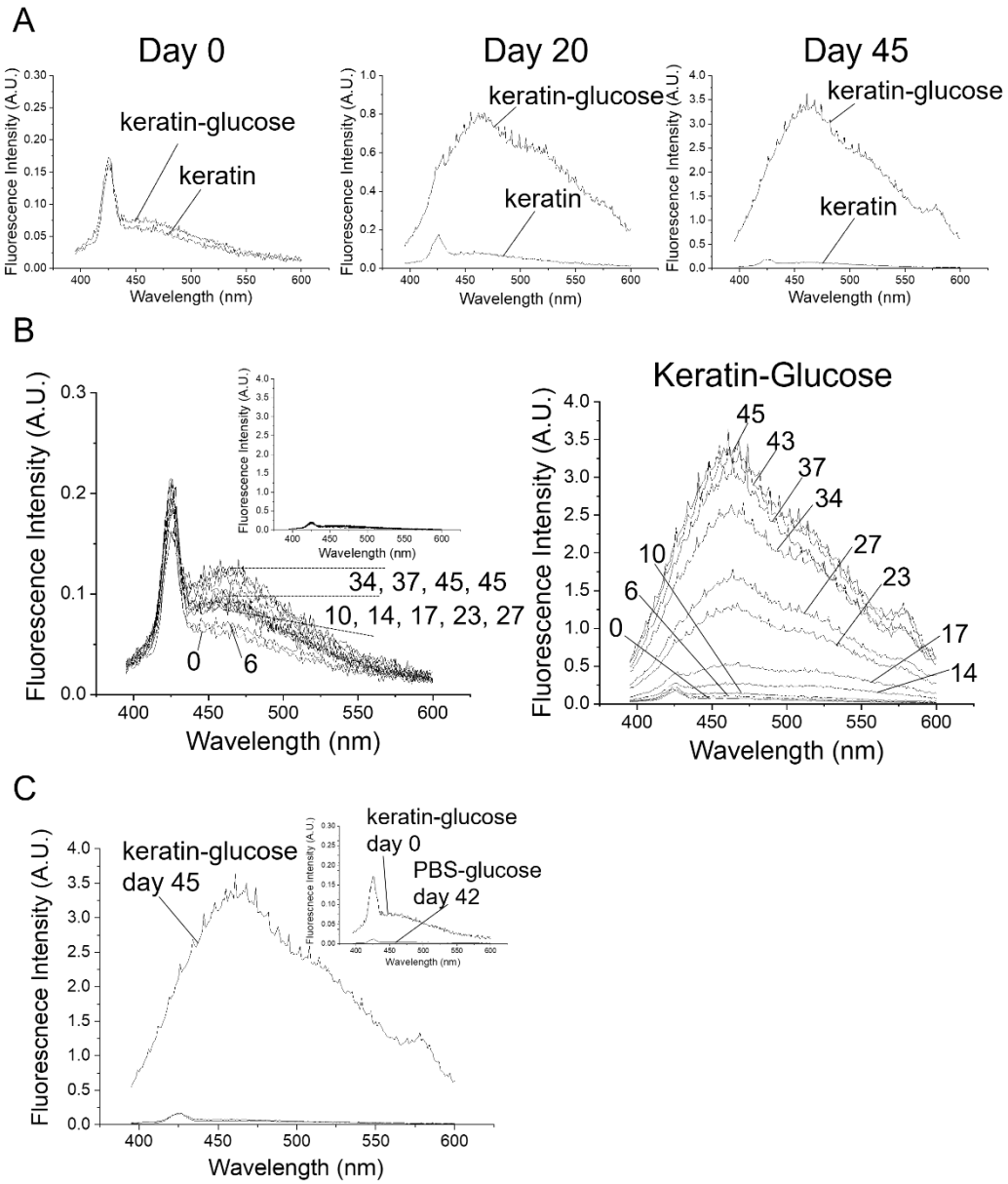

Figure 5.5. Fluorescence emission spectra of keratin and keratin-glucose when excited at 370 nm. Part A shows the spectra obtained for keratin and keratin-glucose on various days after sample preparation. Part B shows how the emission spectra of each sample evolves over time. The units of all plots are the same. Part C shows the fluorescence emission spectra obtained for a PBS-glucose sample, alongside the keratin-glucose spectra for comparison

To quantify the difference in the emission spectra of the two keratin samples for excitation 370 nm, and to illustrate how the spectra evolve over time in more detail, a Gaussian model of fluorescence spectra was fitted to these data.

$$I(v) = \sum_{i=1}^{M} \frac{A_i}{\sigma_i \sqrt{(2\pi)}} e^{-\left(\frac{(v-v_i)^2}{2{\sigma_i}^2}\right)} \qquad [5.2]$$

In this model M is the number of spectral components, A_i is the contribution of each component to fluorescence, v_i is the peak position, and σ_i is the half-width of the distribution. For the pure keratin sample only one component (M=1) was required to describe the spectra throughout the experiment. This was also adequate for the first 9 days in the keratin-glucose sample; however, 2 components (M=2) were required from day 10, and three components (M=3) were required from day 24. Switching to the more complex model was based on the shape of the spectra and the χ^2 goodness of fit criterion. An additional component represented the Raman scatter at ~424 nm. Examples of the experimental fluorescence spectra plotted alongside the model function for keratin and keratin-glucose show relatively good agreement, as can be seen in Appendix D1, Figures D1.1 and D1.2.

The evolution of the recovered parameters of the spectra are plotted in Figure 5.6. The initial peak positions $v_1(0)$ for both samples are the same, approximately 22000 cm^{-1} (Figure 5.6A), which corresponds to the peak for keratin cross-links. For the pure keratin sample this stays consistent throughout the experiment, but in the keratin-glucose sample, the $v_1(t)$ shows a steady decrease through the first 9 days. This drop is likely due to the need for a second component, and indeed when the second component is added to the model, $v_1(t)$ increases back to 22000 cm^{-1}, where it remains for the experiment duration. This component is the most dominant contributor to the emission spectrum for both samples, and its contribution $A_1(t)$ increases substantially in the keratin-glucose sample as the experiment progresses, as illustrated in Figure 5.6C.

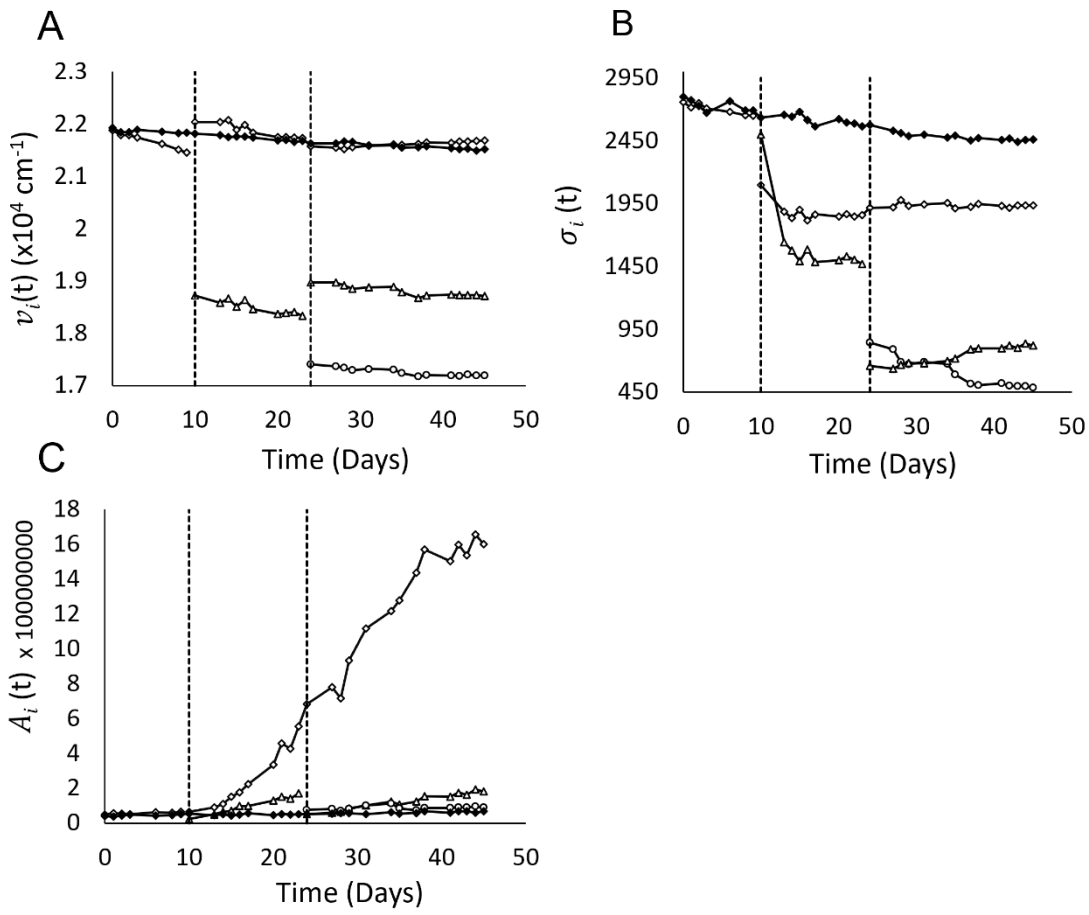

Figure 5.6. Fitted Gaussian parameters for the fluorescence emission spectrum for keratin (closed symbols) and keratin-glucose (open symbols). Plot A shows the time evolution of the peak position $v(t)$ of the emitting fluorophores, Plot B shows the half-width of the distribution σ(t) , and the contribution to the fluorescence intensity A(t) is shown in plot C.

The second component for keratin-glucose also follows the above trend relating to peak position. The $v_2(t)$ shows a steady decrease from 18700 cm^{-1} to 18350 cm^{-1} between days 10 and 23, and then once the 3rd component $v_3(t)$ is added to the model, $v_2(t)$ increases again and remains relatively constant at ~18700 cm^{-1}. The peak wavenumber $v_3(t)$ for this 3rd component is also stable between day 23 and the experiment end, only showing a slight drop from ~17400 cm^{-1} to ~17200 cm^{-1}.

We note that the evolution of the peak wavenumbers $v_i(t)$ is consistent with the evolution of the half-width distributions $\sigma_i(t)$ illustrated in Figure 5.6B. For free keratin, and for keratin-glucose during the first 10 days, the $\sigma_1(t)$ is large. Although it decreases slightly for the keratin sample over time, there is not a significant change. For keratin glucose, the addition of a second component from day 10 causes the $\sigma_1(t)$ to drop significantly as one

component splits into 2, and this happens again at day 24, when the addition of a third component causes $\sigma_2(t)$ to drop as the second component splits again.

This steady state analysis shows how the intrinsic fluorescence of keratin changes in the presence of glucose. The fluorescence of the dominating crosslinks K_{CL} emit at 460 nm and the higher-order crosslinks, K_{CL}' and K_{CL}'', formed at slower rates, emit at 525 nm and 575 nm, respectively. We note that the same result was observed in a repeat experiment, indicating that the changes observed are not due to any errors in experimental technique

Time resolved measurements were also conducted and analysed for the keratin and keratin-glucose samples. Firstly, the fluorescence intensity decays of both samples at the detection wavelength 460 nm were measured with using two excitation wavelengths 280 nm and 370 nm. The results shown in Figure 5.7 were carried out at the end of the experiment, on day 45, to maximise the potential impact of glucose.

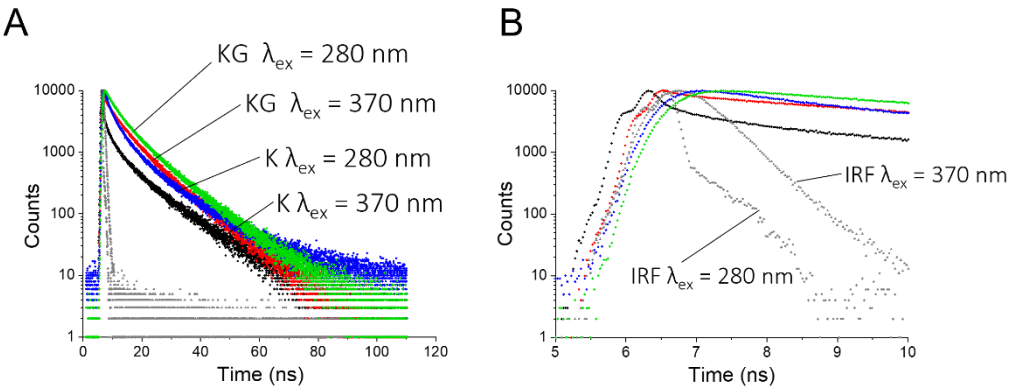

Figure 5.7. Fluorescence decay at 460 nm of keratin and keratin-glucose on day 45. Part A shows the decay over the full time range, while part B is a detailed look early stages of the decay, between 5 and 10 ns. Shown is the decay of keratin when excited at 280 nm (blue) and 370 nm (black), and keratin-glucose when excited at 280 nm (green) and 370 nm (red). The instrument response functions (IRF) are shown for excitation 280 nm (grey diamonds) and 370 nm (grey triangles).

We note, that for the excitation at 370 nm, the samples begin to decay immediately after excitation (black and red curves). However, for the excitation at 280 nm (blue and green), the top sections of the decays are much flatter, indicating that the detected fluorescence is likely to come from the fluorophore which was not excited directly. Again, these results suggest the transfer of the excitation energy from tryptophan to the cross-links. Moreover, as we observe a substantial spectral overlap between the emission spectrum of the amino acids and the absorption of the cross-links (300-400 nm, seen on the excitation spectra, (Figure 5.3), the likely mechanism involved is FRET.

Fluorescence intensity decays at the excitation wavelength of 370 nm and collected at 460 nm at various days following sample preparation are shown in Figure 5.8. Up to day 8, the raw decays for both samples, with and without glucose, are almost identical (Figure 5.8A). This can be seen by direct inspection of the raw decays, however was confirmed by calculation of the mean lifetime on each day, where there was no statistically significant difference between samples until day 16. By day 16, the decays of the glucose-containing sample become slower as compared to those of the pure keratin sample. Figure 5.8B shows the lifetimes and percentage contributions of each component for the data fitted to 3-exponential model decay (Appendix D2 for details). It should be noted that each decay was fit to the model three times, and the resultant parameters averaged.

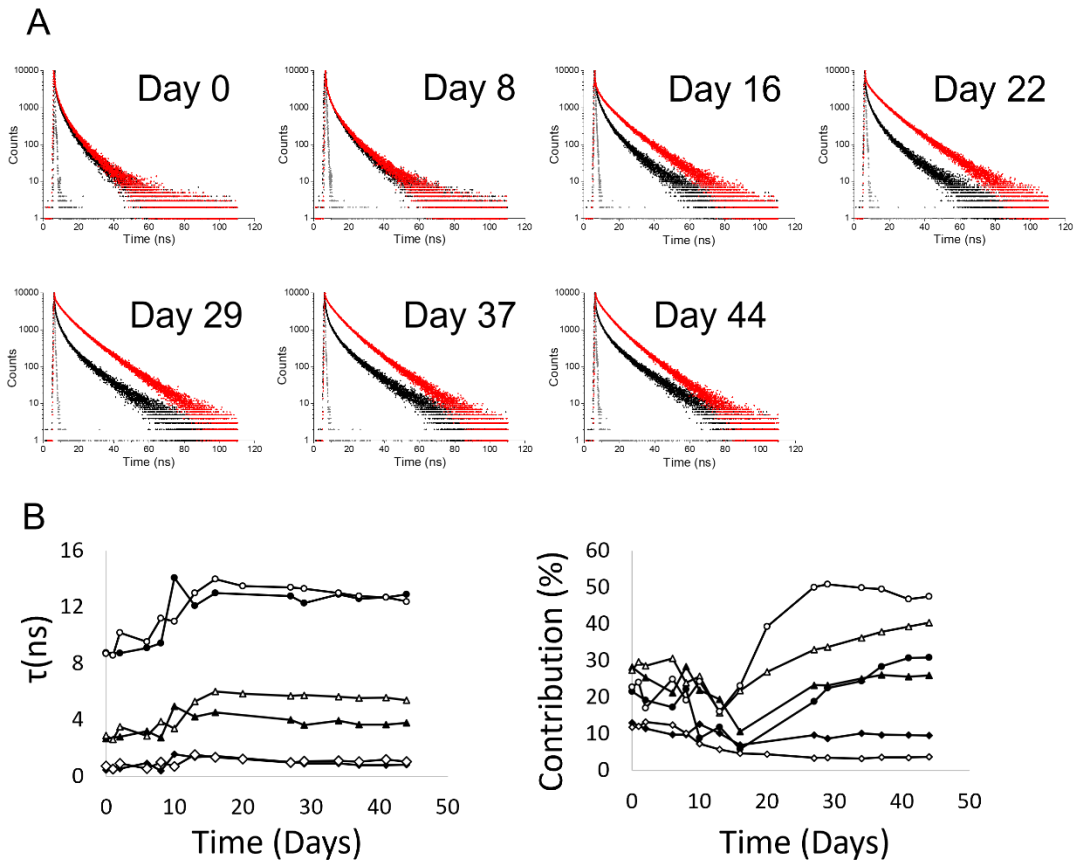

Figure 5.8. Part A shows fluorescence decay at 460 nm of keratin (black) and keratin-glucose (red) alongside the instrument response function (grey) at various days after sample preparation. Part B shows the 3 lifetimes obtained when the decays are fitted to the 3-exponential model for keratin (closed symbols) and keratin-glucose (open symbols). τ1 is shown by diamonds, τ2 is shown by triangles, and τ3 is shown by circles. The percentage contribution of each component to the decay for each sample is also shown. The contribution of the scattered light to each decay has been left out for clarity.

All three lifetimes and their corresponding pre-exponential factors are quite stable and similar between samples during the first ~10 days. Between days 10 and 14 the lifetime components show an increase in both samples, and then stabilise for the remainder of the experiment.

Although the three lifetimes appear similar in glucose and glucose-free samples, the impact of glucose manifests itself in changes of the lifetime contributions to the decay. Indeed, the increases in contributions of the two longer lifetime components are much more pronounced in the sample with glucose. In a repeat experiment the same result was observed, which indicates reliability in the experimental and data processing techniques used.

Our fitted values do not however seem to be similar to what has been observed in literature. Studies have considered the fluorescence decay of hair, which also contains keratin protein. A 2007 study found a 2-exponential model was sufficient to fit the fluorescence decay of hair, and attributed the long lifetime component of 1.4 ns to keratin[222]. A further study in 2012 found the fluorescence decay of hair to have a more complex multi-exponential decay, and thus used phasor plots to represent it[223]. Our results *in vitro* also appear to show keratin as having a complex multi-exponential decay.

Further information has been gathered from the time-resolved emission spectra (TRES) constructed from the fluorescence intensity decays recorded at a range of wavelengths (440 – 550 nm) for both samples. Figure 5.9 shows the normalised TRES for both samples at different times. The curves for the pure keratin sample (black) do not change shape throughout the decay, indicating simple fluorescence kinetics. They also do not change substantially during 44 days of experiment.

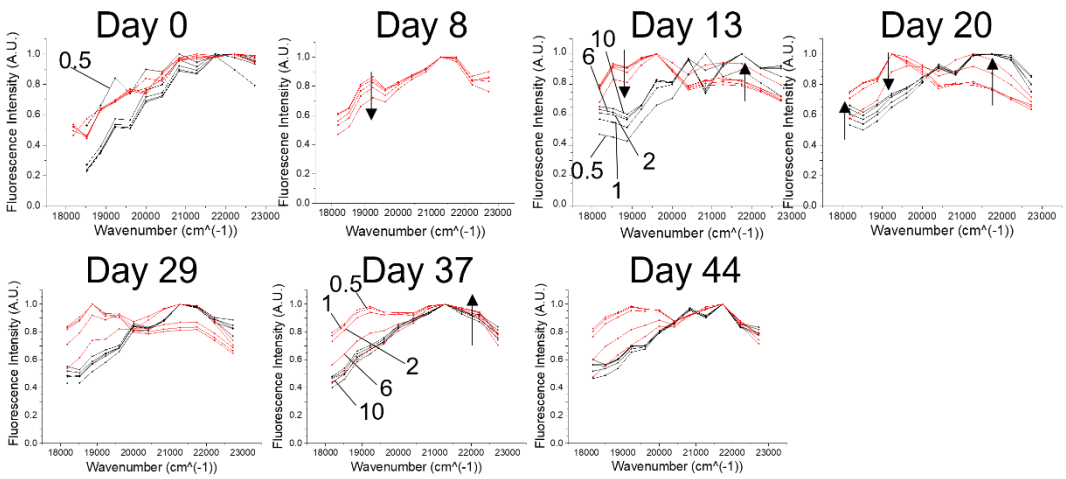

Figure 5.9. Normalised TRES of keratin and keratin-glucose on various days after sample preparation, when excited at 370 nm. The red lines are keratin-glucose, and the black lines are keratin. Each line represents the TRES at a different time after excitation: 0.5, 1, 2, 6, and 10 ns.

Conversely, the shape of the TRES for the keratin-glucose sample does change as the experiment progresses. Initially, at day 0, the TRES resembles the spectrum seen for free keratin, demonstrating no immediate impact of glucose on keratin fluorescence.

By day 13 there seems to be one peak in the TRES, and thus one fluorescent residue, which is consistent with the steady state data. However, after day 13 a second peak can be seen in the TRES, which becomes more pronounced as the experiment progresses. This occurs at 19000 cm^{-1}, and so would correspond to the keratin-glucose complex that forms at approximately 525 nm.

The shape of the spectra also changes in the 10 ns following excitation in the keratin-glucose sample, with the red curves in Figure 5.9 indicating that the fluorescent residue with peak at 525 nm decays faster than the residue at 21500 cm^{-1} (~460 nm). We speculate that the fluorescence at 525 nm originates from a keratin-glucose complex, which requires a longer time to form, thus it is likely to be a bigger structure than the one emitting at 460 nm, for example one formed by an agglomeration of aggregates rather than by unimolecular addition. The other emission maximum observed at 575 nm may come from even larger keratin-glucose structures. In future studies the hypothesis of glucose causing the formation of larger complexes could be confirmed using fluorescence anisotropy measurements.

5.4 Conclusion

The data presented have shown that glucose has a big impact on the intrinsic fluorescence of keratin *in vitro*. In pure keratin, fluorescence shows peak at 340 nm due to Trp, and at 460

nm due to cross-links in the protein. These cross-links can be excited directly at 370 nm, or at 280 nm via FRET from the Trp residues. When glucose is added to a keratin sample, the fluorescence intensity at 460 nm increases greatly due to faster formation of new cross-links. Glucose also causes the formation of two new fluorescent complexes with peak fluorescence at ~525 nm (which appears after ~10 days) and 575 nm (~ 21 days). A schematic diagram illustrating the likely kinetics is shown in Figure 5.10.

We anticipate that the contributions of the three compounds detected in this experiment may be different in different conditions of keratin glycation, e.g. in the nail or hair tissues. As keratin intrinsic fluorescence is sensitive to the extent of glucose in its local environment, studying the fluorescence of nail or hair, where keratin is an abundant protein, may offer a complementary method for monitoring long-term complications of diabetes.

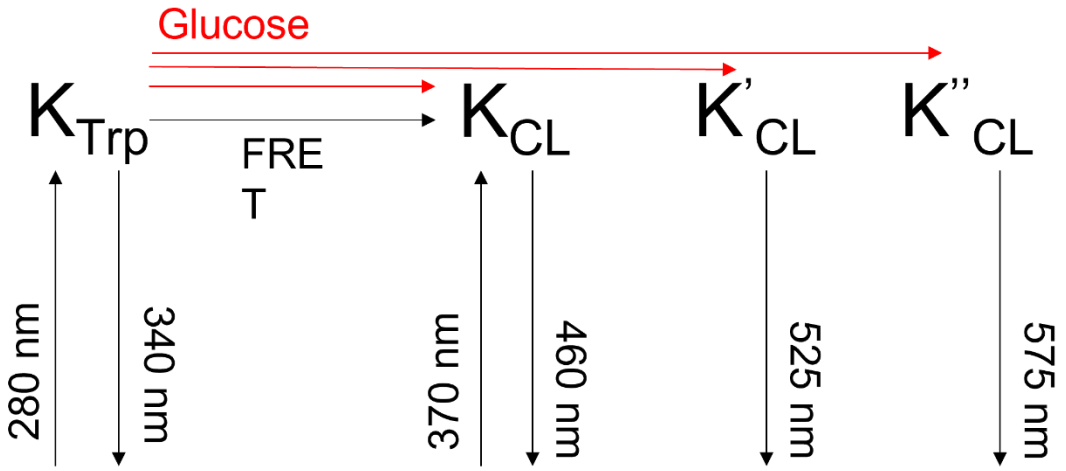

Figure 5.10. A diagram of the potential kinetics of the keratin and glucose interaction.

6. Human Serum Albumin

6.1. Introduction

Human serum albumin (HSA) is the most abundant protein in human serum, accounting for approximately 60% of all serum proteins[224], and normally found at a concentration between 35 and 50g/l[225]. It has many biological functions, including regulating the bloods osmotic pressure and pH, mediating lipid metabolism, working as an antioxidant, and isolating toxins[226,227]. A key role of HSA is that it acts as a transport protein for a variety of solutes such as fatty acids, some hormones, and drugs[228]. It therefore has a profound influence on the pharmacokinetic properties of many drugs[229].

6.1.1. Human Serum Albumin Structure

HSA is a heart shaped, globular protein consisting of a single polypeptide chain with 585 amino acids[230], comprising 67% alpha helices, 10% turns, 23% random coils, and no Beta sheets[231]. It consists of 3 structurally similar domains, I, II, and III, with each of these domains made up of two sub-domains, A and B[232]. Figure 6.1shows an illustration depicting the domain organisation in HSA, which is model generated by previous authors[232]. The A sub-domains of regions II and III are the major sites of drug binding in HSA[226].

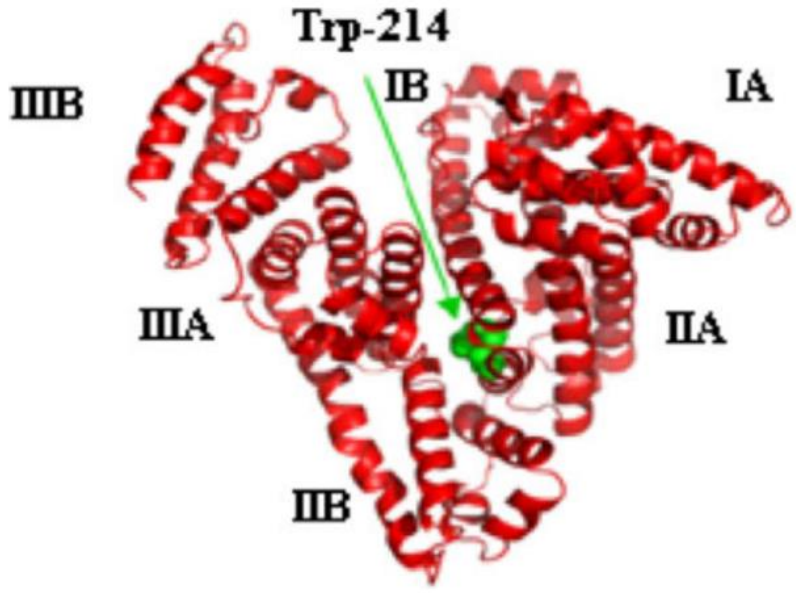

Figure 6.1 The structure of HSA[2] .

Additionally, there are 17 intramolecular disulphide bonds in HSA, which not only ensure rigidity within each sub-domain[233], but also allow the proteins size and shape to change in response to biological influences, such as pH fluctuations.

6.1.2. HSA and Glucose

As discussed briefly in chapter 1, HSA experiences non-enzymatic glycation, and glycated albumin can be used as an indicator of glycaemic control[37,234]. Proteins with a long biological half-life are much more likely to experience glycation due to the length of time it takes for Amadori rearrangement, and HSA has a half-life of 21 days, making it highly susceptible to this process. This, along with the fact that HSA is continuously exposed to glucose in the blood, causes glycation, and thus AGE formation in HSA[225]. The 59 lysine residues and 24 arginine residues are considered as the sites at which glycation occurs[235].

Glycation of HSA also follows the three-step process outlined in Chapter 1 (Figure 1.2), that results in the formation of AGEs. This process heavily modifies the structure of HSA, which influences its function, disrupting normal physiological processes. Glycation alters the intrinsic conformation of the molecule, which can alter the binding efficiency of drug binding regions, and thus have an effect on drug efficacy[236]. HSA AGEs may also interact with their receptor (RAGE) or other macromolecules, initiating various signalling pathways that can lead to tissue damage and metabolic complications[237]. Glycated HSA can also trigger platelet aggregation, causing thrombosis and hindering glucose uptake into cells[238,239]. Finally, glycation of HSA can also lead to severe drug toxicity: HSA is the main drug binding protein in the plasma, and modifications to its structure caused by glucose disrupt its ability to bind to drugs. This leads to an increased amount of free drugs in the bloodstream, and it is these that bind to receptor to produce a therapeutic affect[240]. An increased concentration of free drugs leads to drug toxicity[241,242].

Amadori products are the main form of glycated albumin present, and the level of these increases with increased levels of glucose in the blood, such as occurs in patients with diabetes[243]. In a healthy individual, glycated HSA makes up approximately 1-10% of all HSA in the plasma, but this increases to 20-30% in those with diabetes[230,244]. Glycated albumin therefore could be used as a biomarker in glycation-related diseases such as diabetes. The benefits of this marker compared to traditional HbA1c measurements were discussed in detail in Chapter 1 (section 1.1.2.2 Long Term Monitoring).

6.1.3. HSA Auto-fluorescence

HSA, like the proteins studied elsewhere in this thesis, is auto-fluorescent (AF). Therefore, it has the potential to be detected non-invasively using fluorescence spectroscopy. HSA's fluorescence arises from the aromatic amino acids tryptophan (Trp) and tyrosine (Tyr): there

is a single Trp residue at position 214 in subdomain IIA, and 18 Tyr residues are distributed along the length of the protein[245]. Excitation at 280 nm results in excitation of both Trp and Tyr, giving HSA peak absorbance at this wavelength. Fluorescence from HSA, however, is likely to originate mostly from Trp due to the efficient FRET from Tyr to Trp[245]. This gives peak fluorescence emission at approximately 340 nm.

Previous studies have shown that glycation of HSA *in vitro* changes its steady state intrinsic fluorescence. A 2007 study[246] showed a decrease in Trp fluorescence in glycated HSA, alongside a blue shift in the peak emission from 330 nm to 315 nm. A 2017 study[247] also showed changes in steady state properties, showing glycated HSA to have increased absorption at 280 nm, alongside a higher intensity of fluorescence between 400 and 600 nm. This wavelength range was used not to study Trp, but to investigate the formation of AGEs which emit at longer wavelengths.

There has been less work researching the effect glycation has on the fluorescence lifetime of HSA. One study[248] carried out in 1999 found that the short lifetime component of a fluorescence intensity decay (detected at 345 nm) fitted to a multi-exponential model increased in glycated HSA compared to free (from 1.58 ns to 2.26 ns), while the long lifetime component also increased slightly.

The amount of glycated HSA increases with increased levels of glucose, thus making glycated albumin a potential biomarker for glycaemic control. In this chapter we attempt to determine if changes to HSA due to glycation manifest not only their steady state fluorescent properties, but also in time-resolved fluorescence. Alongside the traditional multi-exponential model analysis, we use the non-Debye model to fit fluorescence decays, in order to gain further understanding on the system, and information on the underlying kinetics of glycation.

6.2. Methodology

6.2.1 HSA Sample Preparation

The effect of glucose on the intrinsic fluorescence of HSA was investigated using two samples: free HSA and HSA-glucose. Albumin from human serum and pH 7.4 (PBS) were purchased from Sigma-Aldrich and used to prepare a 50 µM sample. The HSA-glucose sample was then prepared by the addition of glucose (Sigma-Aldrich) to create a sample containing 50 µM HSA and 100 mM glucose. 3.5 ml of each sample was transferred to a 4x1x1 cm cuvette and sealed with a stopper and parafilm, ready for measurements. The samples were prepared with maintaining the spectroscopic purity, but were not sterile, and the glycated HSA was not

purified from the non-glycated HSA. Both samples were stored in an oven at 37°C (core body temperature) for the experiment duration.

To check for bacterial growth in the samples, and to ensure that the resultant fluorescence was not caused by this, the measurements of a reference sample of glucose in PBS were carried out using the same experimental settings as for the HSA samples. The plots in Figure 6.2 show that the impact of potential bacteria growth on the HSA and HSA-glucose samples' fluorescence in negligible.

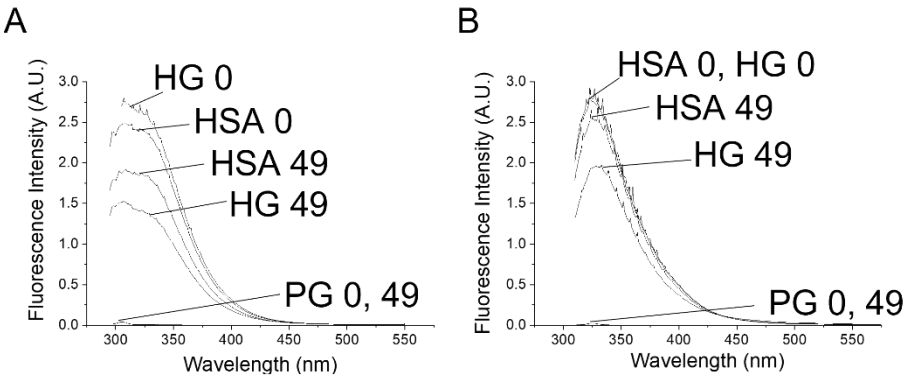

Figure 6.2. Fluorescence emission spectra for HSA (H), HSA-glucose (HG), and PBS-glucose (PG) at day 0 and day 49 when excited at 280 nm (A) and 295 nm (B).

6.2.2 Fluorescence Measurements

Absorption spectra were measured on using PerkinElmer Lambda 2 UV-Vis spectrometer, with a resolution of 1 nm. Corrected fluorescence emission spectra were obtained on a Fluorolog (Horiba Scientific) using a resolution of 1 nm, with both the excitation and emission monochromators set to a slit width of 5 nm. The fluorescence intensity decay measurements, and therefore also the TRES, were obtained using a DeltaFlex fluorescence lifetime system (Horiba Jobin Yvon IBH Ltd, Glasgow), which uses time-correlated single photon counting (TCSPC) to record fluorescence decay. Two NanoLEDs with repetition rate 1MHz and the peak excitation wavelengths at 280 nm (pulse duration <1ns) and 295 nm (pulse duration <1ns) were used to study fluorescence from the different amino acids in HSA. TRES were determined at the beginning and end of the experiment to see fully the impact of glucose over time: the fluorescence decays were recorded between 310 and 400 nm in increments of 10 nm. Details of how TRES were constructed was discussed in Chapter 2 (equations 2.30 and 2.31), and so will not be repeated here.

The first measurements were carried out on day 0, within ~10 minutes of sample preparation, and then repeated on subsequent days in order to see the impact of glucose on HSA fluorescence.

6.3. Results and Discussion

Figure 6.3 shows the absorption spectra for HSA and HSA-glucose over 49 days. In both samples the absorption peak is approximately 280 nm, corresponding to tyrosine peak absorbance, although it is likely Trp absorbance is also contributing to this peak. There is no significant change in the spectra over time in the free HSA sample, however in the sample containing glucose, there is a very slight increase in 280 nm absorbance as the sample ages, which is in keeping with the study[247] discussed earlier, where an increase in 280 nm absorption due to glycation was observed. There is also a slight increase in absorption at longer wavelengths, which we attribute to increased aggregation in the presence of glucose.

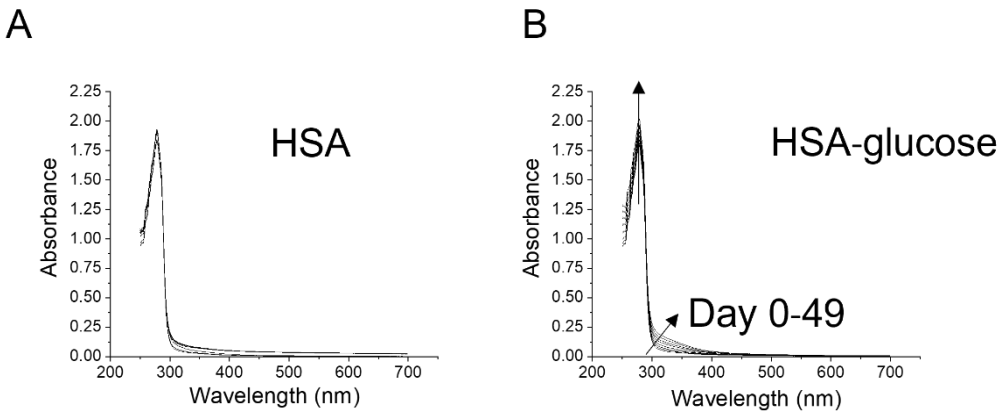

Figure 6.3. Absorption spectra at days 0, 8, 14, 21, 28, 35, 42, and 49 for free HSA (A) and HSA-glucose (B)

Fluorescence emission spectra for excitation 280 nm are then shown in Figure 6.4. Excitation at this wavelength will cause excitation of both Tyr and Trp in HSA. The change over time for both samples is shown in part A, and in all spectra fluorescence from both of these amino acids can be seen by the presence of a double peak, at 305 and 335 nm. In both samples the fluorescence intensity decreases over time, however this decrease is greater in the glucose containing sample. Figure 6.4B then shows a direct comparison of the normalised spectra from the two samples at various days, and although there is no shift in the peak wavelength, at later days (days 35 and 49) the HSA-glucose sample shows a decrease in the Trp fluorescence compared with that of HSA. This has been observed in a previous study[246]. Glucose binding in HSA may affect the conformation of the protein, and thus the

microenvironment of Trp. In turn, this could impact not only its direct fluorescence, but also affect the transfer of energy from Tyr to Trp to cause fluorescence, which often occurs in proteins[1].

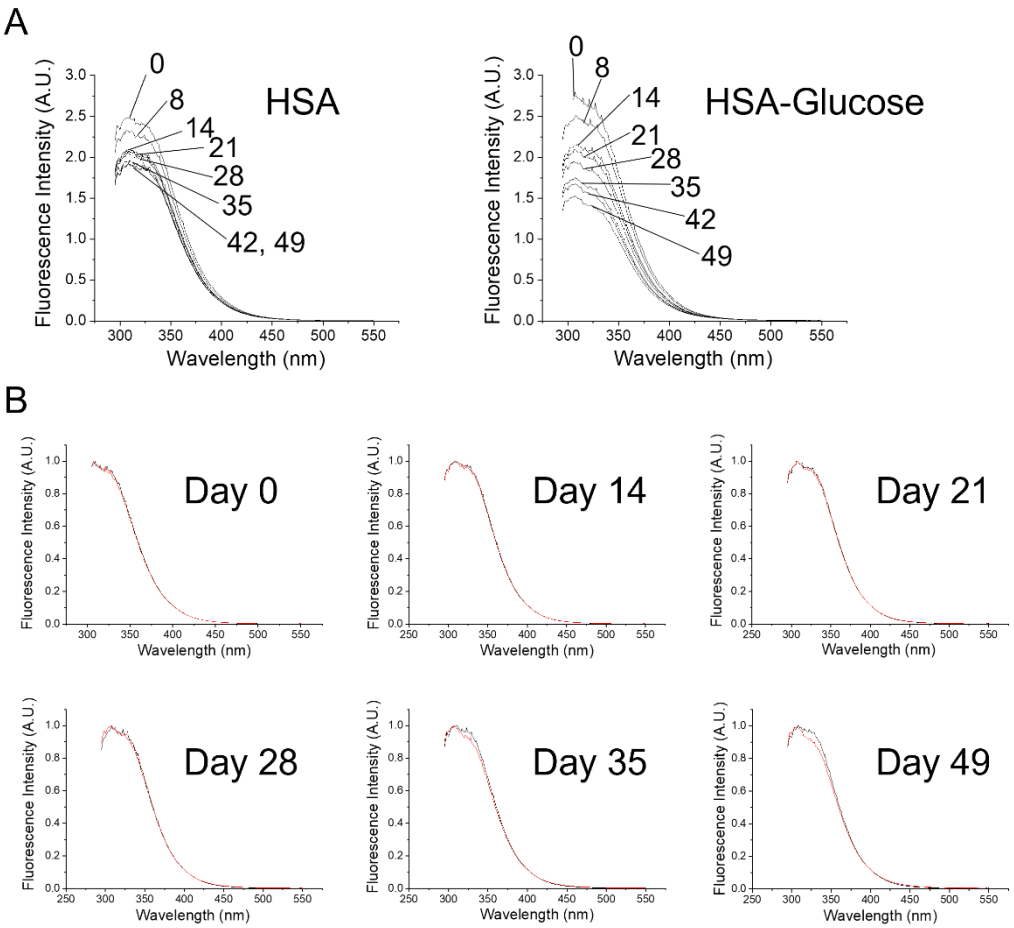

Figure 6.4. Fluorescence emission spectra for free HSA and HSA-glucose when excited at 280 nm. (A) shows fluorescence changes over time for HSA and HSA-glucose, and (B) shows HSA (black) and HSA-glucose (red) on days 0, 14, 21, 28, 35, and 49, with both samples spectra normalised to their peak fluorescence.

Excitation at 295 nm was also considered, and in this instance only Trp in HSA would be excited. The resultant spectra for the two samples are shown in Figure 6.5. Again, part A shows the change over time, and there is a decrease in fluorescence intensity as both samples age, however this decrease is greater in the HSA-glucose sample, in keeping with the previous result that suggests glycation causes a reduction in Trp fluorescence. A direct comparison of the normalised spectra on different days are shown in Figure 6.5B, and these plots show that

there is no shift in the peak emission wavelength over time, however a slight broadening of the spectrum can be seen on day 49 in the glucose-containing sample.

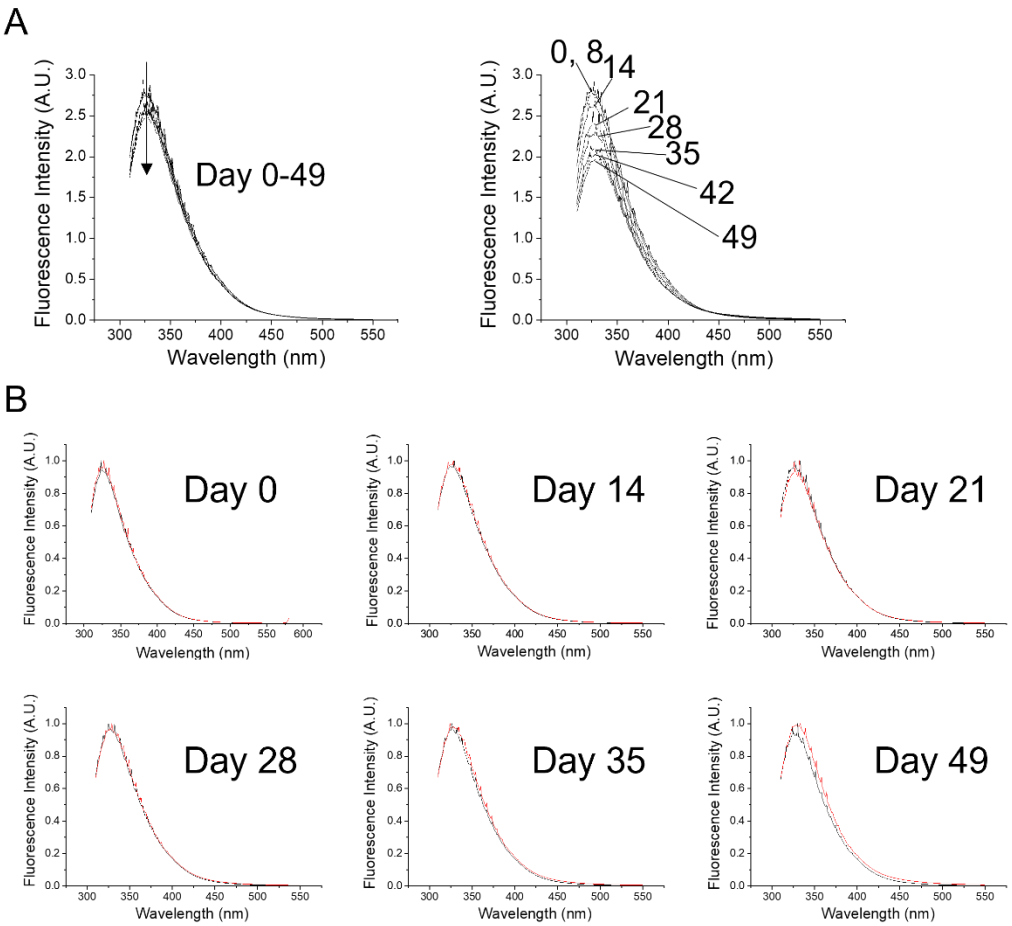

Figure 6.5. Fluorescence emission spectra for free HSA and HSA-glucose when excited at 295 nm. (A) shows fluorescence changes over time for HSA and HSA-glucose, and (B) shows HSA (black) and HSA-glucose (red) on days 0, 14, 21, 28, 35, and 49, with both samples spectra normalised to their peak fluorescence.

The steady state spectrum show that glucose accelerates the reduction in fluorescence intensity of HSA. This was confirmed in a repeat experiment, and so this outcome is not likely to be due to any instrumental or random errors. To more fully investigate the effect of glucose, time resolved measurements were carried out, in the first instance studying the fluorescence intensity decays.

First, the excitation wavelength 280 nm was used, and fluorescence decays were recorded at 340 nm, corresponding to peak Trp fluorescence[1]. The decays for both samples recorded on day 0, 28, and 49 are shown in Figure 6.6.

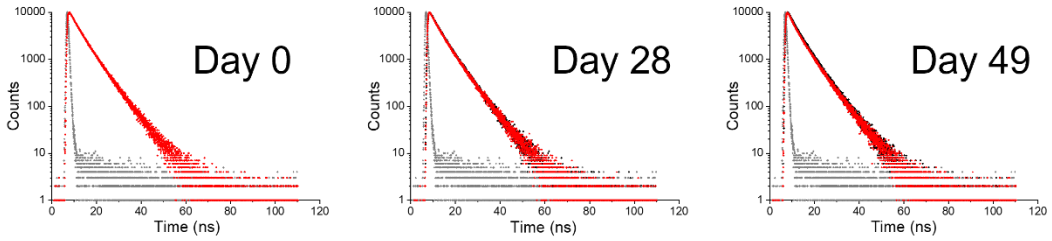

Figure 6.6. Fluorescence intensity decays detected at 340 nm, for excitation 280 nm, for HSA (black) and HSA-glucose (red) alongside the instrument response function (grey).

From inspection of the plots, there appears to be no discernible difference between samples, however to quantify this, the decays were fit to models of fluorescence decay (equation 2.29). For $I(t)$ both the classical multi-exponential model (equation 2.23) and the non-Debye model (equation 2.25) were used.

The fluorescence lifetime in HSA originates from Trp, as tyrosine fluorescence in native proteins is known to be effectively quenched[249]. A 1999 study[248] effectively fitted HSA decay to a 2-exponential model, however, more recent works[250,251] have determined that in HSA Trp has 3 lifetimes, two of which are thought to originate from the structure itself, and the third being the result of Trp interaction with the environment[252]. Interpreting fluorescence decay whereby a physical meaning is attributed to each exponential component however may be naïve. This may be true in some instances, but it is not always the case. In this research, after fitting to both a 2-exponential and 3-exponential model (eq. 2.23), a 2-exponential model (N=2) was found to be sufficient to describe all fluorescence decays on the basis of the goodness-of-fit criterion (χ^2) and the distributions of residuals (see examples of 2- and 3-exponential fitting in Appendix E1, Figures E1.1 and E1.2). Although the 3-exponential model does give slightly lower χ^2 values, the difference is not significant enough to justify the use of a 3-exponential model, which requires an additional 2 parameters.

The resultant parameters for fitting these decays to the 2-exponential model are shown in Figure 6.7. The τ plot shows a short lifetime component at ~3.6 ns and a long lifetime component at ~6.9 ns. Up until day 10, these values are very similar between samples, and relatively stable. After day 10, the value of the second lifetime component shortens gradually in the HSA-glucose sample, reaching 2.9 ns by the end of the experiment, while there is no change observed in the glucose-free sample. The contribution of each component remains

stable throughout the experiment, with the long and short lifetime contributing ~70% and 30% respectively in both samples.

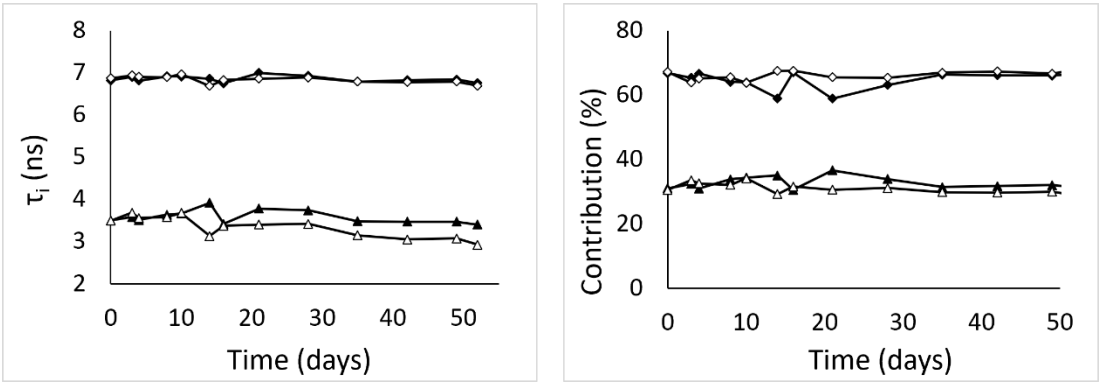

Figure 6.7. The resultant parameters from fitting the decays (excitation 280 nm) to the 2-exponential model for HSA (closed symbols), HSA-glucose (open symbols). The contribution of the scattered light to each decay has been left out for clarity.

The non-Debye model (equation 2.25) was also used to fit the decays in Figure 6.6, to determine if the fluorescence was decaying non exponentially, and if the impact of glucose could be seen more clearly. For all days for both samples, this model gave a good fit based on the χ^2 goodness-of-fit criterion and the distributions of residuals (see examples in Appendix E1, Figures E1.3 and E1.4). The χ^2 values were very similar to those obtained for the 2-exponential model.

Figure 6.8 shows the evolution of the three fitted parameters (α, κ, τ) for both samples as the experiment progresses. It should be noted that α is significantly less than 1 throughout the experiment, which does indicate non-exponential kinetics. In general, if a plot contains the exact same α and τ values, but different κ values neither of which exceed ~0.1, these plots are almost the same, and so changes in kappa below this value are not significant. This is the case in this fitting, where the small changes seen in κ are negligible.

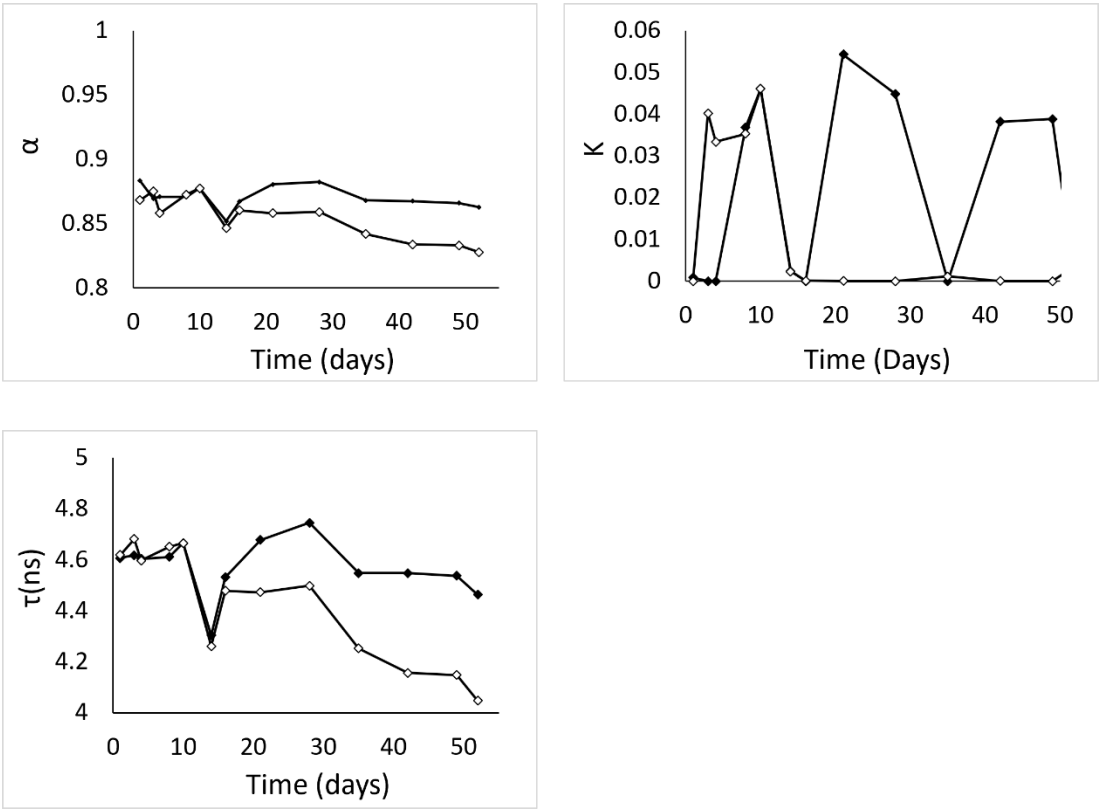

Figure 6.8. The resultant parameters from fitting the decays (excitation 280 nm) to the non-Debye model for HSA (closed symbols), HSA-glucose (open symbols).

Similarly to when fitting to the 2-exponential model, all parameters are similar between samples for the first 10 days. Differences begin to appear from day 14, which can be seen clearly in the α and τ plots. The α value remains relatively stable in the free HSA sample, while it decreases from ~0.86 to 0.83 in the HSA-glucose sample. A similar pattern can be seen in the lifetime value, where this decreases slightly from 4.6 ns to 4.5 ns in the free HSA, while the drop in the HSA-glucose sample is greater, reaching 4.1 ns by day 52.

Using this model, the impact of glucose on the fluorescence of HSA can be seen more clearly than when using the traditional multi-exponential model. However, we do note that there is some scatter in the data points, for example there appears to be an anomaly on day 14, which can be seen most clearly in the τ plot. As this drop in τ appears in both samples on the same day, we are inclined to discount this value, and simply consider it to be an error that occurred on this day, which could be due to a human error when carrying out the measurement or data processing, or a calibration error in the instrument. We do not consider it to be a result of any underlying process in the HSA or HSA-glucose samples. We do however accept the differences demonstrated in these plots over time, as there is consistency over the rest of the experimental time period. As such, and because the non-Debye model has a smaller

number of parameters, we would consider this an appropriate model to use to model the fluorescence intensity decays of HSA and HSA-glucose.

Fluorescence intensity decays were also measured for both samples on various days after preparation for the excitation wavelength 295 nm, where detected fluorescence is purely originating from Trp. These are presented in Figure 6.9. Again, no visible differences can be seen between samples from direct examination of the plots, and so these decays were fitted to the 2 models (multi-exponential and non-Debye) to determine if there was an impact of glucose.

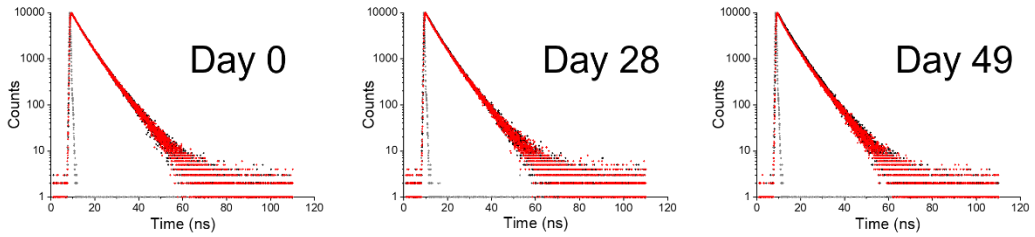

Figure 6.9. Fluorescence intensity decays detected at 340 nm, for excitation 295 nm, for HSA (black) and HSA-glucose (red) alongside the instrument response function (grey).

Firstly, the multi-exponential model was considered, and again a 2-exponential was found to be sufficient to describe the decays for both samples at all days (examples of the raw decays alongside the fitted parameters and plots of residuals for both a 2- and 3-exponential model are shown in Appendix E, Figures E1.5 and E1.6). The 3-exponential model appears to over parameterise the decay in some cases, shown by negative pre-exponential components (Appendix E, Figure 1.5), and adding an additional component did not significantly reduce the χ^2 values.

The evolution of the parameters of fitting to a 2-exponential model are shown in Figure 6.10.

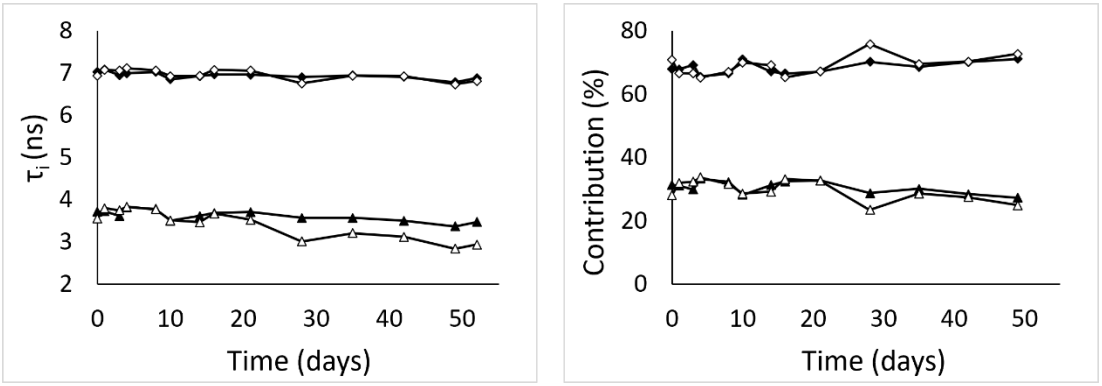

Figure 6.10. The resultant parameters from fitting the decays (excitation 295 nm) to the 2-exponential model for HSA (closed symbols), HSA-glucose (open symbols). The contribution of the scattered light to each decay has been left out for clarity.

This follows the same trend as was observed at excitation 280 nm, where there is one short lifetime component (~3.6 ns) and one long lifetime component (~7 ns), and these remain stable and equal between samples during the first 10-14 days. After 14 days, the short lifetime component decreases gradually in the sample containing glucose, while there is no change in the free HSA sample. This contradicts what was observed previously in a 1999 study[248], where a 2-exponential model was used, and glycation was found to increase both the short and long lifetime components. There is no difference between samples, or change over time in the contribution of each component, with the long and short component contributing ~70% and ~30% respectively.

The similarity in lifetime values and behaviour between these results and those observed for excitation at 280 nm, strengthens previous conclusions that Trp is the dominating fluorescence in HSA, and that Tyr has little influence.

Next, the non-Debye model was fit to the fluorescence decays, and the evolution of the three fitted parameters are shown in Figure 6.11 (see Appendix E1, Figures E1.7 and E1.8 for examples of raw decays, fitted values, and plots of residuals).

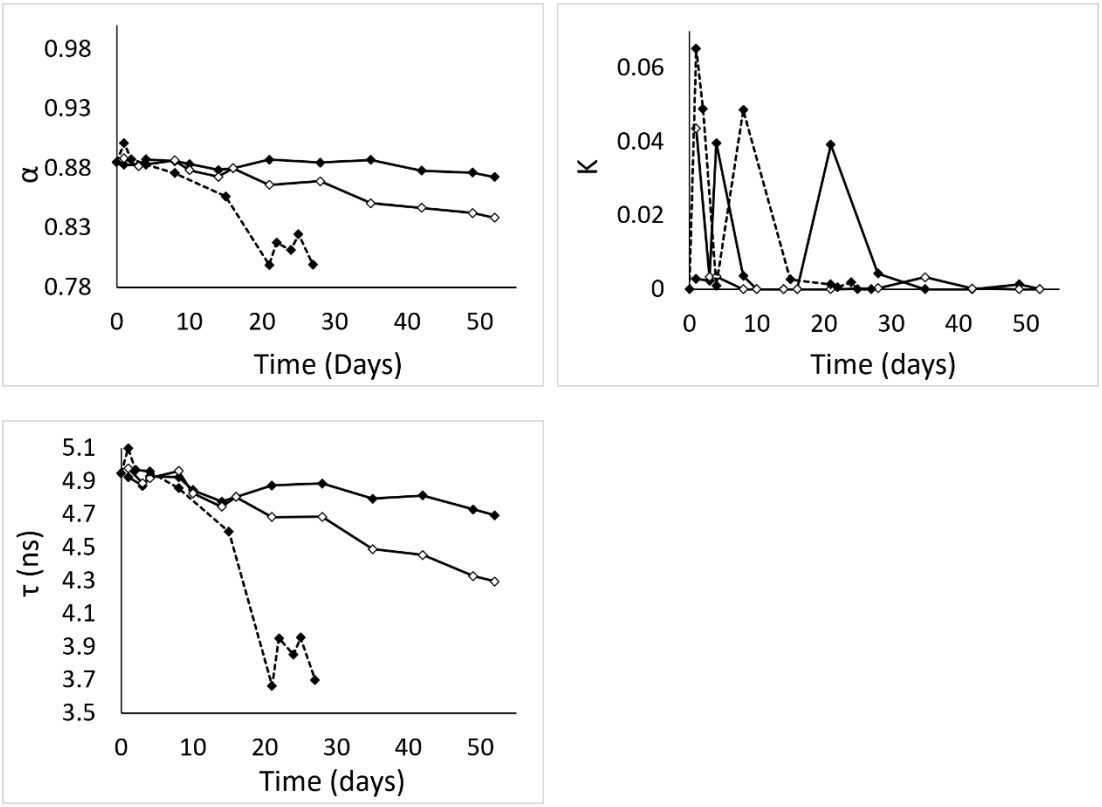

Figure 6.11. The resultant parameters from fitting the decays (excitation 295 nm) to the non-Debye model for HSA (closed symbols), HSA-glucose (open symbols), and HSA-fructose (dashed line).

All χ^2 values were less than 1.20, with the residuals randomly distributed around 0, indicating a good fit. Again, the α value is significantly less than 1 for both samples, suggesting that Trp is decaying non exponentially. The κ values are less than 0.1, and so the differences in this parameter between samples and over time are negligible, and do not signify any changes in the sample. This result follows the same pattern as excitation 280 nm, where both the α and τ value begin to decrease gradually in the HSA-glucose sample after 10-14 days, while they remain stable in the free HSA sample. The fitted parameters for a HSA-fructose sample are also included in these plots, and here the effect of sugar is even more pronounced, illustrated by a greater decrease in both of these values. Fructose is known to cause glycation at a faster rate than glucose[253], which explains why the changes in the fitted values manifest earlier. When compared to the non-Debye fitting for decays at excitation 280 nm, fitting for decays at excitation 295 show a more stable trend, which we expect is due to the more simple kinetics involved, i.e. there is no Tyr which may influence the fluorescence at this excitation wavelength.

This analysis on the fluorescence intensity decays show that the impact of glucose on HSA can be detected using Trp fluorescence, and its influence is more clearly seen when a non-Debye model is used to fit the decays.

Finally, TRES were obtained for HSA and HSA-glucose samples on day 0 and day 52, and these spectra are illustrated in Figure 6.12.

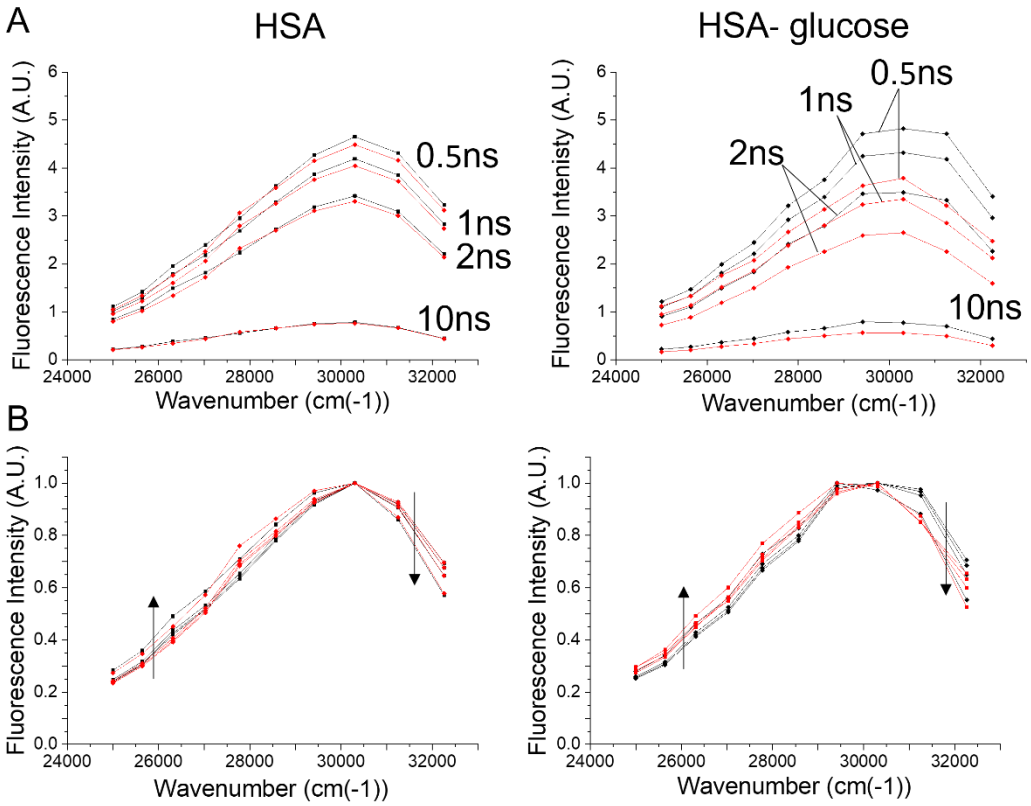

Figure 6.12. TRES spectra of free HSA (black) and HSA-glucose (red) on day 0 and day 52 (A) for excitation 295 nm. (B) shows the same spectra after normalisation.

At day 0, where no effect of glycation is yet expected, the TRES for both samples is extremely similar, with the fluorescence intensity decaying gradually within nanoseconds. The corresponding normalisation plot (Figure 6.12B) shows no change in the shape of the spectra during the decay for either sample, indicating that there are no ns time scale processes occurring. Both samples show a peak at ~30300 cm^{-1} (~330 nm), which corresponds to Trp peak emission[1]. The TRES for day 52 then shows clear differences between the 2 samples: the fluorescent peak in the free HSA sample flattens, stretching from 330 to 340 nm, while the peak wavelength remains unchanged in the glucose containing sample. The HSA-glucose

sample also shows a reduction in fluorescence at higher energies compared to that of free HSA, which is most clear in the related normalisation plot (Figure 6.12B).

6.4. Conclusion

In this chapter, the response of HSA to glucose has been studied using various fluorescence spectroscopy techniques. Tryptophan is the dominating fluorophore in this protein, and changes to its intrinsic fluorescence can be detected using both steady state and time-resolved fluorescence techniques. We believe that the time-resolved measurements such as fluorescence intensity decays and TRES are of more relevance, as more information can be obtained, and results are independent of concentration, which could affect fluorescence intensity in steady state measurements.

Our fluorescence intensity decay analysis indicates that glycation can be detected through a decrease in the short lifetime component when decays are fitted to a 2-exponential model. Fitting to a non-Debye model, however, more clearly highlights the impact of glucose, shown by a significant reduction in both the α and τ value. The ability of the non-Debye model to fit these decays with a α value significantly lower than 1, may also indicate that in HSA, Trp decays non exponentially. A non-Debye model may be more suitable in this type of molecular system, as it is able to represent a stable distribution of fluorescence lifetimes, rather than simply the presence of 2 or 3 distinct lifetimes, which is the case with the multi-exponential model.

To conclude, the intrinsic fluorescence of HSA is sensitive to glycation in an *in vitro* experiment set up. This could potentially pave the way for developing a non-invasive method to detect glycated HSA in blood via a fluorescence-based sensor, as a method for monitoring long term glycaemic control in patients with diabetes.

7. In-vivo Fluorescence: Fluorescence of Skin

7.1. Summary of In Vitro Findings

It is useful at this stage to summarise the *in-vitro* findings already discussed, to provide some clarity on where to look for the impact of glucose in *in-vivo* measurements. A table summarising this information is presented in Table 7.1.

Table 7.1. The effects of glucose on the intrinsic fluorescence characteristics of Collagen, NADH (in Trizma), Keratin, and HSA. The λex(nm), λem(nm) and 'time-resolved fluorescence parameters' columns show the values obtained from the sample without glucose at day 0 (or in the case of collagen over time). The two 'effect of glucose' columns contain values obtained at the last day of the experiment in the glucose-containing sample. Contributions of scattered light to decay parameters and standard deviations have been omitted for clarity.

	λex(nm)	**λem(nm)**	**Effect of Glucose on Fluorescence Emission**	**Time-resolved Fluorescence Parameters**	**Effect of Glucose on Time-Resolved Fluorescence**
Collagen	280 (Tyr)	305 (Tyr)	Narrows emission spectra, due to glucose limiting collagen aggregation.	TRES show systematic red spectral shift over time.	Reduced spectral shifts shown in TRES, due to glucose limiting collagen aggregation
	340 (pepsin-digestible cross-links)	405 (pepsin-digestible cross-links)	Increases fluorescence intensity. Shifts peak wavelength: λem at day 0: 425 nm Due to glucose causing formation of a single type of collagen cross-link.	TRES models show: • monotonic red shift in $v(t)$ parameters. • No discernible pattern in decay rates	TRES models show: • red shift in first 2ns for $v(t)$ parameters • decreasing decay rates over time.
NADH	350	460	NA	Multi-exponential model: τ_1 =0.38 (63.34%) τ_2 =0.76 (16.21)	NA
Keratin	295 (Trp) 350 – 370 (cross-links)	305 (Trp) 460 (cross-links)	Increases intensity at 305 nm and 460 nm due to faster formation of new cross-links. Causes formation of fluorescent residues with peak wavelengths at 525 nm and 575 nm	Multi-exponential model: τ_1= 0.54 (11.5%) τ_2= 2.81 (25.33%) τ_3= 8.75(19.20%)	Increases contribution of longer lifetime components: τ_1= 1.05 (3.66%) τ_2= 5.41 (40.39%) τ_3= 12.4 (47.49%)
HSA	280 (Tyr) 295(Trp)	305 (Tyr) 340 (Trp)	Decreases intensity	Non Debye model: $\alpha = 0.88$ $\tau = 4.61$	Decreases τ and α values: $\alpha = 0.83$ $\tau = 4.05$

As outlined in this table, while our *in vitro* results show that NADH cannot be used to monitor glycation, there is potential for the other three molecules studied. Firstly in collagen, a narrower steady state emission spectra, or a shift in the peak fluorescence emission from 405 nm to 425 nm could indicate glycation. TRES measurements and TRES modelling would more clearly highlight any impacts of glucose, for example if the expected spectral shifts aren't present when exciting at 280 nm (indicating glucose inhibiting collagen aggregation). When exciting at 295 nm, a stable trend of decreasing decay rates over time alongside a red shift in the first 2ns following excitation for the peak wavelength may also indicate glycation.

For keratin, formation of new fluorescent peaks at 525 nm or 575 nm, and an increase in the fluorescence lifetime (in particular an increased contribution of the two long-lifetime components when the fluorescence intensity decay is fit to a multi-exponential model) could indicate glycation.

Finally, for HSA, glycation may be inducated by a decrease in the fluorescence lifetime, shown by a decrease in τ and α values when the fluorescence intensity decay is fit to a non-Debye model.

In the following studies, the changes described above would indicate that glycation is taking place, and would thus suggest that fluorescence spectroscopy can indeed monitor this process.

7.2 Introduction

Skin is the largest organ in the body, responsible for over 10% of the body mass in an average person. Its primary function is to protect the internal organs from the external environment, providing a barrier against radiation, chemicals, allergens, and bacteria. It also has an important role in maintaining heat regulation and blood pressure control, in addition to its sensory function: through the skin a person can feel heat, pain, and pressure among many other sensations. The skin is therefore essential to survival, and it is in a constant state of regeneration and repair.

7.2.1 Skin Structure

7.2.1.1 Human Skin Structure

The skin consists of 4 primary layers: the stratum corneum, the viable epidermis, the dermis, and the subcutaneous tissue. Total skin thickness varies greatly depending on location, with the skin at its thinnest in the upper medial eyelid[254], and thickest in regions such as the soles of the feet.

A diagram of the skin structure is shown in Figure 7.1. The stratum corneum, or non-viable epidermis, is the outermost layer of the skin, and is the main protective barrier between the body and the external environment. Various studies have shown it to be approximately 10–30 µm thick[255], consisting of flattened, stacked, hexagonal, and cornified cells embedded in a mortar of intercellular lipid[256]. The cell thickness across the stratum corneum can vary, with cells in areas of the body with substantial physical contact with the environment, for example the soles of the feet, being significantly thicker. At the volar side of the forearm, which is where we envision any fluorescence measurements occurring, this skin layer is approximately 65 - 100 µm[257]. The stratum corneum consistently renews, with a total turnover occurring every 20 days[258], which helps it to function as a barrier layer.

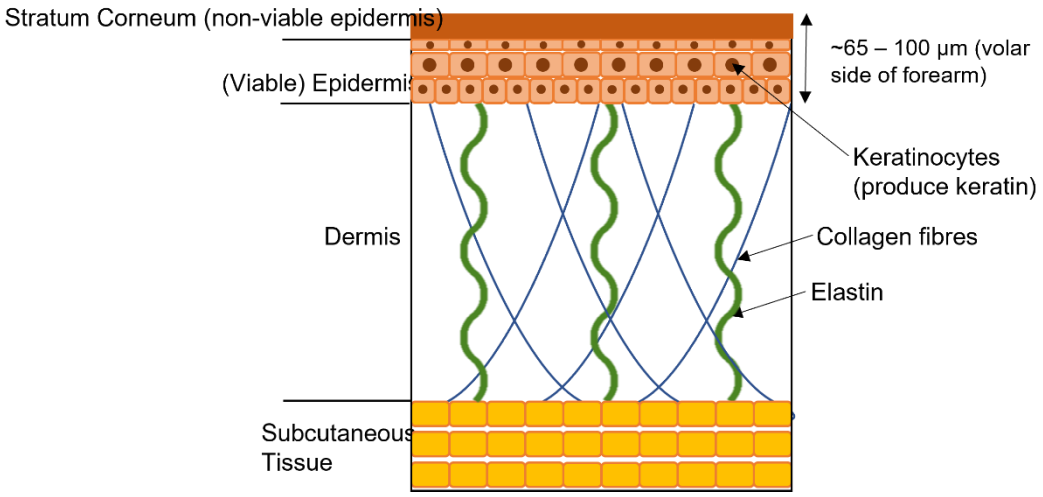

Figure 7.1 Schematic of human skin, showing the 4 structural layers (the stratum corneum, the epidermis, the dermis, and the subcutaneous tissue), alongside fluorophores of interest keratin and collagen.

The next outermost layer underneath the stratum corneum is the viable epidermis, and one of the most important functions of this layer is to generate the stratum corneum. The viable epidermis is multi-layered, consisting of (from outermost to innermost layer) the stratum lucidum, the stratum granulosum, the stratum spinosum and the stratum basale. The viable epidermis consists primarily of keratinocytes[259], alongside Merkel cells, Langerhans cells, and melanocytes. Its thickness can vary, with the thickest part being on the soles of the feet where is can be up to ~1.3 mm thick[260].

The dermis of the skin is below the epidermis and is 0.6 – 3 mm[261] thick depending on location. It consists of collagen fibres which provide support, and elastin connective tissue that provides flexibility[259]. These are embedded within a matrix, which itself has a sparse population of cells including mast cells, fibroblasts, and melanocytes. The dermis also has a vast vascular system, which is used to help regulate body temperature, and to transport oxygen and nutrients to, and remove waste products from tissues. The vasculature also helps to enable wound healing and the immune response. The dermis also contains nerve endings, hair follicles and sweat glands.

The final innermost layer of the skin is the subcutaneous tissue, or the hypodermis. Essentially this is a layer of fat cells connected by collagen and elastin fibres. The primary function of this layer is for insulation, and protection from physical shock.

Various fluorophores can be found in the skin, and in this work we have studied three in detail *in vitro*: collagen, NADH, and keratin. These can be seen in Figure 7.1, and their location

and depth within the skin is important to note, as it gives an approximate depth that any excitation light must penetrate to excite these fluorophores. Collagen can be found in the dermis and in the subcutaneous tissue, NADH can be found in practically all cells[262], (in the mitochondria, cell cytosol, and nucleus[263]) and so is present in all four layers of the skin, and keratin can be found in the epidermis[264].

Considering skin thickness at the volar side of the forearm, as this is the site that would most likely be used for any in-vivo fluorescence measurements on humans, a paper from 2016[257] lists various studies that measured the epidermal thickness of this site. The thickness ranged from 65.1 µm[265] in a study by Trojahn et al. in 2015, to 102.4 µm[266] in 2011 by Jose et al. We therefore assume light must penetrate deeper than 100 µm to excite and detect fluorescence from collagen, and the penetration depth can be less when looking to detect NADH or keratin fluorescence.

The penetration depth of light is limited due to absorption and scattering, and it is highly dependent on wavelength and skin site[267]. Infrared light can travel furthest into the skin, with the depth reducing as the wavelength of light decreases[268]. When incident light is less than 290 nm, it's penetration depth is approximately 20 µm[267] (at the volar side of the forearm), and thus effectively limited to the epidermis[68]. It is therefore able to excite NADH and keratin. Incident light at higher wavelengths can penetrate deeper, and indeed previous studies have shown the ability to detect fluorescence of dermal origin[68]. Collagen, which is present in the dermis, can therefore be detected when the incident light is at higher wavelengths, for example, light at 330 nm can reach 65 µm[269] into the skin with an intensity equal to 37% of the original intensity.

7.2.1.2 Mouse Skin Structure

Briefly, it is appropriate to touch on the differences between human and mouse skin, as mouse models are often used to study skin fluorescence in-vivo. While the two skin types are very similar, and have the same four layers mentioned previously, there are some anatomical and physiological differences.

One of the primary differences is skin thickness: humans have much thicker skin, while in mice total skin thickness is less than 25 um. In the epidermis for example, human skin consists of 5-10 keratinocyte layers, while in mice this is only 2 or 3[270]. The lower number of cell layers in mouse skin decreases its barrier functionality, but enhances its ability for percutaneous absorption. Previous work has shown that excitation light at 295, 335, and 370 nm has been

used to detect fluorescence from both the epidermis and the dermis in mice[68], showing that the thickness is within an appropriate range for fluorescence applications.

A further major difference between mouse skin and human skin is that mouse skin is covered in dense hair. Subsequently, there are a much greater number of hair follicles in mouse skin[271], and mouse hair has a much faster hair cycle than human hair (2-3 weeks vs several years)[272]. Mouse skin also lacks the apocrine sweat glands and dermal papillae (protrusions of dermal tissue into the epidermal layer) that are found in human skin. Finally mouse skin contains a thin layer of muscle known as the panniculus carnosus, which is only found in the neck of humans. This allows much more rapid wound healing following injury.

Despite these differences, there are enough similarities between human and mouse skin that mouse models are appropriate for studies of skin fluorescence. Previous work has shown that excitation spectra from mice and human skin are almost identical for excitation wavelengths less than 400 nm[69], and so this strengthens the reasoning behind using mice for this application.

7.2.2 Auto-fluorescence of Skin

The skin has many endogenous fluorophores that have been reviewed in earlier sections, and so will not be discussed in great detail here. Briefly, some fluorophores that are found in the skin include collagen, elastin, NADH, FAD, porphyrins, flavins, pheomelanin and eumelanin, tryptophan, and keratin, which are all auto-fluorescent. The excitation and emission peak wavelengths of the principal skin fluorophores of interest in this thesis were outlined in Chapter 1, Table 1.1. Various studies have measured the fluorescence of these fluorophores *in-vivo*[69, 218, 273], *ex-vivo*[69, 218, 273, 274], and clinical settings[275].

There are some difficulties that arise when measuring intensity of skin fluorescence, due to interference from other components. Melanin absorbs light, and so can suppress fluorescence intensity from other sources. This means that changes in skin colour due to sunburns, or even differences in race can affect analysis. For example, a preliminary study showed that the fluorescence intensity in the forearm was inversely correlated with melanin content[276]. Another component that can interfere with fluorescence intensity measurements in skin are pigments in the blood such as haemoglobin, and a preliminary study by Yamanaka in 2016[276] showed that the presence or absence of veins at the measurement site influenced results. The intensity at skin with veins approximately 1.5 times greater than the intensity at skin without veins.

7.2.3 Relationship Between Skin fluorescence and Other Biomarkers of Diabetes

As discussed in the introduction of this thesis, there is a significant amount of evidence showing the relationship between skin fluorescence, AGE levels, and diabetes complications[77, 148]. The 2 devices validated for skin AF measurements have shown that AF levels are comparable to the classical HbA1c test in detecting abnormal glucose levels[4,78], and there is also evidence that shows skin AF is correlated to HbA1c. Studies have shown skin AF to correlate with mean HbA1c of the previous year[77], with mean HbA1c over the last 5-10 years[277], and have shown log(SIF) to be significantly associated with mean HbA1c over time[278]. In 2013, Sugisawa et al also showed a correlation between skin fluorescence and HbA1c, however in this instance skin AF correlated with the area under the HbA1c curve over the past 15 years[279].

These studies show that skin AF can be correlated with HbA1c over time, but there is no significant relationship with the most recent HbA1c level. This is most likely due to the difference in the turnover time of the two tissue types. AGEs in the skin form on proteins such as collagen that have a very slow turnover time (up to 10 years[131]), and so the fluorescent AGEs found there capture glycaemic levels over the past decade. HbA1c however is found in blood, which has a very fast turnover rate, and therefore this marker only reflects a period of 12-16 weeks[138]. Skin AF therefore has potential as a long-term marker of glycaemic control, that is comparable to HbA1c, and can take into account a longer time period.

There is also a relationship between skin autofluorescence and complications of diabetes. For example, multiple studies have shown a correlation between skin AF and diabetic retinopathy, nephropathy, and/or neuropathy[277, 279, 280]. Furthermore, a study from 2018 showed that higher baseline skin AF was significantly associated with an increased risk of a major adverse cardiovascular event in patients with T1DM[281], and in 2019 a study that had measured skin AF 4 years prior to a follow up showed that the baseline skin AF was higher in those who developed T2DM, compared to those who did not develop the disease[282]. This suggests that skin AF can be used to predict the development of T2DM, as well as the onset of complications of the disease.

Skin AF has potential as a biomarker for diabetes control and could be used to predict the onset of diabetes or its associated complications. In this section we carry out initial studies on animal and human tissues using various spectroscopy techniques, in order to more fully

understand the glycation process, and how fluorescence could be used to best detect the AGEs.

7.3 Initial Pilot Study (Steady State Only)

7.3.1 Methodology

An initial pilot study was carried out to determine if fluorescence could be detected and matched to the expected emission peaks that are of interest for monitoring glycation (for example, those corresponding to collagen's pepsin-digestible cross-links, NADH, or keratin). We also used this opportunity to optimise the experimental parameters.

We recorded the steady state fluorescence emission from mouse skin *in vivo*, and for this pilot study, four mice were included. The mice were dosed with Streptozotocin (STZ), which is an antibiotic that produces pancreatic islet β-cell destruction, and so produces a model of T1DM.

Hypoglycaemia was expected 8 to 24 hours after the mouse was dosed with STZ, and so the mice were given 10% sucrose water to drink. This is important as the initial β-cell destruction causes an excess release of insulin into the bloodstream, and so the sucrose water prevents potentially fatal hypoglycaemia. After 48 hours the blood glucose level of each mouse was measured, and if the mouse was hyerglycaemic, the sucrose water was discontinued and the mouse was returned to normal drinking water. Blood glucose was measured daily for each mouse in order to monitor the severity of diabetes and so that any deterioration in health could be addressed immediately.

Corrected fluorescence emission spectra were recorded on a SkinSkan (Horiba Scientific), using an excitation wavelength of 340 nm, with fluorescence emission measured between 360 and 480 nm. These parameters were chosen to excite and measure the fluorescence from pepsin-digestible collagen cross-links, as our in vitro protein studies showed that their fluorescence changes significantly through interaction with glucose. The slit width of the monochromators was set to 5 mm, and the integration time was 0.5 ns. The spectra had a resolution of 2mm, which was chosen to speed up the data acquisition time. This was important as the mice remained awake during the fluorescence measurements, and we did not want to cause them stress.

The SkinSkan was calibrated directly before each measurement was taken, in order to ensure no instrumental errors were present in the results. Directly before the measurement was taken, a small patch of fur on the back of the mouse was shaved, the approximate position of which is shown in Figure 7.2. The mouse was held still, and the SkinSkan probe was held directly onto the exposed skin. The measurement was recorded three times and the result averaged, in order to reduce any random errors in the measurement process due to the mouse moving. All the lights in the room were turned off during the measurements to reduce any light from other sources. The first measurement was taken 90 days after the mice had first been dosed with STZ, with subsequent measurements on various days over the following month.

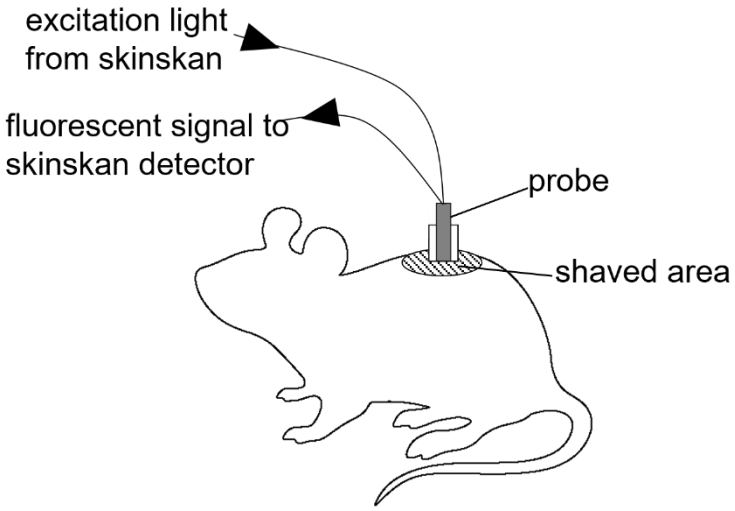

Figure 7.2 Diagram showing the excitation/emission probe placement on the mouse skin for fluorescence measurements.

7.3.2 Results and Discussion

Figure 7.3 shows the fluorescence emission spectra obtained from the skin at day 90, when the excitation wavelength was 340 nm. Part A shows 3 separate spectra from one mouse, that were then averaged, and in most cases each spectra show 3 peaks. The consistency in these peaks shows that there is a robustness and repeatability in the experimental procedure, which gives confidence that the results are scientifically sound. Figure 7.3B then shows the spectra on day 90 for 4 different mice: the spectra are reasonably similar, and 3 peaks can be seen in the majority of spectra measured. Again, this demonstrates the robustness of the experimental techniques used in this study.

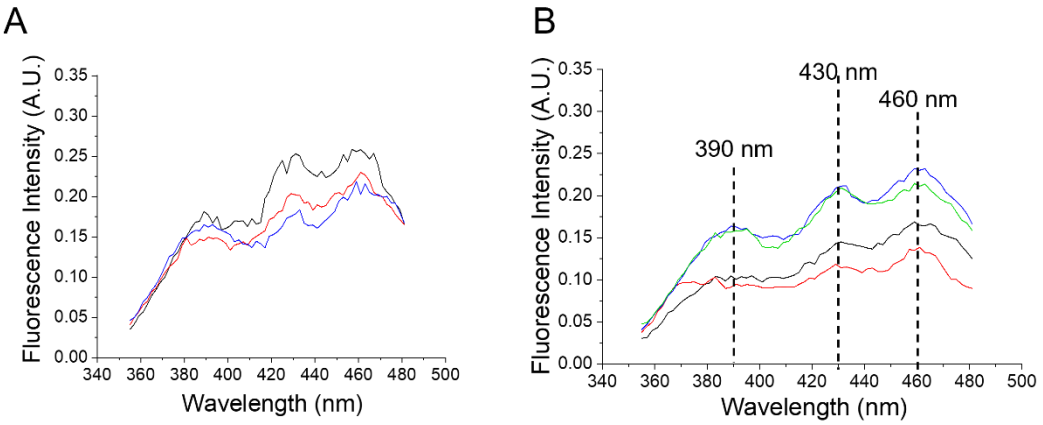

Figure 7.3 Fluorescence emission spectra from mouse skin for excitation 340 nm. Part A shows the 3 spectra recorded from one mouse, and Part B shows the average spectra from 4 different mice, all on day 90.

The first of these occurs at 390 nm, and this is within the range of expected fluorescence from pepsin-digestible collagen cross-links[68]. The second peak in the spectra can be seen at approximately 430 nm, and this may originate from collagenase-digestible cross-links in skin collagen, although their peak wavelength is known to be 440 nm[146]. The final peak seen in Figure 7.3 occurs at 460 nm. There are multiple skin fluorophores that fluoresce at this wavelength, for example NADH and keratin crosslinks. The keratin crosslinks however require a slightly higher excitation wavelength (370 nm), and so we hypothesise that this fluorescence is from NADH.

To monitor how the skin fluorescence changed over time, we measured the fluorescence again at day 97, day 100, and day 107. This result for each individual mouse is shown in Figure 7.4A, B, C, and D.

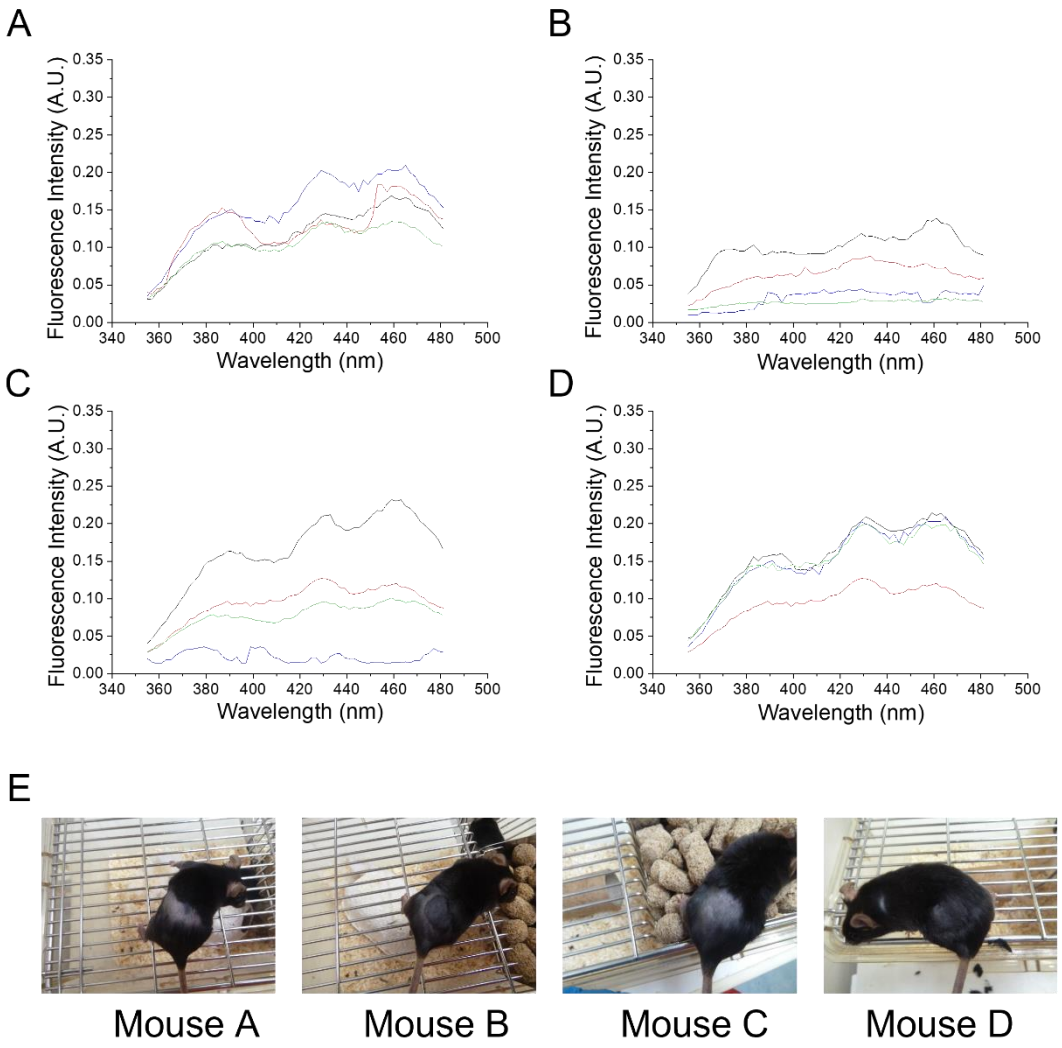

Figure 7.4 Part A shows fluorescence emission spectra from mouse skin for excitation 340 nm, with plots A, B, C, and D showing the result from mouse A, B, C, and D respectively.. The result on day 90 is shown in black, day 97 in red, day 100 in blue, and day 107 in green. Part B shows a photograph of each mouse, with the shaved patch of fur.

In most of the spectra, the 3 peaks can still be seen clearly, showing reliability in the experimental protocol. In addition, the fluorescence intensity seems to be consistent across 3 mice, excluding mouse B. The reason for the, on average, lower fluorescence intensity from this mouse may be explained in Figure 7.4E, which shows photographs of each mouse. Mouse B has dark pigmentation that can be seen in this exposed area of skin, which may be

absorbing the excitation light. This would decrease the intensity used to excite the fluorophores of interest, resulting in a lower fluorescence intensity in this range.

In terms of a trend over time, no clear pattern is observed, with the intensity of the spectra fluctuating over the 4 days of measurements. The shape however remains consistent, with the peaks staying in position. The reason for not seeing a change over time in these steady state spectra may be due to start point of the study: at 90 days, glucose may have already influenced the intrinsic fluorescence of the skin proteins of interest (keratin, collagen, NADH), and so we were not able to capture the change in fluorescence that would have occurred earlier. Fluorescence measurements from day 0 will be essential to accurately monitor any changes in the intrinsic skin fluorescence due to glucose and diabetes. We would expect, from previous studies[6, 60], that the fluorescence intensity increases (fromskin collagen and skin keratin) as the experiment progresses and the diabetes becomes more severe. Additionally, from our *in vitro* work we may expect to see new peaks forming at 525 nm and 575 nm, as keratin reacts with glucose to form new fluorescent residues.

Analysis was then carried out to determine if there was a relationship between skin fluorescence and blood glucose levels, which we considered an indicator of severity of diabetes. From literature, as discussed in Section 7.2.3, skin fluorescence is known to correlate with various measures of diabetes severity, such as mean HbA1c over the previous year, and duration of diabetes. As with this experiment blood glucose was used to monitor disease severity, we considered this an appropriate relationship to investigate. Figure 7.5 shows the plot of this relationship. The area under the curve for blood glucose from day 0 to day 107 was calculated, and plotted against the skin fluorescence at 390 nm (fluorescent peak which we believe corresponds to pepsin-digestible collagen cross-links) on day 107. With only 4 data points it is difficult to see a clear trend, however if point B is discounted (as this is the mouse with the highly pigmented skin which affected the result) the plot shows that as the area under the blood glucose curve increases, skin auto-fluorescence increases. However, the error bars, illustrating the standard deviation of the fluorescence intensity, indicate that this relationship may not be true, and many more samples are required in order to prove this relationship. Nevertheless, this is a promising result, and a finding which we hope can be strengthened in the subsequent study.

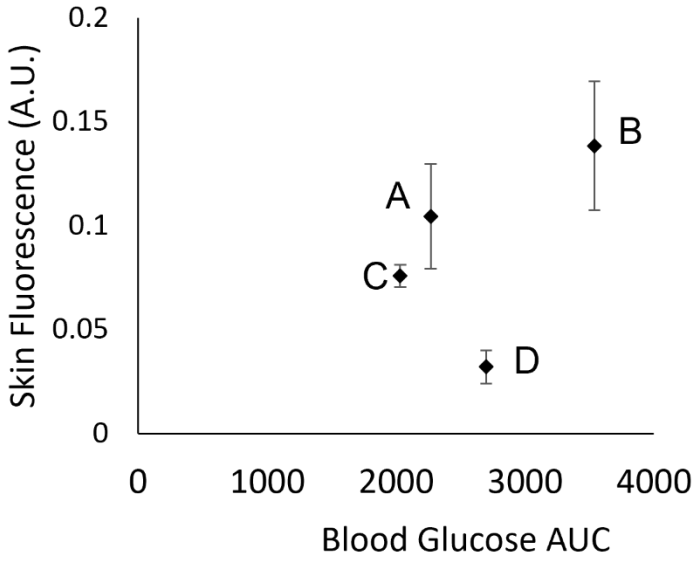

Figure 7.5. Plot showing the relationship between blood glucose (area under blood glucose curve from day 0 to day 107) and the final skin fluorescence intensity (day 107) at 390 nm for four mice. The skin fluorescence values are the mean of three measurements, and the error bars show the standard deviations.

This initial study allowed us to optimise the experimental parameters for the steady state measurements. These results were used to plan a longer-term study, which incorporates fluorescence measurements from day 0, and uses other methods of glycaemic control such as HbA1c for to try and establish a relationship.

7.4 Long Term Study (With Time-Resolved Measurements)

A long-term study was planned to determine if the fluorescence emission spectrum from mice with diabetes evolved as their disease became more severe. Alongside the steady state measurements, time-resolved measurements were to be carried out on tissue samples from these same mice, to obtain further information of the glycation process in the skin proteins.

7.4.1 Methodology

7.4.1.1 Study Overview

A total of 18 (n=18) CD1 mice were included in this study. This breed is albino, and therefore this will negate the problem of any dark skin pigmentation potentially affecting the fluorescence results. A total of 18 mice were included in this study, and were split into 3 groups: a control group (n=6), a low dose group (n=6), and a normal dose group (n=6). This will give a range of disease severity, and will help to establish any correlations.

All mice were dosed with Streptozotocin (STZ) on day 7 of the study. A control group of completely healthy mice was not approved for this study, and so an extremely low dose

group was used instead. The dose given (50 mg/kg) was not expected to cause pancreatic islet β-cell destruction and thus lead to diabetes, providing an almost perfect control group for the study. The second group, the low dose group, received 50 mg/kg of STZ on three consecutive days (150 mg/kg total). This was likely to cause diabetes, however would result in a less severe form of the disease than was expected in the normal dose group, who received 140 mg/kg of STZ once.

The overview of the experiment is shown in Figure 7.6. Steady state fluorescence measurements were carried out on day 0, before the mice had been dosed with STZ. The mice were dosed with STZ as described above on Day 7, (and on Days 8 and 9 for the low dose group), in order to create models of T1DM in the mice. At 7 day intervals (Day 0, Day 7, Day 14 etc) steady state fluorescence measurements and , blood samples were taken from each mouse and frozen for later analysis of HbA1c content. This would allow us to establish if there was a correlation between skin fluorescence and a long-term marker of glycaemic control. Like in the initial study, blood glucose measurements were taken daily for the duration of the experiment in order to monitor the severity of diabetes, and also the health of the mice.

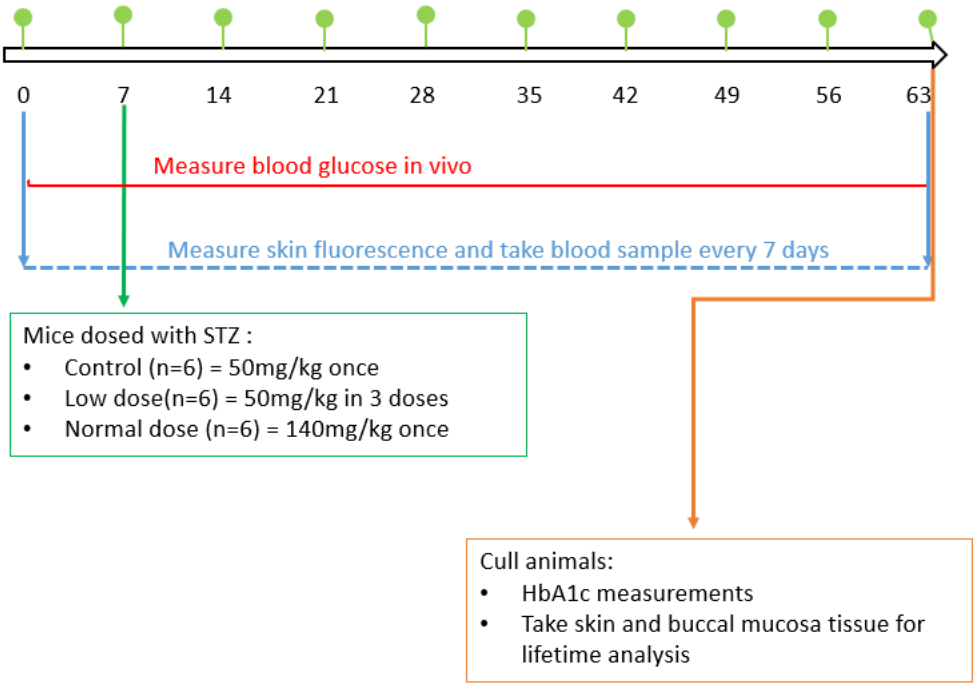

Figure 7.6. Study overview for the long term study looking at in vivo skin fluorescence in mouse skin, showing the time point where the mice are dosed with STZ (day 7), when fluorescence measurements and blood samples are taken (green symbols), when blood glucose is measured, and the end point of the experiment. .

At the completion of the *in vivo* stage of the study (63 days), the animals were culled and a final HbA1c reading was carried out. Tissue from the skin and the buccal mucosa were also then taken for fluorescence lifetime analysis.

7.4.1.2 Fluorescence Measurements

Corrected fluorescence emission spectra were recorded weekly from day 0, using a SkinSkan (Horiba Scientific) with an excitation wavelength of 340 nm, and a measurement range of 360 - 440 nm. All instrumental parameters (slit width, integration time, and resolution) remained the same as for the initial pilot study. Prior to each measurement, a patch of fur on the mice's back (see Figure 7.2) was shaven to expose the skin.

Fluorescence intensity decay measurements were carried out at the end of the study on the skin and buccal muccosa tissue samples. These were performed using liquid light guide-based fluorescence lifetime system, which was developed from a Horiba TemPro system. The equipment is illustrated in Figure 7.7. The working principle of this system is the same as the Horiba Deltaflex System described earlier in this thesis, in that is uses TCSPC to measure fluorescence decay.

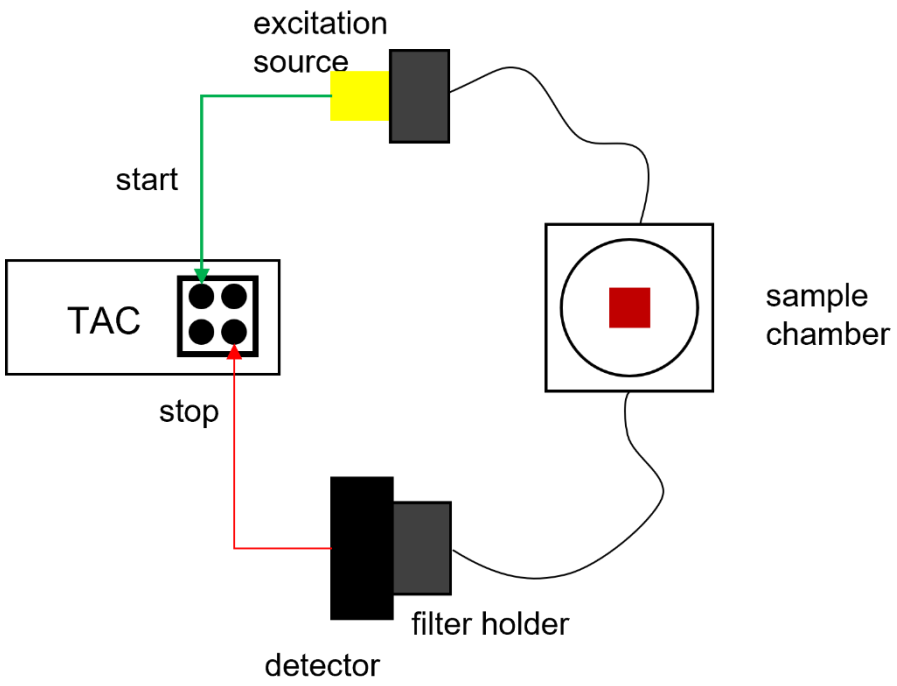

Figure 7.7 Schematic of the modified Horiba TemPro system used to measure fluorescence intensity decays from the mouse tissue samples using TCSPC.

The liquid light guides are used to transmit both the excitation light to the sample, and the fluorescence signal back to the detector. The couplings of the light guides to the excitation source and the detector have space to hold filters as required, and the couplings were made as light tight as possible to minimise any interference from any background light. The benefit of this equipment for this application is that it is a smaller system, and so can be moved between laboratories more easily (which was a requirement for this study), and it enables a much more flexible setup for measuring samples.

To measure fluorescence intensity decays from the animal tissue samples, 3 different excitation/emission pairs were used: 295/340 nm, 340/390 nm, and 370/460 nm. These correspond to the fluorescence maxima of Trp, pepsin-digestible collagen cross-links, and keratin/NADH, all of which have been studied in vitro.

The resultant decays were then fitted to the model of fluorescence decay (equation 2.29), and fitted parameters between samples could be compared. We would expect, in line with the *in vitro* results, that there would be an increase in the two longer lifetime components (where in equation 2.29 $I(t)$ is equation 2.23) for the 370/460 nm excitation emission pair (corresponding to keratin), and decreased τ and α values (where in equation 2.29 $I(t)$ is equation 2.25) for the 295/340 nm excitation/emission pair (corresponding to Trp).

7.4.2 Results and Discussion

The first steady state spectrum for the 12 mice was carried out on day 0, before diabetes had been induced. This result is shown in Figure 7.8. The spectra from each mouse are comparable, and as was the case for the initial pilot study, three peaks can be seen at 390, 430, and 460 nm. Again, we believe these correspond to pepsin-digestible collagen cross-links, collagenase-digestible collagen cross-links, and keratin cross-links or NADH. Monitoring the position and intensities of these peaks as diabetes is induced and becomes more severe will allow us to determine the effect the glycation of these skin proteins has on their fluorescence in vivo. For example, literature and our own *in vitro* work has shown that collagen-linked fluorescence and keratin-linked fluorescence increases with AGE accumulation[60, 148], and we expect AGEs to accumulate as this study progresses.

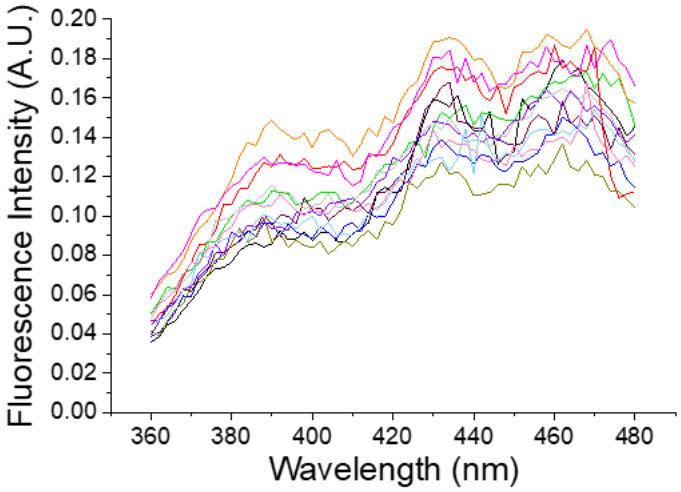

Figure 7.8 Fluorescence emission spectra from mice skin on day 0 for excitation 340 nm. Each colour represents an emission spectra from a different mouse.

Unfortunately, a few days after this first measurement, the UK entered lockdown due to Covid-19 resulting in the complete shutdown of universities and the animal unit where this study was taking place. These mice had to be culled, and the study was ended. There was no possibility of this study restarting due to very tight restrictions present in universities and the animal unit for a long period of time. This was unfortunate, as we believe there was real promise of a significant result.

7.5 Conclusion and next steps (Covid stopped the next study from taking place)

The initial pilot study showed some evidence that the 3 fluorophores that change in response to glucose in vitro could be detected from a skin AF measurement, and that there may be a relationship between skin AF and blood glucose. The long-term study would have allowed us to confirm this relationship, and investigate if there was a correlation between skin AF and HbA1c, a long-term marker of glycaemic control. In addition, the time-resolved fluorescence measurements of animal tissue would have allowed us to gain greater insight into the glycation process occurring in the skin proteins.

8. *Ex Vivo* Fluorescence: Fluorescence of Fingernails

8.1 Introduction

Nails and hair are accessory organs to the skin, and both serve a protective purpose. Nails are characteristic to all primates, and are essentially modified claws found on the distal ends of fingers and toes. They have various roles such as protection, enabling sensation, improving grip, and helping to manage smaller objects[283]. The primary component of nails is keratin, which provides the nail with both hardness and flexibility.

8.1.1 Nail Structure

The nail is made up of 4 primary components: the nail plate, the nail matrix, the nail bed, and the surrounding soft tissue. A diagram of the structure of the nail is shown in Figure 8.1. Part A shows the structure of the nail matrix, nail bed, and nail plate, and Part B shows the structure of the nail plate in more detail.

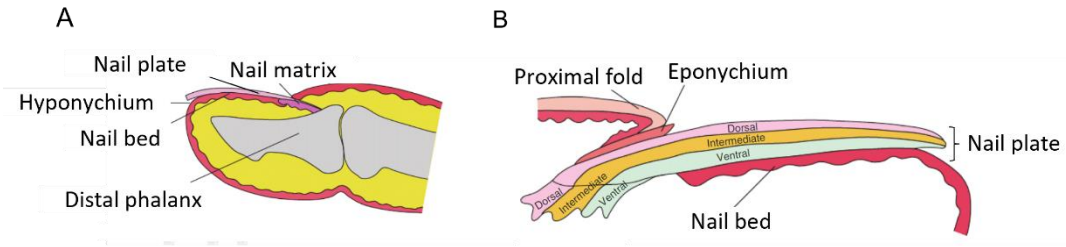

Figure 8.1. Diagram of the structure of the nail showing an overview of the different components (A) and the detailed structure of the nail plate (B)[3]

The nail plate is a modified form of the stratum corneum and lies on the nail bed and the nail matrix[209]. The nail matrix is a thick epithelium that produces the cells that will become the nail plate[284]: new cells are produced continuously by the matrix, and as new cells are produced, older cells are keratinised, compacted, and forced down the nail bed. In this way, the nail plate forms, with a growth rate of approximately 1 mm per week[283].

The lunula is the visible part of the matrix, and is where the nail bed begins. The nail bed itself extends from the lunula to the hyponychium, and is composed of capillary containing epidermal and dermal cells. It's primary function is to keep the nail plate attached[285].

The hyponychium and the eponychium are 2 further components of the nail that have a similar role. The hyponychium is at the tip of the nail bed, and seals the gap between the nail and finger. The eponychium, or the cuticle, is found at the base of the nail and acts as a protective barrier to the nail matrix. Both of these prevent bacteria and infections from entering the nail tissue[285].

The keratin-containing nail plate

The nail plate is of most interest to this research, as it is composed of keratin, which undergoes glycation in response to high glucose levels. Therefore, a more detailed description of its structure is included.

The nail plate is composed of keratin tissue, and contains both hair-type (hard) keratin and epithelial (soft) keratin. Hair-type keratin is the most dominant tissue type, making up 80-90% of the nail plate, with epithelial-type contributing approximately 10-20% of the keratin cells[285].

The nail plate has three different histological layers[286]: the dorsal layer, the intermediate layer, and the ventral layer. Each layer is characterised by a different orientation and/or type of keratin molecule. The dorsal layer is the outermost layer of the nail plate, and is a plate like structure composed of epithelial-type keratin molecules, which are orientated parallel to the nail growth axis. Epithelial-type keratin also makes up the innermost layer, the ventral layer, and in this case the molecules are oriented perpendicular to the nail growth axis. Sandwiched between these two layers is the intermediate layer. This is the thickest, and thus most dominant layer of the nail plate[287] and it is comprised of hair-like alpha-keratin fibres[288]. These are orientated perpendicular to the growth axis.

8.1.2. Nail Glycation

As discussed in Chapter 5, keratin undergoes glycation, and as the dominant component in nails, it follows that glycation occurs in nails. Different forms of epithelial keratins are expressed in the nail plate[289]. These keratins contain a significant number of lysine residues[290], and so nail plate keratins are a potential target for glycation. However, as human nails do not contain blood vessels, and are metabolically inactive, glycation is more difficult to understand.

A study[209] that attempted to explain this determined that nail keratin glycation occurs in the deep layers of the nail: their findings showed a higher concentration of fructosamine, and a higher concentration of glycated keratin in the deep layers compared to the more superficial layers. Thus, this study determined that nail proteins are exposed to blood and extracellular fluid glucose through the nail bed (which is a membrane containing blood vessels), which over time results in glycation. The diffusion of glucose to the more superficial nail layers is very slow, and so these layers contain a lower concentration of glycated keratin.

The process of nail protein glycation can take 6-9 months, as this is the time for a complete human nail replacement[285]. This means that the glycation level in nails is subject to oscillations as the nail is continually replaced.

It has been established that the amount of glycated nail proteins is increased in those with diabetes[204,208,291]. Thus, nail protein glycation could be used as a marker for diabetes or long-term glycaemic control. This offers advantages as fingernails are readily available, and the assessment of the glycated proteins could be done non-invasively.

8.1.3 Nail Auto-fluorescence and Diabetes

Various methods have been used for the assessment of glycated nail proteins. In 2014, a study[291] used a modified photometric nitroblue tetrazolium-based assay to measure the amount of glycated protein in nails, in 2018 a study[210] used NIR spectroscopy on nail clippings to distinguish patients with diabetes from healthy patients, and in 2020 absorption of nail proteins was measured using ATR-FTIR spectroscopy, and absorption was found to be increased in those with diabetes and diabetic retinopathy[211] .

In this work we exploit keratins auto-fluorescent (AF) property as a means of detecting nail glycation. As discussed in Chapter 5, keratin is auto-fluorescent, with two emission peaks at 340 - 350 nm (corresponding to Trp) and 440 – 460 nm (corresponding to keratin crosslinks)[213,218,68]. Keratin is the dominant protein in nails, and indeed these fluorescent bands have been detected *in vivo* on human nails[218]. We therefore aim to determine if nail AF could be a marker for long term glycaemic control using various fluorescence spectroscopy techniques.

8.2 Methodology

8.2.1. Ethical Approvals

For this work to take place, full ethical approval was required. The study was approved by the Leeds East Research Ethics Committee, and was carried out at the diabetes clinic at the Royal Infirmary of Edinburgh, and at the physics department at the University of Strathclyde.

8.2.2. Collection and Preparation of Nail Samples

A total of 14 patients with diabetes were recruited for this study. 2 control participants were also included, however they were not properly screened for diabetes (using HbA1c), and so we simply had to assume that they did not have the disease. In healthy individuals, under 42 mmol/mol is considered normal HbA1c, and in patients with diabetes, the higher this number, the more severe the disease.

The patient group consisted of individuals with diabetes mellitus type 1 and 2 who were under treatment, and were recruited at the Edinburgh Centre for Endocrinology and Diabetes at the Royal Infirmary of Edinburgh. On the day of their visit to the clinic, the patients HbA1c (the measure of the severity of the disease) was measured via a blood sample and recorded.

The preparation of the samples in both groups followed the protocol outlined by Monteyne et. al.[210] Nail clippings (free of nail polish) were collected in Eppendorf tubes from patients with diabetes mellitus and healthy controls. The clippings were washed using 1 ml distilled water in a sonication bath at 37°C for 60 mins. The nails were removed from the tubes, dried using tissues, and then placed in an incubator at 37°C for 24 hours to fully dry the nails. Each clipping was then pulverized using an electric nail drill with a steel head, and suspended in 3.5 ml PBS. The sample was then transferred to a 4x1x1 cm plastic cuvette, and sealed with parafilm, ready for measurements. The measurements took place within ~10 mins of sample preparation.

8.2.3 Fluorescence Measurements

Excitation/emission matrices and corrected fluorescence emission spectra were obtained on a Fluorolog (Horiba Scientific), with both the excitation and emission monochromators set to a slit width of 5 nm. For the matrix measurements, the excitation wavelength spanned from 280 – 400 nm in increments of 5 nm, while fluorescence was collected from 300 – 550 nm in increments of 2 nm. For the fluorescence spectra 2 excitation wavelengths were used: 280 nm (to excite Trp in keratin) and 370 nm (to excite keratin cross-links). The resolution of the spectra was 1 nm. Each sample was measured three times, and the spectra averaged.

The fluorescence intensity decay measurements were obtained using a DeltaFlex fluorescence lifetime system (Horiba Jobin Yvon IBH Ltd, Glasgow), which uses time-correlated single photon counting (TCSPC) to record fluorescence decay. A NanoLED with repetition rate 1MHz and peak excitation wavelength 370 nm (pulse duration <1ns) was used to excite the sample.

8.3. Results and Discussion

Figure 8.2 presents several excitation/emission matrices obtained from nail clippings from patients with diabetes. All samples show the greatest fluorescence intensity at 280/340 nm, which corresponds to Trp fluorescence, a fluorescent band in keratin which is the dominant nail protein. Most samples (excluding E, I, L, M) also show an increased intensity between ~450 and 460 nm: this fluorescence originates from keratin crosslinks.

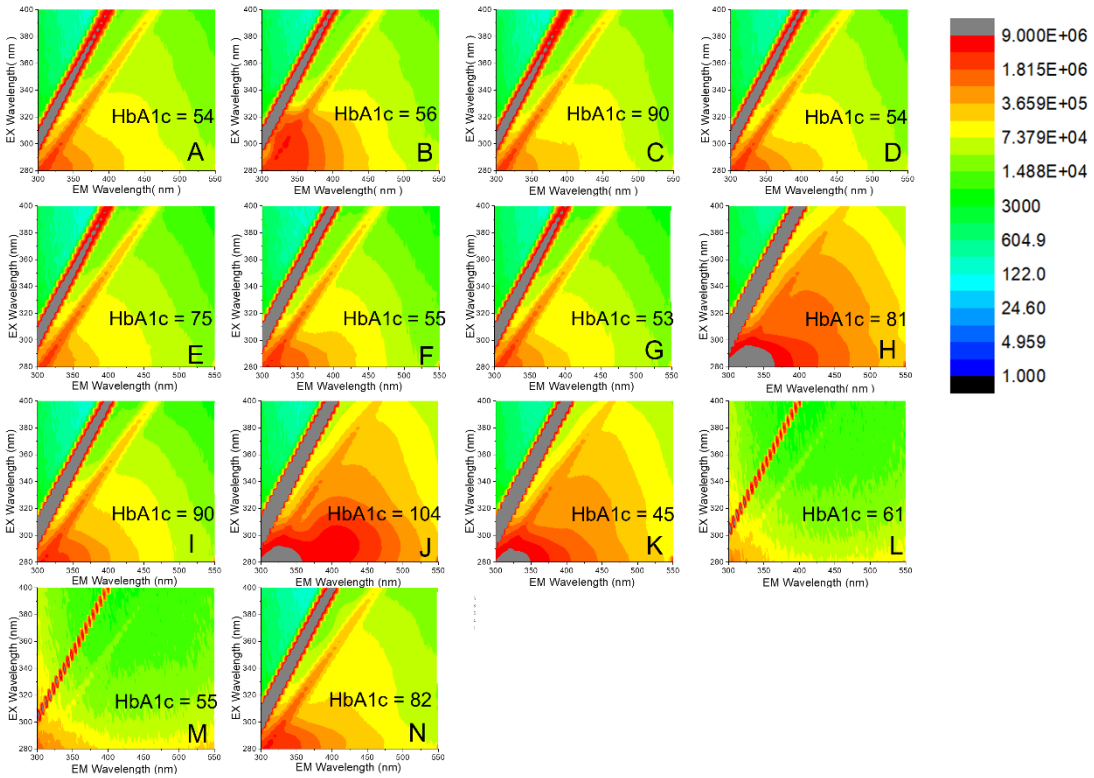

Figure 8.2. 3D spectra of nail clippings from various participants with diabetes. Each plot (A-N) shows the result from a nail clipping of a different patient, alongside the HbA1c value measured on the day the nail clipping was collected.

The excitation/emission matrices included show that keratin protein in nails can be detected using fluorescence spectroscopy. However, it appears there is no relationship between fluorescence intensity and severity of diabetes, determined by HbA1c. For example, from 2 participants with HbA1c of 55 mmol/mol (samples M and F), the excitation/emission matrices are significantly different. The variation in the samples could be due to a number of factors, for example mass of nail clipping, age of participant, type of diabetes and so forth, and so many more samples would be required in order to determine if there is a relationship between fluorescence intensity and HbA1c, which has not yet been proven in any previous studies.

To explore this further, steady state fluorescence emission spectra were obtained using two excitation wavelengths: 280 nm and 370 nm, which correspond to the excitation wavelengths of Trp and keratin crosslinks respectively. The result for excitation at 280 nm is shown in Figure 8.3, with part A showing the emission spectra from the participants with diabetes (black solid line) and the healthy controls (red dashed line). It should be noted that there is

no HbA1c measurement for the control samples, as the Covid 19 restrictions prevented non-patients from entering the hospital to provide a blood sample. The fluorescence results from these control samples are included purely for comparison purposes.

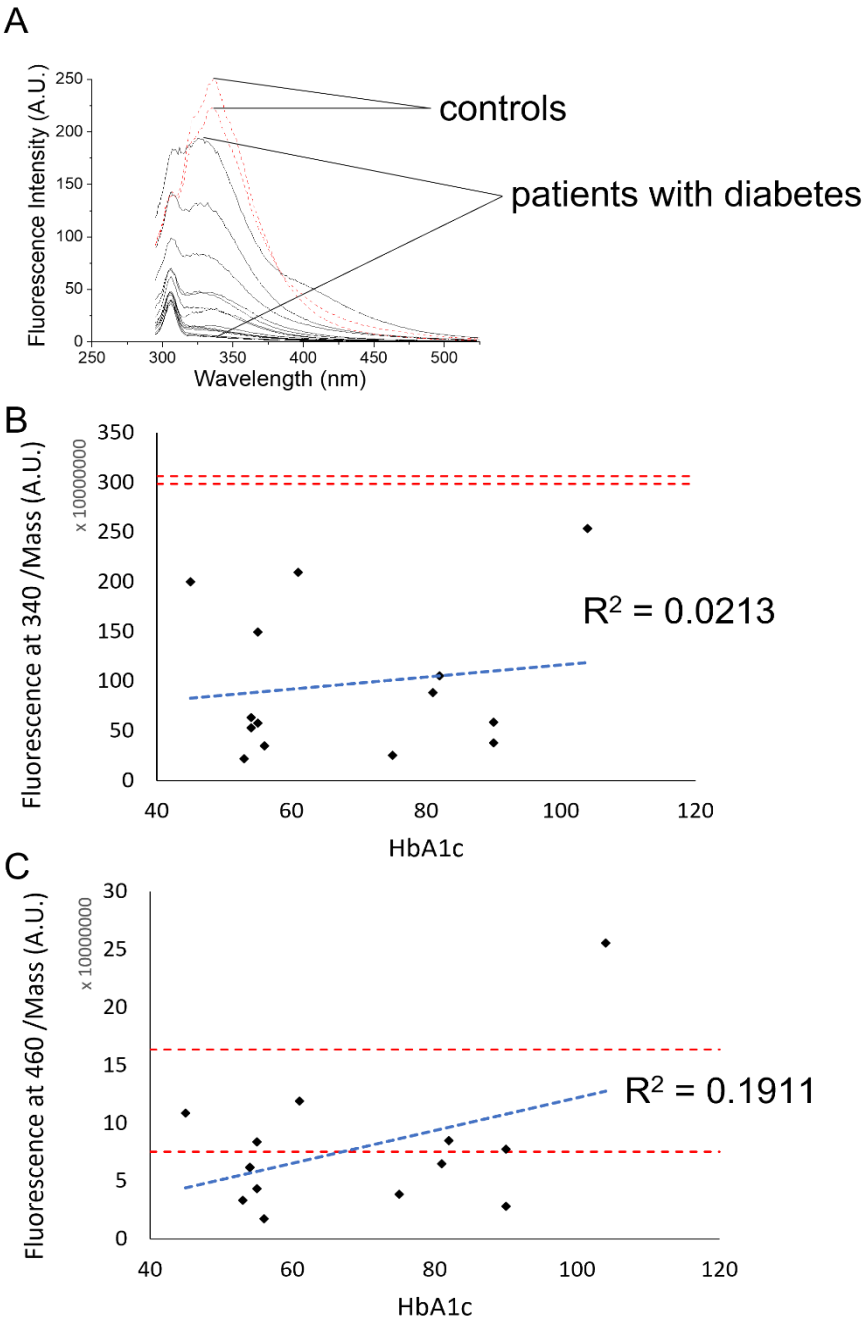

Figure 8.3. Part A. Fluorescence emission spectra from nails of patients with diabetes (black solid line) and healthy controls (red dashed line) when excited at 280 nm. Parts B and C show the relationship between peak fluorescence intensity at 2 wavelengths (340 nm and 460 nm respectively) and HbA1c. Patients with diabetes are given by closed symbols and healthy controls are given by red dashed lines as no HbA1c value was available. The best fit line of the relationship between fluorescence and HbA1c for samples from patients with diabetes is given by the blue dashed lines..

In Figure 8.3A, there is a difference between the 2 groups. All spectra show a peak at 310 nm, the Raman shift for excitation at 280 nm. In the patient group, the peak fluorescence wavelength is ~330 nm, and this is red shifted to ~340 nm in the control group. A peak at 340 nm nm was expected, as this would originate from Trp in nail keratins, however, the peak at the slightly shorter wavelength in the patient group is difficult to interpret. A peak at 460 nm would also be expected in the patient group, as was observed in our study on glycated keratin (Chapter 5, Figure 5.4). This does not seem to be present in the nail clipping samples when excited at 280 nm.

The fluorescence intensity is greater in the control group, which was unexpected considering our results for keratin *in vitro* (Chapter 5 , Figure 5.4). This difference in the spectra illustrated in Figure 8.3A may however be caused by other factors such as mass of clipping. Therefore, plots of fluorescence intensity, corrected for mass, at the 2 key wavelengths (340 nm and 460 nm) against HbA1c are shown in Figure 8.3B,C. Considering first the fluorescence intensity at 340 nm (Figure 8.3B), it is clear that the fluorescence intensity is indeed much higher in control samples than in the samples of patients with diabetes. This contradicts what was observed in Chapter *5* which analysed keratin glycation *in vitro*: Figure 5.4A showed free keratin to have a lower fluorescence intensity than keratin-glucose. Furthermore, there seems to be no relationship between the fluorescence intensity and HbA1c, which is confirmed by the R^2 value. This is also the result when considering the fluorescence intensity at 460 nm (Figure 8.3C): the R^2 value confirms there is no relationship between fluorescence intensity and HbA1c. The control samples (red dashed line) also appear random, and show no significant difference to the result of the samples with diabetes (black diamonds).

It should be noted that error bars representing the standard deviations of the fluorescence intensity for each sample have been omitted from Figure 8.3B,C (and also from Figure 8.4B) for clarity, but these simply confirm what can be seen from the plots: that there is no statistically significant difference between the two groups, and there is no relationship between the fluorescence intensity and HbA1c.

Fluorescence emission spectra were also recorded at excitation 370 nm (Figure 8.4A). All spectra show a peak at 424 nm (Raman shift for excitation 370 nm) and most then show a broad peak between 450-460 nm, which corresponds to keratin crosslinks. Some samples show no evidence of this peak, and have low fluorescence intensity. This could be due to the very low weight sample obtained, resulting in a low concentration.

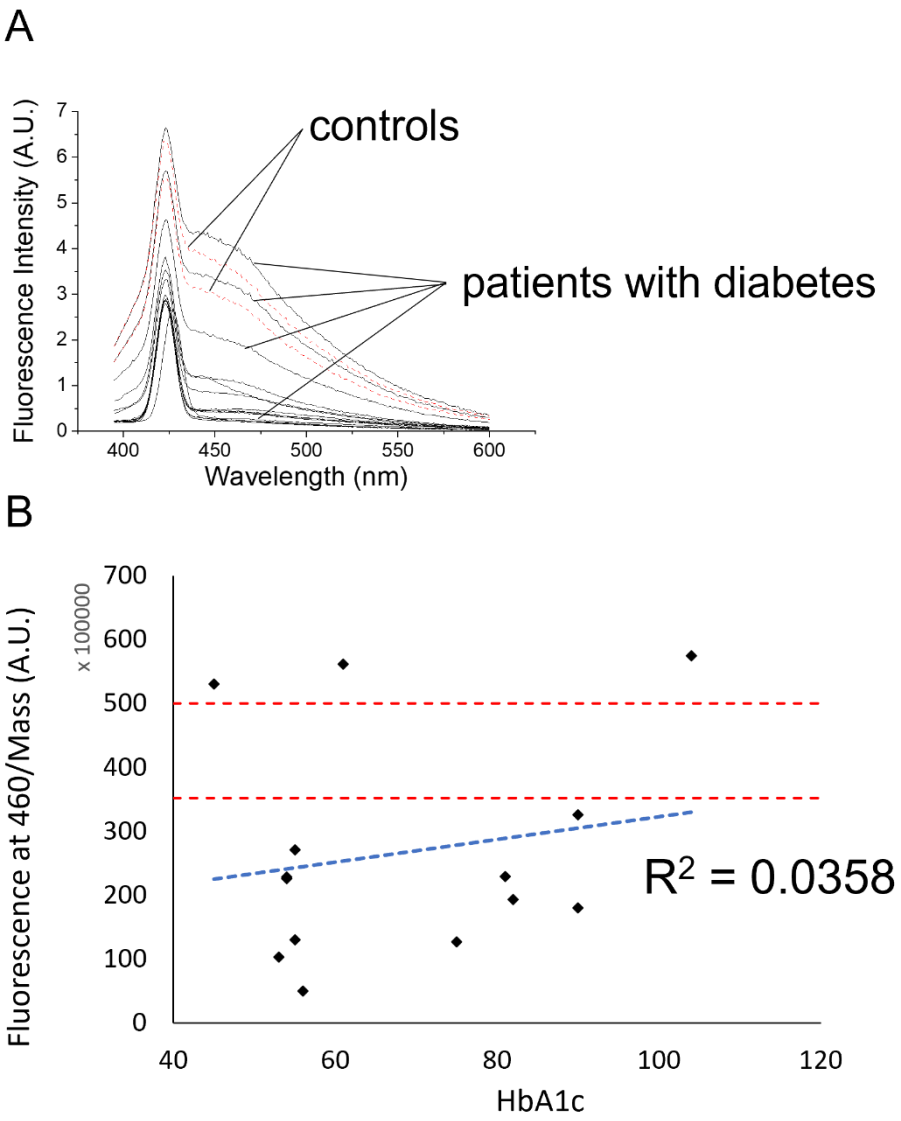

Figure 8.4. Part A. Fluorescence emission spectra from nails of patients with diabetes (black solid line) and healthy controls (red dashed line) when excited at 370nm. Part B shows the relationship between peak fluorescence intensity at 460 nm and HbA1c. The patients with diabetes are given by closed symbols and healthy controls are given by the red dashed line, as no HbA1c value available. A best fit line of the relationship between fluorescence and HbA1c for samples from patients with diabetes is given by the blue dashed line.

Figure 8.4B then shows the relationship between fluorescence intensity at 460 nm and HbA1c. Again, there is no evidence of a relationship, confirmed by the very low R^2 value. In addition, there is no significant difference (error bars showing standard deviations have been omitted for clarity, but confirm this observation) between the intensity in the control samples, and the samples from patients.

The steady state data appears to show no significant difference in the fluorescence from nail clippings of those with diabetes and those without. There is also no evidence of a correlation between fluorescence and severity of the disease. This was unexpected, as our *in vitro* experiments show a significant difference in the fluorescence properties of glycated keratin and free keratin. Previous studies[204] have also confirmed that there is a higher concentration of glycated keratin in nails of those with diabetes, and that glycated keratin in nails correlates with glycated haemoglobin (HbA1c). This result could not be realised from the fluorescence emission spectra. The data presented (Figures 7.3 and 7.4) indicate that a much larger number of samples are needed to properly demonstrate a correlation between fluorescence intensity and HbA1c, but unfortunately availability of samples was seriously limited by Covid 19 restrictions.

There is a broad range of nail properties that may influence the steady state results. For example, the structure and chemical content will impact its fluorescence emission spectra. Thus, measured fluorescence intensities are unlikely to represent glycation only. Fluorescence intensity decay measurements were therefore carried out. Fluorescence intensity decays can reveal fluorescence lifetimes, which are intrinsic to a molecule, and thus we can be sure we are considering solely keratin fluorescence. These measurements were used to obtain more information on the system, and to attempt to establish if there was a relationship between fluorescence decay and diabetes severity.

The decays, detected at 460 nm (using excitation 370 nm), of the samples from patients with diabetes and the healthy controls are illustrated in Figure 8.5. From direct inspection of the plot, it appears that there are differences in the fluorescence decay between samples, and that the decays from the healthy controls (open triangles) seem shorter.

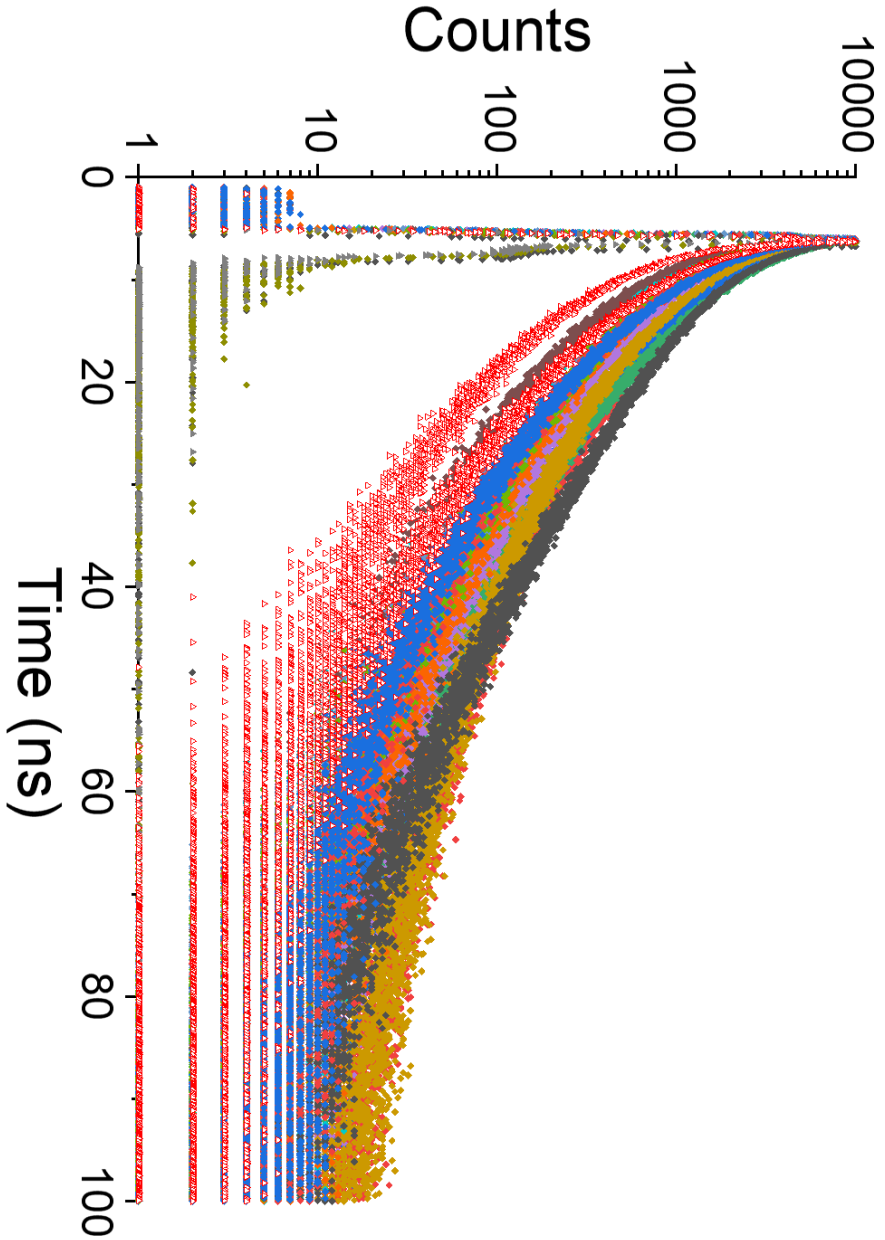

Figure 8.5 . Fluorescence intensity decay at excitation wavelength 370 nm and detection wavelength 460 nm from patients with diabetes (solid diamonds) and healthy controls (open triangles).

To quantify these differences, and to determine if there was a relationship between any parameter and severity of diabetes, the fluorescence intensity decays were fit to various models, following equation 2.29. First, the classical exponential model was used (equation 2.23 describes $I_{exp}(t)$), and for all decays a 3-exponential model was required (based on χ^2 goodness of fit criterion and plots of residuals, see Appendix F, Figure F1.1). As before, and

contrary to the common approach, we do not claim that this indicates 3-exponential kinetics, but rather that the 3-exponential function is a good mathematical representation of the observed decays. Figure 8.6 shows the resultant parameters (τ_1, τ_2, τ_3, alongside their pre-exponential factors) plotted against HbA1c, to determine if any of these could be used as a marker for long term diabetes control or severity.

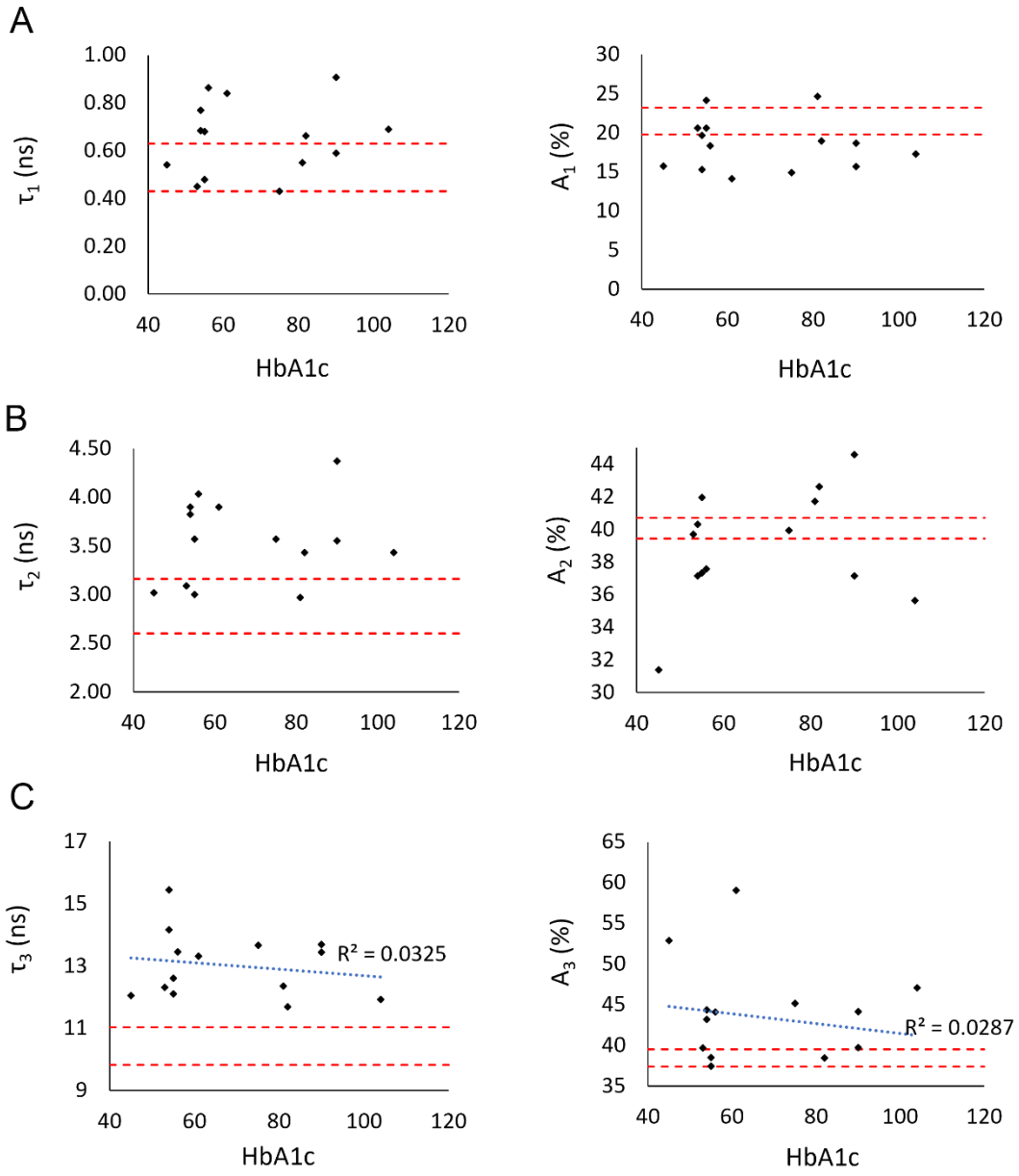

Figure 8.6. The 3 lifetimes obtained when the decays are fitted to the 3-exponential model for patients with diabetes (closed symbols) and healthy controls (red dashed line, as no HbA1c value available). The percentage contribution of each component to the decay for each sample is also shown. The blue dashed lines in (C) show the best fit lines of the relationship between HbA1c and the respective fluorescent parameter for the samples of patients with diabetes. The contribution of the scattered light to each decay has been left out for clarity.

First, it should be noted that the three lifetimes have values of ~0.4-0.8 ns, ~2.5-4 ns, and ~11-15 ns. These broadly match the 3 values obtained for the decays of keratin and keratin-glucose samples *in vitro* (see Figure 5.8, Chapter 5). This suggests that the fluorescence recorded is indeed from keratin proteins in the nail samples. The main difference in the decays of the keratin and keratin-glucose samples *in vitro,* was that the contribution of the second and third component to the decay was much greater in the keratin-glucose sample. By the end of the experiment, these were approximately 40% and 50% respectively, while in free keratin these remained at approximately 25% and 30%. In the nail samples from the diabetic patients, the contribution of τ_2 fluctuates between 38% and 44%, and for τ_3, this has a contribution of less than 45% in most samples. This seems to be between the values for keratin and keratin-glucose samples *in vitro*. In addition, there seems to be no difference between the values obtained for diabetic patients and healthy controls in any plots.

In terms of a relationship between any resultant fitted value and HbA1c, from direct inspection of the plots (Figure 8.6A,B) it is clear that there is no relationship between τ_1, τ_2, A_1 or A_2 and HbA1c. The parameter that looked to show a slight correlation was the third longer lifetime component (Figure 8.6C). However, when a linear best fit line was added, the R^2 value is very low, indicating no correlation.

The final analysis carried out on the decays using this model was calculating the mean lifetime $\bar{\tau}$

$$\bar{\tau} = \frac{\sum_{i=1}^{n}(\alpha_i \tau_i)^2}{\sum_{i=1}^{n} \alpha_i \tau_i} \qquad [8.1]$$

The $\bar{\tau}$ for each fluorescence intensity decay are shown in Figure 8.7, plotted against HbA1c values. Firstly, an unpaired t-test was carried out to determine if there was a significant statistical difference between the two participant groups. The calculation is outlined in Appendix F2. The p value equals 0.2119, and so by conventional criteria ($p<0.05$ indicates statistically significant difference), this difference is not statistically significant. This is not the most robust statistical analysis, since there were only 14 participants in one group, and 2 in the other. This result does however support the previous results looking at individual parameters, in that there is no discernible difference between the fluorescence from healthy

individuals and those with diabetes. This plot also shows no correlation between mean lifetime and HbA1c.

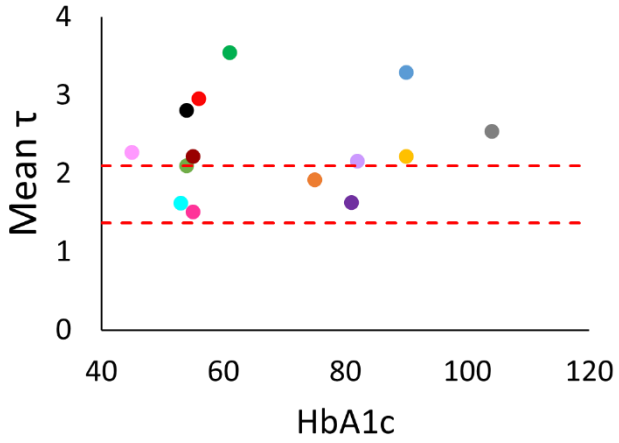

Figure 8.7. Mean lifetime obtained for patient samples (solid symbols) and healthy controls (dashed lines, as no HbA1c value available).

This multi-exponential analysis shows no difference between decays of patients with diabetes and healthy controls. This could be because fluorescence intensity decays cannot accurately detect glycated keratin in an *in vivo* environment. However, there is also the possibility that the multi-exponential model is not the best model to describe these decays, and is in fact hiding potential relationships or differences between groups. For this reason, the non-Debye model (equation 2.25) was also considered, and the resultant parameters from this model, plotted against HbA1c, are presented in Figure 8.8 (Examples of raw decays alongside fitted parameters and plots of the residuals are shown in Appendix F1, Figure F1.2). It should be noted that the χ^2 values for this model were not ideal, reaching as high as 3.28 in one case. However, this model was still considered to determine if it revealed any differences between groups, or trends with HbA1c.

Figure 8.8A shows α for the participants with diabetes and the healthy controls. Like with the exponential model, the values appear to be random, with no difference between the 2 groups, and no obvious correlation with HbA1c (confirmed by the low R^2 value).

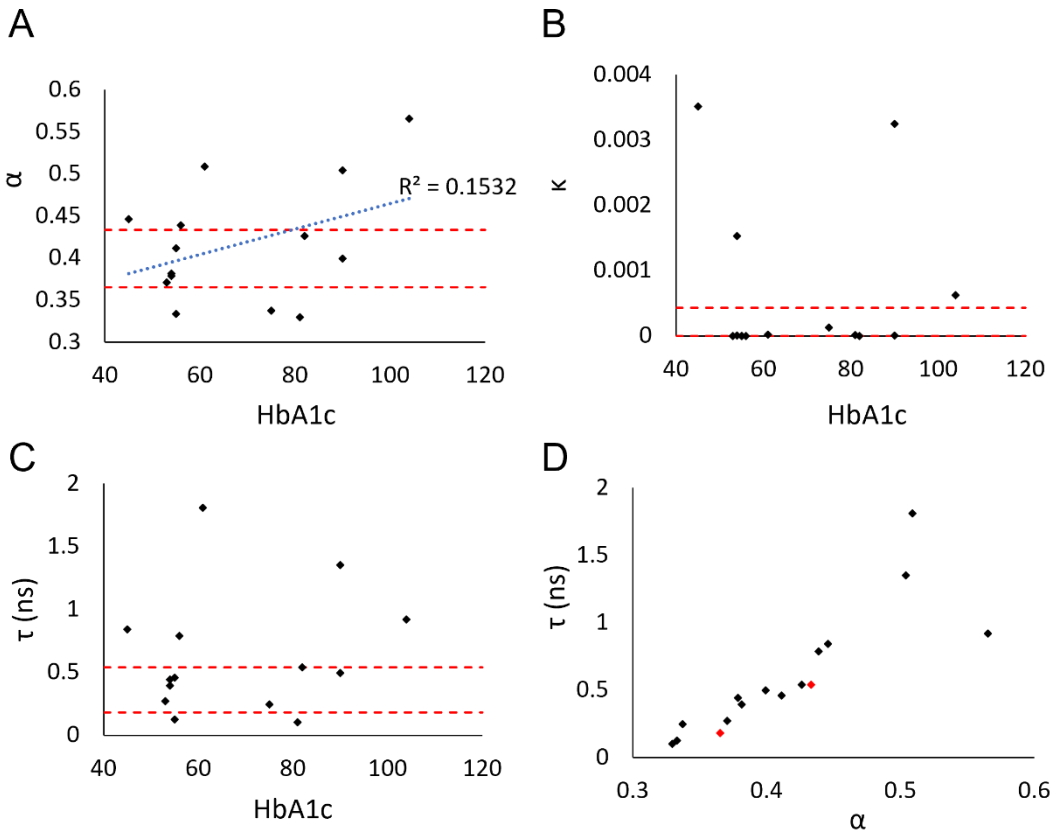

Figure 8.8. Resultant parameters from fitting fluorescence intensity decays to the non-Debye model, including results from patients with diabetes (black symbols) and healthy controls (red dashed line, as no HbA1c value available). The contribution of scattered light to the decay has been left out for clarity. In (A), the blue dashed line shows the best fit line for the relationship between HbA1c and α for the samples from patients with diabetes. Part D shows the relationship between α and τ.

The τ values (Figure 8.8C) gave a similar result, with no difference between the two groups, and no discernible relationship with HbA1c. Finally, all κ values (Figure 8.8B) were very low, which indicates that these decays are likely to follow a stretched exponential model.

Figure 8.8D then shows α plotted against τ for all samples. A clear correlation between these two parameters is observed, and although these non-Debye parameters do not seem to relate to HbA1c, the non-Debye kinetics do seem to be relevant to nail auto-fluorescence.

To try and improve the fit, a second component was added to the non-Debye model. Both components had the same α and κ values, but τ_1 and τ_2 were different. For this model, the plots of the residuals and χ^2 values indicated a good fit (see Appendix F Figure F1.3). The resultant parameters from fitting to this model are shown in Figure 8.9. From inspection,

none of the parameters show any differences between the 2 participant groups. In addition, there does not appear to be a correlation between any of the parameters and severity of diabetes (indicated by HbA1c).

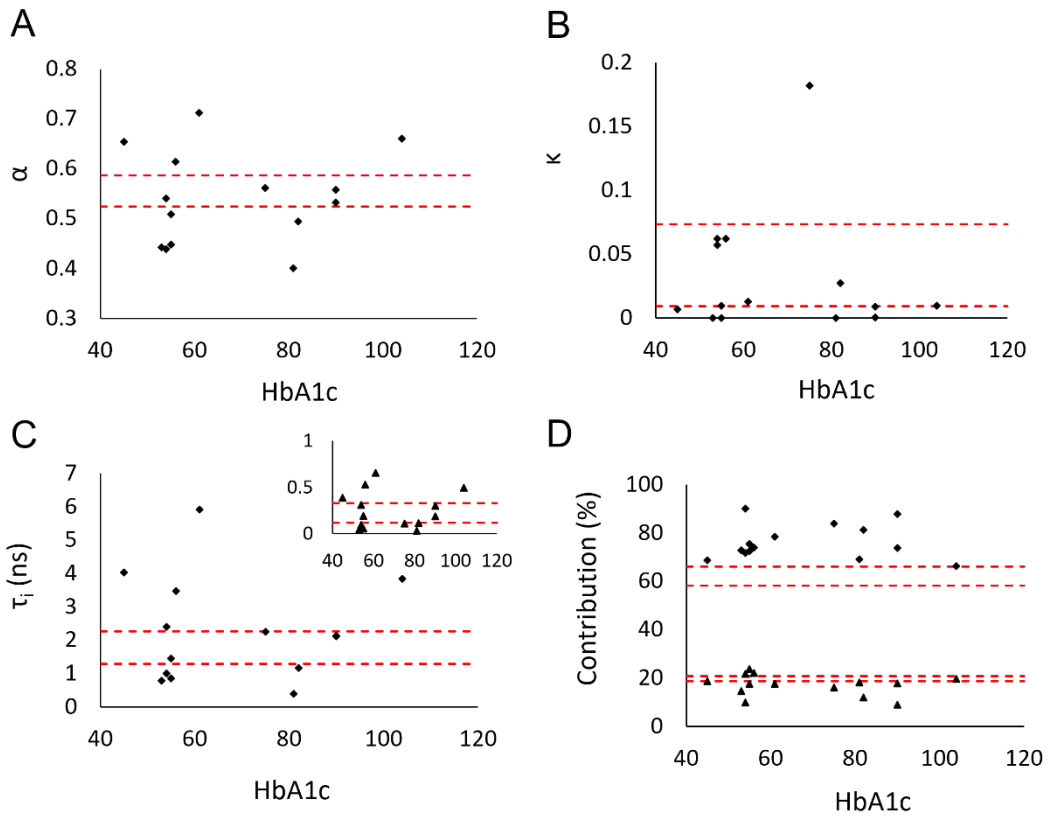

Figure 8.9. Resultant parameters from fitting fluorescence intensity decays to the 2 component non Debye model, including results from patients with diabetes (black symbols) and healthy controls (dashed line as no HbA1c value was available). The contribution of scattered light to the decay has been left out for clarity.

8.4. Conclusions and Future Work

Despite promising results in our *in vitro* keratin glycation experiments, the results presented in this chapter show no significant finding. Indeed, both the peak emission wavelengths, and the fitted exponential parameters indicate that we are detecting keratin fluorescence however there is no evidence that glycated keratin can be sensed through a nail clipping. Although small variations between the two participant groups are observed, there are no significant differences in either the steady state spectra or fluorescence intensity decays. Furthermore, our analysis does not reveal a correlation between any of the extracted fluorescence parameters and HbA1c.

There could be several reasons why increased amounts of glycated keratin could not be detected in those with diabetes, or why no correlation with HbA1c was found. As discussed in the introduction, nail glycation occurs in the deep layers of the nail plate, and diffusion of glycated keratin to the superficial layer is very slow. Our clippings may have been from the superficial nail layer, where there will be a reduced amount of glycated keratin.

The number of participants included in this study was also very small, and so it was difficult to establish any type of relationship. If further studies were to be carried out, a higher number of samples should be included, and additional information from participants should be taken, for example age and duration of diabetes, to see if any of these factors correlate with glycated haemoglobin.

9. Conclusions and Future Work

In this thesis, the impact of glucose on various biological fluorophores has been investigated in both *in vitro*, *in vivo* and *ex vivo* settings using various fluorescence spectroscopy techniques. The fluorophores studied *in vitro* included collagen, NADH, keratin, and HSA, and changes to these molecules due to glucose was detected via changes in their auto-fluorescence.

From our *in vitro* studies, NADH showed the least potential as a marker for long term glycaemic control, as our results showed no evidence of glycation. The studies on collagen, keratin, and HSA however were much more promising.

In collagen, the impact of glucose on both Tyr and collagen cross-links was investigated. Tyr in collagen does not seem to be affected by glucose, but glucose does affect the formation of pepsin-digestible collagen cross-links. These changes in collagen were detected using steady state fluorescence spectra and time-resolved emission spectra, which could reveal more detail.

Similarly, glucose has a great impact on the intrinsic fluorescence of keratin *in vitro*. While keratin has intrinsic fluorescence at 340 nm and 460 nm due to Trp and crosslinks respectively, the addition of glucose caused the formation of 2 new fluorescent complexes that emit at longer wavelengths. Again, this was detected via steady state and time-resolved fluorescence measurements.

The final fluorophore studied *in vitro* was human serum albumin (HSA). The dominating fluorophore in this protein is Trp, and our work has shown that Trp fluorescence is sensitive to glucose in its microenvironment. Glycated albumin has been used in clinical settings as a marker for long term glycaemic control, and this result may pave the way for a new fluorescent-based sensor that can detect glycated HSA non-invasively.

Work was also carried out in environments where the auto-fluorescence of mouse skin and human nails was investigated. The purpose of these studies was to determine if the results obtained *in vitro* translated to *in vivo* and *ex vivo* environments, and determine if any parameter of fluorescence correlated with long term glycaemic control.

The initial pilot mouse study showed potential, as fluorescent spectra from the mouse skin showed peaks corresponding to skin fluorophores of interest: collagen, NADH, and keratin.

There also seemed to be a correlation between skin AF and blood glucose, however further studies would be needed to confirm this.

The *ex vivo* study was carried out with the aim of determining if nail AF could be a marker for long term glycaemic control. Although results indicated that keratin in nail samples was indeed being detected (via steady state and fluorescence intensity decay measurements), no significant difference was observed between the samples from the patients with diabetes and the healthy controls. Furthermore, there seemed to be no correlation between any extracted fluorescent parameter and HbA1c, the gold standard for determining long term glycaemic control. This study however was very small, with only 14 participants in the group with diabetes, and so if studies were to be carried out in future, a higher number of participants should be included.

This thesis also focused on alternative methods of describing fluorescence decays. In several cases (HSA, nail samples), the non-Debye model was equally or more effective at describing the fluorescence decays as the traditional multi-exponential model. A non-Debye model may be more suitable in certain molecular systems, as it can represent a stable distribution of fluorescence lifetimes, rather than simply the presence of 2 or 3 distinct lifetimes. It must be noted however that a stable distribution is not stable in the traditional sense, where it does not change, rather that it is a broad class of distribution functions. This may have use in complex biological environments where the decay is non-exponential.

The focus on fluorescence intensity decays was important, as these provide more information than steady state spectra. This thesis has demonstrated that the choice of model used to fit the fluorescence intensity decays is extremely important. For example, the impact of glucose was hidden when the decays of the HSA-glucose samples were fit to the multi-exponential model, but revealed when fit to the non-Debye model.

In this work, in all cases the most suitable model for fluorescence decay was determined via manually fitting each decay multiple times to different models, and determining the most appropriate based on the χ^2 goodness of fit criterion and plot of the residuals. This is highly time consuming and based on human choices. Future work in this area could therefore involve this becoming automated, where artificial intelligence and big data are used to quickly choose the most appropriate model, and then quickly fit multiple fluorescence decays. This would speed up the process and remove the possibility of human error. Indeed, recent work has used deep learning to fit complex fluorescence decays in fluorescence

lifetime imaging microscopy (FLIM)[292], and used artificial neural networks to estimate the lifetimes in decay data from FLIM images[293].

Overall, this thesis has investigated the process of glycation, where the molecular processes involved have been studied using various fluorescence spectroscopy techniques. Our most significant findings show that the impact of glucose on collagen, keratin, and HSA *in vitro* can be detected via their autofluorescence. An attempt to explain the kinetics and process involved in the glycation of these fluorophores has been attempted.

This is very early-stage research, but from this we expect that that fluorescence spectroscopy may be a valuable tool that can detect long term glycaemic control. The next steps would therefore be to translate these studies to *in vivo* environments, in studies more comprehensive than the ones included here. The aim should be to determine if similar results can be obtained from, for example, skin, hair, and nails. There were of course limitations on our work, which would lead to obstacles when translating to *in vivo*, as our results were obtained in a well-defined *in vitro* environment, where there was no outside influence on the result. To effectively translate these results *in vivo*, more thorough studies will be required.

We hope that these results will inspire researchers in the medical field, and may in the future lead to the development of a fluorescent based sensor that can detect glycated proteins, for example in skin or nails, and be used to monitor long term glycaemic control in patients with diabetes.

10. References

(1) Lakowicz, J. R. *Principles of Fluorescence Spectroscopy*; Springer, 2006. DOI: 10.1007/978-0-387-46312-4.
(2) Belatik, A.; Hotchandani, S.; Carpentier, R.; Tajmir-Riahi, H.-A. Locating the Binding Sites of Pb(II) Ion with Human and Bovine Serum Albumins. *PLoS ONE* **2012**, *7* (5), e36723. DOI: 10.1371/journal.pone.0036723.
(3) Tan, E. S. T.; Chong, W.-S.; Tey, H. L. Nail Psoriasis. *American Journal of Clinical Dermatology* **2012**, *13* (6), 375-388. DOI: 10.2165/11597000-000000000-00000.
(4) Hull, E. L.; Matter, N. I.; Olson, B. P.; Ediger, M. N.; Magee, A. J.; Way, J. F.; Vugrin, K. E.; Maynard, J. D. Noninvasive skin fluorescence spectroscopy for detection of abnormal glucose tolerance. *Journal of Clinical & Translational Endocrinology* **2014**, *1* (3), 92-99. DOI: 10.1016/j.jcte.2014.06.003.
(5) HORIBA. Förster resonance energy transfer (FRET).
(6) Meerwaldt, R.; Graaff, R.; Oomen, P. H. N.; Links, T. P.; Jager, J. J.; Alderson, N. L.; Thorpe, S. R.; Baynes, J. W.; Gans, R. O. B.; Smit, A. J. Simple non-invasive assessment of advanced glycation endproduct accumulation. *Diabetologia* **2004**, *47* (7), 1324-1330. DOI: 10.1007/s00125-004-1451-2.
(7) World Health Organisation. *Global Report on Diabetes*; 2016.
(8) Bodiga, V. L.; Eda, S. R.; Bodiga, S. Advanced glycation end products: role in pathology of diabetic cardiomyopathy. *Heart Failure Reviews* **2014**, *19* (1), 49-63. DOI: 10.1007/s10741-013-9374-y.
(9) Solomon, S. D.; Chew, E.; Duh, E. J.; Sobrin, L.; Sun, J. K.; Vanderbeek, B. L.; Wykoff, C. C.; Gardner, T. W. Diabetic Retinopathy: A Position Statement by the American Diabetes Association. *Diabetes Care* **2017**, *40* (3), 412-418. DOI: 10.2337/dc16-2641. Nathan, D. M. Long-Term Complications of Diabetes Mellitus. *New England Journal of Medicine* **1993**, *328* (23), 1676-1685. DOI: 10.1056/nejm199306103282306.
(10) Resnick, H. E.; Howard, B. V. Diabetes and Cardiovascular Disease. *Annual Review of Medicine* **2002**, *53* (1), 245-267. DOI: 10.1146/annurev.med.53.082901.103904.
(11) Orasanu, G.; Plutzky, J. The Pathologic Continuum of Diabetic Vascular Disease. *Journal of the American College of Cardiology* **2009**, *53* (5), S35-S42. DOI: 10.1016/j.jacc.2008.09.055.
(12) Khoury, J. C.; Kleindorfer, D.; Alwell, K.; Moomaw, C. J.; Woo, D.; Adeoye, O.; Flaherty, M. L.; Khatri, P.; Ferioli, S.; Broderick, J. P.; et al. Diabetes Mellitus. *Stroke* **2013**, *44* (6), 1500-1504. DOI: 10.1161/strokeaha.113.001318.
(13) Schrijvers, B. F.; De Vriese, A. S.; Flyvbjerg, A. From Hyperglycemia to Diabetic Kidney Disease: The Role of Metabolic, Hemodynamic, Intracellular Factors and Growth Factors/Cytokines. *Endocrine Reviews* **2004**, *25* (6), 971-1010. DOI: 10.1210/er.2003-0018.
(14) Frank, R. N. Diabetic Retinopathy. *New England Journal of Medicine* **2004**, *350* (1), 48-58. DOI: 10.1056/nejmra021678.
(15) Marshall, S. M. Recent advances in diabetic nephropathy. *Postgraduate Medical Journal* **2004**, *80* (949), 624-633. DOI: 10.1136/pgmj.2004.021287.
(16) Papatheodorou, K.; Banach, M.; Edmonds, M.; Papanas, N.; Papazoglou, D. Complications of Diabetes. *Journal of Diabetes Research* **2015**, *2015*, 1-5. DOI: 10.1155/2015/189525.
(17) World Health Organisation. *The top 10 causes of death*. 2020. (accessed 2021 10.05.21).
(18) *IDF Diabetes Atlas*; rev. 8

2017.

(19) *IDF Diabetes Atlas*; rev. 4; Federation, I. D., 2009.
(20) Saeedi, P.; Petersohn, I.; Salpea, P.; Malanda, B.; Karuranga, S.; Unwin, N.; Colagiuri, S.; Guariguata, L.; Motala, A. A.; Ogurtsova, K.; et al. Global and regional diabetes prevalence estimates for 2019 and projections for 2030 and 2045: Results from the International Diabetes Federation Diabetes Atlas, 9th edition. *Diabetes Research and Clinical Practice* **2019**, *157*, 107843. DOI: 10.1016/j.diabres.2019.107843.
(21) Diabetes.co.uk. *Type 2 Diabetes*. 2019. https://www.diabetes.co.uk/type2-diabetes.html#:~:text=Type%202%20diabetes%20was%20formerly,of%20all%20diabetes%20cases%20worldwide. (accessed 12.05.21).
(22) The Diabetes Control and Complications Trial Research Group. The Effect of Intensive Treatment of Diabetes on the Development and Progression of Long-Term Complications in Insulin-Dependent Diabetes Mellitus. *New England Journal of Medicine* **1993**, *329* (14), 977-986. DOI: 10.1056/nejm199309303291401.
(23) National Institute for Health and Care Excellence. NICE Guidelines, Type 1 diabetes in adults: diagnsosis and management. United Kingdom, 2015.
(24) Turner, A. P. F.; Chen, B.; Piletsky, S. A. In Vitro Diagnsotics in Diabetes: Metting the Challenge. *Clinical Chemistry* **1999**, *45* (9), 1596-1601.
(25) Peyrot, M.; Rubin, R. R.; Lauritzen, T.; Snoek, F. J.; Matthews, D. R.; Skovlund, S. E. Psychosocial problems and barriers to improved diabetes management: results of the Cross-National Diabetes Attitudes, Wishes and Needs (DAWN) Study. *Diabetic Medicine* **2005**, *22* (10), 1379-1385. DOI: 10.1111/j.1464-5491.2005.01644.x. Simmons, J. H.; Chen, V.; Miller, K. M.; McGill, J. B.; Bergenstal, R. M.; Goland, R. S.; Harlan, D. M.; Largay, J. F.; Massaro, E. M.; Beck, R. W. Differences in the Management of Type 1 Diabetes Among Adults Under Excellent Control Compared With Those Under Poor Control in the T1D Exchange Clinic Registry. *Diabetes Care* **2013**, *36* (11), 3573-3577. DOI: 10.2337/dc12-2643.
(26) NHS. *Continuous Glucose Monitoring (CGM) and flash*. NHS, 2021. https://www.nhs.uk/conditions/type-1-diabetes/managing-blood-glucose-levels/continuous-glucose-monitoring-cgm-and-flash/ (accessed 2022 12.05.2022).
(27) Alva, S.; Bailey, T.; Brazg, R.; Budiman, E. S.; Castorino, K.; Christiansen, M. P.; Forlenza, G.; Kipnes, M.; Liljenquist, D. R.; Liu, H. Accuracy of a 14-Day Factory-Calibrated Continuous Glucose Monitoring System With Advanced Algorithm in Pediatric and Adult Population With Diabetes. *Journal of Diabetes Science and Technology* **2022**, *16* (1), 70-77. DOI: 10.1177/1932296820958754.
(28) NHS. *Continuous Glucose Monitoring (CGMs)*. 2018. https://www.nhs.uk/conditions/type-1-diabetes/continuous-glucose-monitoring-cgms/#:~:text=You%20can%20check%20your%20sugar,is%20too%20high%20or%20low. (accessed 12.05.21).
(29) Haak, T.; Hanaire, H.; Ajjan, R.; Hermanns, N.; Riveline, J.-P.; Rayman, G. Flash Glucose-Sensing Technology as a Replacement for Blood Glucose Monitoring for the Management of Insulin-Treated Type 2 Diabetes: a Multicenter, Open-Label Randomized Controlled Trial. *Diabetes Therapy* **2017**, *8* (1), 55-73. DOI: 10.1007/s13300-016-0223-6.
(30) Wada, E.; Onoue, T.; Kobayashi, T.; Handa, T.; Hayase, A.; Ito, M.; Furukawa, M.; Okuji, T.; Okada, N.; Iwama, S.; et al. Flash glucose monitoring helps achieve better glycemic control than conventional self-monitoring of blood glucose in non-insulin-treated type 2 diabetes: a randomized controlled trial. *BMJ Open Diabetes Research & Care* **2020**, *8* (1), e001115. DOI: 10.1136/bmjdrc-2019-001115.
(31) Yaron, M.; Roitman, E.; Aharon-Hananel, G.; Landau, Z.; Ganz, T.; Yanuv, I.; Rozenberg, A.; Karp, M.; Ish-Shalom, M.; Singer, J.; et al. Effect of Flash Glucose Monitoring Technology on Glycemic Control and Treatment Satisfaction in Patients With Type 2 Diabetes. *Diabetes Care* **2019**, *42* (7), 1178-1184. DOI: 10.2337/dc18-0166.

(32) NHS. Lifechanging technology to be rolled out to all type 1 diabetes patients. NHS England: www.england.nhs.uk, 2022.
(33) Sherwani, S. I.; Khan, H. A.; Ekhzaimy, A.; Masood, A.; Sakharkar, M. K. Significance of HbA1c Test in Diagnosis and Prognosis of Diabetic Patients. *Biomarker Insights* **2016**, *11*, BMI.S38440. DOI: 10.4137/bmi.s38440.
(34) Radin, M. S. Pitfalls in Hemoglobin A1c Measurement: When Results may be Misleading. *Journal of General Internal Medicine* **2014**, *29* (2), 388-394. DOI: 10.1007/s11606-013-2595-x.
(35) Ahmad, J.; Rafat, D. HbA1c and iron deficiency: a review. *Diabetes Metab Syndr* **2013**, *7* (2), 118-122. DOI: 10.1016/j.dsx.2013.02.004 From NLM.
(36) Gan, T.; Liu, X.; Xu, G. Glycated Albumin Versus HbA1c in the Evaluation of Glycemic Control in Patients With Diabetes and CKD. *Kidney International Reports* **2018**, *3* (3), 542-554. DOI: 10.1016/j.ekir.2017.11.009.
(37) Anguizola, J.; Matsuda, R.; Barnaby, O. S.; Hoy, K. S.; Wa, C.; DeBolt, E.; Koke, M.; Hage, D. S. Review: Glycation of human serum albumin. *Clin Chim Acta* **2013**, *425*, 64-76. DOI: 10.1016/j.cca.2013.07.013 From NLM.
(38) Furusyo, N.; Hayashi, J. Glycated albumin and diabetes mellitus. *Biochim Biophys Acta* **2013**, *1830* (12), 5509-5514. DOI: 10.1016/j.bbagen.2013.05.010 From NLM.
(39) Kim, I. Y.; Kim, M. J.; Lee, D. W.; Lee, S. B.; Rhee, H.; Song, S. H.; Seong, E. Y.; Kwak, I. S. Glycated albumin is a more accurate glycaemic indicator than haemoglobin A_{1c}in diabetic patients with pre-dialysis chronic kidney disease. *Nephrology* **2015**, *20* (10), 715-720. DOI: 10.1111/nep.12508.
(40) Peacock, T. P.; Shihabi, Z. K.; Bleyer, A. J.; Dolbare, E. L.; Byers, J. R.; Knovich, M. A.; Calles-Escandon, J.; Russell, G. B.; Freedman, B. I. Comparison of glycated albumin and hemoglobin A1c levels in diabetic subjects on hemodialysis. *Kidney International* **2008**, *73* (9), 1062-1068. DOI: 10.1038/ki.2008.25.
(41) Tsuruta, Y.; Ichikawa, A.; Kikuchi, K.; Echida, Y.; Onuki, T.; Nitta, K. Glycated albumin is a better indicator of the glucose excursion than predialysis glucose and hemoglobin A1c in hemodialysis patients. *Renal Replacement Therapy* **2016**, *2* (1). DOI: 10.1186/s41100-016-0013-7.
(42) Singh, V. P.; Bali, A.; Singh, N.; Jaggi, A. S. Advanced Glycation End Products and Diabetic Complications. *The Korean Journal of Physiology & Pharmacology* **2014**, *18* (1), 1. DOI: 10.4196/kjpp.2014.18.1.1.
(43) Negre-Salvayre, A.; Salvayre, R.; Auge, N.; Pamplona, R.; Portero-Otin, M. Hyperglycaemia and Glycation in Diabetic Complications. *Antioxidants and Redox Signaling* **2009**, *11* (12).
(44) Maillard, L. C. Action des acides aminés sur les sucres; formation des méla-noidines par voie methodique. *Comptes Rendus de l'Académie des Sciences* **1912**, *154*, 66-68.
(45) Simm, A.; Müller, B.; Nass, N.; Hofmann, B.; Bushnaq, H.; Silber, R.-E.; Bartling, B. Protein glycation — Between tissue aging and protection. *Experimental Gerontology* **2015**, *68*, 71-75. DOI: 10.1016/j.exger.2014.12.013.
(46) Sadowska-Bartosz, I.; Bartosz, G. Effect of glycation inhibitors on aging and age-related diseases. *Mechanisms of Ageing and Development* **2016**, *160*, 1-18. DOI: 10.1016/j.mad.2016.09.006.
(47) Schmidt, A. M.; Yan, S. D.; Wautier, J.-L.; Stern, D. Activation of Receptor for Advanced Glycation End Products. *Circulation Research* **1999**, *84* (5), 489-497. DOI: 10.1161/01.res.84.5.489.
(48) Stitt, A. W. AGEs and Diabetic Retinopathy. *Investigative Opthalmology & Visual Science* **2010**, *51* (10), 4867. DOI: 10.1167/iovs.10-5881.

(49) Ahmed, N. Advanced glycation endproducts—role in pathology of diabetic complications. *Diabetes Research and Clinical Practice* **2005**, *67* (1), 3-21. DOI: 10.1016/j.diabres.2004.09.004.
(50) Hsieh, C.-L.; Yang, M.-H.; Chyau, C.-C.; Chiu, C.-H.; Wang, H.-E.; Lin, Y.-C.; Chiu, W.-T.; Peng, R. Y. Kinetic analysis on the sensitivity of glucose- or glyoxal-induced LDL glycation to the inhibitory effect of Psidium guajava extract in a physiomimic system. *Biosystems* **2007**, *88* (1-2), 92-100. DOI: 10.1016/j.biosystems.2006.04.004.
(51) Furber, J. D. Extracellular Glycation Crosslinks: Prospects for Removal. *Rejuvenation Research* **2006**, *9* (2), 274-278.
(52) Ott, C.; Jacobs, K.; Haucke, E.; Navarrete Santos, A.; Grune, T.; Simm, A. Role of advanced glycation end products in cellular signaling. *Redox Biology* **2014**, *2*, 411-429. DOI: 10.1016/j.redox.2013.12.016.
(53) Bucala, R.; Makita, Z.; Vega, G.; Grundy, S.; Koschinsky, T.; Cerami, A.; Vlassara, H. Modification of low density lipoprotein by advanced glycation end products contributes to the dyslipidemia of diabetes and renal insufficiency. *Proceedings of the National Academy of Sciences* **1994**, *91* (20), 9441-9445. DOI: 10.1073/pnas.91.20.9441.
(54) Vitek, M. P.; Bhattacharya, K.; Glendening, J. M.; Stopa, E.; Vlassara, H.; Bucala, R.; Manogue, K.; Cerami, A. Advanced glycation end products contribute to amyloidosis in Alzheimer disease. *Proceedings of the National Academy of Sciences* **1994**, *91* (11), 4766-4770. DOI: 10.1073/pnas.91.11.4766.
(55) Berg, T. J.; Bangstad, H. J.; Torjesen, P. A.; Osterby, R.; Bucala, R.; Hanssen, K. F. Advanced glycation end products in serum predict changes in the kidney morphology of patients with insulin-dependent diabetes mellitus. *Metabolism* **1997**, *46* (6), 661-665.
(56) Kilhovd, B. K.; Berg, T. J.; Birkeland, K. I.; Thorsby, P.; Hanssen, K. F. Serum levels of advanced glycationd end products are increased with pateints with type 2 diabetes and coronary heart disease *Diabetes Care* **1999**, *22* (9), 1543-1548.
(57) Yoshida, N.; Okumara, K.-i.; Aso, Y. High serum pentosidine concentrations are associated with increased arterial stiffness and thickness in patients with type 2 diabetes. *Metabolism* **2005**, *54* (3), 345-350.
(58) Beisswenger, P. J.; Makita, Z.; Curphey, T. J.; Moore, L. L.; Jean, S.; Brinck-Johnsen, T.; Bucala, R.; Vlassara, H. Formation of Immunochemical Advanced Glycosylation End Products Precedes and Correlates With Early Manifestations of Renal and Retinal Disease in Diabetes. *Diabetes* **1995**, *44* (7), 824-829. DOI: 10.2337/diab.44.7.824.
(59) The DCCT Research Group. The Effect of Intensive Treatment of Diabetes on the Development and Progression of Long-Term Complications in Insulin-Dependent Diabetes Mellitus. *New England Journal of Medicine* **1993**, *329* (14), 977-986. DOI: 10.1056/nejm199309303291401.
(60) Monnier, V. M. M. D.; Vishwanath, V. B. A.; Frank, K. E. M. D.; Elmets, C. A. M. D.; Dauchot, P. M. D.; Kohn, R. R. P. M. D. Relation between Complications of Type I Diabetes Mellitus and Collagen-Linked Fluorescence. *The New England Journal of Medicine* **1986**, *314* (7), 403-408. DOI: http://dx.doi.org/10.1056/NEJM198602133140702 SciTech Premium Collection.
(61) Sell, D. R.; Lapolla, A.; Odetti, P.; Fogarty, J.; Monnier, V. M. Pentosidine Formation in Skin Correlates With Severity of Complications in Individuals With Long-Standing IDDM. *Diabetes* **1992**, *41* (10), 1286-1292. DOI: 10.2337/diab.41.10.1286.
(62) Genuth, S.; Sun, W.; Cleary, P.; Sell, D. R.; Dahms, W.; Malone, J.; Sivitz, W.; Monnier, V. M. Glycation and Carboxymethyllysine Levels in Skin Collagen Predict the Risk of Future 10-Year Progression of Diabetic Retinopathy and Nephropathy in the Diabetes Control and Complications Trial and Epidemiology of Diabetes Interventions and Complications P. *Diabetes* **2005**, *54* (11), 3103-3111. DOI: 10.2337/diabetes.54.11.3103.

(63) Monnier, V. M.; Bautista, O.; Kenny, D.; Sell, D. R.; Fogarty, J.; Dahms, W.; Cleary, P. A.; Lachin, J.; Genuth, S. Skin collagen glycation, glycoxidation, and crosslinking are lower in subjects with long-term intensive versus conventional therapy of type 1 diabetes: relevance of glycated collagen products versus HbA1c as markers of diabetic complications. . *Diabetes* **1999**, *48* (4), 870-880. DOI: 10.2337/diabetes.48.4.870.
(64) Petrova, R.; Yamamoto, Y.; Muraki, K.; Yonekura, H.; Sakurai, S.; Watanabe, T.; Li, H.; Takeuchi, M.; Makita, Z.; Kato, I.; et al. Advanced glycation endproduct-induced calcium handling impairment in mouse cardiac myocytes. *J Mol Cell Cardiol* **2002**, *34* (10), 1425-1431. DOI: 10.1006/jmcc.2002.2084 From NLM.
(65) Hof, M.; Fidler, V.; Hutterer, R. Basics of Fluorescence Spectroscopy in Biosciences. Springer-Verlag, 2005; pp 3-29.
(66) Croce, A. C.; Bottiroli, G. Autofluorescence spectroscopy and imaging: a tool for biomedical research and diagnosis. *European Journal of Histochemistry* **2014**, *58* (4). DOI: 10.4081/ejh.2014.2461.
(67) Georgakoudi, I.; Jacobson, B. C.; Müller, M. G.; Sheets, E. E.; Badizadegan, K.; Carr-Locke, D. L.; Crum, C. P.; Boone, C. W.; Dasari, R. R.; Van Dam, J.; et al. NAD(P)H and Collagen as in Vivo> Quantitative Fluorescent Biomarkers of Epithelial Precancerous Changes. *Cancer Research* **2002**, *62* (3), 682-687. Tajaddini, A.; Scoffone, H. M.; Botek, G.; Davis, B. L. Laser-induced auto-fluorescence (LIAF) as a method for assessing skin stiffness preceding diabetic ulcer formation. *Journal of Biomechanics* **2007**, *40* (4), 736-741. DOI: 10.1016/j.jbiomech.2006.10.011.
(68) Kollias, N.; Zonios, G.; Stamatas, G. N. Fluorescence spectroscopy of skin. *Vibrational Spectroscopy* **2002**, *28* (1), 17-23. DOI: 10.1016/s0924-2031(01)00142-4.
(69) Gillies, R.; Zonios, G.; Rox Anderson, R.; Kollias, N. Fluorescence Excitation Spectroscopy Provides Information About Human Skin In Vivo. *Journal of Investigative Dermatology* **2000**, *115* (4), 704-707. DOI: 10.1046/j.1523-1747.2000.00091.x.
(70) De Ruyck, J.; Famerée, M.; Wouters, J.; Perpète, E. A.; Preat, J.; Jacquemin, D. Towards the understanding of the absorption spectra of NAD(P)H/NAD(P)+ as a common indicator of dehydrogenase enzymatic activity. *Chemical Physics Letters* **2007**, *450* (1-3), 119-122. DOI: 10.1016/j.cplett.2007.10.092.
(71) Perrone, A.; Giovino, A.; Benny, J.; Martinelli, F. Advanced Glycation End Products (AGEs): Biochemistry, Signaling, Analytical Methods, and Epigenetic Effects. *Oxidative Medicine and Cellular Longevity* **2020**, *2020*, 1-18. DOI: 10.1155/2020/3818196.
(72) Smit, A. J.; Gerrits, E. G. Skin autofluorescence as a measure of advanced glycation endproduct deposition: a novel risk marker in chronic kidney disease. *Current Opinion in Nephrology and Hypertension* **2010**, *19* (6), 527-533. DOI: 10.1097/MNH.0b013e32833e9259. Samborski, P.; Naskręt, D.; Araszkiewicz, A.; Niedźwiecki, P.; Zozulińska-Ziółkiewicz, D.; Wierusz-Wysocka, B. Assessment of skin autofluorescence as a marker of advanced glycation end product accumulation in type 1 diabetes. *Pol Arch Med Wewn* **2011**, *121* (3), 67-72. From NLM.
(73) Jager, J.; Oomen, P. H. N.; Sluiter, W. J.; Reitsma, W. D.; Smit, A. J. Improved Reproducibility of the 'Large-Window' Method of Assessing Transcapillary and Interstitial Fluorescein Diffusion in the Skin in Healthy Subjects and in Subjects with Insulin-Dependent Diabetes mellitus. *International Journal of Microcirculation* **1997**, *17* (3), 150-158. DOI: 10.1159/000179223.
(74) Sternberg, M.; M'Bemba, J.; Urios, P.; Borsos, A.-M.; Selam, J.-L.; Peyroux, J.; Slama, G. Skin collagen pentosidine and fluorescence in diabetes were predictors of retinopathy progression and creatininemia increase already 6years after punch-biopsy. *Clinical Biochemistry* **2016**, *49* (3), 225-231. DOI: 10.1016/j.clinbiochem.2015.10.011.

(75) Dorrian, C. A.; Cathcart, S.; Clausen, J.; Shapiro, D.; Dominiczak, M. H. Factors in human serum interfere with the measurement of advanced glycation endproducts. *Cell Mol Biol (Noisy-le-grand)* **1998**, *44* (7), 1069-1079. From NLM.
(76) Lutgers, H. L.; Graaff, R.; Links, T. P.; Ubink-Veltmaat, L. J.; Bilo, H. J.; Gans, R. O.; Smit, A. J. Skin Autofluorescence as a Noninvasive Marker of Vascular Damage in Patients With Type 2 Diabetes. *Diabetes Care* **2006**, *29* (12), 2654-2659. DOI: 10.2337/dc05-2173. Gerrits, E. G.; Lutgers, H. L.; Kleefstra, N.; Graaff, R.; Groenier, K. H.; Smit, A. J.; Gans, R. O.; Bilo, H. J. Skin Autofluorescence: A tool to identify type 2 diabetic patients at risk for developing microvascular complications. *Diabetes Care* **2008**, *31* (3), 517-521. DOI: 10.2337/dc07-1755.
(77) Meerwaldt, R.; Links, T. P.; Graaff, R.; Hoogenberg, K.; Lefrandt, J. D.; Baynes, J. W.; Gans, R. O. B.; Smit, A. J. Increased accumulation of skin advanced glycation end-products precedes and correlates with clinical manifestation of diabetic neuropathy. *Diabetologia* **2005**, *48* (8), 1637-1644. DOI: 10.1007/s00125-005-1828-x.
(78) Tentolouris, N.; Lathouris, P.; Lontou, S.; Tzemos, K.; Maynard, J. Screening for HbA1c-defined prediabetes and diabetes in an at-risk greek population: performance comparison of random capillary glucose, the ADA diabetes risk test and skin fluorescence spectroscopy. *Diabetes Res Clin Pract* **2013**, *100* (1), 39-45. DOI: 10.1016/j.diabres.2013.01.002 From NLM.
(79) Stokes, G. G. XXX. On the change of refrangibility of light. *Philosophical Transactions of the Royal Society of London* **1852**, *142* (0), 463-562. DOI: 10.1098/rstl.1852.0022.
(80) Birch, D. J. S.; Chen, Y.; Rolinski, O. J. Fluorescence. In *Photonics*, 2015; pp 1-58.
(81) Valeur, B.; Berberan-Santos, M. N. A Brief History of Fluorescence and Phosphorescence before the Emergence of Quantum Theory. *Journal of Chemical Education* **2011**, *88* (6), 731-738. DOI: 10.1021/ed100182h.
(82) Jabłoński, A. Über den Mechanismus der Photolumineszenz von Farbstoffphosphoren. *Zeitschrift für Physik* **1935**, *94* (1-2), 38-46. DOI: 10.1007/bf01330795.
(83) Kasha, M. Characterization of electronic transitions in complex molecules. *Discussions of the Faraday Society* **1950**, *9*, 14. DOI: 10.1039/df9500900014.
(84) Herzberg, G. *Molecular Spectra and Molecular Structure*; D.Van Nostrand Company Inc., 1950.
(85) Toptygin, D.; Brand, L. Spectrally- and time-resolved fluorescence emission of indole during solvent relaxation: a quantitative model. *Chemical Physics Letters* **2000**, *322* (6), 496-502. DOI: 10.1016/s0009-2614(00)00460-7.
(86) Franck, J.; Dymond, E. G. Elementary processes of photochemical reactions. *Transactions of the Faraday Society* **1926**, *21* (February), 536. DOI: 10.1039/tf9262100536.
(87) Condon, E. A Theory of Intensity Distribution in Band Systems. *Physical Review* **1926**, *28* (6), 1182-1201. DOI: 10.1103/physrev.28.1182.
(88) Condon, E. U. Nuclear Motions Associated with Electron Transitions in Diatomic Molecules. *Physical Review* **1928**, *32* (6), 858-872. DOI: 10.1103/physrev.32.858.
(89) Valeur, B. *Molecular Fluorescence: Principles and Applications*; Wiley-VCH, 2001. DOI: 10.1002/3527600248.
(90) Becker, W.; Bergmann, A.; Hink, M. A.; Konig, K.; Benndorf, K.; Biskup, C. Fluorescence lifetime imaging by time-correlated single-photon counting. *Microsc Res Tech* **2004**, *63* (1), 58-66. DOI: 10.1002/jemt.10421.
(91) Meredith, S. A.; Kusunoki, Y.; Connell, S. D.; Morigaki, K.; Evans, S. D.; Adams, P. G. Self-Quenching Behavior of a Fluorescent Probe Incorporated within Lipid Membranes Explored Using Electrophoresis and Fluorescence Lifetime Imaging Microscopy. *The Journal of Physical Chemistry B* **2023**, *127* (8), 1715-1727. DOI: 10.1021/acs.jpcb.2c07652.

(92) Arık, M.; Çelebi, N.; Onganer, Y. Fluorescence quenching of fluorescein with molecular oxygen in solution. *Journal of Photochemistry and Photobiology A: Chemistry* **2005**, *170* (2), 105-111. DOI: 10.1016/j.jphotochem.2004.07.004.
(93) Giri, R. Fluorescence quenching of coumarins by halide ions. *Spectrochimica Acta Part A: Molecular and Biomolecular Spectroscopy* **2004**, *60* (4), 757-763. DOI: 10.1016/s1386-1425(03)00287-7.
(94) Förster, T. Energy migration and fluorescence. *Journal of Biomedical Optics* **2012**, *17* (1), 1. DOI: 10.1117/1.JBO.17.1.011002.
(95) Chhabra, D.; dos Remedios, C. G. Fluorescence Resonance Energy Transfer. *Nature Encyclopedia of Life Sciences* **2005**. DOI: https://doi.org/10.1038/npg.els.0004170.
(96) Sobakinskaya, E.; Schmidt Am Busch, M.; Renger, T. Theory of FRET "Spectroscopic Ruler" for Short Distances: Application to Polyproline. *J Phys Chem B* **2018**, *122* (1), 54-67. DOI: 10.1021/acs.jpcb.7b09535.
(97) Gobrecht, A.; Bendoula, R.; Roger, J.-M.; Bellon-Maurel, V. Combining linear polarization spectroscopy and the Representative Layer Theory to measure the Beer–Lambert law absorbance of highly scattering materials. *Analytica Chimica Acta* **2015**, *853*, 486-494. DOI: 10.1016/j.aca.2014.10.014. Leblanc, S. E.; Atanya, M.; Burns, K.; Munger, R. Quantitative impact of small angle forward scatter on whole blood oximetry using a Beer–Lambert absorbance model. *The Analyst* **2011**, *136* (8), 1637. DOI: 10.1039/c0an00996b.
(98) Quaranta, A.; McGarvey, D. J.; Land, E. J.; Brettreich, M.; Burghardt, S.; Schönberger, H.; Hirsch, A.; Gharbi, N.; Moussa, F.; Leach, S.; et al. Photophysical properties of a dendritic methano[60]fullerene octadeca acid and its tert-butyl ester: evidence for aggregation of the acid form in water. *Physical Chemistry Chemical Physics* **2003**, *5* (5), 843-848. DOI: 10.1039/b209258a. Kang, Y.; Cai, Z.; Tang, X.; Liu, K.; Wang, G.; Zhang, X. An Amylase-Responsive Bolaform Supra-Amphiphile. *ACS Applied Materials & Interfaces* **2016**, *8* (7), 4927-4933. DOI: 10.1021/acsami.5b12573. Helmich, F.; Lee, C. C.; Nieuwenhuizen, M. M. L.; Gielen, J. C.; Christianen, P. C. M.; Larsen, A.; Fytas, G.; Leclère, P. E. L. G.; Schenning, A. P. H. J.; Meijer, E. W. Dilution-Induced Self-Assembly of Porphyrin Aggregates: A Consequence of Coupled Equilibria. *Angewandte Chemie International Edition* **2010**, *49* (23), 3939-3942. DOI: 10.1002/anie.201000162.
(99) HORIBA. Time-resolved fluorescence anisotropy, Tech. Note TRFT-2.
(100) HORIBA. Time-resolved fluorescence lifetime measurements Tech. note TRFT.1.
(101) HORIBA. DataStation v2.4: Software for single photon counting data acquisition, Operating Guide.
(102) Rolinski, O. J.; Wellbrock, T.; Birch, D. J. S.; Vyshemirsky, V. Tyrosine Photophysics During the Early Stages of β-Amyloid Aggregation Leading to Alzheimer's. *The Journal of Physical Chemistry Letters* **2015**, *6* (15), 3116-3120. DOI: 10.1021/acs.jpclett.5b01285.
(103) Rolinski, O. J.; Vyshemirsky, V. Fluorescence kinetics of tryptophan in a heterogeneous environment. *Methods and Applications in Fluorescence* **2016**, *4*. DOI: 10.1088/2050-6120.
(104) Rolinski, O. J.; McLaughlin, D.; Birch, D. J. S.; Vyshemirsky, V. Resolving environmental microheterogeneity and dielectric relaxation in fluorescence kinetics of protein. *Methods and Applications in Fluorescence* **2016**, *4* (2), 024001. DOI: 10.1088/2050-6120/4/2/024001.
(105) Weron, K.; Jurlewicz, A. Two forms of self-similarity as a fundamental feature of the power-law dielectric response. *Journal of Physics A: Mathematical and General* **1993**, *26* (2), 395-410. DOI: 10.1088/0305-4470/26.
(106) Berberan-Santos, M. N.; Bodunov, E. N.; Valeur, B. Mathematical functions for the analysis of luminescence decays with underlying distributions: 2. Becquerel (compressed hyperbola) and related decay functions. *Chemical Physics* **2005**, *317* (1), 57-62. DOI: https://doi.org/10.1016/j.chemphys.2005.05.026.

(107) HORIBA. DAS6: Fluorescence Decay Analysis Software, User Guide.
(108) Ganoza-Quintana, J. L.; Fanjul-Velez, F.; Arce-Diego, J. L. Light propogation in highly scattering biological tissues analysed by Green's functions. In *SPIE BiOS* San Francisco, California. United States, 2019; Vol. 10876.
(109) Easter, J. H.; Detoma, R. P.; Brand, L. Nanosecond time-resolved emission spectroscopy of a fluorescence probe adsorbed to L-alpha-egg lecithin vesicles. *Biophysical Journal* **1976**, *16* (6), 571-583. DOI: 10.1016/s0006-3495(76)85712-8.
(110) Meech, S. R.; O'Connor, D. V.; Roberts, A. J.; Phillips, D. On the Construction of Nanosecond Time-Resolved Emission Spectra. *Photochemistry and Photobiology* **1981**, *33* (2), 159-172. DOI: 10.1111/j.1751-1097.1981.tb05319.x.
(111) Burnham, K. P.; Anderson, D. R. *Model Selection and Multimodel Inference: A Practical Information-Theoretic Approach*; Springer, 2002.
(112) Leblanc, L.; Dufour, Ã. R. Monitoring the identity of bacteria using their intrinsic fluorescence. *FEMS Microbiology Letters* **2002**, *211* (2), 147-153. DOI: 10.1111/j.1574-6968.2002.tb11217.x.
(113) Fratzl, P. Collagen: Structure and Mechanics, an Introduction. In *Collagen*, Springer US, 2008; pp 1-13.
(114) Ottani, V.; Raspanti, M.; Ruggeri, A. Collagen structure and functional implications. *Micron* **2001**, *32* (3), 251-260. DOI: 10.1016/s0968-4328(00)00042-1 From NLM.
(115) Fratzl, P. Cellulose and collagen: From fibres to tissues. *Current Opinion in Colloid & Interface Science* **2003**, *8*, 32-39. DOI: 10.1016/S1359-0294(03)00011-6.
(116) Shoulders, M. D.; Raines, R. T. Collagen Structure and Stability. *Annual Review of Biochemistry* **2009**, *78* (1), 929-958. DOI: 10.1146/annurev.biochem.77.032207.120833.
(117) Cheng, W.; Yan-hua, R.; Fang-gang, N.; Guo-an, Z. The content and ratio of type I and III collagen in skin differ with age and injury *African Journal of Biotechnology* **2011**, *10* (13), 2524-2529. DOI: 10.4314/ajb.v10i13.
(118) Chang, S.-W.; Buehler, M. J. Molecular biomechanics of collagen molecules. *Materials Today* **2014**, *17* (2), 70-76. DOI: 10.1016/j.mattod.2014.01.019.
(119) Boudko, S. P.; Engel, J.; Okuyama, K.; Mizuno, K.; Bächinger, H. P.; Schumacher, M. A. Crystal Structure of Human Type III Collagen Gly991–Gly1032 Cystine Knot-containing Peptide Shows Both 7/2 and 10/3 Triple Helical Symmetries. *Journal of Biological Chemistry* **2008**, *283* (47), 32580-32589. DOI: 10.1074/jbc.m805394200.
(120) Myllyharju, J. Prolyl 4-hydroxylases, the key enzymes of collagen biosynthesis. *Matrix Biol* **2003**, *22* (1), 15-24. DOI: 10.1016/s0945-053x(03)00006-4 From NLM.
(121) Prockop, D. J.; Kivirikko, K. I.; Tuderman, L.; Guzman, N. A. The biosynthesis of collagen and its disorders (first of two parts). *N Engl J Med* **1979**, *301* (1), 13-23. DOI: 10.1056/nejm197907053010104 From NLM.
(122) Canelón, S. P.; Wallace, J. M. β-Aminopropionitrile-Induced Reduction in Enzymatic Crosslinking Causes In Vitro Changes in Collagen Morphology and Molecular Composition. *PLOS ONE* **2016**, *11* (11). DOI: 10.1371/journal.pone.0166392.
(123) Bulleid, N. J.; Wilson, R.; Lees, J. F. Type-III procollagen assembly in semi-intact cells: chain association, nucleation and triple-helix folding do not require formation of inter-chain disulphide bonds but triple-helix nucleation does require hydroxylation. *Biochemical Journal* **1996**, *317* (1), 195-202. DOI: 10.1042/bj3170195.
(124) Orgel, J. P. R. O.; Irving, T. C.; Miller, A.; Wess, T. J. Microfibrillar structure of type I collagen in situ. *Proceedings of the National Academy of Sciences* **2006**, *103* (24), 9001-9005. DOI: 10.1073/pnas.0502718103.
(125) Hulmes, D. J.; Miller, A.; Parry, D. A.; Piez, K. A.; Woodhead-Galloway, J. Analysis of the primary structure of collagen for the origins of molecular packing. *J Mol Biol* **1973**, *79* (1), 137-148. DOI: 10.1016/0022-2836(73)90275-1 From NLM.

(126) Bozec, L.; Odlyha, M. Thermal Denaturation Studies of Collagen by Microthermal Analysis and Atomic Force Microscopy. *Biophysical Journal* **2011**, *101* (1), 228-236. DOI: 10.1016/j.bpj.2011.04.033.
(127) Avery, N. C.; Sims, T. J.; Bailey, A. J. Quantitative Determination of Collagen Cross-links. Humana Press, 2009; pp 103-121.
(128) Snedeker, J. G.; Gautieri, A. The role of collagen crosslinks in ageing and diabetes - the good, the bad, and the ugly. *Muscles Ligaments Tendons J* **2014**, *4* (3), 303-308. PubMed.
(129) Bailey, A. J. Molecular mechanisms of ageing in connective tissues. *Mech Ageing Dev* **2001**, *122* (7), 735-755. DOI: 10.1016/s0047-6374(01)00225-1 From NLM.
(130) Culav, E. M.; Clark, C. H.; Merrilees, M. J. Connective tissues: matrix composition and its relevance to physical therapy. *Phys Ther* **1999**, *79* (3), 308-319. From NLM.
(131) Avery, N. C.; Bailey, A. J. The effects of the Maillard reaction on the physical properties and cell interactions of collagen. *Pathologie Biologie* **2006**, *54* (7), 387-395. DOI: 10.1016/j.patbio.2006.07.005.
(132) Verzijl, N.; DeGroot, J.; Oldehinkel, E.; Bank, R. A.; Thorpe, S. R.; Baynes, J. W.; Bayliss, M. T.; Bijlsma, J. W.; Lafeber, F. P.; Tekoppele, J. M. Age-related accumulation of Maillard reaction products in human articular cartilage collagen. *Biochem J* **2000**, *350 Pt 2* (Pt 2), 381-387. PubMed.
(133) Reigle, K. L.; Di Lullo, G.; Turner, K. R.; Last, J. A.; Chervoneva, I.; Birk, D. E.; Funderburgh, J. L.; Elrod, E.; Germann, M. W.; Surber, C.; et al. Non-enzymatic glycation of type I collagen diminishes collagen-proteoglycan binding and weakens cell adhesion. *Journal of Cellular Biochemistry* **2008**, *104* (5), 1684-1698. DOI: 10.1002/jcb.21735.
(134) Usha, R.; Jaimohan, S. M.; Rajaram, A.; Mandal, A. B. Aggregation and self assembly of non-enzymatic glycation of collagen in the presence of amino guanidine and aspirin: an in vitro study. *Int J Biol Macromol* **2010**, *47* (3), 402-409. DOI: 10.1016/j.ijbiomac.2010.06.009 From NLM.
(135) Cooper, M. E.; Bonnet, F.; Oldfield, M.; Jandeleit-Dahm, K. Mechanisms of diabetic vasculopathy: an overview. *Am J Hypertens* **2001**, *14* (5 Pt 1), 475-486. DOI: 10.1016/s0895-7061(00)01323-6 From NLM.
(136) Yuen, A.; Laschinger, C.; Talior, I.; Lee, W.; Chan, M.; Birek, J.; Young, E. W.; Sivagurunathan, K.; Won, E.; Simmons, C. A.; et al. Methylglyoxal-modified collagen promotes myofibroblast differentiation. *Matrix Biol* **2010**, *29* (6), 537-548. DOI: 10.1016/j.matbio.2010.04.004 From NLM.
(137) Makita, Z.; Radoff, S.; Rayfield, E. J.; Yang, Z.; Skolnik, E.; Delaney, V.; Friedman, E. A.; Cerami, A.; Vlassara, H. Advanced Glycosylation End Products in Patients with Diabetic Nephropathy. *New England Journal of Medicine* **1991**, *325* (12), 836-842. DOI: 10.1056/nejm199109193251202.
(138) Fokkens, B. T.; Smit, A. J. Skin fluorescence as a clinical tool for non-invasive assessment of advanced glycation and long-term complications of diabetes. *Glycoconjugate Journal* **2016**, *33* (4), 527-535. DOI: 10.1007/s10719-016-9683-1.
(139) Hori, M.; Yagi, M.; Nomoto, K.; Ichijo, R.; Shimoda, A.; Kitano, T.; Yonei, Y. Experimental models for advanced glycation end product formation using albumin, collagen, elastin, keratin and proteoglycan. *Anti-Aging Medicine* **2012**, *9*, 125-134.
(140) Brennan, M. Changes in Solubility, Non-Enzymatic Glycation, and Fluorescence of Collagen in Tail Tendons from Diabetic Rats. *Journal of Biological Chemistry* **1989**, *264* (35), 20947-20952. DOI: 10.1016/s0021-9258(19)30028-6.
(141) Kollias, N.; Gillies, R.; Moran, M.; Kochevar, I. E.; Anderson, R. R. Endogenous skin fluorescence includes bands that may serve as quantitative markers of aging and photoaging. *J Invest Dermatol* **1998**, *111* (5), 776-780. DOI: 10.1046/j.1523-1747.1998.00377.x From NLM.

(142) Nguyen, T. T.; Gobinet, C.; Feru, J.; Pasco, S. B.; Manfait, M.; Piot, O. Characterization of Type I and IV Collagens by Raman Microspectroscopy: Identification of Spectral Markers of the Dermo-Epidermal Junction. *Spectroscopy: An International Journal* **2012**, *27*, 421-427. DOI: 10.1155/2012/686183.
(143) Teale, F. W. J.; Weber, G. Ultraviolet fluorescence of the aromatic amino acids. *Biochemical Journal* **1957**, *65* (3), 476-482. DOI: 10.1042/bj0650476.
(144) Nuytinck, L. Glycine to tryptophan substitution in type I collagen in a patient with OI type III: a unique collagen mutation. *Journal of Medical Genetics* **2000**, *37* (5), 371-375. DOI: 10.1136/jmg.37.5.371.
(145) Shen, Y.; Zhu, D.; Lu, W.; Liu, B.; Li, Y.; Cao, S. The Characteristics of Intrinsic Fluorescence of Type I Collagen Influenced by Collagenase I. *Applied Sciences* **2018**, *8* (10), 1947. DOI: 10.3390/app8101947.
(146) Kollias, N.; Gillies, R.; Moran, M.; Kochevar, I. E.; Anderson, R. R. Endogenous Skin Fluorescence In Vivo on Human Skin. *Journal of Investigative Dermatology* **1998**, *111* (5), 776-780.
(147) Na, R.; Stender, I. M.; Henriksen, M.; Wulf, H. C. Autofluorescence of human skin is age-related after correction for skin pigmentation and redness. *J Invest Dermatol* **2001**, *116* (4), 536-540. DOI: 10.1046/j.1523-1747.2001.01285.x From NLM.
(148) Meerwaldt, R.; Hartog, J. W. L.; Graaff, R.; Huisman, R. J.; Links, T. P.; Den Hollander, N. C.; Thorpe, S. R.; Baynes, J. W.; Navis, G.; Gans, R. O. B.; et al. Skin Autofluorescence, a Measure of Cumulative Metabolic Stress and Advanced Glycation End Products, Predicts Mortality in Hemodialysis Patients. *Journal of the American Society of Nephrology* **2005**, *16* (12), 3687-3693. DOI: 10.1681/asn.2005020144.
(149) Menter, J. M. Temperature dependence of collagen fluorescence. *Photochemical & Photobiological Sciences* **2006**, *5* (4), 403. DOI: 10.1039/b516429j.
(150) Bolboaca, S.; Jantschi, L. Amino Acids Sequence Analysis on Collagen. *Bulletin USAMV-CN* **2007**, *63-64*.
(151) Pollak, N.; Dölle, C.; Ziegler, M. The power to reduce: pyridine nucleotides – small molecules with a multitude of functions. *Biochemical Journal* **2007**, *402* (2), 205-218. DOI: 10.1042/bj20061638.
(152) Ma, N.; Digman, M. A.; Malacrida, L.; Gratton, E. Measurements of absolute concentrations of NADH in cells using the phasor FLIM method. *Biomed. Opt. Express* **2016**, *7* (7), 2441-2452. DOI: 10.1364/BOE.7.002441.
(153) Hassa, P. O.; Haenni, S. S.; Elser, M.; Hottiger, M. O. Nuclear ADP-ribosylation reactions in mammalian cells: where are we today and where are we going? *Microbiol Mol Biol Rev* **2006**, *70* (3), 789-829. DOI: 10.1128/mmbr.00040-05 From NLM.
(154) Ying, W. NAD+/NADH and NADP+/NADPH in cellular functions and cell death: regulation and biological consequences. *Antioxid Redox Signal* **2008**, *10* (2), 179-206. DOI: 10.1089/ars.2007.1672 From NLM.
(155) Mailloux, R. J.; Lemire, J.; Appanna, V. D. Metabolic networks to combat oxidative stress in Pseudomonas fluorescens. *Antonie van Leeuwenhoek* **2011**, *99* (3), 433-442. DOI: 10.1007/s10482-010-9538-x.
(156) Collins, Y.; Chouchani, E. T.; James, A. M.; Menger, K. E.; Cochemé, H. M.; Murphy, M. P. Mitochondrial redox signalling at a glance. *Journal of Cell Science* **2012**, *125* (4), 801-806. DOI: 10.1242/jcs.098475.
(157) Wu, J.; Jin, Z.; Zheng, H.; Yan, L.-J. Sources and implications of NADH/NAD+ redox imbalance in diabetes and its complications. *Diabetes, Metabolic Syndrome and Obesity: Targets and Therapy* **2016**, 145. DOI: 10.2147/dmso.s106087.

(158) Jankovic, A.; Korac, A.; Buzadzic, B.; Otasevic, V.; Stancic, A.; Daiber, A.; Korac, B. Redox implications in adipose tissue (dys)function—A new look at old acquaintances. *Redox Biology* **2015**, *6*, 19-32. DOI: 10.1016/j.redox.2015.06.018.
(159) Luo, X.; Li, R.; Yan, L.-J. Roles of Pyruvate, NADH, and Mitochondrial Complex I in Redox Balance and Imbalance inβCell Function and Dysfunction. *Journal of Diabetes Research* **2015**, *2015*, 1-12. DOI: 10.1155/2015/512618.
(160) Boesten, D. M. P. H. J.; Von Ungern-Sternberg, S. N. I.; Den Hartog, G. J. M.; Bast, A. Protective Pleiotropic Effect of Flavonoids on NAD+Levels in Endothelial Cells Exposed to High Glucose. *Oxidative Medicine and Cellular Longevity* **2015**, *2015*, 1-7. DOI: 10.1155/2015/894597.
(161) Nikiforov, A.; Kulikova, V.; Ziegler, M. The human NAD metabolome: Functions, metabolism and compartmentalization. *Critical Reviews in Biochemistry and Molecular Biology* **2015**, *50* (4), 284-297. DOI: 10.3109/10409238.2015.1028612. Massudi, H.; Grant, R.; Guillemin, G. J.; Braidy, N. NAD+metabolism and oxidative stress: the golden nucleotide on a crown of thorns. *Redox Report* **2012**, *17* (1), 28-46. DOI: 10.1179/1351000212y.0000000001.
(162) Yan, L.-J. Pathogenesis of Chronic Hyperglycemia: From Reductive Stress to Oxidative Stress. *Journal of Diabetes Research* **2014**, *2014*, 1-11. DOI: 10.1155/2014/137919.
(163) Ames, B. N.; Shigenaga, M. K. Oxidants Are a Major Contributor to Aging. *Annals of the New York Academy of Sciences* **1992**, *663* (1 Aging and Cel), 85-96. DOI: 10.1111/j.1749-6632.1992.tb38652.x. Berlett, B. S.; Stadtman, E. R. Protein Oxidation in Aging, Disease, and Oxidative Stress. *Journal of Biological Chemistry* **1997**, *272* (33), 20313-20316. DOI: 10.1074/jbc.272.33.20313. Anderson, E. J.; Katunga, L. A.; Willis, M. S. Mitochondria as a source and target of lipid peroxidation products in healthy and diseased heart. *Clinical and Experimental Pharmacology and Physiology* **2012**, *39* (2), 179-193. DOI: 10.1111/j.1440-1681.2011.05641.x.
(164) Williamson, J. R.; Chang, K.; Frangos, M.; Hasan, K. S.; Ido, Y.; Kawamura, T.; Nyengaard, J. R.; van den Enden, M.; Kilo, C.; Tilton, R. G. Hyperglycemic pseudohypoxia and diabetic complications. *Diabetes* **1993**, *42* (6), 801-813. DOI: 10.2337/diab.42.6.801 From NLM. Ido, Y.; Kilo, C.; Williamson, J. R. Cytosolic NADH/NAD + , free radicals, and vascular dysfunction in early diabetes mellitus. *Diabetologia* **1997**, *40* (14), S115-S117. DOI: 10.1007/s001250051422.
(165) Yan, L.-J. Redox imbalance stress in diabetes mellitus: Role of the polyol pathway. *Animal Models and Experimental Medicine* **2018**, *1* (1), 7-13. DOI: 10.1002/ame2.12001.
(166) Chance, B.; Cohen, P.; Jobsis, F.; Schoener, B. Intracellular oxidation-reduction states in vivo. *Science* **1962**, *137* (3529), 499-508. DOI: 10.1126/science.137.3529.499 From NLM. Balu, M.; Mazhar, A.; Carole; Mittal, R.; Tatiana; König, K.; Venugopalan, V.; Bruce. In Vivo Multiphoton NADH Fluorescence Reveals Depth-Dependent Keratinocyte Metabolism in Human Skin. *Biophysical Journal* **2013**, *104* (1), 258-267. DOI: 10.1016/j.bpj.2012.11.3809.
(167) Stewart, H.; Hupp, T.; Birch, D. J. NADPH as a potential intrinsic probe for tumour margin estimation. 2018, 2018; SPIE. DOI: 10.1117/12.2287414.
(168) Blacker, T. S.; Marsh, R. J.; Duchen, M. R.; Bain, A. J. Activated barrier crossing dynamics in the non-radiative decay of NADH and NADPH. *Chemical Physics* **2013**, *422*, 184-194. DOI: 10.1016/j.chemphys.2013.02.019.
(169) Evans, N. D.; Gnudi, L.; Rolinski, O. J.; Birch, D. J. S.; Pickup, J. C. Glucose-dependent changes in NAD(P)H-related fluorescence lifetime of adipocytes and fibroblasts in vitro: Potential for non-invasive glucose sensing in diabetes mellitus. *Journal of Photochemistry and Photobiology B: Biology* **2005**, *80* (2), 122-129. DOI: 10.1016/j.jphotobiol.2005.04.001.
(170) Schneckenburger, H. Fluorescence decay kinetics and imaging of NAD(P)H and flavins as metabolic indicators. *Optical Engineering* **1992**, *31* (7). DOI: 10.1117/12.57704.full.

(171) Lakowicz, J. R.; Szmacinski, H.; Nowaczyk, K.; Johnson, M. L. Fluorescence lifetime imaging of free and protein-bound NADH. *Proceedings of the National Academy of Sciences* **1992**, *89* (4), 1271-1275. DOI: 10.1073/pnas.89.4.1271.
(172) Gafni, A.; Brand, L. Fluorescence decay studies of reduced nicotinamide adenine dinucleotide in solution and bound to liver alcohol dehydrogenase. *Biochemistry* **1976**, *15* (15), 3165-3171. DOI: 10.1021/bi00660a001. König, K.; Berns, M. W.; Tromberg, B. J. Time-resolved and steady-state fluorescence measurements of beta-nicotinamide adenine dinucleotide-alcohol dehydrogenase complex during UVA exposure. *J Photochem Photobiol B* **1997**, *37* (1-2), 91-95. DOI: 10.1016/s1011-1344(96)07327-7 From NLM.
(173) Wakita, M.; Nishimura, G.; Tamura, M. Some Characteristics of the Fluorescence Lifetime of Reduced Pyridine Nucleotides in Isolated Mitochondria, Isolated Hepatocytes, and Perfused Rat Liver In Situ. *The Journal of Biochemistry* **1995**, *118* (6), 1151-1160. DOI: 10.1093/oxfordjournals.jbchem.a125001.
(174) Zheng, W.; Li, D.; Qu, J. Y. Monitoring changes of cellular metabolism and microviscosity in vitro based on time-resolved endogenous fluorescence and its anisotropy decay dynamics. *Journal of Biomedical Optics* **2010**, *15* (3). DOI: 10.1117/1.3449577.full.
(175) Jameson, D. M.; Thomas, V.; Zhou, D. Time-resolved fluorescence studies on NADH bound to mitochondrial malate dehydrogenase. *Biochimica et Biophysica Acta (BBA) - Protein Structure and Molecular Enzymology* **1989**, *994* (2), 187-190. DOI: https://doi.org/10.1016/0167-4838(89)90159-3.
(176) Blacker, T. S.; Mann, Z. F.; Gale, J. E.; Ziegler, M.; Bain, A. J.; Szabadkai, G.; Duchen, M. R. Separating NADH and NADPH fluorescence in live cells and tissues using FLIM. *Nature Communications* **2014**, *5* (1). DOI: 10.1038/ncomms4936.
(177) Kalinina, S.; Freymueller, C.; Naskar, N.; Von Einem, B.; Reess, K.; Sroka, R.; Rueck, A. Bioenergetic Alterations of Metabolic Redox Coenzymes as NADH, FAD and FMN by Means of Fluorescence Lifetime Imaging Techniques. *International Journal of Molecular Sciences* **2021**, *22* (11), 5952. DOI: 10.3390/ijms22115952.
(178) Cannon, T. M.; Lagarto, J. L.; Dyer, B. T.; Garcia, E.; Kelly, D. J.; Peters, N. S.; Lyon, A. R.; French, P. M. W.; Dunsby, C. Characterization of NADH fluorescence properties under one-photon excitation with respect to temperature, pH, and binding to lactate dehydrogenase. *OSA Contin* **2021**, *4* (5), 1610-1625. DOI: 10.1364/osac.423082 From NLM.
(179) Wu, J. T.; Wu, L. H.; Knight, J. A. Stability of NADPH: Effect of Various Factors on the Kinetics of Degradation. *Clinical Chemistry* **1986**, *32* (2), 314-319.
(180) Kierdaszuk, B.; Malak, H.; Gryczynski, I.; Callis, P.; Lakowicz, J. R. Fluorescence of reduced nicotinamides using one- and two-photon excitation. *Biophys Chem* **1996**, *62* (1-3), 1-13. DOI: 10.1016/s0301-4622(96)02182-5 From NLM.
(181) Fjeld, C. C.; Birdsong, W. T.; Goodman, R. H. Differential binding of NAD ⁺ and NADH allows the transcriptional corepressor carboxyl-terminal binding protein to serve as a metabolic sensor. *Proceedings of the National Academy of Sciences* **2003**, *100* (16), 9202-9207. DOI: 10.1073/pnas.1633591100.
(182) McGuinness, C. D.; Sagoo, K.; McLoskey, D.; Birch, D. J. S. A new sub-nanosecond LED at 280 nm: application to protein fluorescence. *Measurement Science and Technology* **2004**, *15*. DOI: 10.1088/0957-0233/15.
(183) Malcolm, A. D. B. Temperature dependence of the spectroscopic properties of NADH. In *Methods in Enzymology*, Vol. 66; Academic Press, 1980; pp 8-11.
(184) Rover, L.; Fernandes, J. C. B.; Neto, G. d. O.; Kubota, L. T.; Katekawa, E.; Serrano, S. l. H. P. Study of NADH Stability Using Ultraviolet–Visible Spectrophotometric Analysis and Factorial Design. *Analytical Biochemistry* **1998**, *260* (1), 50-55. DOI: https://doi.org/10.1006/abio.1998.2656.

(185) Visser, A. J. W. G.; Hoek, A. V. THE FLUORESCENCE DECAY OF REDUCED NICOTINAMIDES IN AQUEOUS SOLUTION AFTER EXCITATION WITH A UV-MODE LOCKED Ar ION LASER. *Photochemistry and Photobiology* **1981**, *33* (1), 35-40. DOI: 10.1111/j.1751-1097.1981.tb04293.x.
(186) McKittrick, J.; Chen, P. Y.; Bodde, S. G.; Yang, W.; Novitskaya, E. E.; Meyers, M. A. The Structure, Functions, and Mechanical Properties of Keratin. *JOM* **2012**, *64* (4), 449-468. DOI: 10.1007/s11837-012-0302-8.
(187) Coulombe, P. A.; Omary, M. B. 'Hard' and 'soft' principles defining the structure, function and regulation of keratin intermediate filaments. *Current Opinion in Cell Biology* **2002**, *14* (1), 110-122. DOI: https://doi.org/10.1016/S0955-0674(01)00301-5.
(188) Wegst, U. G. K.; Ashby, M. F. The mechanical efficiency of natural materials. *Philosophical Magazine* **2004**, *84* (21), 2167-2186. DOI: 10.1080/14786430410001680935.
(189) Wang, B.; Yang, W.; McKittrick, J.; Meyers, M. A. Keratin: Structure, mechanical properties, occurrence in biological organisms, and efforts at bioinspiration. *Progress in Materials Science* **2016**, *76*, 229-318. DOI: 10.1016/j.pmatsci.2015.06.001.
(190) Gillespie, J. M. The Proteins of Hair and Other Hard Keratins. In *Cellular and Molecular Biology of Intermediate Filaments*, Goldman, R. D., Steinert, P. M. Eds.; Springer, 1990.
(191) Fraser, R. D. B. M. T. P. R. G. E. *Keratins : Their composition, structure and biosynthesis*; Charles C. Thomas, 1972.
(192) Fraser, R. D.; Parry, D. A. The structural basis of the filament-matrix texture in the avian/reptilian group of hard β-keratins. *J Struct Biol* **2011**, *173* (2), 391-405. DOI: 10.1016/j.jsb.2010.09.020 From NLM.
(193) Giroud, A.; Leblond, C. P. THE KERATINIZATION OF EPIDERMIS AND ITS DERIVATIVES, ESPECIALLY THE HAIR, AS SHOWN BY X-RAY DIFFRACTION AND HISTOCHEMICAL STUDIES. *Annals of the New York Academy of Sciences* **1951**, *53* (3), 613-626. DOI: 10.1111/j.1749-6632.1951.tb31963.x.
(194) Mercer, E. H. *Keratin and Keratinization An essay in molecular biology*; Pergamon Press, 1961.
(195) Squire, J. M.; Vibert, P. J. *Fibrous Protein Structure*; Academic Press, 1987.
(196) Cooper, G. M. The Cell: A Molecular Approach. 2 ed.; Sinauer Associates, 2000.
(197) Moll, R.; Franke, W. W.; Schiller, D. L.; Geiger, B.; Krepler, R. The catalog of human cytokeratins: patterns of expression in normal epithelia, tumors and cultured cells. *Cell* **1982**, *31* (1), 11-24. DOI: 10.1016/0092-8674(82)90400-7 From NLM.
(198) Dowling, L. M.; Crewther, W. G.; Parry, D. A. Secondary structure of component 8c-1 of α-keratin. An analysis of the amino acid sequence. *Biochemical Journal* **1986**, *236* (3), 705-712. DOI: 10.1042/bj2360705.
(199) Moll, R.; Divo, M.; Langbein, L. The human keratins: biology and pathology. *Histochemistry and Cell Biology* **2008**, *129* (6), 705-733. DOI: 10.1007/s00418-008-0435-6.
(200) Chou, C.-C.; Buehler, M. J. Structure and Mechanical Properties of Human Trichocyte Keratin Intermediate Filament Protein. *Biomacromolecules* **2012**, *13* (11), 3522-3532. DOI: 10.1021/bm301254u.
(201) Steinert, P. M.; Parry, D. A. D. Intermediate Filaments: Conformity and Diversity of Expression and Structure. *Annual Review of Cell Biology* **1985**, *1* (1), 41-65. DOI: 10.1146/annurev.cb.01.110185.000353.
(202) Fraser, R. D. B.; MacRae, T. P.; Sparrow, L. G.; Parry, D. A. D. Disulphide bonding in α-keratin. *International Journal of Biological Macromolecules* **1988**, *10* (2), 106-112. DOI: https://doi.org/10.1016/0141-8130(88)90017-7.
(203) Paisey, R. B.; Clamp, J. R.; Kent, M. J.; Light, N. D.; Hopton, M.; Hartog, M. Glycosylation of hair: possible measure of chronic hyperglycaemia. *BMJ* **1984**, *288* (6418), 669-671. DOI: 10.1136/bmj.288.6418.669.

(204) Bakan, E.; Bakan, N. Glycosylation of nail in diabetics: possible marker of long-term hyperglycemia. *Clin Chim Acta* **1985**, *147* (1), 1-5. DOI: 10.1016/0009-8981(85)90003-8 From NLM.
(205) Delbridge, L.; Ellis, C. S.; Robertson, K.; Lequesne, L. P. Non-enzymatic glycosylation of keratin from the stratum corneum of the diabetic foot. *Br J Dermatol* **1985**, *112* (5), 547-554. DOI: 10.1111/j.1365-2133.1985.tb15262.x From NLM.
(206) Ansari, N. A.; Moinuddin; Ali, R. Glycated lysine residues: a marker for non-enzymatic protein glycation in age-related diseases. *Dis Markers* **2011**, *30* (6), 317-324. DOI: 10.3233/dma-2011-0791 From NLM. Mennella, C.; Visciano, M.; Napolitano, A.; Del Castillo, M. D.; Fogliano, V. Glycation of lysine-containing dipeptides. *Journal of Peptide Science* **2006**, *12* (4), 291-296. DOI: 10.1002/psc.722.
(207) Horvat, Š.; Jakas, A. Peptide and amino acid glycation: new insights into the Maillard reaction. *Journal of Peptide Science* **2004**, *10* (3), 119-137. DOI: 10.1002/psc.519.
(208) Marova, I.; Zahejsky, J.; Sehnalova, H. Non-enzymatic glycation of epidermal proteins of the stratum corneum in diabetic patients. *Acta Diabetologica* **1995**, *32* (1), 38-43. DOI: 10.1007/bf00581043.
(209) Kishabongo, A. S.; Katchunga, P.; Van Aken, E. H.; Speeckaert, R.; Lagniau, S.; Coopman, R.; Speeckaert, M. M.; Delanghe, J. R. Glycation of Nail Proteins: From Basic Biochemical Findings to a Representative Marker for Diabetic Glycation-Associated Target Organ Damage. *PLOS ONE* **2015**, *10* (3), e0120112. DOI: 10.1371/journal.pone.0120112.
(210) Monteyne, T.; Coopman, R.; Kishabongo, A. S.; Himpe, J.; Lapauw, B.; Shadid, S.; Van Aken, E. H.; Berenson, D.; Speeckaert, M. M.; De Beer, T.; et al. Analysis of protein glycation in human fingernail clippings with near-infrared (NIR) spectroscopy as an alternative technique for the diagnosis of diabetes mellitus. *Clinical Chemistry and Laboratory Medicine (CCLM)* **2018**, *56* (9), 1551-1558. DOI: 10.1515/cclm-2018-0239.
(211) Jurgeleviciene, I.; Stanislovaitiene, D.; Tatarunas, V.; Jurgelevicius, M.; Zaliuniene, D. Assessment of Absorption of Glycated Nail Proteins in Patients with Diabetes Mellitus and Diabetic Retinopathy. *Medicina* **2020**, *56* (12), 658. DOI: 10.3390/medicina56120658.
(212) Pena, A. M.; Strupler, M.; Boulesteix, T.; Schanne-Klein, M. C. Spectroscopic analysis of keratin endogenous signal for skin multiphoton microscopy. *Optics Express* **2005**, *13* (16), 6268. DOI: 10.1364/opex.13.006268.
(213) Voloshina, O. V.; Shirshin, E. A.; Lademann, J.; Fadeev, V. V.; Darvin, M. E. Fluorescence detection of protein content in house dust: the possible role of keratin. *Indoor Air* **2017**, *27* (2), 377-385. DOI: 10.1111/ina.12326.
(214) Dyer, J. M.; Bringans, S. D.; Bryson, W. G. Characterisation of photo-oxidation products within photoyellowed wool proteins: tryptophan and tyrosine derived chromophores. *Photochemical & Photobiological Sciences* **2006**, *5* (7), 698. DOI: 10.1039/b603030k.
(215) Block, R. J. THE COMPOSITION OF KERATINS. *Journal of Biological Chemistry* **1939**, *128* (1), 181-186. DOI: 10.1016/s0021-9258(18)73740-x.
(216) Ghisaidoobe, A.; Chung, S. Intrinsic Tryptophan Fluorescence in the Detection and Analysis of Proteins: A Focus on Förster Resonance Energy Transfer Techniques. *International Journal of Molecular Sciences* **2014**, *15* (12), 22518-22538. DOI: 10.3390/ijms151222518.
(217) Chen, Y.; Barkley, M. D. Toward understanding tryptophan fluorescence in proteins. *Biochemistry* **1998**, *37* (28), 9976-9982. DOI: 10.1021/bi980274n From NLM.
(218) McMullen, R. L.; Chen, S.; Moore, D. J. Spectrofluorescence of skin and hair. *International Journal of Cosmetic Science* **2012**, *34* (3), 246-256. DOI: 10.1111/j.1468-2494.2012.00709.x.

(219) Strnad, P.; Usachov, V.; Debes, C.; Gräter, F.; Parry, D. A. D.; Omary, M. B. Unique amino acid signatures that are evolutionarily conserved distinguish simple-type, epidermal and hair keratins. *Journal of Cell Science* **2011**, *124* (24), 4221-4232. DOI: 10.1242/jcs.089516.
(220) Fukunaga, Y.; Katsuragi, Y.; Izumi, T.; Sakiyama, F. Fluorescence Characteristics of Kynurenine and N'-Formylkynurenine, Their Use as Reporters of the Environment of Tryptophan 62 in Hen Egg-White Lysozyme1. *The Journal of Biochemistry* **1982**, *92* (1), 129-141. DOI: 10.1093/oxfordjournals.jbchem.a133909.
(221) Davis, I.; Liu, A. What is the tryptophan kynurenine pathway and why is it important to neurotherapeutics? *Expert Review of Neurotherapeutics* **2015**, *15* (7), 719-721. DOI: 10.1586/14737175.2015.1049999.
(222) Ehlers, A.; Riemann, I.; Stark, M.; König, K. Multiphoton fluorescence lifetime imaging of human hair. *Microscopy Research and Technique* **2007**, *70* (2), 154-161. DOI: 10.1002/jemt.20395.
(223) Krasieva, T. B.; Stringari, C.; Liu, F.; Sun, C.-H.; Kong, Y.; Balu, M.; Meyskens, F. L.; Gratton, E.; Tromberg, B. J. Two-photon excited fluorescence lifetime imaging and spectroscopy of melaninsin vitroandin vivo. *Journal of Biomedical Optics* **2012**, *18* (3), 031107. DOI: 10.1117/1.jbo.18.3.031107.
(224) Lee, E. Y.; Lee, B.-W.; Kim, D.; Lee, Y.-H.; Kim, K. J.; Kang, E. S.; Cha, B.-S.; Lee, E. J.; Lee, H. C. Glycated albumin is a useful glycation index for monitoring fluctuating and poorly controlled type 2 diabetic patients. *Acta Diabetologica* **2011**, *48* (2), 167-172. DOI: 10.1007/s00592-010-0242-0.
(225) Rondeau, P.; Bourdon, E. The glycation of albumin: Structural and functional impacts. *Biochimie* **2011**, *93* (4), 645-658. DOI: https://doi.org/10.1016/j.biochi.2010.12.003.
(226) Friedrichs, B. Th. Peters. Jr.: All about Albumin. Biochemistry, Genetics, and Medical Applications. . In *Food / Nahrung*, Vol. 41; John Wiley & Sons, Ltd, 1997; pp 382-382.
(227) Hadichegeni, S.; Goliaei, B.; Taghizadeh, M.; Davoodmanesh, S.; Taghavi, F.; Hashemi, M. Characterization of the interaction between human serum albumin and diazinon via spectroscopic and molecular docking methods. *Human & Experimental Toxicology* **2018**, *37* (9), 959-971. DOI: 10.1177/0960327117741752.
(228) Otagiri, M. A molecular functional study on the interactions of drugs with plasma proteins. *Drug Metab Pharmacokinet* **2005**, *20* (5), 309-323. DOI: 10.2133/dmpk.20.309 From NLM.
(229) Ghuman, J.; Zunszain, P. A.; Petitpas, I.; Bhattacharya, A. A.; Otagiri, M.; Curry, S. Structural basis of the drug-binding specificity of human serum albumin. *J Mol Biol* **2005**, *353* (1), 38-52. DOI: 10.1016/j.jmb.2005.07.075 From NLM.
(230) Shaklai, N.; Garlick, R. L.; Bunn, H. F. Nonenzymatic glycosylation of human serum albumin alters its conformation and function. *J Biol Chem* **1984**, *259* (6), 3812-3817. From NLM.
(231) Murayama, K.; Tomida, M. Heat-induced secondary structure and conformation change of bovine serum albumin investigated by Fourier transform infrared spectroscopy. *Biochemistry* **2004**, *43* (36), 11526-11532. DOI: 10.1021/bi0489154 From NLM.
(232) Mishra, V.; Heath, R. J. Structural and Biochemical Features of Human Serum Albumin Essential for Eukaryotic Cell Culture. *International Journal of Molecular Sciences* **2021**, *22* (16), 8411. DOI: 10.3390/ijms22168411.
(233) Castellanos, M. M.; Colina, C. M. Molecular Dynamics Simulations of Human Serum Albumin and Role of Disulfide Bonds. *The Journal of Physical Chemistry B* **2013**, *117* (40), 11895-11905. DOI: 10.1021/jp402994r.

(234) Zhang, M.; Xu, W.; Deng, Y. A New Strategy for Early Diagnosis of Type 2 Diabetes by Standard-Free, Label-Free LC-MS/MS Quantification of Glycated Peptides. *Diabetes* **2013**, *62* (11), 3936-3942. DOI: 10.2337/db13-0347.
(235) Qiu, H.-Y.; Hou, N.-N.; Shi, J.-F.; Liu, Y.-P.; Kan, C.-X.; Han, F.; Sun, X.-D. Comprehensive overview of human serum albumin glycation in diabetes mellitus. *World Journal of Diabetes* **2021**, *12* (7), 1057-1069. DOI: 10.4239/wjd.v12.i7.1057.
(236) Oettl, K.; Stauber, R. E. Physiological and pathological changes in the redox state of human serum albumin critically influence its binding properties. *British Journal of Pharmacology* **2007**, *151* (5), 580-590. DOI: 10.1038/sj.bjp.0707251.
(237) Cohen, M. P.; Shea, E.; Chen, S.; Shearman, C. W. Glycated albumin increases oxidative stress, activates NF-kappa B and extracellular signal-regulated kinase (ERK), and stimulates ERK-dependent transforming growth factor-beta 1 production in macrophage RAW cells. *J Lab Clin Med* **2003**, *141* (4), 242-249. DOI: 10.1067/mlc.2003.27 From NLM.
(238) Rubenstein, D. A.; Yin, W. Glycated albumin modulates platelet susceptibility to flow induced activation and aggregation. *Platelets* **2009**, *20* (3), 206-215. DOI: 10.1080/09537100902795492 From NLM.
(239) Doweiko, J. P.; Bistrian, B. R. The effect of glycosylated albumin on platelet aggregation. *JPEN J Parenter Enteral Nutr* **1994**, *18* (6), 516-520. DOI: 10.1177/0148607194018006516 From NLM.
(240) Smith, D. A.; Di, L.; Kerns, E. H. The effect of plasma protein binding on in vivo efficacy: misconceptions in drug discovery. *Nature Reviews Drug Discovery* **2010**, *9* (12), 929-939. DOI: 10.1038/nrd3287.
(241) Dasgupta, A. Clinical utility of free drug monitoring. *Clin Chem Lab Med* **2002**, *40* (10), 986-993. DOI: 10.1515/cclm.2002.172 From NLM.
(242) Baraka-Vidot, J.; Guerin-Dubourg, A.; Bourdon, E.; Rondeau, P. Impaired drug-binding capacities of in vitro and in vivo glycated albumin. *Biochimie* **2012**, *94* (9), 1960-1967. DOI: 10.1016/j.biochi.2012.05.017 From NLM.
(243) Cohen, M. P. Intervention strategies to prevent pathogenetic effects of glycated albumin. *Arch Biochem Biophys* **2003**, *419* (1), 25-30. DOI: 10.1016/j.abb.2003.08.012 From NLM.
(244) Bourdon, E.; Loreau, N.; Blache, D. Glucose and free radicals impair the antioxidant properties of serum albumin. *Faseb j* **1999**, *13* (2), 233-244. DOI: 10.1096/fasebj.13.2.233 From NLM.
(245) Ibrahim, N.; Ibrahim, H.; Kim, S.; Nallet, J.-P.; Nepveu, F. Interactions between Antimalarial Indolone-N-oxide Derivatives and Human Serum Albumin. *Biomacromolecules* **2010**, *11* (12), 3341-3351. DOI: 10.1021/bm100814n.
(246) Ali Khan, M. W.; Rasheed, Z.; Ali Khan, W.; Ali, R. Biochemical, biophysical, and thermodynamic analysis of in vitro glycated human serum albumin. *Biochemistry (Moscow)* **2007**, *72* (2), 146-152. DOI: 10.1134/s0006297907020034.
(247) Raghav, A.; Ahmad, J.; Alam, K. Nonenzymatic glycosylation of human serum albumin and its effect on antibodies profile in patients with diabetes mellitus. *PLOS ONE* **2017**, *12* (5), e0176970. DOI: 10.1371/journal.pone.0176970.
(248) Narahari, V. J.; Virgina Otero de, J.; Silvia, C.; Herminia, G.; Honorio, M.; Aleksander, S. Fluorescence lifetime measurements of native and glycated human serum albumin and bovine serum albumin. In *Proc.SPIE*, 1999; Vol. 3602, pp 124-131. DOI: 10.1117/12.347514.
(249) Zhdanova, N. G.; Shirshin, E. A.; Maksimov, E. G.; Panchishin, I. M.; Saletsky, A. M.; Fadeev, V. V. Tyrosine fluorescence probing of the surfactant-induced conformational changes of albumin. *Photochemical & Photobiological Sciences* **2015**, *14* (5), 897-908. DOI: 10.1039/c4pp00432a.

(250) Tayeh, N.; Rungassamy, T.; Albani, J. R. Fluorescence spectral resolution of tryptophan residues in bovine and human serum albumins. *J Pharm Biomed Anal* **2009**, *50* (2), 107-116. DOI: 10.1016/j.jpba.2009.03.015 From NLM.
(251) Amiri, M.; Jankeje, K.; Albani, J. R. Characterization of human serum albumin forms with pH. Fluorescence lifetime studies. *Journal of Pharmaceutical and Biomedical Analysis* **2010**, *51* (5), 1097-1102. DOI: https://doi.org/10.1016/j.jpba.2009.11.011.
(252) Amiri, M.; Jankeje, K.; Albani, J. R. Origin of Fluorescence Lifetimes in Human Serum Albumin. Studies on Native and Denatured Protein. *Journal of Fluorescence* **2010**, *20* (3), 651-656. DOI: 10.1007/s10895-010-0597-1.
(253) Suárez, G.; Rajaram, R.; Oronsky, A. L.; Gawinowicz, M. A. Nonenzymatic glycation of bovine serum albumin by fructose (fructation). Comparison with the Maillard reaction initiated by glucose. *J Biol Chem* **1989**, *264* (7), 3674-3679. From NLM.
(254) Chopra, K.; Calva, D.; Sosin, M.; Tadisina, K. K.; Banda, A.; De La Cruz, C.; Chaudhry, M. R.; Legesse, T.; Drachenberg, C. B.; Manson, P. N.; et al. A Comprehensive Examination of Topographic Thickness of Skin in the Human Face. *Aesthetic Surgery Journal* **2015**, *35* (8), 1007-1013. DOI: 10.1093/asj/sjv079.
(255) Czekalla, C.; Karl; Lademann, J.; Martina. Noninvasive Determination of Epidermal and Stratum Corneum Thickness in vivo Using Two-Photon Microscopy and Optical Coherence Tomography: Impact of Body Area, Age, and Gender. *Skin Pharmacology and Physiology* **2019**, *32* (3), 142-150. DOI: 10.1159/000497475.
(256) Walters, K. A.; Roberts, M. S. The structure and function of skin. In *Dermatological and transdermal formulations*, CRC Press, 2002; pp 19-58.
(257) Maiti, R.; Gerhardt, L.-C.; Lee, Z. S.; Byers, R. A.; Woods, D.; Sanz-Herrera, J. A.; Franklin, S. E.; Lewis, R.; Matcher, S. J.; Carre, M. J. In vivo measurement of skin surface strain and sub-surface layer deformation induced by natural tissue stretching. *Journal of the Mechanical Behaviour of Biomedical Materials* **2016**, *62*, 556-569.
(258) Takahashi, M.; Machida, Y.; Marks, R. Measurement of turnover time of stratum corneum using dansyl chloride fluorescence. *J. Soc. Cosmet. Chem.* **1987**, *38*, 321-331.
(259) Menon, G. K. New insights into skin structure: scratching the surface. *Advanced Drug Delivery Reviews* **2002**, *54*, S3-S17. DOI: 10.1016/s0169-409x(02)00121-7.
(260) Strzalkowski, N. D. J.; Triano, J. J.; Lam, C. K.; Templeton, C. A.; Bent, L. R. Thresholds of skin sensitivity are partially influenced by mechanical properties of the skin on the foot sole. *Physiological Reports* **2015**, *3* (6), e12425. DOI: 10.14814/phy2.12425.
(261) Brannon, H. L. *The Individual Layers of Skin and their Functions*. 2021. https://www.verywellhealth.com/skin-anatomy-1068880 (accessed 2021 04.08.21).
(262) Bugaj, O.; Zieliński, J.; Kusy, K.; Kantanista, A.; Wieliński, D.; Guzik, P. The Effect of Exercise on the Skin Content of the Reduced Form of NAD and Its Response to Transient Ischemia and Reperfusion in Highly Trained Athletes. *Front Physiol* **2019**, *10*, 600-600. DOI: 10.3389/fphys.2019.00600 PubMed.
(263) White, A. T.; Schenk, S. NAD+/NADH and skeletal muscle mitochondrial adaptations to exercise. *American Journal of Physiology-Endocrinology and Metabolism* **2012**, *303* (3), E308-E321. DOI: 10.1152/ajpendo.00054.2012.
(264) Baroni, A.; Buommino, E.; De Gregorio, V.; Ruocco, E.; Ruocco, V.; Wolf, R. Structure and function of the epidermis related to barrier properties. *Clinics in Dermatology* **2012**, *30* (3), 257-262. DOI: 10.1016/j.clindermatol.2011.08.007.
(265) Trojahn, C.; Dobos, G.; Richter, C.; Blume-Peytavi, U.; Kottner, J. Measuring skin aging using optical coherence tomography in vivo: a validation study. *Journal of Biomedical Optics* **2015**, *20* (4). DOI: 10.1117/1.jbo.20.4.045003.short.

(266) Josse, G.; George, J.; Black, D. Automatic measurement of epidermal thickness from optical coherence tomography images using a new algorithm. *Skin Research and Technology* **2011**, *17* (3), 314-319. DOI: 10.1111/j.1600-0846.2011.00499.x.
(267) Meinhardt, M.; Krebs, R.; Anders, A. Wavelength-dependent penetration depths of ultraviolet radiation in human skin. *Journal of Biomedical Optics* **2008**, *13* (4). DOI: 10.1117/1.2957970.full.
(268) Kwon, K.; Son, T.; Lee, K.-J.; Jung, B. Enhancement of light propagation depth in skin: cross-validation of mathematical modeling methods. *Lasers in Medical Science* **2009**, *24* (4), 605-615. DOI: 10.1007/s10103-008-0625-4. Ash, C.; Dubec, M.; Donne, K.; Bashford, T. Effect of wavelength and beam width on penetration in light-tissue interaction using computational methods. *Lasers in Medical Science* **2017**, *32* (8), 1909-1918. DOI: 10.1007/s10103-017-2317-4.
(269) Anderson, R. R.; Parrish, J. A. The Optics of Human Skin. *Journal of Investigative Dermatology* **1981**, *77* (1), 13-19. DOI: 10.1111/1523-1747.ep12479191.
(270) Pasparakis, M.; Haase, I.; Nestle, F. O. Mechanisms regulating skin immunity and inflammation. *Nature Reviews Immunology* **2014**, *14* (5), 289-301. DOI: 10.1038/nri3646.
(271) Gudjonsson, J. E.; Johnston, A.; Dyson, M.; Valdimarsson, H.; Elder, J. T. Mouse Models of Psoriasis. *Journal of Investigative Dermatology* **2007**, *127* (6), 1292-1308. DOI: 10.1038/sj.jid.5700807.
(272) Porter, R. M. Mouse models for human hair loss disorders. *Journal of Anatomy* **2003**, *202* (1), 125-131. DOI: 10.1046/j.1469-7580.2003.00140.x.
(273) Dimitrow, E.; Ziemer, M.; Koehler, M. J.; Norgauer, J.; König, K.; Elsner, P.; Kaatz, M. Sensitivity and Specificity of Multiphoton Laser Tomography for In Vivo and Ex Vivo Diagnosis of Malignant Melanoma. *Journal of Investigative Dermatology* **2009**, *129* (7), 1752-1758. DOI: 10.1038/jid.2008.439.
(274) Patalay, R.; Talbot, C.; Alexandrov, Y.; Munro, I.; Neil, M. A. A.; König, K.; French, P. M. W.; Chu, A.; Stamp, G. W.; Dunsby, C. Quantification of cellular autofluorescence of human skin using multiphoton tomography and fluorescence lifetime imaging in two spectral detection channels. *Biomed. Opt. Express* **2011**, *2* (12), 3295-3308. DOI: 10.1364/BOE.2.003295.
(275) Stirban, A.; Nandrean, S.; Negrean, M.; Kischinsky, T.; Tschoepe, D. Skin Autofluorescence Increases Postprandially in Human Subjects. *Diabetes Technology & Therapeutics* **2008**, *10* (3), 200-205. DOI: 10.1089/dia.2007.0275. Richter, C.; Trojahn, C.; Dobos, G.; Blume-Peytavi, U.; Kottner, J. Follicular fluorescence quantity to characterize acne severity: a validation study. *Skin Research and Technology* **2016**, *22* (4), 451-459. DOI: 10.1111/srt.12286.
(276) Yamanaka, M.; Matsumura, T.; Ohno, R.-I.; Fujiwara, Y.; Shinagawa, M.; Sugawa, H.; Hatano, K.; Shirakawa, J.-I.; Kinoshita, H.; Ito, K.; et al. Non-invasive measurement of skin autofluorescence to evaluate diabetic complications. *Journal of Clinical Biochemistry and Nutrition* **2016**, *58* (2), 135-140. DOI: 10.3164/jcbn.15-132.
(277) Genevieve, M.; Vivot, A.; Gonzalez, C.; Raffaitin, C.; Barberger-Gateau, P.; Gin, H.; Rigalleau, V. Skin autofluorescence is associated with past glycaemic control and complications in type 1 diabetes mellitus. *Diabetes Metab* **2013**, *39* (4), 349-354. DOI: 10.1016/j.diabet.2013.03.003 From NLM.
(278) Cleary, P. A.; Braffett, B. H.; Orchard, T.; Lyons, T. J.; Maynard, J.; Cowie, C.; Gubitosi-Klug, R. A.; Way, J.; Anderson, K.; Barnie, A.; et al. Clinical and Technical Factors Associated with Skin Intrinsic Fluorescence in Subjects with Type 1 Diabetes from the Diabetes Control and Complications Trial/Epidemiology of Diabetes Interventions and Complications Study. *Diabetes Technology & Therapeutics* **2013**, *15* (6), 466-474. DOI: 10.1089/dia.2012.0316.

(279) Sugisawa, E.; Miura, J.; Iwamoto, Y.; Uchigata, Y. Skin Autofluorescence Reflects Integration of Past Long-Term Glycemic Control in Patients With Type 1 Diabetes. *Diabetes Care* **2013**, *36* (8), 2339-2345. DOI: 10.2337/dc12-1077.
(280) Wang, X.; Zhao, X.; Lian, T.; Wei, J.; Yue, W.; Zhang, S.; Chen, Q. Skin autofluorescence and the complexity of complications in patients with type 2 diabetes mellitus: a cross-sectional study. *BMC Endocrine Disorders* **2021**, *21* (1). DOI: 10.1186/s12902-021-00725-6.
(281) Blanc-Bisson, C.; Velayoudom-Cephise, F. L.; Cougnard-Gregoire, A.; Helmer, C.; Rajaobelina, K.; Delcourt, C.; Alexandre, L.; Blanco, L.; Mohammedi, K.; Monlun, M.; et al. Skin autofluorescence predicts major adverse cardiovascular events in patients with type 1 diabetes: a 7-year follow-up study. *Cardiovascular Diabetology* **2018**, *17* (1). DOI: 10.1186/s12933-018-0718-8.
(282) Van Waateringe, R. P.; Fokkens, B. T.; Slagter, S. N.; Van Der Klauw, M. M.; Van Vliet-Ostaptchouk, J. V.; Graaff, R.; Paterson, A. D.; Smit, A. J.; Lutgers, H. L.; Wolffenbuttel, B. H. R. Skin autofluorescence predicts incident type 2 diabetes, cardiovascular disease and mortality in the general population. *Diabetologia* **2019**, *62* (2), 269-280. DOI: 10.1007/s00125-018-4769-x.
(283) Farren, L.; Shayler, S.; Ennos, A. R. The fracture properties and mechanical design of human fingernails. *Journal of Experimental Biology* **2004**, *207* (5), 735-741. DOI: 10.1242/jeb.00814.
(284) Tosti, A.; Piraccini, B. M. Chapter 89. Biology of Nails and Nail Disorders. In *Fitzpatrick's Dermatology in General Medicine, 8e*, Goldsmith, L. A., Katz, S. I., Gilchrest, B. A., Paller, A. S., Leffell, D. J., Wolff, K. Eds.; The McGraw-Hill Companies, 2012.
(285) Cashman, M. W.; Sloan, S. B. Nutrition and nail disease. *Clinics in Dermatology* **2010**, *28* (4), 420-425. DOI: 10.1016/j.clindermatol.2010.03.037.
(286) Caputo, R.; Gasparini, G.; Contini, D. A freeze-fracture study of the human nail plate. *Arch Dermatol Res* **1982**, *272* (1-2), 117-125. DOI: 10.1007/bf00510401 From NLM.
(287) Farran, L.; Ennos, A. R.; Starkie, M.; Eichhorn, S. J. Tensile and shear properties of fingernails as a function of a changing humidity environment. *Journal of Biomechanics* **2009**, *42* (9), 1230-1235. DOI: 10.1016/j.jbiomech.2009.03.020.
(288) Garson, J. C.; Baltenneck, F.; Leroy, F.; Riekel, C.; Müller, M. Histological structure of human nail as studied by synchrotron X-ray microdiffraction. *Cell Mol Biol (Noisy-le-grand)* **2000**, *46* (6), 1025-1034. From NLM.
(289) De Berker, D.; Wojnarowska, F.; Sviland, L.; Westgate, G. E.; Dawber, R. P. R.; Leigh, I. M. Keratin expression in the normal nail unit: markers of regional differentiation. *British Journal of Dermatology* **2000**, *142* (1), 89-96. DOI: 10.1046/j.1365-2133.2000.03246.x.
(290) National Center for Biotechnology Information. *National Library of Medicine*. https://www.ncbi.nlm.nih.gov/protein (accessed 2022 25.07.22).
(291) Kishabongo, A. S.; Katchunga, P.; Van Aken, E. H.; Speeckaert, M. M.; Lagniau, S.; Husein, D.; Taes, Y. E.; Delanghe, J. R. Glycated nail proteins: a new approach for detecting diabetes in developing countries. *Tropical Medicine & International Health* **2014**, *19* (1), 58-64. DOI: 10.1111/tmi.12218.
(292) Smith, J. T.; Yao, R.; Sinsuebphon, N.; Rudkouskaya, A.; Un, N.; Mazurkiewicz, J.; Barroso, M.; Yan, P.; Intes, X. Fast fit-free analysis of fluorescence lifetime imaging via deep learning. *Proceedings of the National Academy of Sciences* **2019**, *116* (48), 24019-24030. DOI: 10.1073/pnas.1912707116.
(293) Sagar, A. K.; Cheng, K. P.; Ouellette, J. N.; Williams, J. C.; Watters, J. J.; Eliceiri, K. W. Machine Learning Methods for Fluorescence Lifetime Imaging (FLIM) Based Label-Free Detection of Microglia. *Frontiers in Neuroscience* **2020**, *14*.

10.1 Appendix A

10.1.1 Appendix A1: Comparison of Fitting Methods for the Multi-Exponential Model

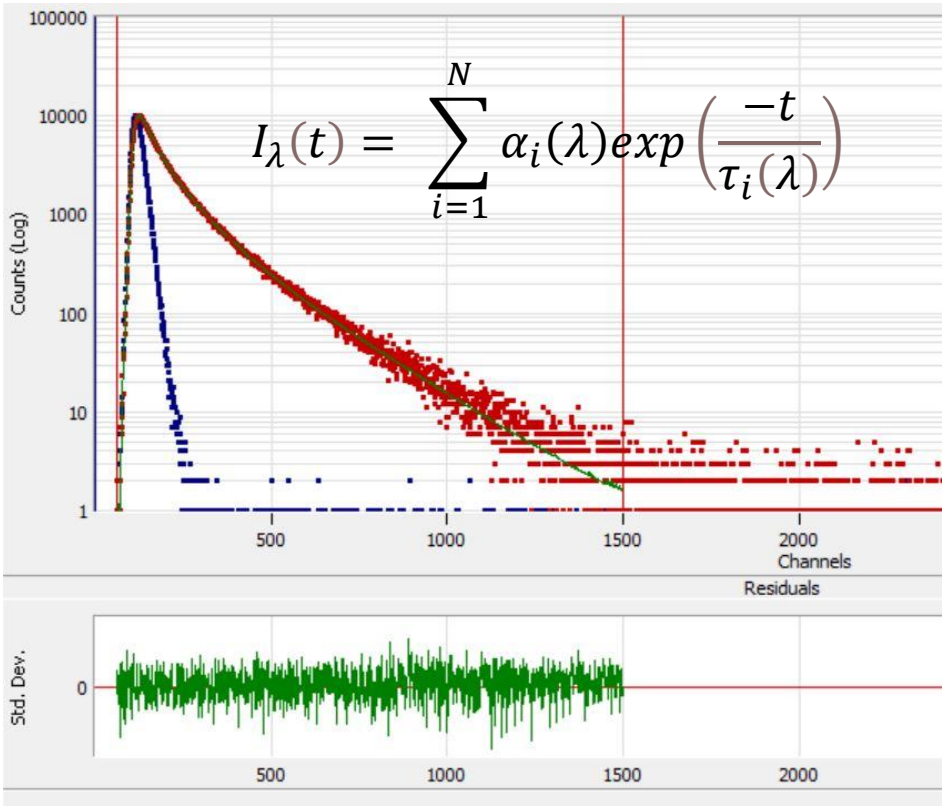

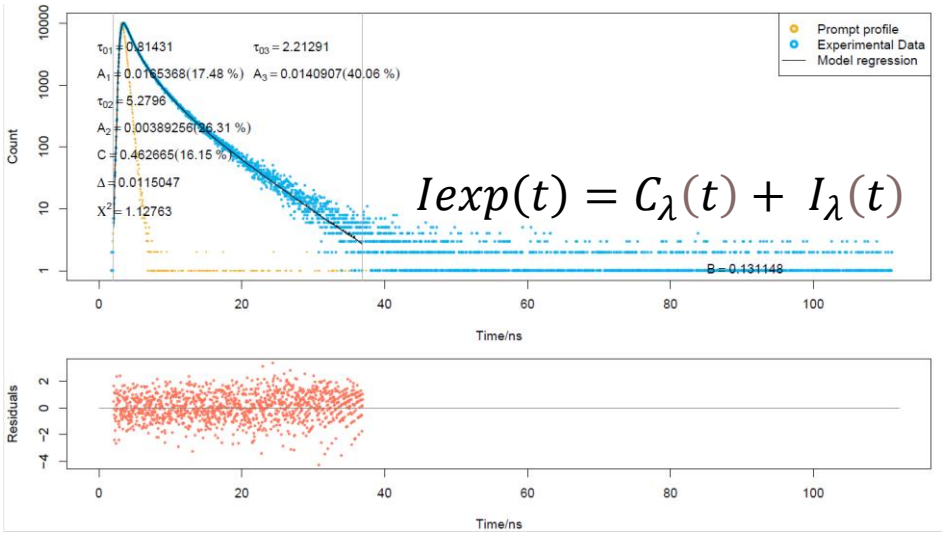

	τ_1(ns)	A1 /%	τ_2(ns)	A2 /%	τ_3(ns)	A3 /%	τ_4(ps)	A4 /%	C (%)	X^2
3+1 - exponential	0.84	0.0173 (13.63)	2.25	0.0139 (29.41)	5.30	0.00382 (19.02)	13.67	2.96 (37.94)		1.10
3 - exponential + scatter function	0.81	0.0165 (17.48)	2.22	0.0141 (40.06)	5.28	0.00389 (26.31)			16.15	1.13

Figure A1.1. Result of fitting of the fluorescence intensity decay of the sample collagen-glucose, day 0. Excitation wavelength 280 nm, detection wavelength 330 nm.

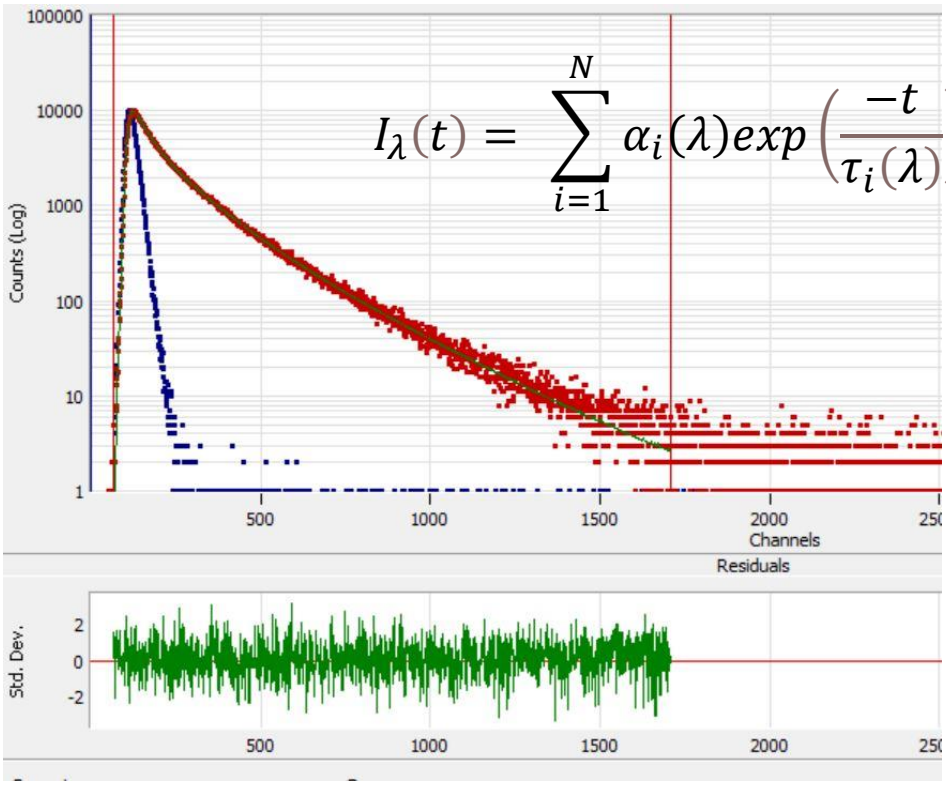

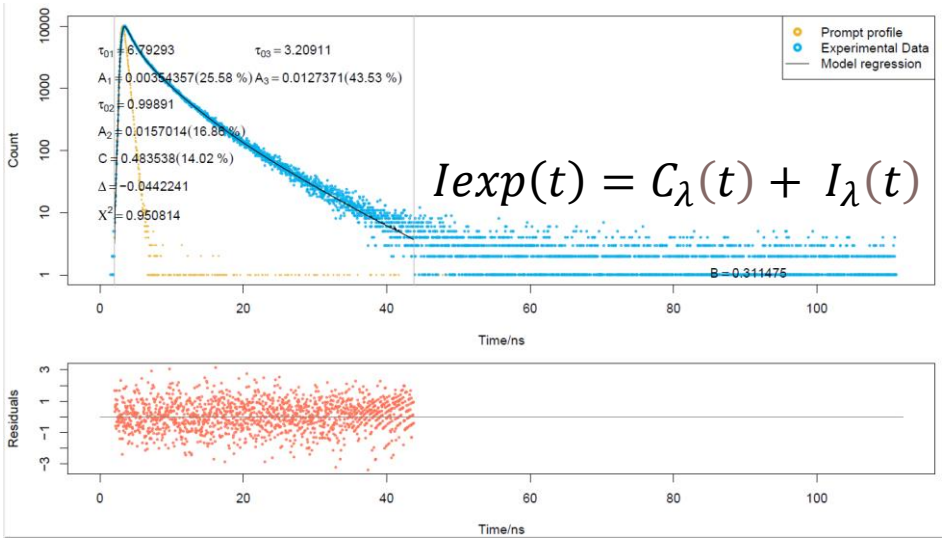

	τ_1(ns)	A1 /%	τ_2(ns)	A2 /%	τ_3(ns)	A3 /%	τ_4(ps)	A4 /%	C (%)	X^2
3+1 - exponential	0.99	0.0159 (12.7)	3.13	0.0128 (32.54)	6.65	0.00387 (20.82)	13.67	3.07 (33.93)		0.97
3 - exponential + scatter function	0.99	0.0157 (16.86)	3.21	0.0127 (43.53)	6.79	0.00354 (25.58)			14.02	0.95

Figure A1.2. Result of fitting of the fluorescence intensity decay of the sample free collagen, day 14. Excitation wavelength 280 nm, detection wavelength 360 nm.

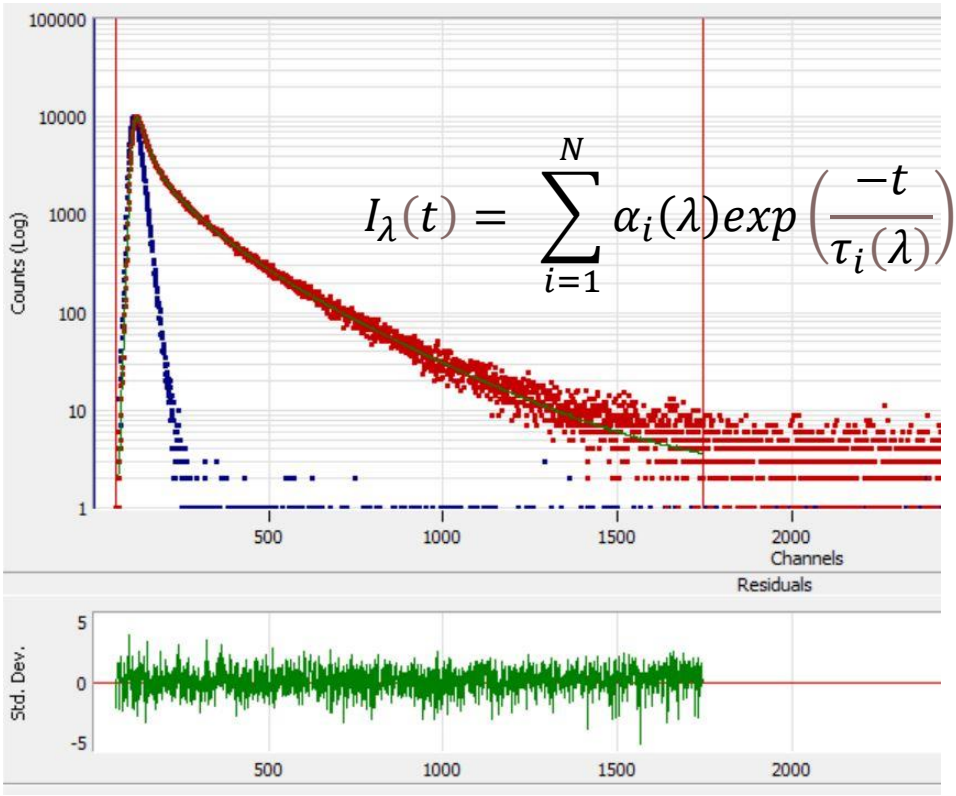

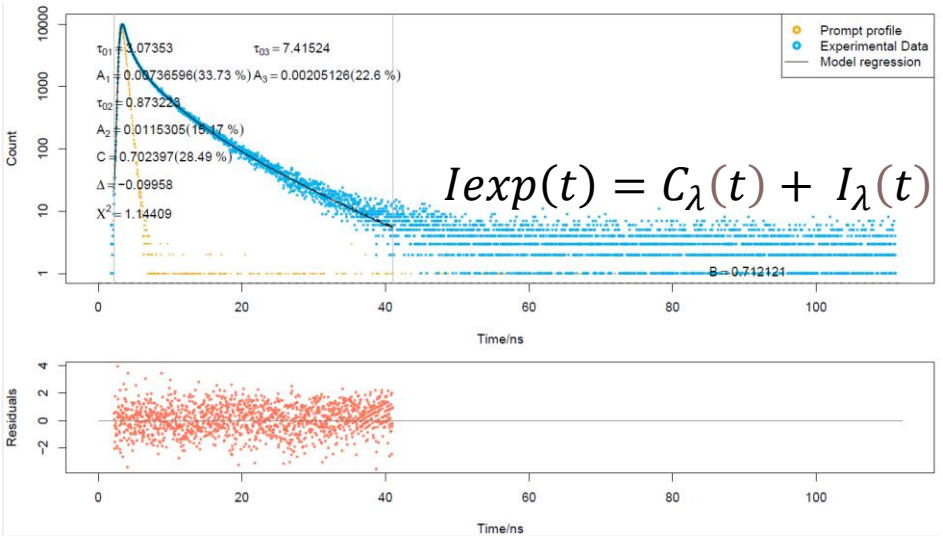

	τ_1(ns)	A1 /%	τ_2(ns)	A2 /%	τ_3(ns)	A3 /%	τ_4(ps)	A4 /%	C (%)	X^2
3+1 - exponential	0.90	0.0118 (9.65)	3.10	0.00727 (20.55)	7.34	0.00207 (13.86)	13.67	4.49 (55.94)		1.15
3 - exponential + scatter function	0.87	0.0115 (15.17)	3.07	0.00767 (33.73)	7.42	0.00205 (22.16)			28.49	1.14

Figure A1.3. Result of fitting of the fluorescence intensity decay of the sample collagen-glucose, day 28. Excitation wavelength 280 nm, detection wavelength 390 nm.

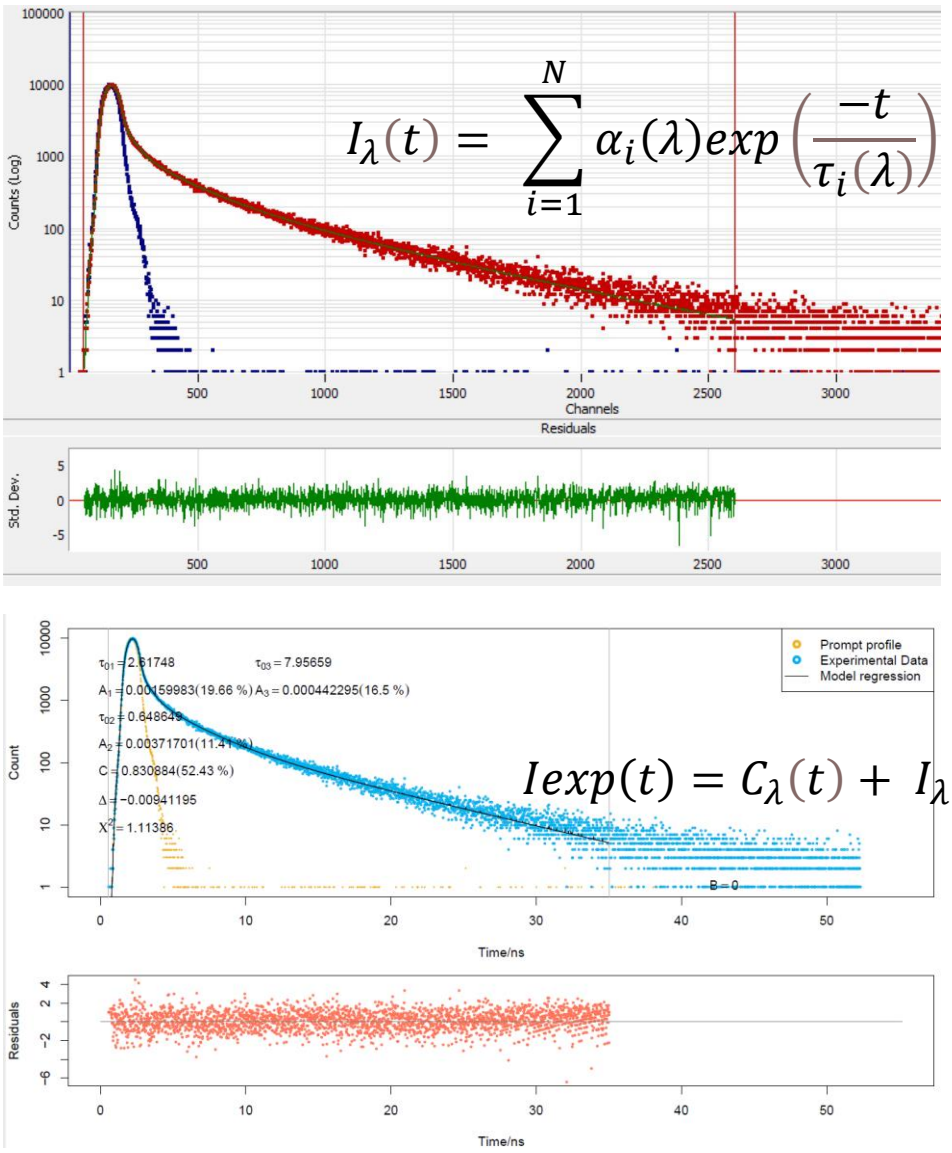

	τ_1(ns)	A1 /%	τ_2(ns)	A2 /%	τ_3(ns)	A3 /%	τ_4(ps)	A4 /%	C (%)	X^2
3+1 - exponential	0.63	0.00367 (5.06)	2.44	0.00164 (8.71)	7.43	0.000512 (8.28)	6.74	5.32 (77.95)		1.11
3 - exponential + scatter function	0.65	0.00372 (11.41)	2.62	0.00160 (19.66)	7.96	0.000442 (16.5)			52.43	1.11

Figure A1.4. Result of fitting of the fluorescence intensity decay of the sample free collagen, day 0. Excitation wavelength 340 nm, detection wavelength 440 nm.

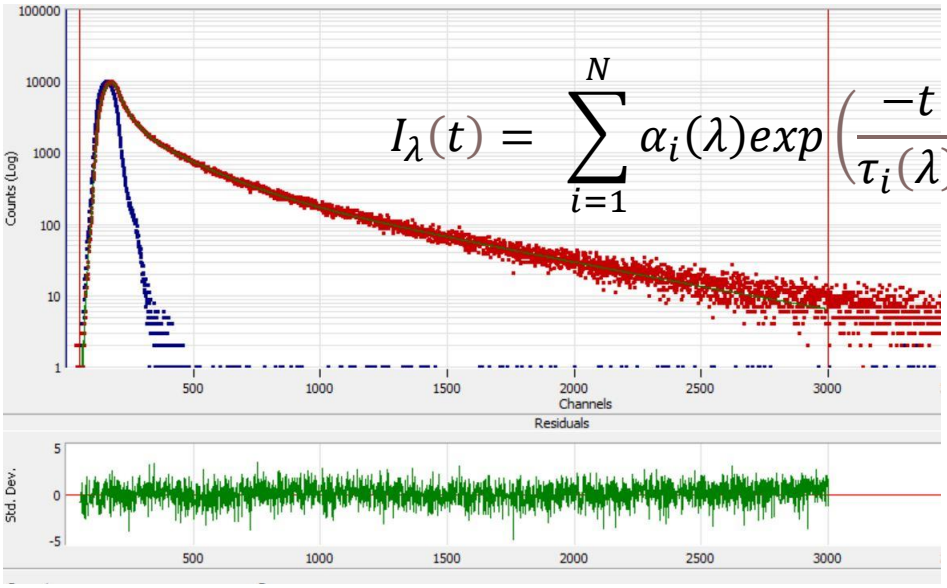

$$I_\lambda(t) = \sum_{i=1}^{N} \alpha_i(\lambda) exp\left(\frac{-t}{\tau_i(\lambda)}\right)$$

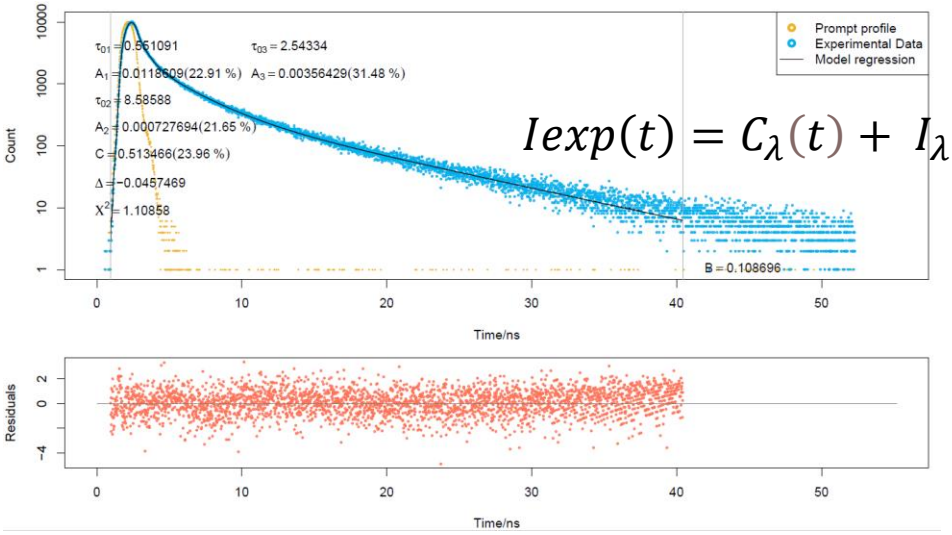

$$Iexp(t) = C_\lambda(t) + I_\lambda(t)$$

	τ_1(ns)	A1 /%	τ_2(ns)	A2 /%	τ_3(ns)	A3 /%	τ_4(ps)	A4 /%	C (%)	X^2
3+1 - exponential	0.52	0.0132 (15. 8)	2.46	0.00371 (21.04)	8.34	0.000778 (14.97)	6.74	3.10 (48.19)		1.11
3 - exponential + scatter function	0.56	0.0119 (22.91)	2.54	0.00356 (31.48)	8.59	0.000728 (21.65)			23.96	1.11

Figure A1.5. Result of fitting of the fluorescence intensity decay of the sample collagen-glucose, day 14. Excitation wavelength 340 nm, detection wavelength 400 nm.

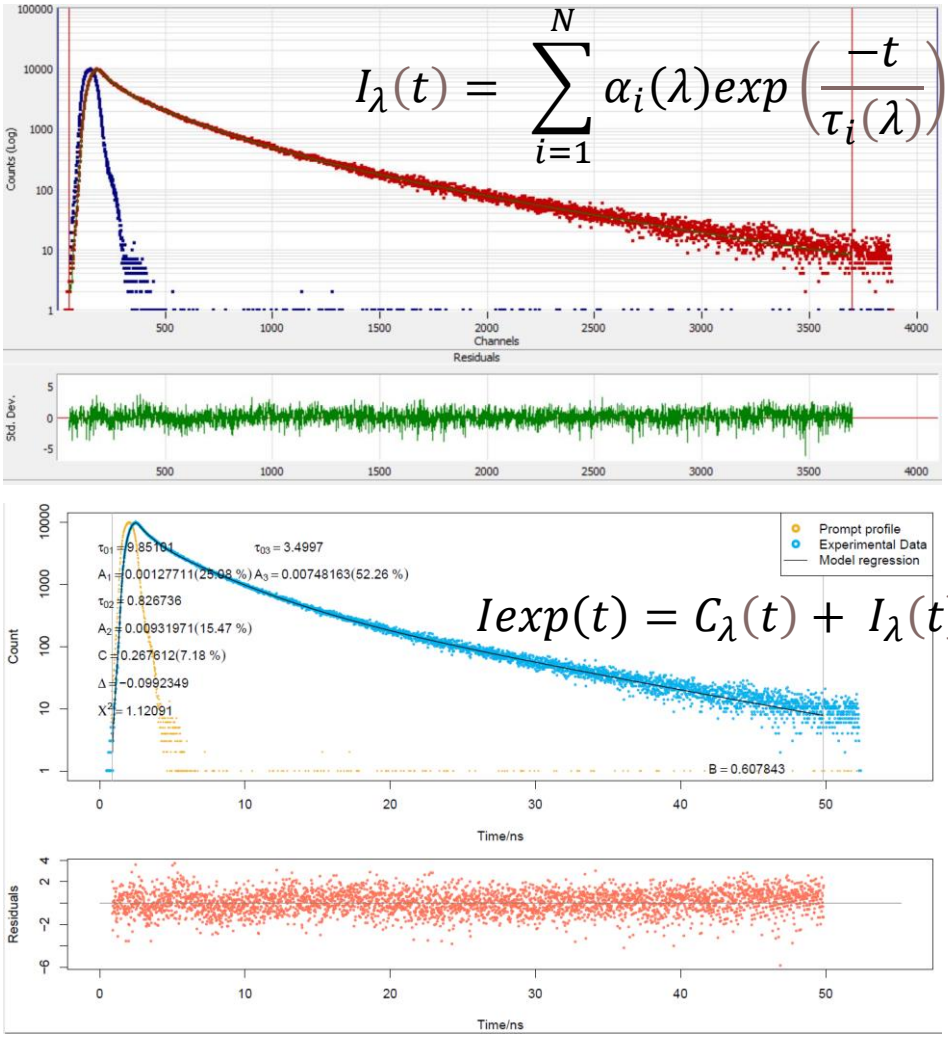

	τ_1(ns)	A1 /%	τ_2(ns)	A2 /%	τ_3(ns)	A3 /%	τ_4(ps)	A4 /%	C (%)	X^2
3+1 - exponential	0.81	0.00932 (12.94)	3.39	0.00755 (44.04)	9.39	0.00144 (23.23)	6.74	1.71 (19.79)		1.09
3 - exponential + scatter function	0.83	0.00932 (15.47)	3.50	0.00748 (52.26)	9.85	0.00128 (25.08)			7.18	1.12

Figure A1.6. Result of fitting of the fluorescence intensity decay of the sample collagen-glucose, day 35. Excitation wavelength 340nm, detection wavelength 480 nm.

10.2 Appendix B: Collagen

10.2.1 Appendix B1: Raw TCSPC Data Analysis

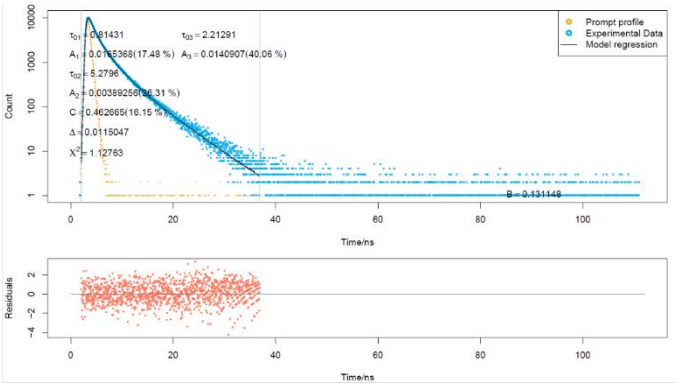

	τ_1(ns)	A1 /%	τ_2(ns)	A2 /%	τ_3(ns)	A3 /%	C (%)	X^2
3 - exponential + scatter function	0.81	0.0165 (17.48)	2.22	0.0141 (40.06)	5.28	0.00389 (26.31)	16.15	1.13

Figure B1.1. Result of fitting of the fluorescence intensity decay of the sample collagen-glucose, day 0. Excitation wavelength 280 nm, detection wavelength 330 nm.

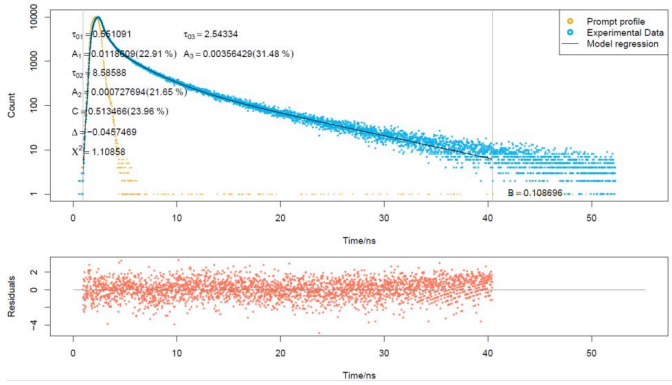

	τ_1(ns)	A1 /%	τ_2(ns)	A2 /%	τ_3(ns)	A3 /%	C (%)	X^2
3 - exponential + scatter function	0.56	0.0119 (22.91)	2.54	0.00356 (31.48)	8.59	0.000728 (21.65)	23.96	1.11

Figure B1.2. Result of fitting of the fluorescence intensity decay of the sample collagen-glucose, day 14. Excitation wavelength 340nm, detection wavelength 400 nm.

10.2.2 Appendix B2: Calculated TRES Values vs TRES Model (eq. 2.35) curves

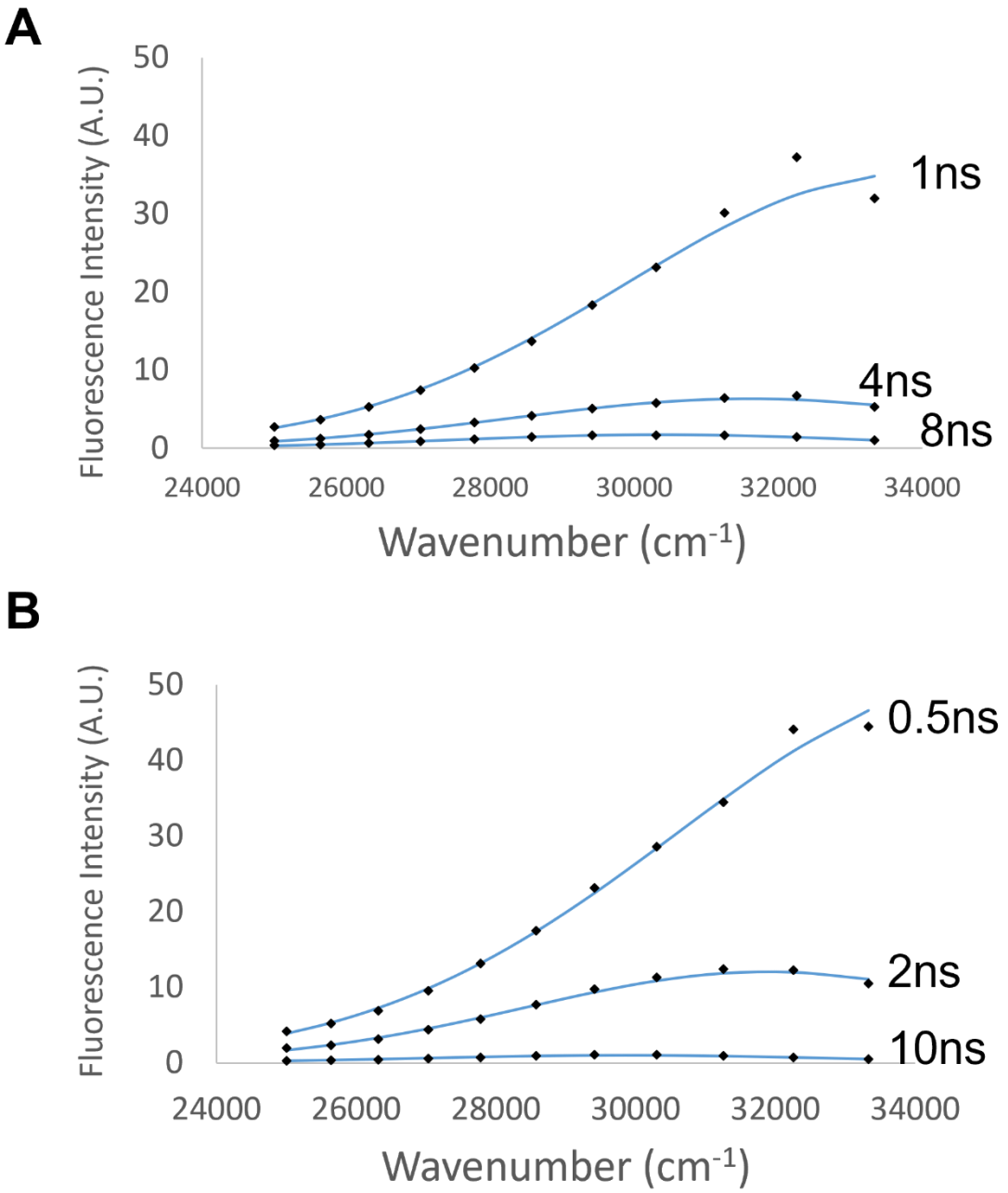

Figure B2.1. Examples of the model and experimental TRES for excitation 280 nm. TRES calculated from experimental data are shown as black markers, while the model is shown as a blue line. Part A shows an example from collagen-glucose at day 0, while part B shows an example from collagen at day 56.

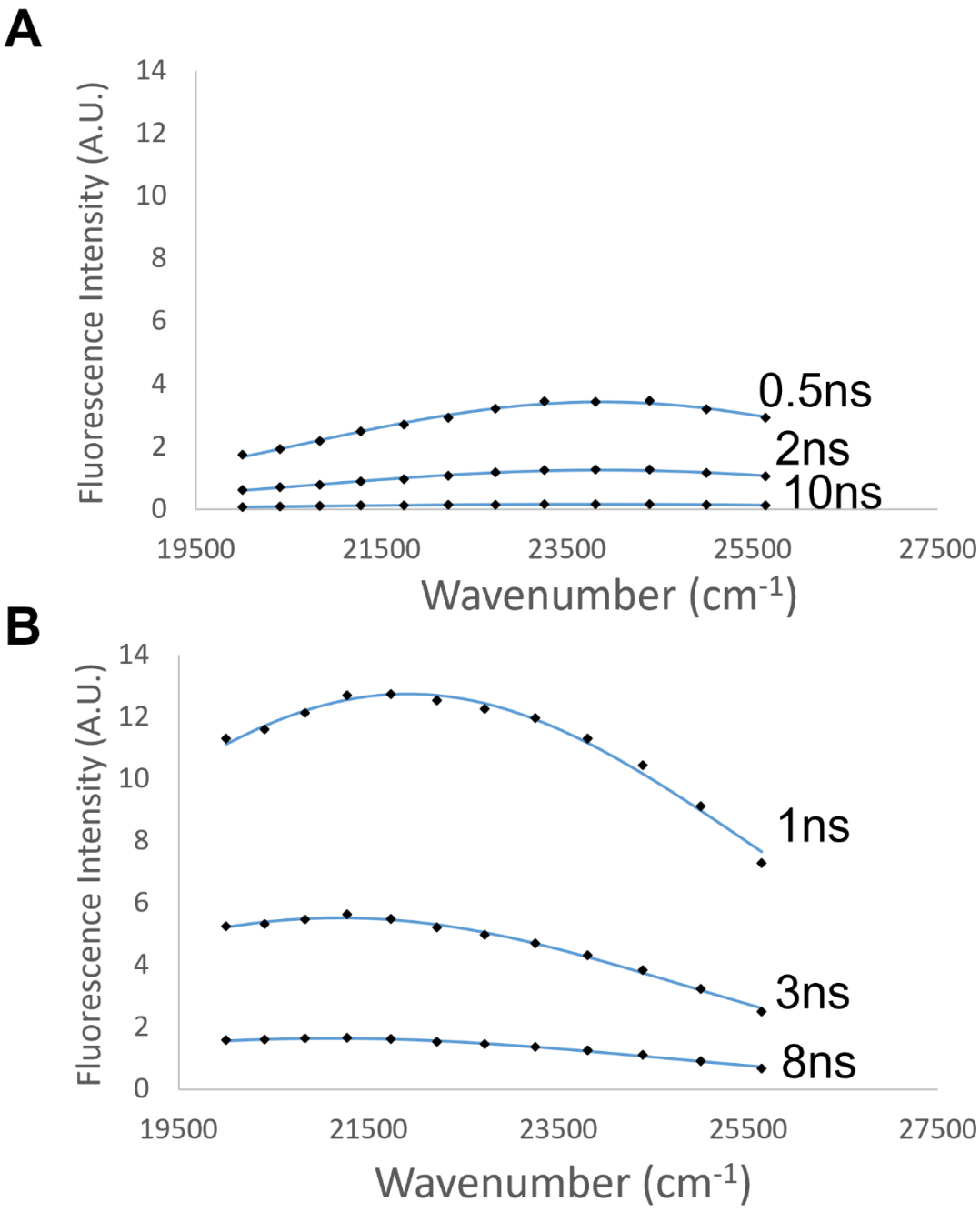

Figure B2.2. Examples of the model and experimental TRES for excitation 340 nm. TRES calculated from experimental data are shown as black markers, while the model is shown as a blue line. Part A shows an example from collagen at day 0, while part B shows an example from collagen-glucose at day 21.

10.2.3 Appendix B3: Akaike's Information Criterion Values for Collagen Samples

Table B3.1. Examples of AICc values for the one-and two-component Toptygin model of the TRES for free collagen and collagen glucose when exciting at 280 nm. The smaller AICc value indicates a more adequate model. A small selection of TRES spectra at different days and times after excitation have been included.

TRES Spectra		Single Toptygin AIC_c	Double Toptygin AIC_c
Collagen Day 0	1ns	49.25	47.67
	4ns	7.14	9.15
	8ns	-34.57	-27.59
Collagen – Glucose Day 21	1ns	40.24	33.59
	4ns	-4.86	-4.31
	8ns	-42.71	-36.27
Collagen Day 56	1ns	40.96	42.72
	4ns	-3.61	6.32
	8ns	-40.68	-28.10

Table B3.2. Examples of AICc values for the one-and two-component Toptygin model of the TRES for free collagen and collagen glucose when exciting at 340 nm. The smaller AICc value indicates a more adequate model. A small selection of TRES spectra at different days and times after excitation have been included**.**

TRES Spectra		Single Toptygin AICc	Double Toptygin AICc
Collagen Day 0	1ns	-71.71	-68.21
	4ns	-108.57	-101.68
	8ns	-132.53	-119.44
Collagen – Glucose Day 21	1ns	-32.26	-28.97
	4ns	-59.25	-50.79
	8ns	-81.12	-82.58
Collagen Day 3556	1ns	-53.64	-46.18
	4ns	-86.15	-79.81
	8ns	-106.51	-96.47

10.3 Appendix C: NADH

10.3.1 Appendix C1: Experimental vs Toptygin Model of Emission Spectrum of NADH and NADH-glucose samples in PBS

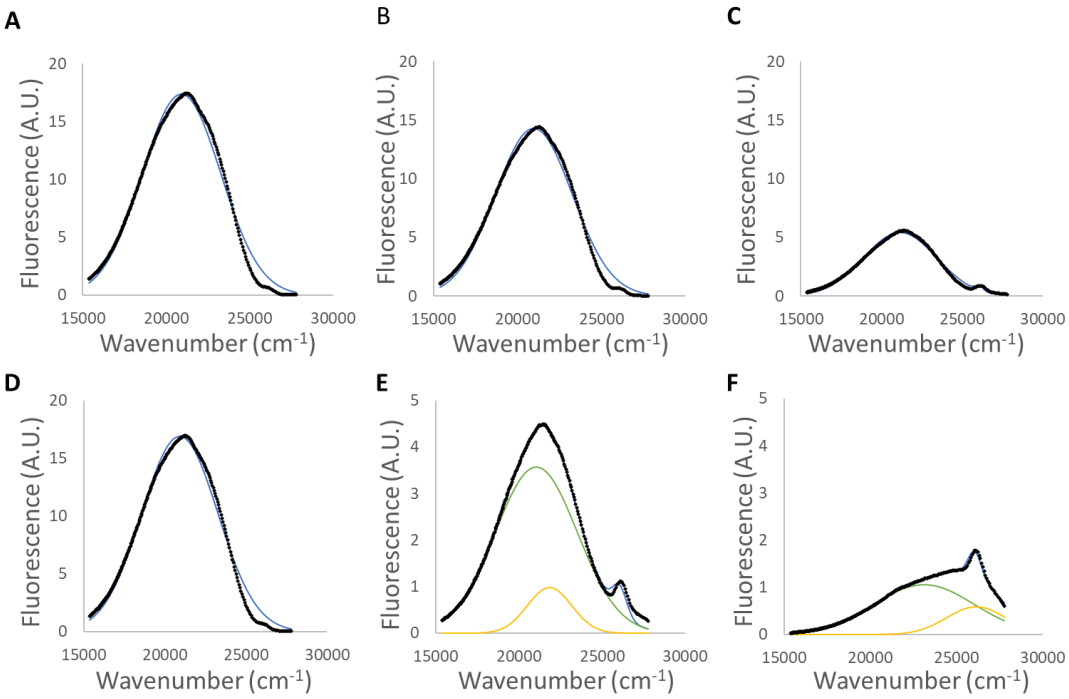

Figure C1.1 Examples of fitting the fluorescence emission spectra for NADH and NADH glucose in PBS to a Toptygin model. Plots A, B, and C show NADH, and plots D, E, and F show NADH-glucose. The experimental emission spectra is shown by the black markers, and the model is shown as the blue line. For Days 14 and 25 for NADH-glucose, the green and yellow lines show the first and second components of the model respectively. Days 4, 14, and 25 are shown as examples.

10.3.2 Appendix C2: Raw TCSPC Analysis for NADH and NADH-Glucose Samples

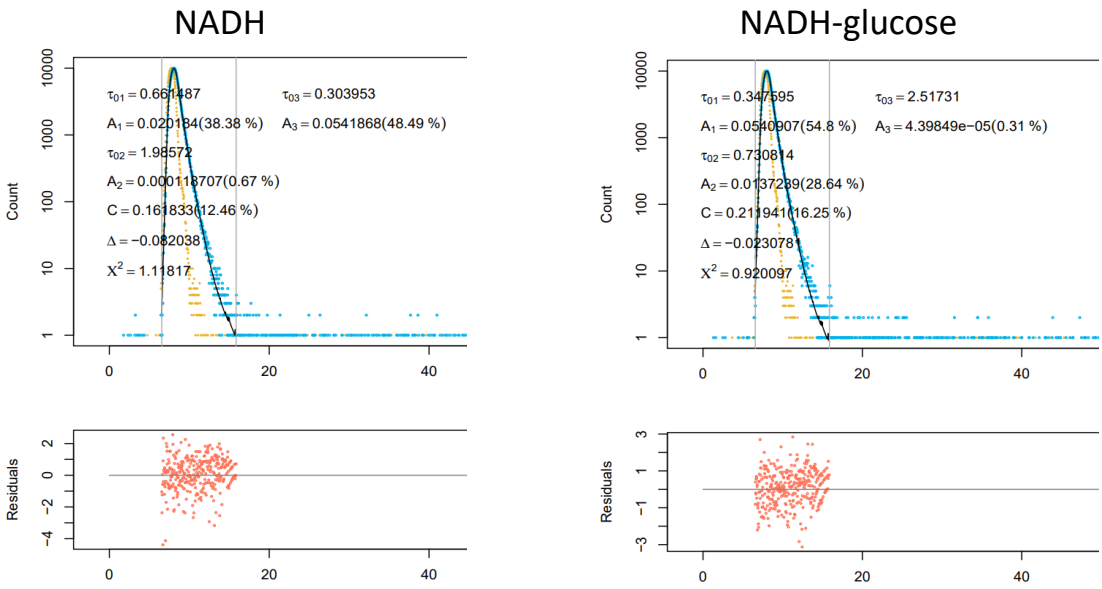

	τ_1 (ns)	A_1/%	τ_2 (ns)	A_2/%	τ_3 (ns)	A_3/%	C (%)	X^2
NADH	0.30	0.0542/ 48.49	0.66	0.0202/ 38.38	1.99	1.19E-4/ 0.67	12.46	1.12
NADH+ glucose	0.35	0.0541/ 54.8	0.73	0.0137/ 28.64	2.52	4.40E-5/ 0.31	16.25	0.92

Figure C2.1. Result of fitting of the fluorescence intensity decay of the samples NADH and NADH-glucose in PBS at day 2. Excitation wavelength 340 nm, detection wavelength 525 nm.

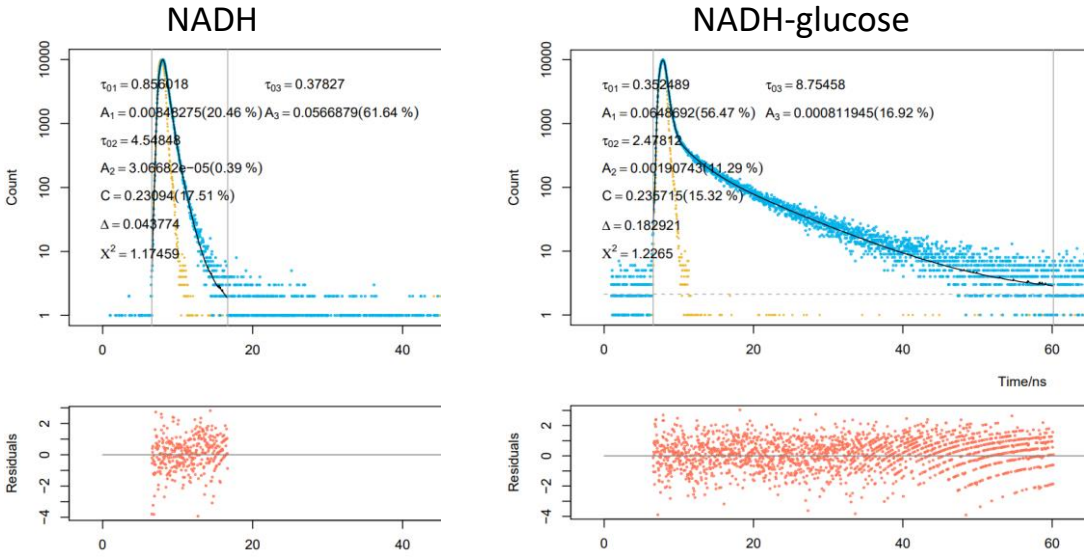

	τ_1 (ns)	A_1/%	τ_2 (ns)	A_2/%	τ_3 (ns)	A_3/%	C (%)	X^2
NADH	0.38	0.0567/ 61.64	0.86	0.00848/ 20.46	4.55	3.07E-5/ 0.39	17.51	1.18
NADH+ glucose	0.35	0.0649/ 56.47	2.48	0.00191/ 11.29	8.75	8.12E-4/ 16.92	15.32	1.23

Figure C2.2. Result of fitting of the fluorescence intensity decay of the samples NADH and NADH-glucose in PBS at day 23. Excitation wavelength 340 nm, detection wavelength 525

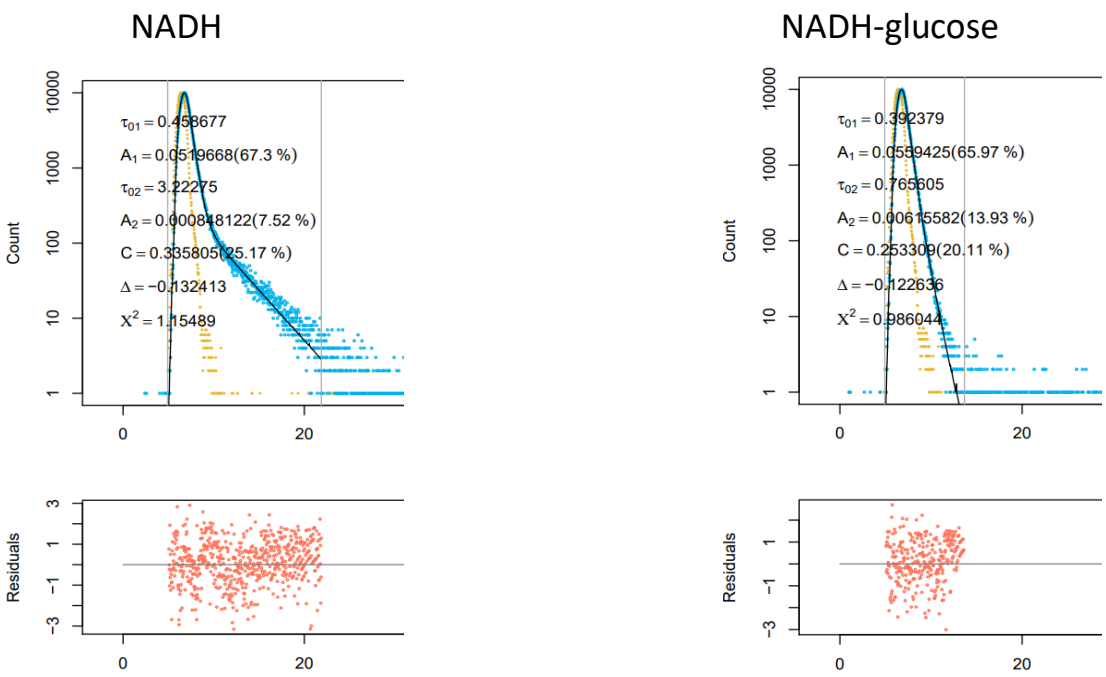

	τ_1 (ns)	A_1/%	τ_2 (ns)	A_2/%	τ_3 (ns)	A_3/%	C (%)	X^2
NADH	0.45	0.0520/ 67.3	3.22	0.000848/ 7.52			25.17	1.15
NADH+ glucose	0.39	0.0559/ 65.97	0.77	0.00616/ 13.93			20.11	0.99

Figure C2.3. Result of fitting of the fluorescence intensity decay of the samples NADH and NADH-glucose in Trizma at day 2. Excitation wavelength 340 nm, detection wavelength 525 nm.

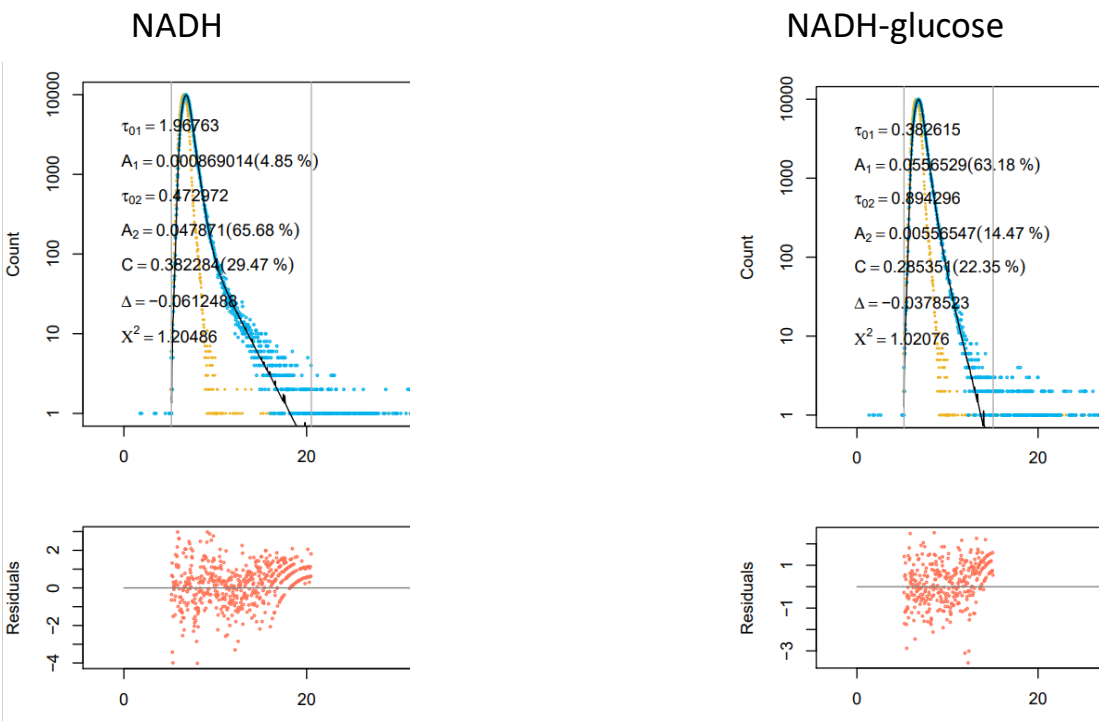

	τ_1 (ns)	A_1/%	τ_2 (ns)	A_2/%	τ_3 (ns)	A_3/%	C (%)	X^2
NADH	0.47	0.0478/ 65.68	1.97	0.000869/ 4.85			29.47	1.20
NADH+ glucose	0.38	0.0557/ 63.18	0.89	0.00557/ 14.47			22.35	1.02

Figure C2.4. Result of fitting of the fluorescence intensity decay of the samples NADH and NADH-glucose in Trizma at day 24. Excitation wavelength 340 nm, detection wavelength 525 nm.

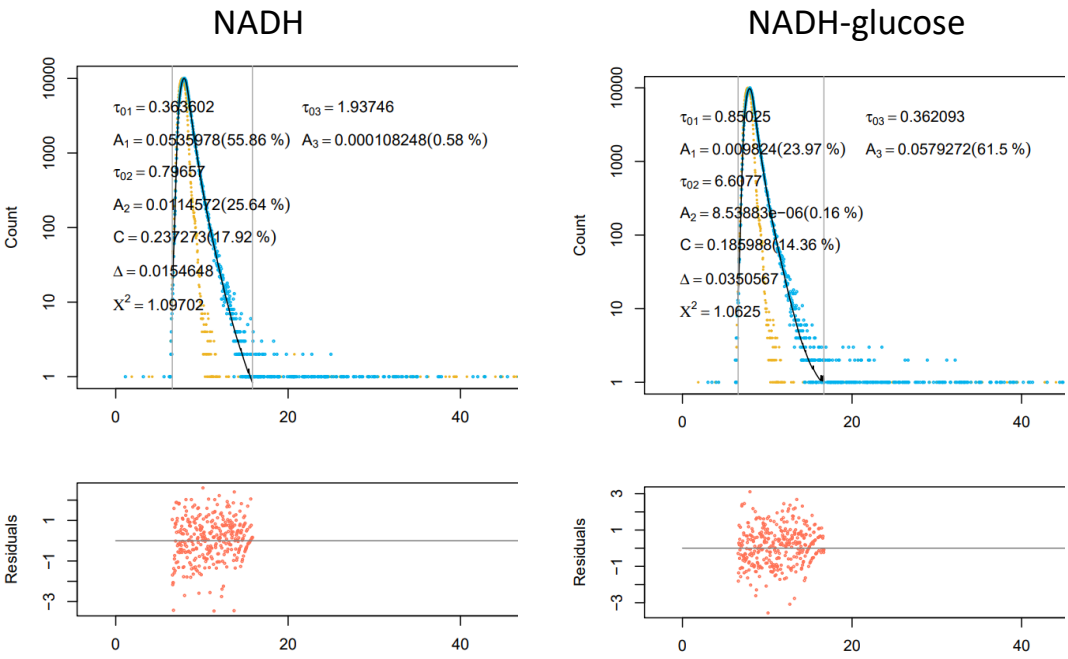

	τ_1 (ns)	A_1/%	τ_2 (ns)	A_2/%	τ_3 (ns)	A_3/%	C (%)	X^2
NADH	0.36	0.0536/ 55.86	0.80	0.0115/ 25.64	1.94	1.08E-4/ 0.58	17.92	1.10
NADH+ glucose	0.36	0.0579/ 61.5	0.85	0.00982/ 23.97	6.61	8.54E-6/ 0.16	14.36	1.06

Figure C2.. Result of fitting of the fluorescence intensity decay of the samples NADH and NADH-glucose in PBS at day 4. Excitation wavelength 340 nm, detection wavelength 470 nm.

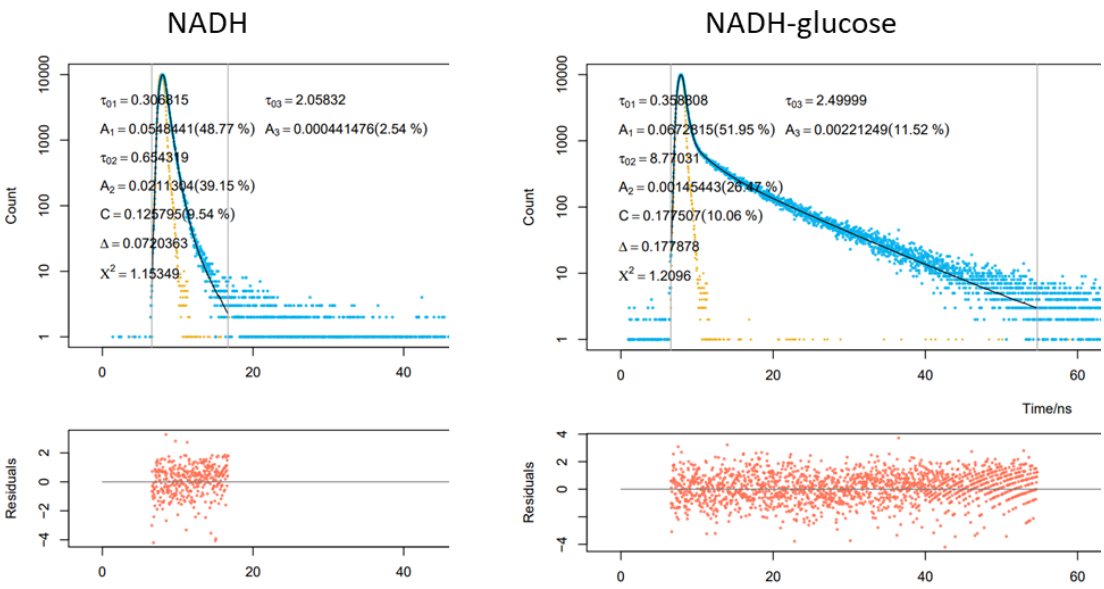

	τ_1 (ns)	A_1/%	τ_2 (ns)	A_2/%	τ_3 (ns)	A_3/%	C (%)	X^2
NADH	0.31	0.0548/ 48.77	0.65	0.0211/ 39.15	2.06	4.41E-4/ 2.54	9.54	1.15
NADH+ glucose	0.36	0.0673/ 51.95	2.50	0.00221/ 11.52	8.77	0.00145/ 26.47	10.06	1.21

Figure C2 Result of fitting of the fluorescence intensity decay of the samples NADH and NADH-glucose in PBS at day 23. Excitation wavelength 340 nm, detection wavelength 470 nm.

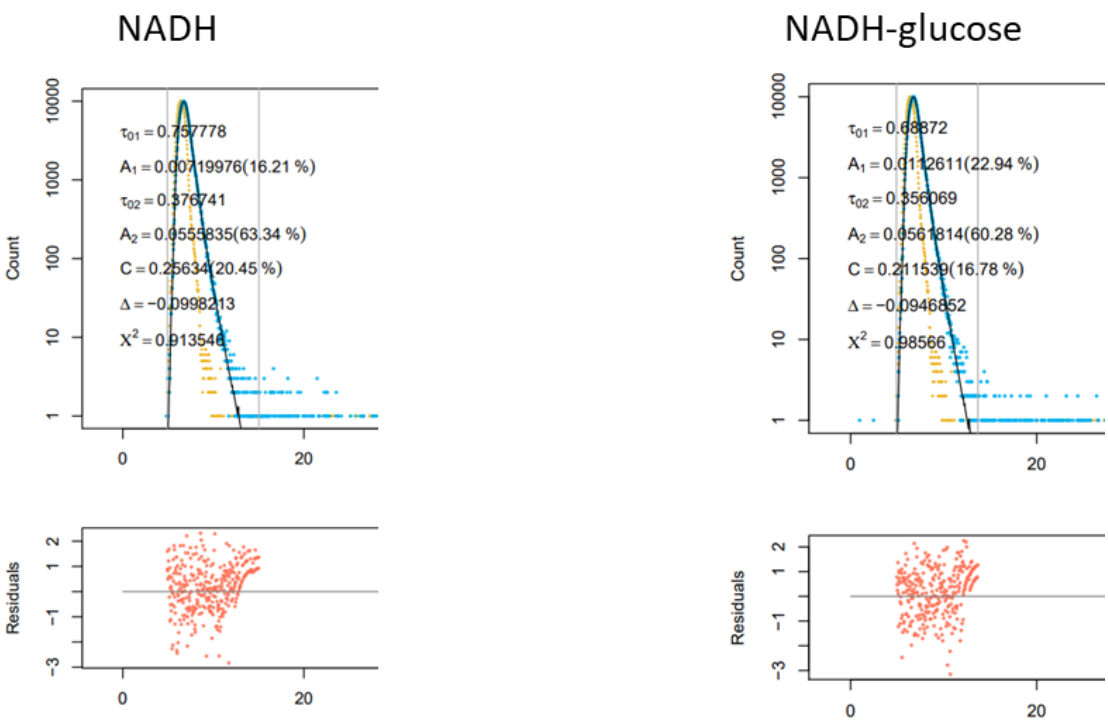

	τ_1 (ns)	A_1/%	τ_2 (ns)	A_2/%	τ_3 (ns)	A_3/%	C (%)	X^2
NADH	0.38	0.0556/ 63.34	0.76	0.0072/ 16.21			20.45	0.91
NADH+ glucose	0.36	0.0562/ 60.28	0.69	0.0113/ 22.94			16.78	0.99

Figure C2.7. Result of fitting of the fluorescence intensity decay of the samples NADH and NADH-glucose in Tris at day 2. Excitation wavelength 340 nm, detection wavelength 470 nm.

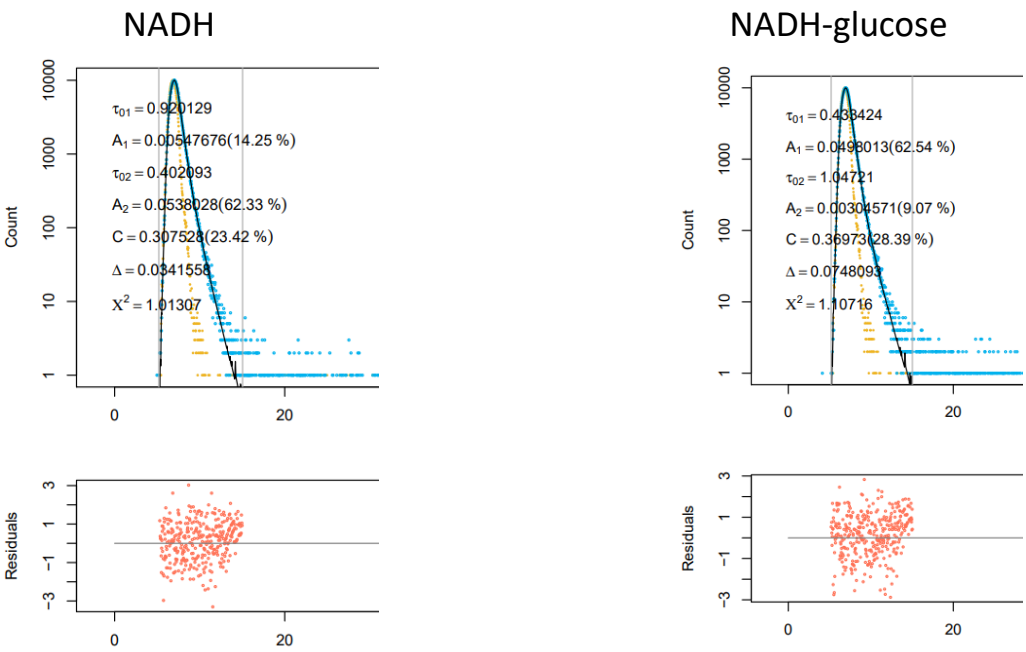

	τ_1 (ns)	A_1/%	τ_2 (ns)	A_2/%	τ_3 (ns)	A_3/%	C (%)	X^2
NADH	0.40	0.0538/ 62.33	0.92	0.00548/ 14.25			23.42	1.01
NADH+ glucose	0.43	0.0498/ 62.54	1.05	0.00305/ 9.07			28.39	1.11

Figure C2.8. Result of fitting of the fluorescence intensity decay of the samples NADH and NADH-glucose in Tris at day 21. Excitation wavelength 340 nm, detection wavelength 470 nm.

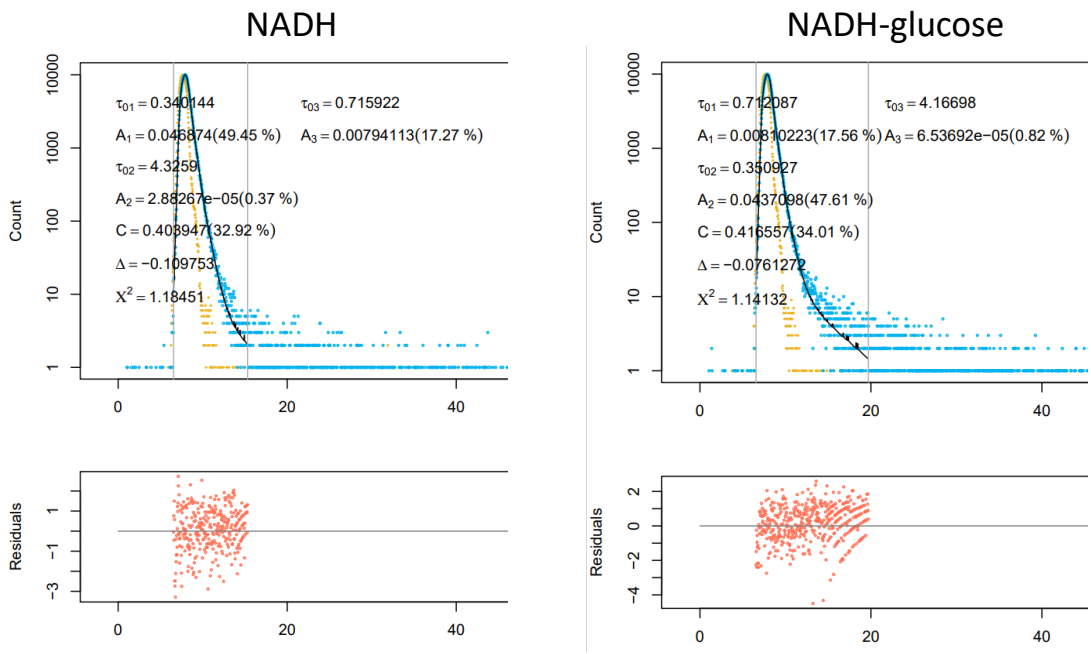

	τ_1 (ns)	A_1/%	τ_2 (ns)	A_2/%	τ_3 (ns)	A_3/%	C (%)	X^2
NADH	0.34	0.0469/ 49.45	0.72	0.00794/ 17.27	4.33	2.88E-5/ 0.37	32.92	1.18
NADH+ glucose	0.35	0.0437/ 47.61	0.71	0.00810/ 17.56	4.17	6.54E-5/ 0.82	34.01	1.14

Figure C2.9. Result of fitting of the fluorescence intensity decay of the samples NADH and NADH-glucose in PBS at day 0. Excitation wavelength 340 nm, detection wavelength 390 nm.

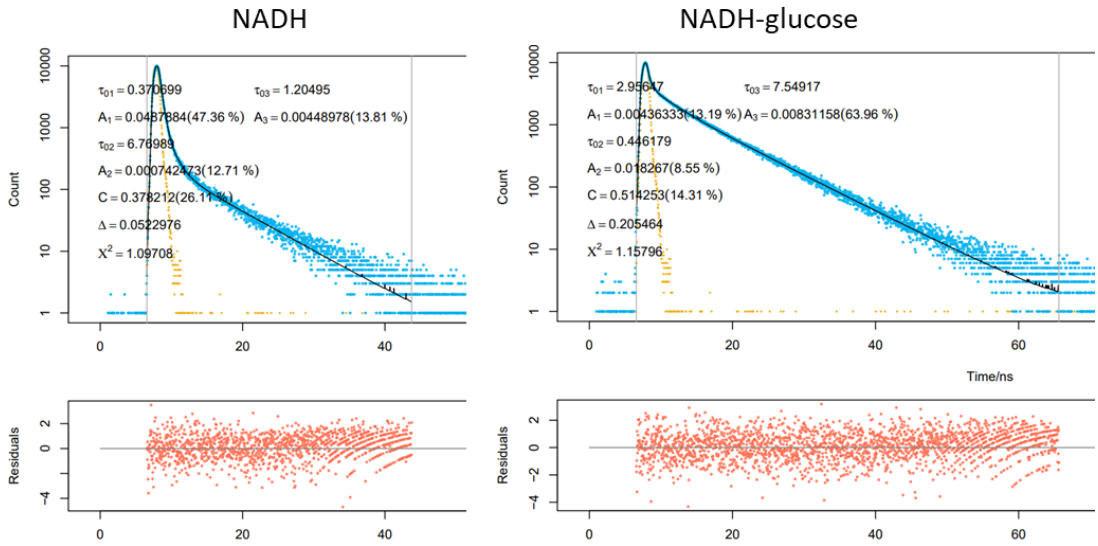

	τ_1 (ns)	A_1/%	τ_2 (ns)	A_2/%	τ_3 (ns)	A_3/%	C (%)	X^2
NADH	0.37	0.0488/ 47.36	1.20	0.00449/ 13.81	6.77	7.42E-4/ 12.71	26.11	1.10
NADH+ glucose	0.45	0.0183/ 8.55	2.96	0.00436/ 13.19	7.55	0.00831/ 63.96	14.31	1.16

Figure C2.10. Result of fitting of the fluorescence intensity decay of the samples NADH and NADH-glucose in PBS at day 23. Excitation wavelength 340 nm, detection wavelength 390 nm.

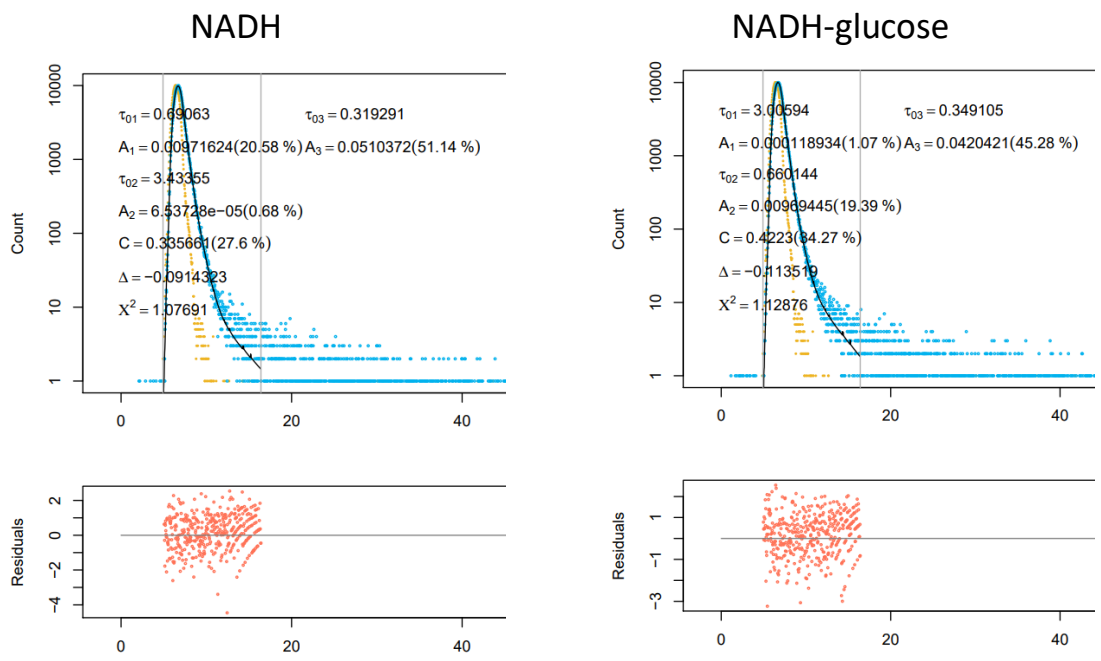

	τ_1 (ns)	A_1/%	τ_2 (ns)	A_2/%	τ_3 (ns)	A_3/%	C (%)	X^2
NADH	0.32	0.0510/ 51.14	0.69	0.00972/ 20.58	3.43	6.54E-5/ 0.68	27.60	1.08
NADH+ glucose	0.35	0.0420/ 45.28	0.66	0.00969/ 19.39	3.01	0.00119/ 1.07	34.27	1.13

Figure C2.11. Result of fitting of the fluorescence intensity decay of the samples NADH and NADH-glucose in Trizma at day 2. Excitation wavelength 340 nm, detection wavelength 390 nm.

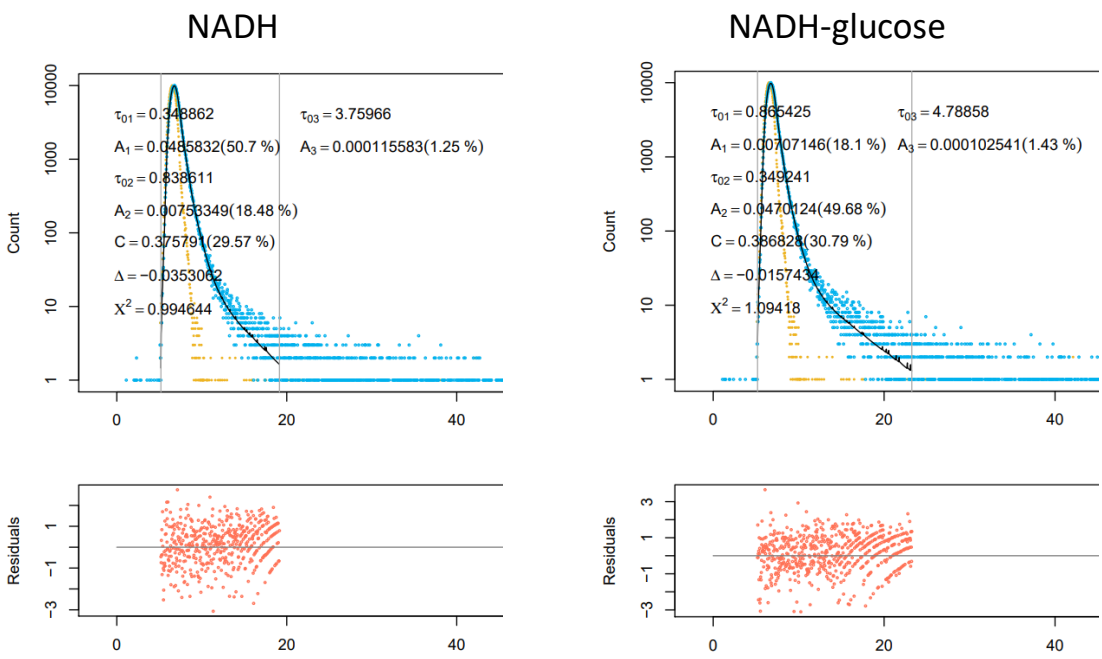

	τ_1 (ns)	A_1/%	τ_2 (ns)	A_2/%	τ_3 (ns)	A_3/%	C (%)	X^2
NADH	0.35	0.0486/ 50.07	0.84	0.00753/ 18.48	3.76	1.16E-4/ 1.25	29.57	0.99
NADH+ glucose	0.35	0.0470/ 49.68	0.87	0.00707/ 18.10	4.79	1.03E-4/ 1.43	30.79	1.09

Figure C2.12. Result of fitting of the fluorescence intensity decay of the samples NADH and NADH-glucose in Trizma at day 24. Excitation wavelength 340 nm, detection wavelength 390 nm.

10.4 Appendix D: Keratin

10.4.1 Appendix D1: Experimental vs Model of Fluorescence Emission of Keratin and Keratin-glucose Samples

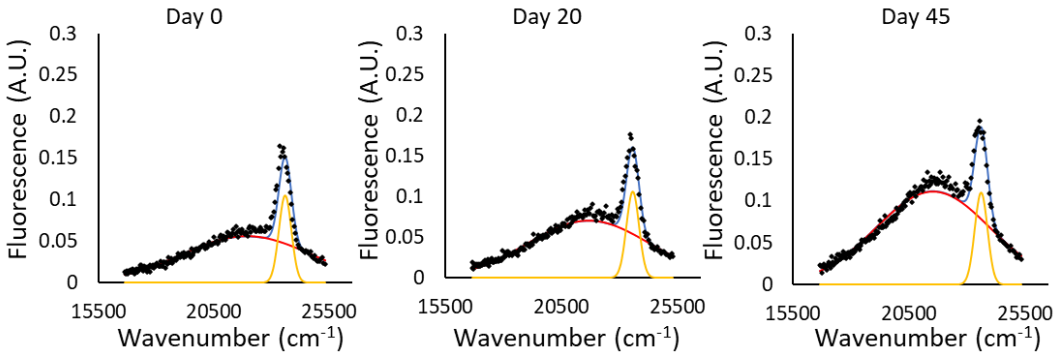

Figure D1.1. Examples of fitting the fluorescence emission spectra for keratin to a Gaussian model. The experimental emission spectra is shown by the black markers, and the model is shown as the blue line. The component that was fixed to account for Raman scattering is shown by the yellow line, and the one model component required is shown by the red line.

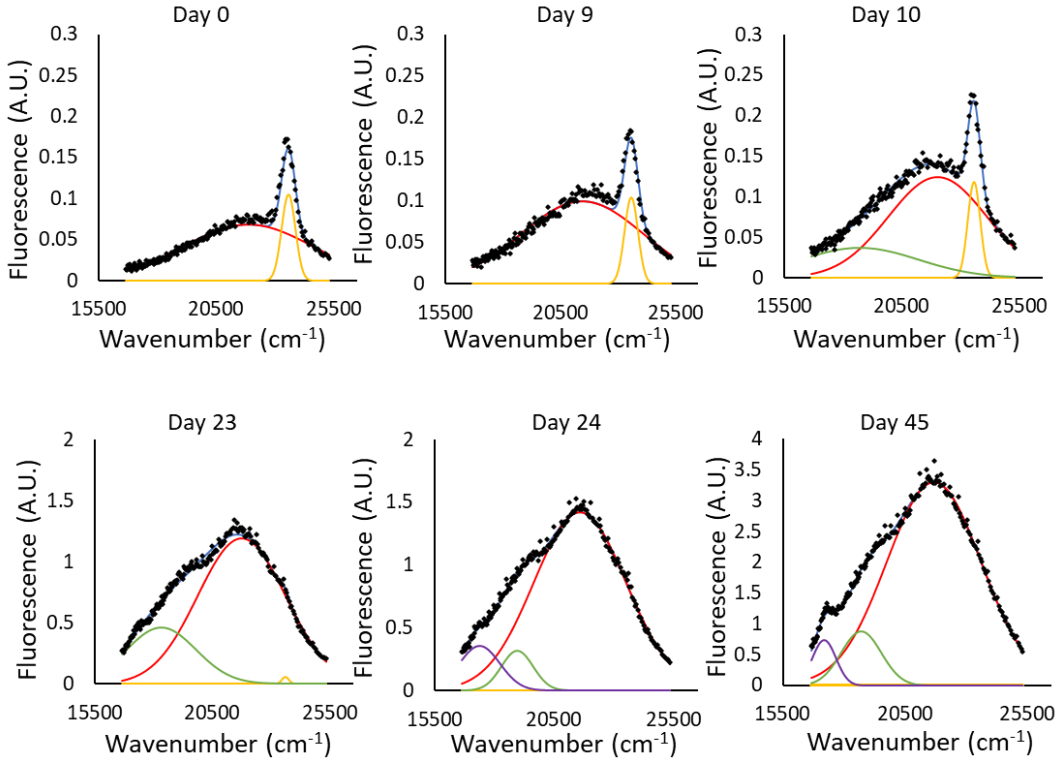

Figure D1.2. Examples of fitting the fluorescence emission spectra for keratin-glucose to a Gaussian model. The experimental emission spectra is shown by the black markers, and the model is shown as the blue line. The component that was fixed to account for Raman scattering is shown by the yellow line. The first model component is shown by the red line, the second component (required from day 10) and the third component (required from day 24) are shown by the green and purple lines respectively.

10..4.2 Appendix D2: Raw TCSPC Analysis for Keratin and Keratin-Glucose Samples

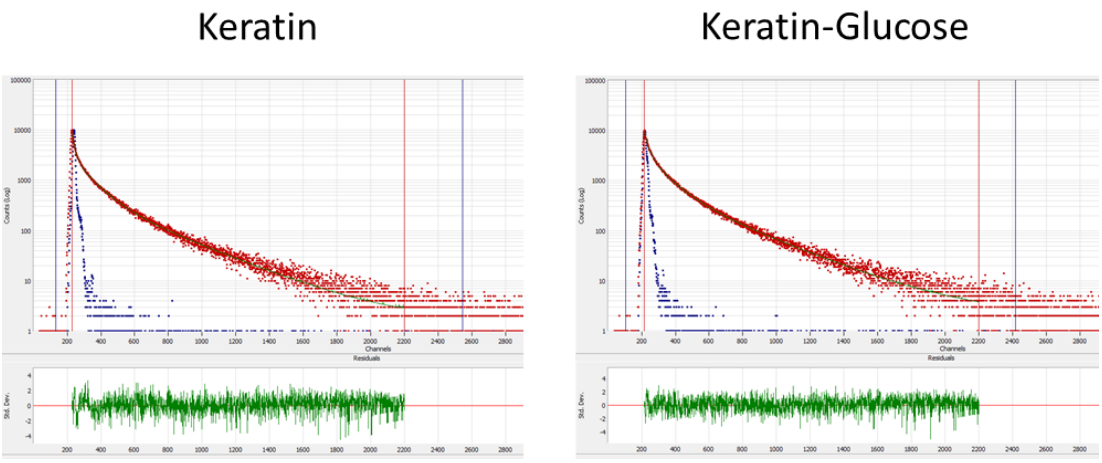

	τ_1 (ns)	A_1/%	τ_2 (ns)	A_2/%	τ_3 (ns)	A_3/%	C (%)	X^2
Keratin	0.47	0.0386/ 12.96	2.70	0.0147/ 28.24	8.76	0.00347/ 21.58	37.22	1.24
Keratin-glucose	0.75	0.0237/ 12.01	2.94	0.0140/ 27.62	8.81	0.00377/ 2.38	37.98	1.13

Figure D2.1. Result of fitting of the fluorescence intensity decay of the samples keratin and keratin-glucose at day 0. Excitation wavelength 370 nm, detection wavelength 460 nm.

Keratin Keratin-Glucose

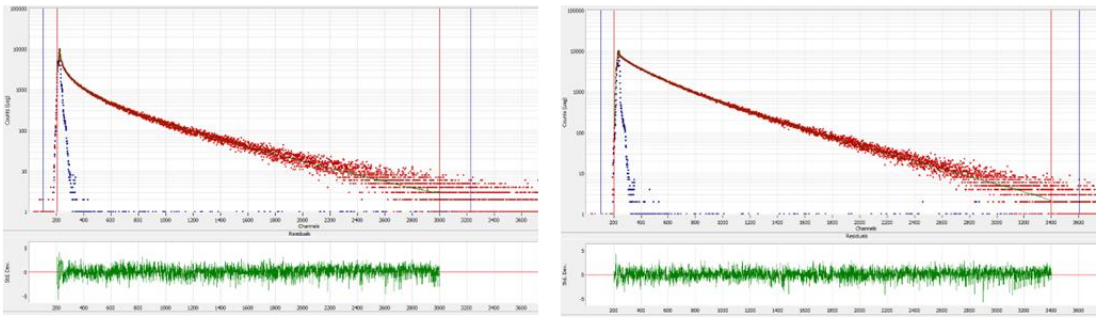

	τ_1 (ns)	A_1/%	τ_2 (ns)	A_2/%	τ_3 (ns)	A_3/%	C (%)	X^2
Keratin	0.84	0.0196/ 9.47	3.79	0.0117/ 25.95	12.94	0.00408/ 30.85	33.69	1.19
Keratin-glucose	1.05	0.0132/ 3.66	5.41	0.0283/ 40.38	12.44	0.0145/ 47.50	8.47	1.09

Figure D2.2. Result of fitting of the fluorescence intensity decay of the samples keratin and keratin-glucose at day 44. Excitation wavelength 370 nm, detection wavelength 460 nm.

10. 5 Appendix E: Human Serum Albumin

10. 5.1Appendix E1: Raw TCSPC Analysis for HSA and HSA-Glucose Samples

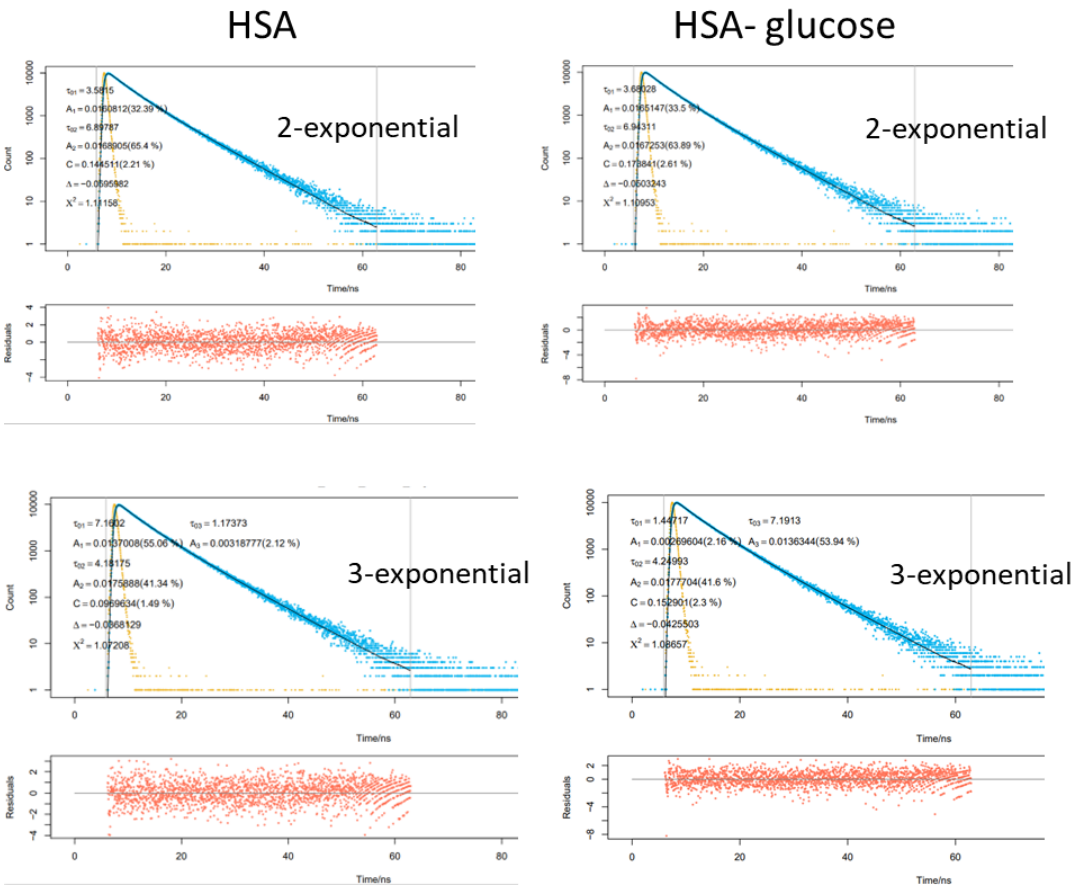

	τ_1 (ns)	A_1/%	τ_2 (ns)	A_2/%	τ_3 (ns)	A_3/%	C (%)	X^2
HSA (2 exp)	6.90	0.0169/ 65.41	3.58	0.0161/ 32.39			2.21	1.11
HSA- glucose (2 exp)	6.94	0.0167/ 63.89	3.68	0.0165/ 33.5			2.1	1.11
HSA (3 exp)	7.16	0.0137/ 55.06	4.18	0.0176/ 41.34	1.17	0.00319/ 2.12	1.49	1.07
HSA-glucose (3 exp)	7.19	0.0136/ 53. 94	4.25	0.0178/ 41.00	1.45	0.00296/ 2.16	2.3	1.09

Figure E1.1. Result of fitting of the fluorescence intensity decay to a 2-exponential and 3- exponential model for HSA and HSA-glucose at day 3. Excitation wavelength 280 nm, detection wavelength 340 nm**.**

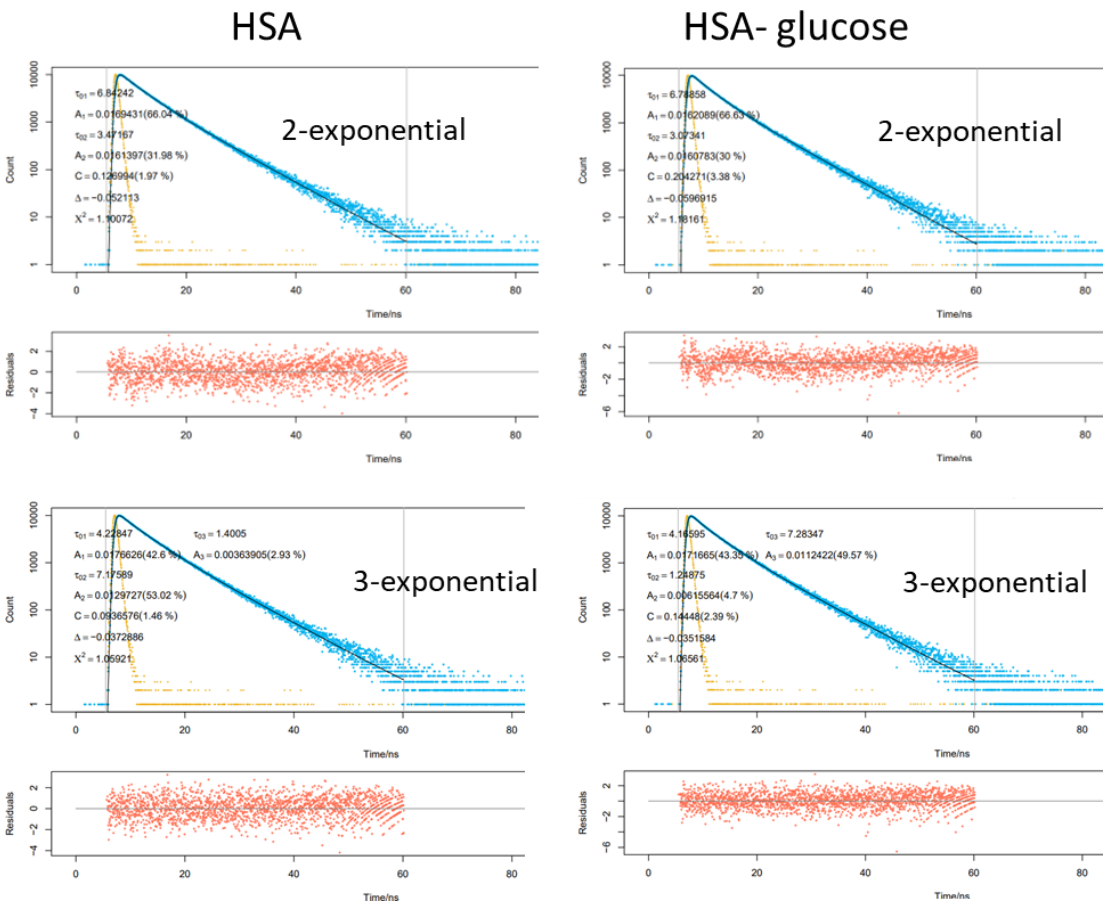

	τ_1 (ns)	A_1/%	τ_2 (ns)	A_2/%	τ_3 (ns)	A_3/%	C (%)	X^2
HSA (2 exp)	6.84	0.0169/ 66.04	3.47	0.0161/ 31.98			1.97	1.10
HSA- glucose (2 exp)	6.79	0.0162/ 66.63	3.07	0.0161/ 30.00			3.38	1.18
HSA (3 exp)	7.17	0.0123/ 53.02	4.23	0.0177/ 42.60	1.40	0.00364/ 2.93	1.46	1.06
HSA-glucose (3 exp)	7.28	0.0112/ 49.57	4.12	0.0172/ 43.35	1.25	0.00616/ 4.7	2.39	1.07

Figure E1.2. Result of fitting of the fluorescence intensity decay to 2-exponential and 3-exponential model for HSA and HSA-glucose at day 49. Excitation wavelength 280 nm, detection wavelength 340 nm.

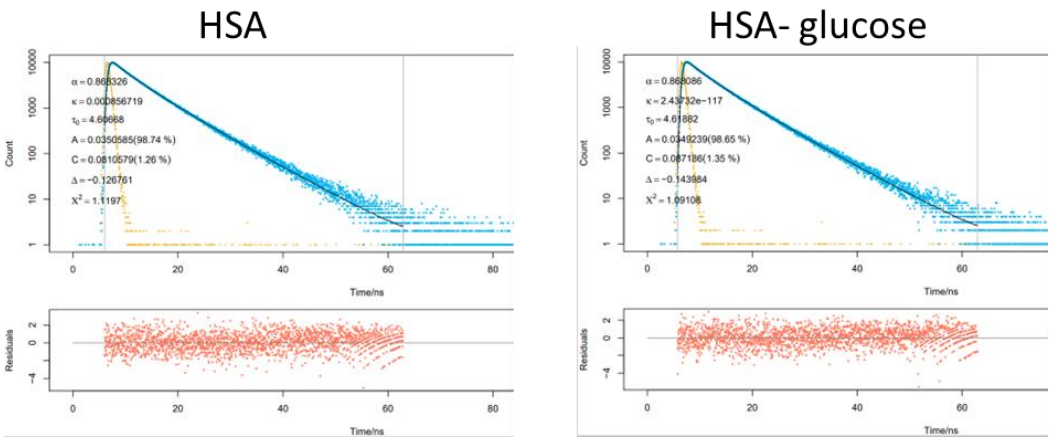

	α	κ	τ (ns)	C (%)	X^2
HSA	0.88	8.57E-4	4.61	1.26	1.12
HSA- glucose	0.87	2.44E-117	4.62	1.35	1.09

Figure E1.3. Result of fitting of the fluorescence intensity decay to a non-Debye model for HSA and HSA-glucose at day 0. Excitation wavelength 280 nm, detection wavelength 340 nm.

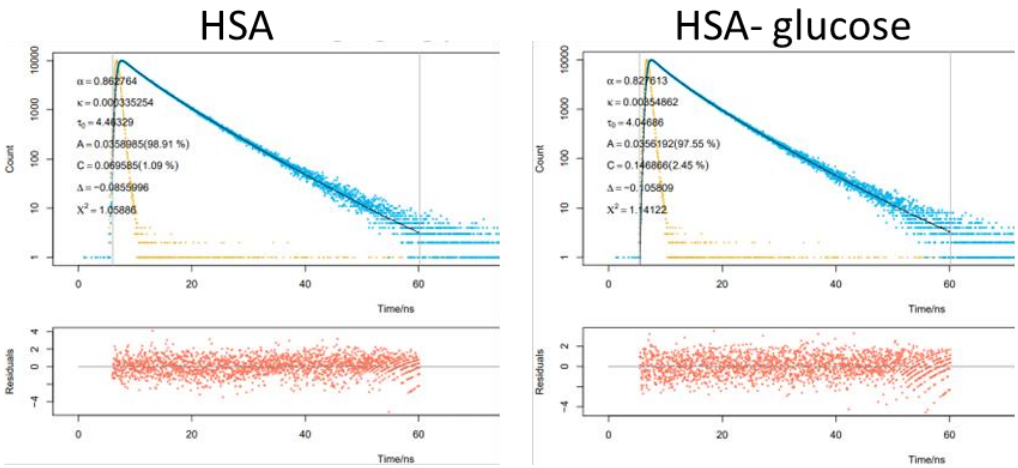

	α	κ	τ (ns)	C (%)	X^2
HSA	0.86	3.35E-4	4.46	1.09	1.06
HSA- glucose	0.83	3.55E-3	4.05	2.45	1.14

Figure E1.4. Result of fitting of the fluorescence intensity decay to a non-Debye model for HSA and HSA-glucose at day 52. Excitation wavelength 280 nm, detection wavelength 340 nm.

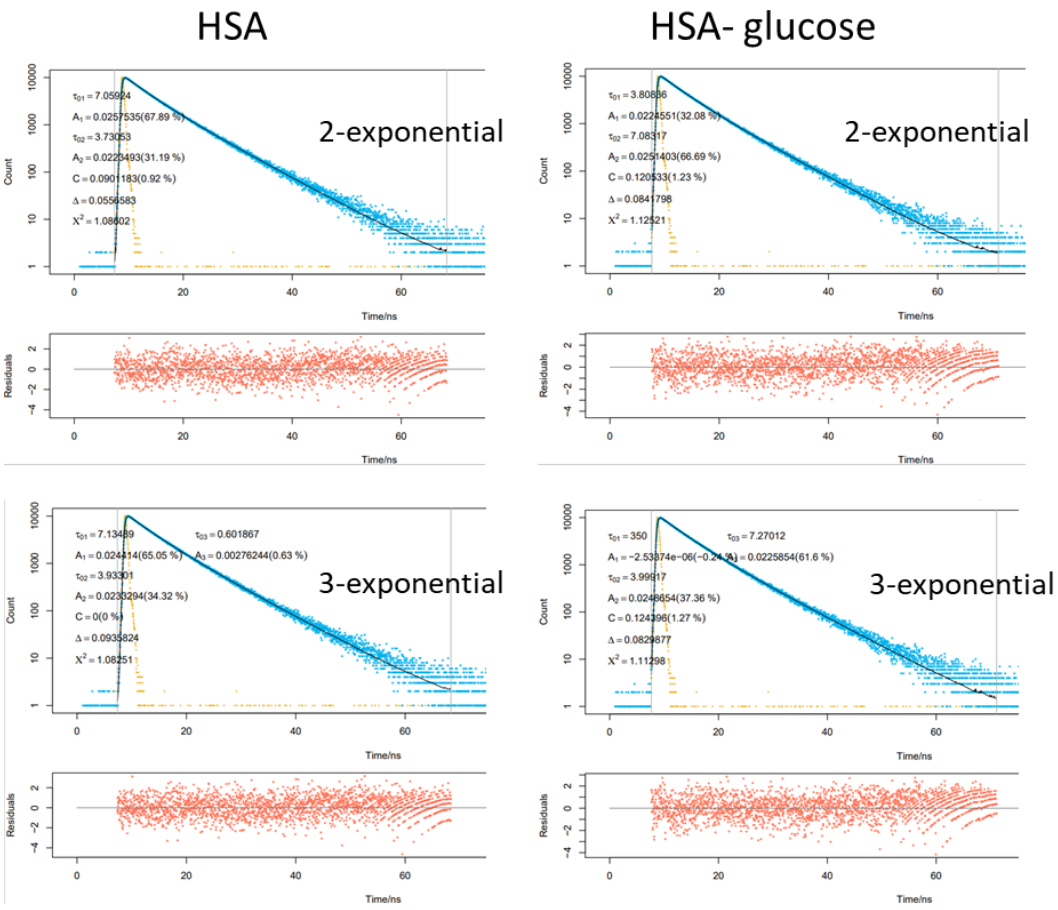

	τ_1 (ns)	A_1/%	τ_2 (ns)	A_2/%	τ_3 (ns)	A_3/%	C (%)	X^2
HSA (2 exp)	7.09	0.0258/ 67.89	3.73	0.0223/ 31.19			0.92	1.09
HSA- glucose (2 exp)	7.08	0.021/ 66.69	3.81	0.0225/ 32.08			1.23	1.13
HSA (3 exp)	7.13	0.0244/ 65.05	3.93	0.0233/ 34.32	0.60	0.00276/ 0.63	0	1.08
HSA-glucose (3 exp)	7.27	0.0226/ 61.6	4.00	0.0249/ 37.36	350	-2.53E-6/ -0.24	1.27	1.11

Figure E1.5. Result of fitting of the fluorescence intensity decay to a 2-exponential and 3-exponential model for HSA and HSA-glucose at day 1. Excitation wavelength 295 nm, detection wavelength 340 nm.

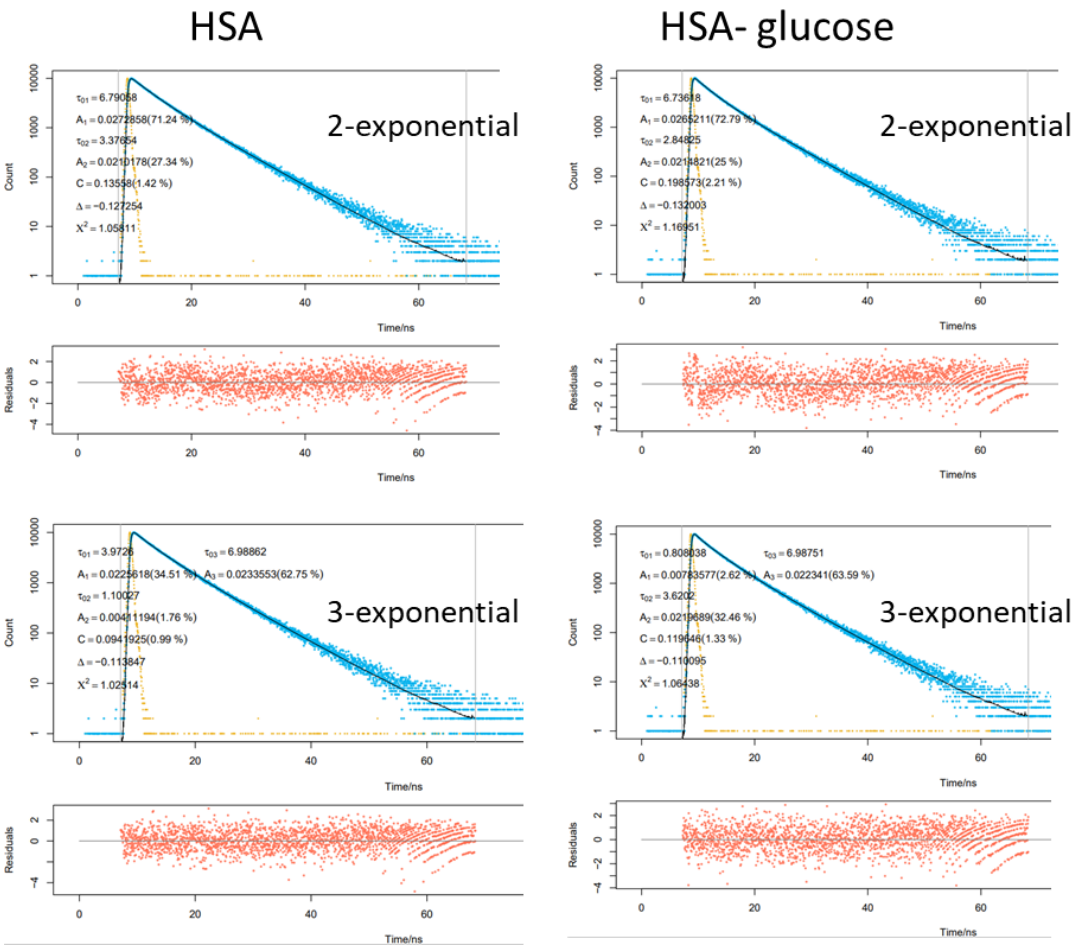

	τ_1 (ns)	A_1/%	τ_2 (ns)	A_2/%	τ_3 (ns)	A_3/%	C (%)	X^2
HSA (2 exp)	6.79	0.0273/ 71.24	3.38	0.0210/ 27.34			1.42	1.06
HSA- glucose (2 exp)	6.74	0.0265/ 72.79	2.85	0.0215/ 25.00			1.21	1.17
HSA (3 exp)	6.98	0.0234/ 62.75	3.97	0.0226/ 34.51	1.10	0.00411/ 1.76	0.99	1.03
HSA-glucose (3 exp)	6.98	0.0223/ 63.59	3.26	0.0220/ 32.46	0.81	0.00784/ 2.62	1.33	1.06

Figure E1.6. Result of fitting of the fluorescence intensity decay to a 2-exponential and 3-exponential model for HSA and HSA-glucose at day 49. Excitation wavelength 295 nm, detection wavelength 340 nm.

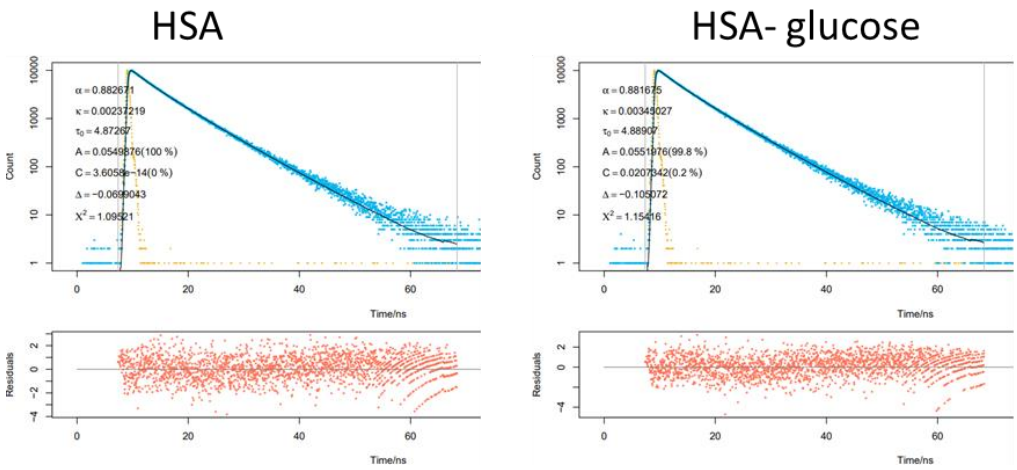

	α	κ	τ (ns)	C (%)	X^2
HSA	0.88	0.00397	4.87	0	1.10
HSA- glucose	0.88	0.00345	4.90	0.2	1.15

Figure E1.7. Result of fitting of the fluorescence intensity decay to a non-Debye model for HSA and HSA-glucose at day 3. Excitation wavelength 295 nm, detection wavelength 340 nm.

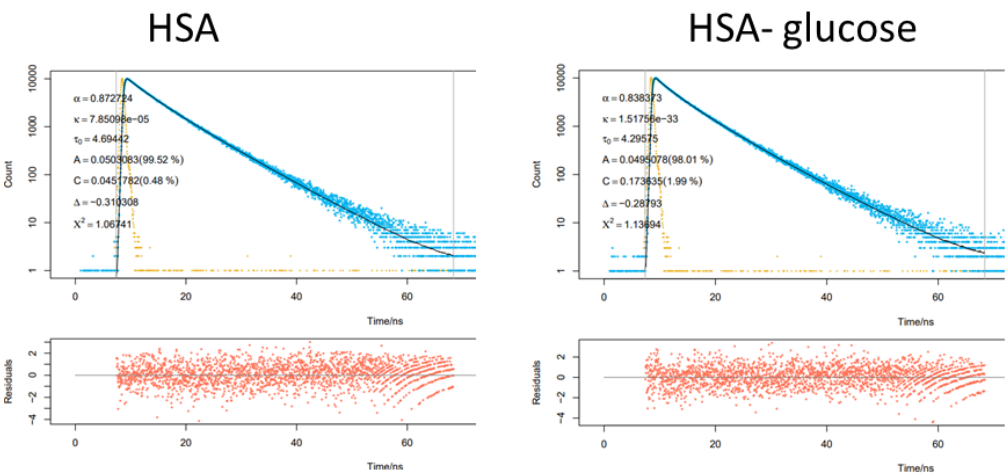

	α	κ	τ (ns)	C (%)	X^2
HSA	0.87	7.8E-5	4. 69	0.48	1.07
HSA- glucose	0.84	1.52E-33	4.30	1.99	1.14

Figure E1.8. Result of fitting of the fluorescence intensity decay to a non-Debye model for HSA and HSA-glucose at day 52. Excitation wavelength 295 nm, detection wavelength 340 nm.

10.6 Appendix F: Nail Glycation

10.6.1 Appendix F1: Raw TCSPC Analysis for Fluorescence Intensity Decays from Nail Samples

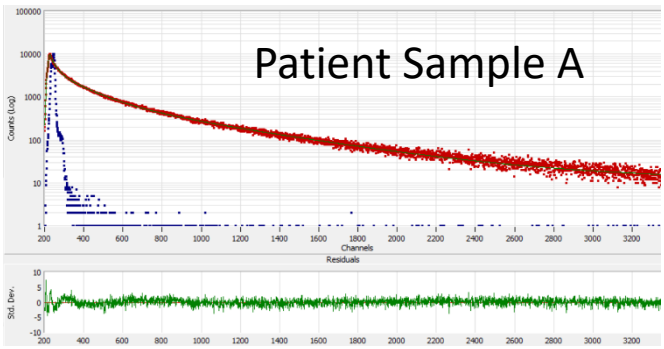

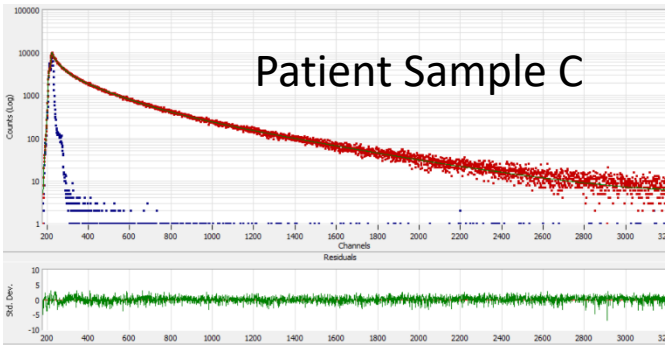

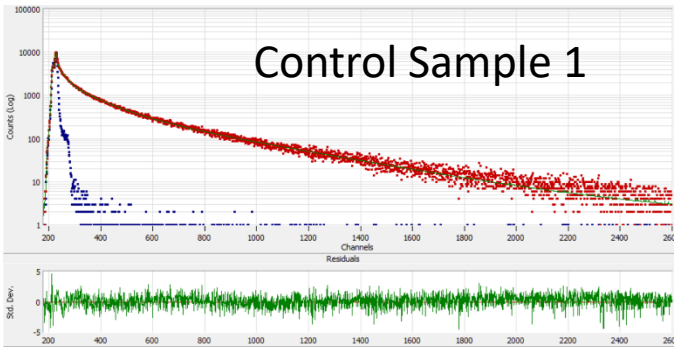

	τ_1 (ns)	A_1/%	τ_2 (ns)	A_2/%	τ_3 (ns)	A_3/%	X^2
Sample A	0.68	0.628/ 15.31	3.90	0.291/40.31	15.45	0.0808/ 44.38	1.22
Sample C	0.91	0.568/ 15.66	4.37	0.335/ 44.59	13.44	0.0972/ 39.75	1.11
Control 1	0. 63	0.655/ 19.8	3.16	0.270/ 40.70	11.04	0.0750/ 39.50	1.15

Figure F1.1. Result of fitting of the fluorescence intensity decay from 3 nail samples to a 3-exponential model. Excitation wavelength 370 nm, detection wavelength 460 nm. A 4th component set equal to 0.5 channel width was added to account for scatter. This was then manually removed and the A parameters were recalculated.

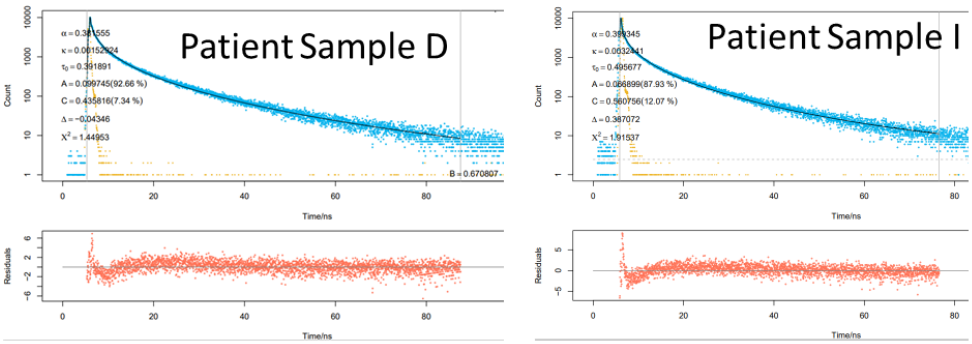

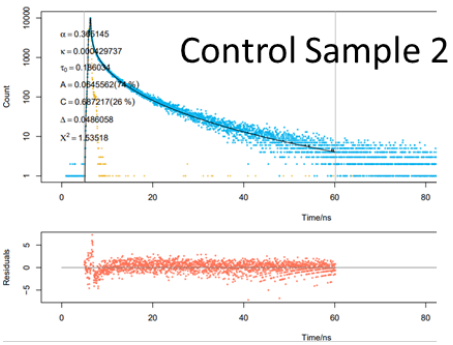

	α	κ	τ (ns)	C (%)	X^2
Sample D	0.38	0.00153	0.39	7.34	1.45
Sample I	0.40	0.00324	0. 50	12.07	1.92
Control 2	0.37	0.000430	0.18	26	1.54

Figure F1.2. Result of fitting of the fluorescence intensity decay from 3 nail samples to a non-Debye model. Excitation wavelength 370 nm, detection wavelength 460 nm

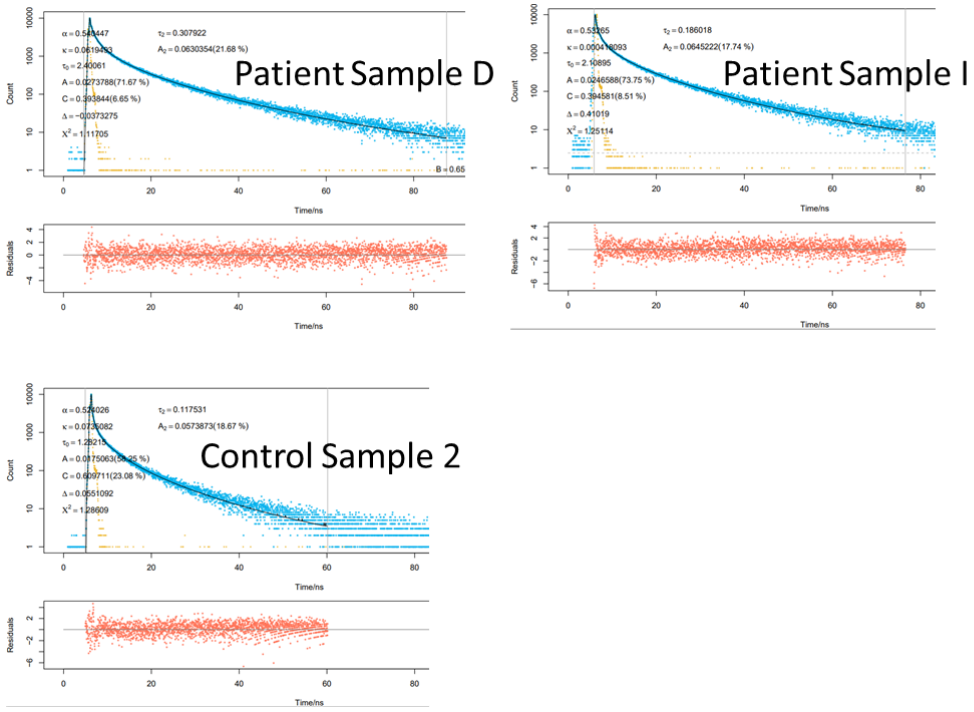

	α	κ	τ_1 (ns)/%	τ_2 (ns)/%	C (%)	X^2
Sample D	0.54	0.0619	2.40/ 71.67	0.31/ 21.68	6.65	1.12
Sample I	0.53	4.18E-4	2.11/ 73.75	0.19/ 17.74	8.51	1.2
Control 2	0.52	0.0735	1.28/ 58.25	0.12/ 18.67	23.08	1.29

Figure F1.3. Result of fitting of the fluorescence intensity decay from 3 nail samples to a 2 component non-Debye model. Excitation wavelength 370 nm, detection wavelength 460 nm

10.6.2 Appendix F2: Unpaired T-Test for Mean Lifetime of Nail Samples from Patients with Diabetes and Heathy Controls

Table F1.1 Summarised data from the 2 participant groups, where $\bar{x}$ is the mean, S is the standard deviation, and n is the number of samples included

	Patients (p)	**Control (c)**
$\bar{x}$	2.3429	1.7350
S	0. 6216	0. 5162
n	14	2

T-Test Calculation

To determine if there was a statistically significant difference between the mean lifetimes of the two participant groups, the following calculation was used.

1. Difference in means:
   $\bar{x}_p - \bar{x}_c = 0.6079$

2. Pooled Standard Deviation:

   $$S_p = \sqrt{\frac{(n_p\text{-}1)s_p{}^2+(n_c\text{-}1)s_c{}^2}{n_p+n_c\text{-}2}} = 0.614673$$

3. Standard Error:

   $$SE(\bar{x}_p - \bar{x}_c) = S_p\sqrt{\frac{1}{n_p}+\frac{1}{n_p}} = 0.464648$$

4. T Statistic:

   $$t = \frac{\bar{x}_p - \bar{x}_c}{SE} = \frac{0.6079}{0.464648} = 1.3083$$

5. Degrees of Freedom DF:
   $DF = n_p + n_c - 2 = 14$

For t=1.3083 and DF =14, the critical p value $p = 0.2119$

By conventional criteria, the difference between the two sample groups is not statistically significant, and there is no difference in the mean fluorescence lifetime between the two sample groups.